

ADVERTIMENT. L'accés als continguts d'aquesta tesi queda condicionat a l'acceptació de les condicions d'ús establertes per la següent llicència Creative Commons:  <https://creativecommons.org/licenses/?lang=ca>

ADVERTENCIA. El acceso a los contenidos de esta tesis queda condicionado a la aceptación de las condiciones de uso establecidas por la siguiente licencia Creative Commons:  <https://creativecommons.org/licenses/?lang=es>

WARNING. The access to the contents of this doctoral thesis it is limited to the acceptance of the use conditions set by the following Creative Commons license:  <https://creativecommons.org/licenses/?lang=en>

Characterization, Modeling and Simulation of Variability and Stochastic Resonance Phenomena in RRAM Devices

Ph.D. Thesis

Written by
Emili Salvador Aguilera

Under supervision of
Enrique Miranda Castellano
and
Rosana Rodríguez Martínez

Ph. D. programme in Electronic and Telecommunication Engineering
Universitat Autònoma de Barcelona
Electronic Engineering Department

Bellaterra (Cerdanyola del Vallès), March 2025.



The undersigned, **Enrique Miranda Castellano** and **Rosana Rodríguez Martínez**, Professors of the Electronic Engineering Department (Engineering School) of the *Universitat Autònoma de Barcelona*,

CERTIFY:

That the thesis entitled “*Characterization, Modeling and Simulation of Variability and Stochastic Resonance Phenomena in RRAM Devices*” has been written by the Ph.D. candidate **Emili Salvador Aguilera** under their supervision, in fulfilment of the requirements of the Ph.D. programme in Electronic and Telecommunication Engineering.

And hereby to acknowledge the above, sign the present.

Signature: Emili Salvador Aguilera

Signature: Enrique Miranda Castellano

.....

.....

Signature: Rosana Rodríguez Martínez

.....

Universitat Autònoma de Barcelona
Engineering School
Electronic Engineering Department

Bellaterra (Cerdanyola del Vallès), July 2024.

Contents

| | |
|---|----|
| Contents..... | i |
| Acknowledgments | v |
| Motivation and Thesis Structure..... | 1 |
| 1. Introduction | 7 |
| 1.1 Resistive Switching Phenomenology | 8 |
| 1.1.1 Resistive Switching Modes..... | 8 |
| 1.1.2 Physical Mechanisms of Resistive Switching..... | 11 |
| 1.2 State of the Art: Properties and Challenges..... | 13 |
| 1.2.1 Variability in RRAM Devices | 15 |
| 1.2.2 Stochastic Resonance..... | 17 |
| 1.3 Applications | 21 |
| 1.3.1 Spike Timing-Dependent Plasticity | 26 |
| 1.3.2 Homeostasis | 28 |
| 1.4 RRAM Modeling..... | 30 |
| 1.4.1 Classification of RRAM Models..... | 31 |

| | | |
|-----------|---|-----------|
| 1.4.2. | Modeling C2C Variability in RRAMs | 34 |
| 1.4.3. | Modeling Stochastic Resonance in RRAMs | 38 |
| 1.5. | Highlights | 41 |
| 2. | Equipment and Fabrication..... | 43 |
| 2.1 | Equipment | 43 |
| 2.2 | Fabrication Process of RRAM Devices..... | 46 |
| 2.3 | Typical <i>I</i> - <i>V</i> Curves and Figures of Merit..... | 50 |
| 2.4 | Highlights | 52 |
| 3. | Modeling RRAM Devices and Cycle-to-Cycle Variability | 53 |
| 3.1. | Spice Modeling of Uncorrelated C2C Variability..... | 54 |
| 3.1.2 | Uncorrelated C2C Variability using the QMM | 60 |
| 3.1.3 | Uncorrelated C2C Variability using the DMM | 65 |
| 3.2 | Modeling Correlated C2C Variability | 70 |
| 3.2.1 | The Ornstein-Uhlenbeck Process | 72 |
| 3.2.2 | Correlated C2C Variability in LTspice..... | 73 |
| 3.2.3 | Correlated C2C Variability in the DMM | 76 |
| 3.3. | Matlab Version of the Dynamic Memdiode Model | 79 |
| 3.3.1. | Matlab Modeling of Uncorrelated C2C Variability | 83 |
| 3.4. | Highlights | 85 |
| 4. | Stochastic Resonance in RRAM Devices | 87 |
| 4.1. | Stochastic Resonance Applying DC Voltage Sweeps | 88 |
| 4.1.1. | Experimental SR Applying DC Voltage Sweeps | 88 |
| 4.1.2. | Simulating SR Applying DC Voltage Sweeps..... | 94 |
| 4.2. | Stochastic Resonance Applying AC Voltage Inputs..... | 96 |
| 4.2.1. | AC Setup 1 | 96 |
| 4.2.2. | AC Setup 2 | 100 |
| 4.2.3. | AC Setup 3 | 102 |

| | | |
|--------|---|------------|
| 4.3. | Impact of External Noise on the Binary STDP Protocol..... | 106 |
| 4.3.1. | Experimental Noise-Induced Binary STDP | 106 |
| 4.3.2. | Simulating STDP Activation via SR..... | 116 |
| 4.4. | Homeostasis in Memristor-Based Neuromorphic Systems | 118 |
| 4.4.1. | Noise-Induced Potentiation..... | 120 |
| 4.4.2. | Noise-Induced Homeostasis..... | 122 |
| 4.5. | Highlights | 125 |
| 5. | Conclusions and Future Work..... | 127 |
| | Conclusions..... | 127 |
| | Future Work..... | 129 |
| | References | 131 |
| | Articles in this Ph.D. Thesis..... | 151 |
| | Article SSE21 | 152 |
| | Article SSE23 | 159 |
| | Article SSE24 | 170 |
| | Article JLPEA24..... | 177 |
| | Article EDL24..... | 190 |
| | Article TED24..... | 195 |
| | Article TNANO24 | 202 |
| | TNANO24-SM Supplementary Material | 210 |
| | Complementary Works in the Ph.D. Thesis..... | 216 |
| | Conference MIEL21..... | 217 |
| | Review Section AIS23..... | 222 |
| | Conference ISCAS22..... | 229 |
| | Publications by the Author..... | 234 |
| | Journal Publications..... | 234 |
| | Workshop Contributions | 236 |

Acknowledgments

I would like to express my deepest gratitude to my supervisors, Prof. Enrique Miranda and Prof. Rosana Rodríguez, for their guidance, support, mentorship, and wisdom throughout the entire research process. Their experience and dedication have been pivotal to both the progress and outcome of this thesis. I feel incredibly fortunate to have worked under their supervision; they are truly elite professionals and exceptional individuals.

Special thanks to Prof. Albert Crespo for his invaluable mentorship and direction throughout this journey, particularly during its early stages. His expertise in the subject and equipment has been indispensable. I am also deeply grateful to Prof. Javier Martín for his proficiency with the equipment and software, Prof. Montse Nafría for her unwavering support and insight across the project, and Dr. Francesca Campabadal and Dr. Mireia Bargalló for their work in fabricating the devices for the experimental measurements in this thesis. Their collective contributions have been irreplaceable.

I would also like to recognize my colleagues Jonathan Muñoz, Alvaro Jaque, Anna Ruiz, Martí Raya, Matteo Villani, and Jan Coromina, who became essential parts of this journey. Initially, they introduced me to the department, and they quickly became not only colleagues but solid friends. Their support made this journey far richer, and now that they've moved on, I truly miss those early days.

To Carlos, Amir, Daniyal, Amir Hossein, Ahsan, Bruno and Zeyuan, thank you for the camaraderie we continue to share. I wish you all strength and motivation on your own paths toward achieving the Ph.D.

To my friends in Sabadell and my basketball teammates: your presence has been a quiet but powerful source of encouragement. You may not realize it, but your company and the good moments we share have contributed significantly to the completion of this work.

Finally, to my family, Josefa, Emilio, and Amaia, each of you is a pillar in my life, and each of you inspires me. Thank you for standing by my side, not only during this thesis journey but throughout all my life. I love you.

Heartfelt thanks to everyone who generously shared their time, love, and positivity, enriching my journey towards these years.

I like to say that life is all about learning, and I have learned so much from each of you.

Motivation and Thesis Structure

In recent decades, electronic devices have become essential elements in our daily lives. They are present in all aspects of our society, like communications, entertainment, home automation, health, emergency systems, among many others. The demand for smaller and more efficient devices forces the traditional semiconductor industry to reduce the size of its main elements. During the last years, the integration level has followed the trend of Moore's Law, however, nowadays it is facing its physical scaling limits, at the atomic scale. To address these challenges, emerging technologies are being explored, offering the potential to either complement or disrupt traditional approaches. Among these, memristors have garnered significant attention for their implementations in memory technologies such as resistive random-access memories (RRAMs). Beyond memory, their unique non-linear properties have opened new possibilities in fields like logic operations, analog circuits, cryptography, and neuromorphic systems. In neuromorphic computing, memristors are particularly promising for advancing beyond the limitations of traditional Von Neumann architectures, where separate memory and processing units create a bottleneck in speed and energy efficiency. With the increasing demands of artificial intelligence (AI) and the Internet of Things (IoT), post-Von Neumann paradigms that integrate memory and computation are essential. Memristors,

which can emulate biological phenomena with scalability and CMOS compatibility, offer a path toward realizing these architectures. Despite the extraordinary properties of memristors and their potential, for reaching full commercialization, this technology must overcome its most critical drawback, the dispersion or variability in the conduction characteristics.

This thesis tackles two critical aspects of the memristor technology. First, it focuses on characterizing and modeling the intrinsic variability of memristors. Experimental studies combined with robust compact models are essential for understanding, simulating, and predicting the behavior of these devices. Second, it investigates the impact of the stochastic resonance (SR) phenomenon on memristor's performance. SR, observed in non-linear systems exposed to noise, enhances system performance at optimal noise levels. Here, SR is examined at both individual memristor level, by analyzing the effects of injected noise on memristors, and within memristor-based neuromorphic systems, which aim to emulate brain functionality. As the brain is inherently noisy, exploring the influence of noise in neuromorphic systems is vital for developing practical and realistic implementations. These contributions help the advance of RRAM technology and promote the development of memristor-based neuromorphic systems.

This Ph.D. thesis has been written as a **compendium of articles**. Therefore, most of the research topics presented have been already published in international journals or conference proceedings. The list below presents the references for the articles related to this thesis:

SSE21: E. Salvador, M.B. Gonzalez, F. Campabadal, J. Martin-Martinez, R. Rodriguez, E. Miranda, ‘SPICE modeling of cycle-to-cycle variability in RRAM devices’, Solid-State Electronics, vol. 185, 108040, 2021.

SSE23: E. Salvador, M.B. Gonzalez, F. Campabadal, J. Martin-Martinez, R. Rodriguez, E. Miranda, ‘Assessment of the variability of the I-V characteristic of HfO₂-based resistive switching devices and its simulation using the quasi-static memdiode model’, Solid State Electronics, vol. 206, 108667, 2023.

SSE24: E. Salvador, R. Rodriguez, E. Miranda, ‘SPICE simulation of the time-dependent clustering model for dielectric breakdown’, *Solid-State Electronics*, vol. 215, 108895, 2024.

JLPEA24: E. Salvador, R. Rodriguez, E. Miranda, ‘A Simple, Robust, and Versatile MATLAB Formulation of the Dynamic Memdiode Model for Bipolar-Type Resistive Random Access Memory Devices’, *J. Low Power Electron. Appl.*, vol. 14, no. 2, p. 30, 2024.

EDL24: E. Salvador, R. Rodriguez, E. Miranda, J. Martin-Martinez, A. Rubio, A. Crespo-Yepes, V. Ntinis, G. Ch. Sirakoulis, M. Nafria, ‘Noise-induced homeostasis in memristor-based neuromorphic systems’, *IEEE Electron Device Letters*, vol. 45, no. 8, pp. 1524-1527, 2024.

TED24: E. Salvador, R. Rodriguez, E. Miranda, J. Martin-Martinez, A. Rubio, A. Crespo-Yepes, V. Ntinis, G. Ch. Sirakoulis, M. Nafria, ‘Stochastic Resonance in HfO₂-Based Memristors: Impact of External Noise on the Binary STDP Protocol’, *IEEE Transactions on Electron Devices*, vol. 71, no. 9, pp. 5761-5766, 2024.

TNANO24: E. Salvador, M.B. Gonzalez, F. Campabadal, J. Martin-Martinez, R. Rodriguez, E. Miranda, ‘Modeling and Simulation of Correlated Cycle-to-Cycle Variability in the Current-Voltage Hysteresis Loops of RRAM Devices’, *IEEE Transactions on Nanotechnology*, vol. 23, pp. 758-764, 2024.

The articles are included at the end of this thesis in the **Articles in this Ph.D. Thesis** section whereas in **Publications by the Author** listed all author's publications and conferences contributions. The publications have been co-authored by researchers from other institutions: Universitat Politècnica de Catalunya (UPC), Institut de Microelectrònica de Barcelona (IMB-CNM, CSIC), and the Democritus University of Thrace (DUTH).

The thesis is structured as follows:

- **Chapter 1** is an overview of RRAM technology, its mechanisms and applications. In addition, it presents the main topics related to this thesis, like RRAM modeling and stochastic resonance.

- **Chapter 2** presents the different equipment and setups used for RRAM characterization. The current-voltage (I - V) characteristics of RRAM devices and the intrinsic variability are shown and discussed in this chapter.
- **Chapter 3** contains the different strategies followed for incorporating the cycle to cycle (C2C) variability in a compact model for memristors. The chapter includes the previous considerations regarding the model and simulation process, the different approaches and the results obtained during this thesis. This chapter joins and completes information published in **SSE21**, **SSE23**, **SSE24** and **TNANO24** and in the complementary works **MIEL21** and **AIS23**.
- **Chapter 4** compiles the findings related to the Stochastic Resonance phenomenon. Firstly, the presented study is carried out at device level in DC and AC input signals. Secondly, the approaches for using RRAMs for neuromorphic system applications are incorporated. These applications are the spike-timing dependent plasticity (STDP) learning protocol, and the homeostatic regulation. This chapter joins and completes information published in **EDL24**, **TED24** and the complementary work **ISCAS22**.
- **Chapter 5** outlines the most important findings and results reported in this thesis as a conclusion. Considering all the advances in the different research lines, some future work emerging from the contents in this thesis is proposed.

The work conducted during the realization of this thesis was carried out within the research teams NANOCOMP (Computational Nanoelectronics) and REDEC (Reliability on Electron Device and Electric Circuits) both forming part of the SGR E2DEVICE group from the UAB Electronic Engineering Department.

This work has been funded by the Catalan and Spanish government through different projects. The projects that have given support to the developed activities are listed below:

- Project TEC2016-75151-C3-1-R funded by the Spanish ‘Programa Estatal de Investigación, Desarrollo e Innovación’.
- Project PID2019-103869RB-C32 funded by the Spanish ‘Ministerio de Ciencia e Innovación’ (MCIN) and ‘Agencia Estatal de Investigación’ (AEI).
- Project PID2022-136949OB-C22 funded by the Spanish ‘Ministerio de Ciencia e Innovación’ (MCIN) and ‘Agencia Estatal de Investigación’ (AEI).
- Project PID2022-139586NB-C41 funded by the Spanish ‘Ministerio de Ciencia e Innovación’ (MCIN) and ‘Agencia Estatal de Investigación’ (AEI).

Finally, this Ph.D. thesis has been supported by the predoctoral fellowship 2020FISDU00261 from the Catalan ‘Agència de Gestió d'Ajuts Universitaris i de Recerca (AGAUR)’.

Introduction

This chapter provides the fundamental concepts necessary for the further understanding of the contents in this thesis. Firstly, an introduction of the resistive switching (RS) phenomenon, presenting the properties and challenges of the RS devices, highlighting the intrinsic variability, and the different application fields reported in the recent literature. Two different processes in the memristor-based neuromorphic systems field, which are key topics in this thesis, are discussed: the STDP learning protocol and the homeostatic regulation. Secondly, the stochastic resonance phenomenon is investigated and linked with the memristors framework incorporating the current state of the art. Thirdly, the importance of modeling in emerging technologies is highlighted and general insights about modeling in memristors are presented.

As an important note, in the context of resistive switching technologies, the terms ‘memristor’ and ‘RRAM’ are often used interchangeably in the literature, reflecting the overlap between the theoretical concept of the memristor and its practical implementation in resistive memory devices. While a memristor is a theoretical construction that links resistance to the history of charge and flux, RRAM specifically refers to non-volatile memory technologies that utilize resistive switching mechanisms. Despite their distinctions, the shared principles of resistance change, and non-volatile behavior have led to a convergence in

terminology, particularly in discussions of neuromorphic systems and memory applications. In this thesis, this convergence is acknowledged and the terms are used interchangeably when the context allows.

1.1 Resistive Switching Phenomenology

Resistive switching (RS) is a phenomenon whereby the resistance of a dielectric material changes by applying a suitable external electric field. In contrast to the dielectric breakdown, where the resistance change is permanent, the RS phenomenon is reversible and can be repeated. Typically, RS is non-volatile, i.e. the resistance state does not change once the external stimulus is removed. RS has been studied since the 60's, where a thin dielectric layer was sandwiched between two electrodes and cycled [Hickmott1962]. Generally, the triple layer consists of a metallic top electrode, a dielectric material, and a bottom electrode that can either be a metal or a semiconductor. The resulting structures are metal-insulator-metal (MIM) and metal-insulator-semiconductor (MIS) devices. These devices, in which the phenomenon of resistive switching occurs, are known as memristive devices or memristors. The term memristor is a contraction of the words memory and resistor, meaning that its resistance at any given moment depends on its previous history. Memristors were first predicted by 1971, when Prof. Chua claimed the existence of a 'Forth missing element' joining the resistor, the capacitor and the inductor [Chua1971]. Although not exempt from criticism, this device was experimentally demonstrated in 2008 by Dr. Strukov [Strukov2008].

The following subsections provide a comprehensive overview of the key aspects of the switching dynamics, properties and applications of RS devices.

1.1.1 Resistive Switching Modes

Figure 1.1 shows the current as a function of the external applied voltage (V_{ext}) for the different processes involved in the resistive switching. In the pristine state (PS) of the device, the dielectric materials have a very high resistance. To observe resistive switching, the first experimental step consists in the

application of a high external voltage to the device (V_{forming}) in order to induce a new stable state with lower resistance. This process is called ‘electroforming’ or just ‘forming’. An abrupt current jump occurs during the forming process, so it is of utmost importance to limit the current, which is referred to as compliance current, to avoid an irrecoverable dielectric breakdown. After the forming process, the device is considered switchable. However, some devices have no distinction between pristine state and high-resistance state (OFF state or HRS), and those are called forming-free devices. The second step is the reset process, which consists in switching the device from the low resistance state (ON state or LRS) to the HRS through the application of an external voltage (V_{reset}). The third process is called set, which switches the device from the HRS to the LRS through the application of an external voltage called V_{set} . At this stage, successive set and reset processes can be performed (cycling). During the set process a compliance current also needs to be set, but, for the reset process, the current limit is usually not required because this is not a self-accelerated process. It has been observed that not all the RS devices exhibit the same type of switching. Three different types of RS can be distinguished: unipolar, bipolar and threshold switching.

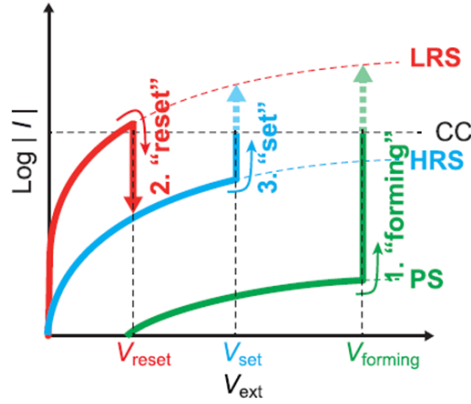


Figure 1.1. Schematic I - V curves showing the RS operation. The initial forming process and further reset and set processes are presented and ordered in green, red, and blue, respectively.

1. Unipolar Resistive Switching

In this type of RS only one polarity of the external voltage source is required for successively switching the device. This is the reason for the ‘unipolar’ term.

The typical I - V relationship for unipolar devices is illustrated in Figs. 1.2a and 1.2b. Notice that these devices can either work for negative (a) or positive (b) polarities. Using the positive polarity example ($V_{\text{ext}} > 0$), when the voltage V_{reset} is reached, the resistance sharply increases, entering the HRS. While in the HRS, if a V_{set} voltage is applied, the resistance value drops, turning back to the LRS. In unipolar RS devices, the set process, which needs to be current limited, typically occurs at higher voltages than the reset voltage. The same procedure is replicable for negative polarity devices, where the set process occurs at higher negative voltages than the reset process. Some dielectric materials showing the above-described characteristics are for example CuO_x , FeO_x , TiO_x , and ZnO_x [Lee2015, Fujiwara2008, Chae2008, Inoue2008].

2. Bipolar Resistive Switching

For successively switching bipolar RS devices, both positive and negative polarities of the external voltage source are required. The typical I - V relationship for bipolar devices is presented in Fig. 1.2c. One polarity is needed to reset the device, and the opposite polarity is employed to induce the set process. Since both polarities of V_{ext} are needed for this type of RS, the switching is called ‘bipolar’. Due to the hysteretic I - V relation shape, it is often called ‘butterfly’ plot, or ‘figure of eight’. The area in the hysteresis lobes is usually called memory window. Again, the set process requires current limitation. Different dielectric materials are reported to exhibit this type of switching, such as TiO_2 , HfO_x , Al_2O_3 , TaO_x , graphene oxide, WO_x or SrTiO_3 [Jeong2011, Ielmini2012, Jeong2010, Sawa2004].

For certain dielectric materials, like TiO_2 or NiO , coexistence of unipolar and bipolar switching is reported [Lee2015].

3. Threshold switching

In addition, a less frequent type of RS is threshold switching, where only one resistance state is stable, generally the HRS, meanwhile the LRS is only stable if a certain bias range (positive or negative) is applied [Seo2004]. This unstable LRS is non-volatile and is presented in Fig. 1.2d.

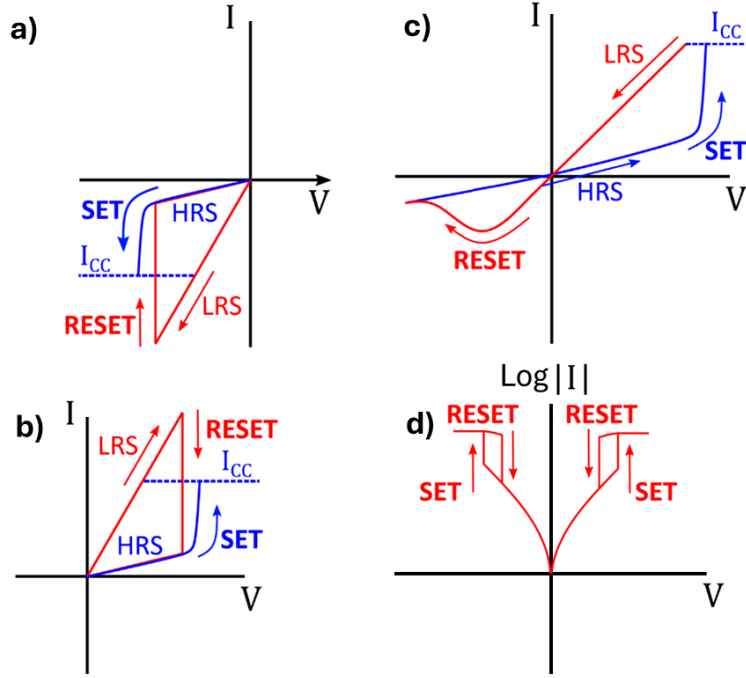


Figure 1.2. Schematic of the I - V curves for RS devices after the electroforming process, if needed. a) for negative unipolar devices, b) for positive unipolar devices, c) for bipolar devices and d) for threshold devices. Both HRS/LRS states and set/reset processes are highlighted. The current limitation is indicated for the set process.

1.1.2 Physical Mechanisms of Resistive Switching

The RS phenomenon is driven by a number of physical mechanisms which strongly depend on the dielectric material and the electrode composition. Also, different factors determine the instantaneous resistive state of the device. Some of them can be controlled externally, i.e. applied electric field and current compliance and some are material and fabrication dependent, i.e. electron mobility, species concentrations, gradient of temperature within the insulator region and lattice defects. In terms of the physical mechanisms involved in the RS, after intense investigation carried out by the research community, it is possible to identify four different types of RS: nanoionic, electronic, phase changing and nanomechanic [Tetzlaff2004, Vaidyanathan2024, Zahoor2020, Wong2012].

1. **Nanoionic:** In these devices the structural changes involving the change in resistance state are ruled by ion movement within the dielectric layer, which leads to the formation and dissolution of a conductive filament (CF) connecting both electrodes, see Fig. 1.3. Due to this filament-based mechanism, this type of resistive switching is also referred to as filamentary [Celano2016, Coll2019]. Inside the nanoionic type of RS, three categories emerge:

- a. **Valence change:** In this category, the resistance changes are induced by the movement of oxygen vacancies in the dielectric material, usually a transition metal oxide. This type of device is also known as valence change memories (VCMs) [Padovani2015]. This is the case for most of the characterized devices in this thesis, more precisely, HfO_2 based memristors [Poblador2018].
- b. **Electrochemical metallization:** In this case, the device must have an active metal electrode, whose ions can diffuse into the dielectric layer, and a second inert metal electrode. Also known as conductive bridge RAMs (CBRAMs) [Kozicki2016, Valov2011].
- c. **Thermochemical:** In this instance both previous categories might be present simultaneously [Waser2007].

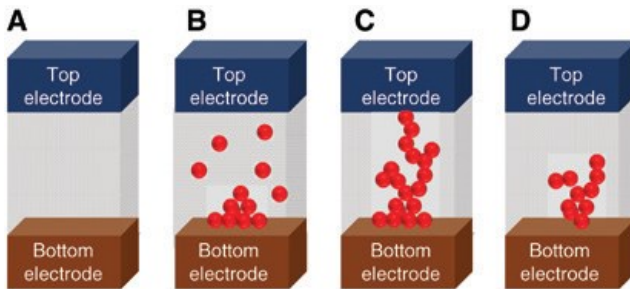


Figure 1.3. Schematic of the dielectric material for different resistive states in filamentary type RS. (a) Pristine state, (b) creating conductive channels during the electroforming process, (c) complete CF after a set process (LRS) and (d) filament rupture after a reset process (HRS). Adapted from [Mohammad2016].

2. **Electronic:** In this instance, the RS mechanism is linked with changes in the electronic conduction of the devices. It can be separated into two sub-categories:
 - a. **Ferroelectric:** The layer in between the electrodes is a ferroelectric material, whose polarization is affected by the external electric field leading to a change in the charge state [Chanthbouala2019].
 - b. **Charge-trapping:** These devices include a dielectric layer capable of trapping and releasing electrons as a function of the external electric field [Fan2017].
3. **Phase Changing:** This type of RS device includes chalcogenides in its fabrication process. The property of these materials to modify their atomic network from amorphous to crystalline state induce the resistance state change. An external heat source is required for these devices to operate [Wouters2015].
4. **Nanomechanic:** In this case, the mechanical deformation of the dielectric material is responsible for the changes in the resistance state [Wu2011].

1.2. State of the Art: Properties and Challenges

Even though RRAM technology has garnered significant attention due to its unique features and potential applications, it is facing some hurdles to be handled for industrialization in the different application fields. In this section the main properties and challenges to be addressed are presented.

1. In terms of **endurance**, the consecutive set and reset processes can damage the device in the long term, meaning degradation and performance loss. Endurance represents the number of set/reset cycles a memristor is able to perform maintaining a minimum resistance ratio (R_{Ratio}) between the HRS and LRS, indicating that these two states are

still clearly distinguishable [Hui2017]. The common endurance levels are around 10^7 , however for some cases 10^{12} has been reported [Lee2011].

2. The **state retention** quantifies the amount of time a state can be maintained after a set or reset process. A correct retention for non-volatile memories is 10 years at 85°C [Lanza19, Cagli2008, Cheng2010].
3. The **active area** of RRAM devices can reach really low dimensions due to its filamentary nature. It is pivotal not only for the size limits of single memories but also for building more complex configurations, like crossbar arrays and 3D architectures. Generally, there is a compromise between the active area and the power required by the forming process. For smaller areas (under 100 nm^2) higher forming voltages are needed compared with larger areas (around few μm^2) [Lanza19]. This is because of the Poisson area scaling of dielectric breakdown.
4. **Switching time** and **energy consumption** are two related properties since for a general characterization assay, the more time it takes to switch, the more power is consumed. In RRAMs the range of switching time is around a nanosecond and the energy consumption in the range between 0.1 to 1 pJ/bit [Carboni19].
5. In RRAM technology different phenomena inducing fluctuations in the switching behavior coexist. Firstly, endurance can be considered as a long-term fluctuation since the distance between HRS and LRS is affected by cycling and time [Dozortsev2018, Lanza2021]. In Fig. 1.4a, a typical endurance test is presented. The current evolution related to the HRS and LRS states (I_{on} and I_{off}) is shown against the cycle number. Both currents were extracted at a fixed voltage (0.1 V) after a transition pulse to ensure the set and reset events respectively. Notice the gap between both currents is narrowed with cycling due to the reduction of the HRS-LRS window [Roldán2023]. Secondly, **random telegraph noise** (RTN) causes random fluctuations between two different levels over time. The origin of this phenomenon is the capture and emission of charges in the insulating layer of the memristor. It can affect the reliability of the device in terms of data retention and reading accuracy [Pal2020]. Thirdly, one of the major issues for the further development

of the RRAM devices is their **intrinsic stochastic variability**, thoroughly detailed in the following subsection.

6. Representing accurately the RS phenomenon in **models** is crucial for better understanding its mechanisms. Nowadays, there is a lack of robust and well-established models. Solid mathematic tools are required for extracting and analyzing experimental data to use the information as inputs for modeling. It is a key issue for the well-development of an emerging technology like RRAM devices [Shao2022, Im2020, Yu2016].

1.2.1. Variability in RRAM Devices

In RRAM devices, variability refers to unintended fluctuations in the device performance or characteristics. It can be split into device-to-device (D2D) and cycle-to-cycle (C2C) variability. D2D variability is linked to the manufacturing process, the material properties and the environmental influences [Perez2019]. For nanoionic memristors, which is the type of device considered in this thesis, the intrinsic C2C variability in RRAM devices is related to the randomness of the switching process. This variability is inherently rooted in the morphological changes occurring in the CF connecting both electrodes at the atomic scale because of charge traps, mobile ions or oxygen vacancies, depending on the filamentary RS mechanisms [Chen2011, Piccolboni2016]. Understanding and controlling this variability has become one of the biggest challenges for this technology. In addition, the analysis of the C2C variability in RRAM devices is crucial for building optimal designs and models for further supporting the development of this technology. These fluctuations are often non-desired for real applications but also become useful to develop random number generators (RNGs) for security, cryptography and stochastic applications. C2C variability is typically characterized by the sequential use of voltage sweeps in the same device, as shown in Figure 1.4b [Roldán2023]. Notice the variability in HRS is significantly more spread than in the LRS. This is a common phenomenon related to the gap distance between the broken CF and the metal electrode after a reset process. Hence, as a consequence of the HRS variability, the set event C2C variability is often significantly higher than the reset voltage C2C variability. Other key variability issues are detected in the literature. Figure 1.5

exemplifies some of these issues. Usually, an initial stage of higher C2C variability is experienced before the switching stabilization of the device is achieved. Sometimes, the number of cycles can last from tens to hundreds. This effect is appreciated in Fig. 1.5a. Instead, in Fig. 1.5b, a situation where the LRS presents multiple levels is illustrated. A reduction in the gap between HRS and LRS is evidenced in Fig. 1.5c due to a degradation of the switching characteristics.

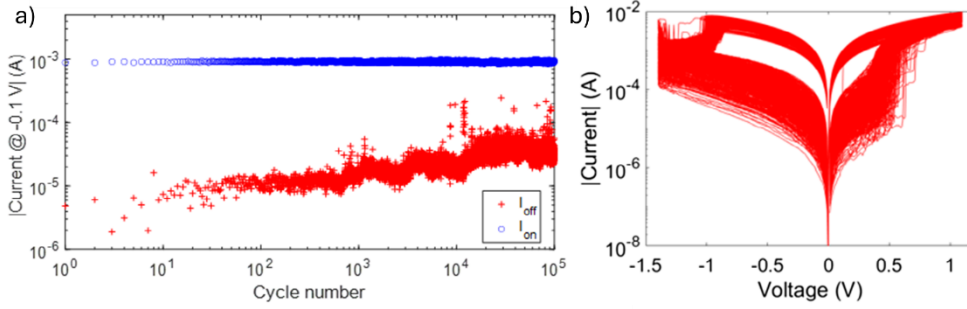


Figure 1.4. HfO₂-based RRAMs variability study. a) Evolution of HRS and LRS currents measured at -0.1 V as a function of the number of pulsed cycles. b) Typical RS current-voltage characteristics for 3000 voltage sweeping cycles. Adapted from [Roldán2023].

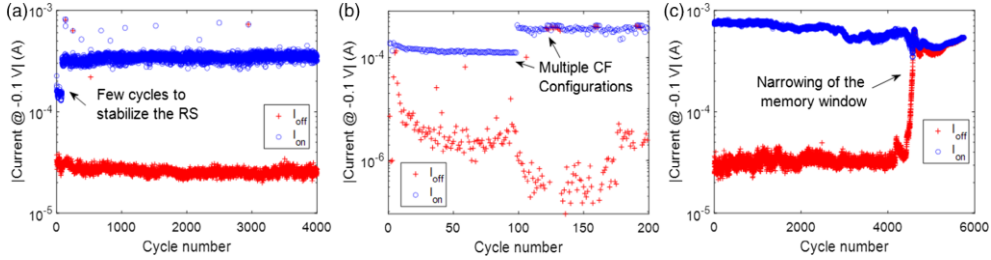


Figure 1.5. Evolution of the HRS and LRS currents measured at -0.1 V in filamentary RRAMs. C2C variability issues are evidenced: a) Resistive switching instabilities in the first cycles. b) Formation of multiple stable CF configurations. c) Progressive reduction of the memory window after the degradation of the insulator. Adapted from [Roldán2023].

1.2.2. Stochastic Resonance

While noise in electronics is typically considered as a major drawback that needs to be eliminated, in nonlinear systems it can play a favorable role. This counterintuitive phenomenon is called stochastic resonance (SR), where the presence of a certain level of external noise can enhance the performance or response of the considered system [Krauss2017]. By dynamically adjusting the noise level, as an optimization process, the output performance plot generally presents a maximum, as visible in Fig. 1.6. SR was first introduced in [Benzi1981], and it has been observed in several research fields including biology, physics, and engineering.

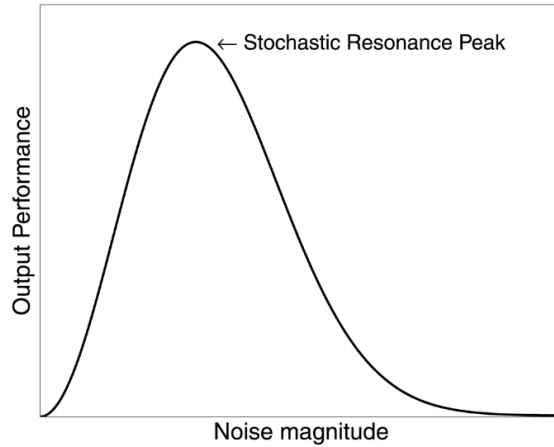


Figure 1.6. Typical theoretical stochastic resonance curve, illustrating the relationship between noise magnitude and output performance. The curve exhibits a peak shape, highlighting the optimal noise level at which the system's output performance is maximized. Adapted from [McDonnell2009].

In [Wiesenfeld1995], the SR beneficial effect is discussed in different fields: climate science, biological systems like sensory neurons in crayfish using noise to detect certain signals, or physical systems like superconducting quantum interference devices (SQUIDs), where noise can help detecting weak magnetic fields. In [Anderson2000], the authors explored the role of noise in the visual cortex and its contribution to maintain contrast invariance in the neuronal response. This study demonstrated that noise introduced in the neural processing pathways can stabilize the perception of optical signals, ensuring robust visual processing even under varying stimulus conditions. Additionally,

in [Longtin1997], the phenomenon of autonomous stochastic resonance (SR) in bursting neurons was investigated. The results showed that intrinsic noise within neuronal systems enhances the sensitivity of neurons to weak stimuli, thereby improving their responsiveness and efficiency. This work attributed the increased sensitivity to the SR effect, which helps amplify subthreshold signals in neuronal networks, providing key insights into how biological systems utilize noise for functional optimization.

In [Harmer2002], a technical guide in terms of theory, mechanisms, circuit implementation and measurement techniques related to SR is reported. In [Kasai2014], a study of the impact of SR in nanoelectronic devices is presented, showing its potential in the development and optimization of advanced electronic devices and emerging technologies. A detailed discussion of the SR phenomenon, its research approaches and its applications is presented in [Naprstek2017]. This last book chapter disseminates the approaches from analytical, using sophisticated mathematical techniques to study the SR phenomenon, to numerical approaches, where researchers model the SR phenomenon using computational models or Monte Carlo simulations. Moreover, it highlights that SR can improve sensing performance or communication systems and benefit signal transmission in neurons. Memristors present nonlinear current-voltage characteristics and nonlinear dynamical behavior enabling the utilization of properties linked with nonlinear systems, as stochastic resonance [Ntinis2021]. From the literature, some works have considered noise as a beneficial element in these devices. An approach using manganite-based memristors is presented in [Patterson2013]. This work highlights the beneficial role of noise in these materials, emphasizing how noise can optimize resistive switching dynamics. In addition, they state that the noise-enhancement is partially volatile and reaches a saturation point, as can be seen in Fig. 1.7, where the mean values and standard deviation of the OFF (HRS) and ON (LRS) state resistances are presented against the noise amplitude 1 ms (red) and 10 ms (green) after the input signal was turned off.

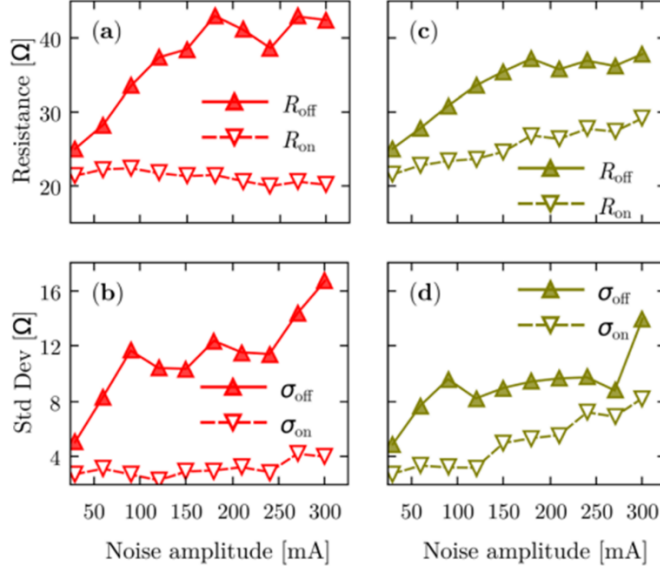


Figure 1.7. R_{off} and R_{on} , a) and c), and σ_{off} and σ_{on} , b) and d) vs. noise amplitudes. Data in red corresponds to 1 ms, and in green to 10 ms after the signal was turned off. Adapted from [Patterson2013].

In contrast, in [Maldonado2023], the SR phenomenon was analyzed using ramped input signals (0.28 V/s) with added noise of different standard deviations (σ) and three statistical distributions: normal, uniform, and exponential. 100 complete I - V switching curves were analyzed for each case. The evolution of HRS and LRS resistance, and resistance ratio are presented in Fig. 1.8. The HRS resistance shows clear resistance variations with increasing noise. The normal distribution exhibited the largest variation, while the exponential distribution's changes were intermediate between normal and uniform. The mean R_{OFF}/R_{ON} ratio versus noise intensity confirmed the SR effect.

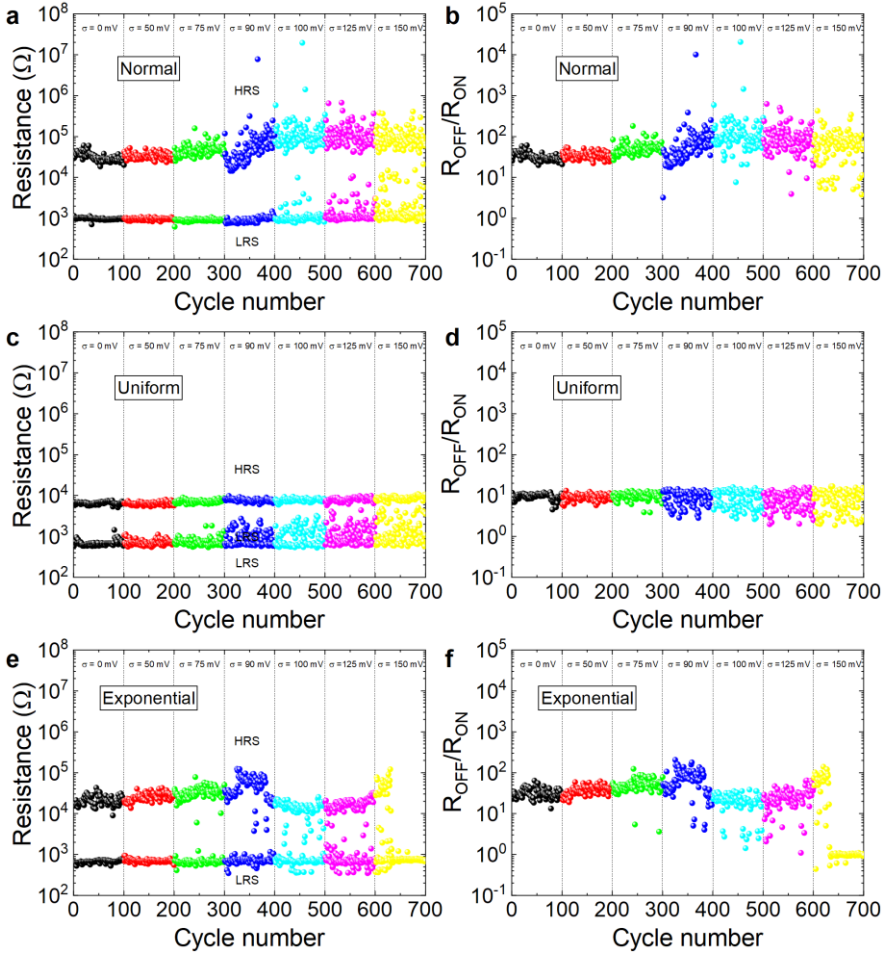


Figure 1.8. LRS and HRS resistance versus cycle number. The values were obtained at 0.2 V of the applied ramp with added noise of different distributions: a) normal or Gaussian, c) uniform, e) exponential. HRS/LRS resistance ratio versus cycle number calculated for the data corresponding to figures a), c) and e) for the noise generated with b) normal or Gaussian, d) uniform, and f) exponential statistical distributions. Adapted from [Maldonado2023].

Finally, SR in 2D materials-based memristors is analyzed in [Roldán2024]. This investigation revealed how noise interacts with the unique electronic properties of 2D materials, offering novel insights into optimizing device functionality through SR. The findings illustrate the potential of integrating these materials into future energy-efficient memory and computational architectures.

This thesis presents a comprehensive study of the positive impact of noise on isolated RRAM device performance. Experimental measurements and simulations were combined to this end. In memristor-based neuromorphic systems, noise improvement was tested in applications like the STDP learning protocol and homeostasis, which are introduced in the next sections.

1.3. Applications

Because of all the outstanding properties of memristors and the potential they represent, nowadays there is a significant research effort that is currently ongoing to integrate these devices into a wide range of applications. This includes security applications, control systems, quantum computing, neuromorphic systems, RRAMs, logic gates among others [Lv2021]. Some of the main applications of this technology are detailed as follows:

1. For **security applications**, physical unclonable functions (PUFs) [Koeberl2013] and RNGs [Aziza2020, Arumi2023] can be implemented with memristors due to their stochastic properties. The variable parameters of the switching mechanism (set and reset voltages, HRS and LRS, current fluctuations in a certain period) are used to implement circuits for these applications. The RTN [Li2021] have attracted interest in this type of applications since the fluctuations do not require the creation or destruction of the CF [Karpov2016]. Thus, in terms of endurance and power consumption it is clearly favorable since not so high voltages or drastic changes must be forced to the devices.
2. The most studied application for memristors has been the memory devices called **RRAM**, where the information is stored as a logic “0” or “1” associated with the device state HRS or LRS respectively [Shen2020, Wang2023, Ielmini2018]. This kind of memory is considered to be a very promising candidate for the future of digital information storage. The switching time allows high frequency applications. In addition, the state retention and robustness can translate into high endurance and reliable memories. Higher device density can be achieved since RRAM devices can be smaller than the actual transistor technology limits.

3. Memristors can implement **logical operations**. Different logic gates have been studied and reported in the bibliography [Gopal2015, Su2022]. As examples, in Fig. 1.9, two different logic functions (IMPLY and NAND) using memristor-based circuits are presented. In this application, memristors can build a non-volatile logic unit integrating the processor and memory which represents an improvement compared to the conventional computing architectures [Maestro-Izquierdo2019]. There is also the possibility to integrate these devices into logic gates matrices or field-programmable gate arrays (FPGAs) leading to smaller architectures and lower power consumption [Zhang2023].

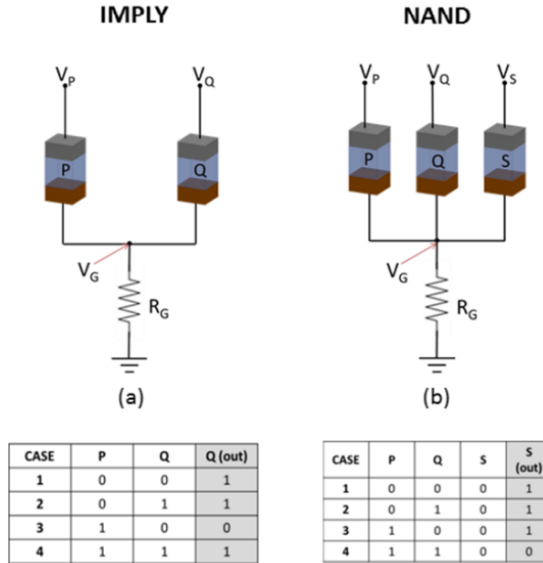


Figure 1.9. Memristor-based logic operations and its equivalent circuit. a) IMPLY function and b) NAND function. Adapted from [Maestro-Izquierdo2019].

4. Memristors can be used to fabricate **neuromorphic systems**, where these devices could either mimic the biological synapses or act as artificial neurons [Zheng2015]. In this sense, biological neurons are the fundamental building blocks of the nervous system, responsible for transmitting and processing information. A neuron consists of three primary components: the soma (cell body), dendrites (input structures), and the axon (output structure), see Fig. 1.10. Information is transmitted through electrical impulses called action potentials, which

propagate along the axon to synapses which are the junctions between neurons. At the synapse, chemical neurotransmitters are released, modulating the electrical activity of the postsynaptic neuron. By mimicking these processes in artificial devices like memristors, researchers aim to replicate the brain's computational efficiency and energy conservation. This complex but efficient mechanism of signal transmission and adaptation has inspired the development of neuromorphic computing systems, where memristor-based structures are considered to be an alternative to the von Newman architectures [Ogban2007] by allowing the computation and the memory units to be joined in a single operational structure.

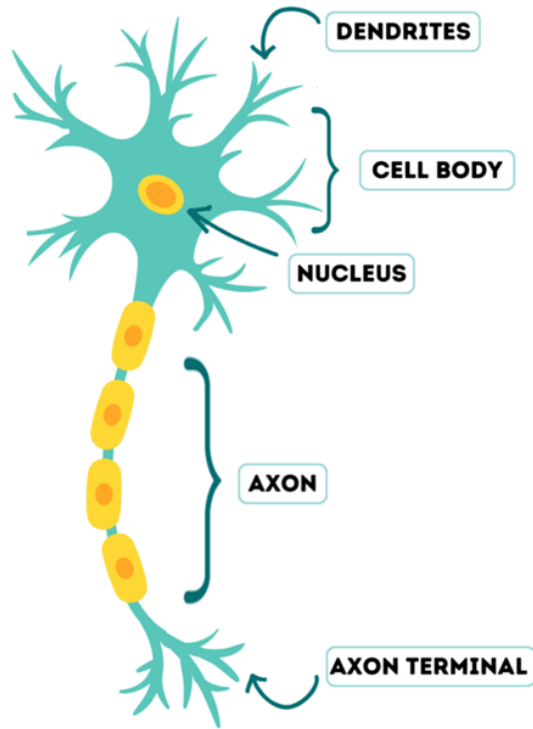


Figure 1.10. Structure of a neuron, highlighting its main components: dendrites, cell body (soma), nucleus, axon and axon terminals. These elements enable the transmission of electrical and chemical signals essential for neural communication.

In addition, there have been attempts to construct **artificial neural networks** (ANNs) capable of performing complex operations [Yang2013, Ye2022]. ANNs are computational models to mimic the human brain and are configured for certain applications such as data classification or pattern recognition by means of a learning process. A network working principle consists in transmitting events from one source node (in this case neurons) to other nodes (synapse), and the learning is implemented by updating the strength (weight) of those interconnections, organized in layers [Kim2012]. ANNs and the human brain both exhibit learning and storing knowledge in the internal neurons by means of a magnitude called synaptic weights. The first model for an ANN generation was presented in [McCulloch1943] and it was called perceptron. The perceptron learning is based on adjusting the synaptic weights depending on the output error. It consists of a single layer of neurons capable of performing simple tasks like binary classification [De-Benito2019]. On the one hand, **deep neural networks** (DNNs), also known as deep learning, are based on continuous data representation in time, and can solve more complex problems (i.e. image recognition, language processing and others). DNNs consist of multiple layers of neurons (one input layer, one or more hidden layers and one output layer) interconnected by adjustable synaptic weights [Aguirre2024, Yuan2019]. In Fig. 1.11a the general structure for a DNN is presented.

On the other hand, **spiking neural networks** (SNNs) are a type of neural network where the information is coded in an alternative way, using time-dependent spikes. Its functioning is much more similar to the biological neural networks, and they are known for its potential in terms of energy consumption and processing temporal information [Wang2023]. In Fig. 1.11b the general structure for a SNN is shown.

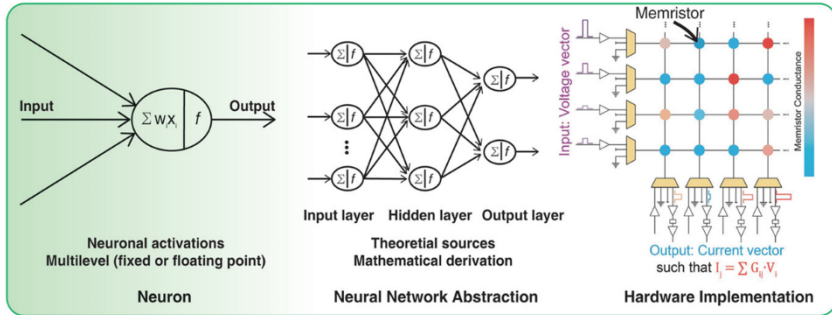
Notice both types of ANNs are similar in terms of layer structure, interconnection of neurons and adjustment of synaptic weights for the learning process. The main differences consist in the input and output signals and the communication between layers. On the one hand, in DNNs, the input is continuous data, the output is a continuous prediction, and the communication is operated in discrete time steps.

On the other hand, in SNN, the inputs are spike trains, the outputs are spike patterns, and the communication is spike or event-driven and asynchronous.

Integrating memristors into ANNs offers different advantages in terms of processing memory and efficiency, adaptability in learning, fast computations and robustness. However, some challenges still need to be overcome regarding integration into existing technologies, fabrication and variability before unlocking the full potential of neuromorphic computing [Aguirre2024].

In this thesis, two different neuromorphic processes have been reproduced with memristive devices. They are, the **spike timing-dependent plasticity** (STDP) and the **homeostasis** which are thoroughly discussed in the following subsections.

a) Deep Neural Networks



b) Spiking Neural Networks

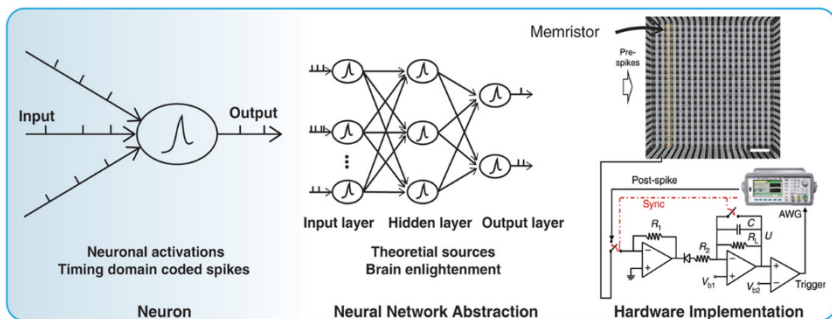


Figure 1.11. Comparison of a) Deep Neural Networks (DNNs) and b) Spiking Neural Networks (SNNs), illustrating their structural similarities but emphasizing differences in input and output signal processing as well as hardware implementation approaches. Adapted from [Wang2023].

1.3.1. Spike Timing-Dependent Plasticity

Neuromorphic systems draw inspiration from biological neural networks, aiming to replicate their efficiency and adaptability in hardware. Over the decades, this field has evolved from analog VLSI circuits to nanoscale technologies like memristors, which offer unique advantages for implementing synaptic behaviors due to their non-volatility, compact size, and dynamic conductance properties [Gerstner1993, Im2020]. Among various biologically inspired learning rules (Hebbian learning, Spike Rate-Timing Dependent Plasticity, gradient-based learning, and others), Spike-Timing-Dependent Plasticity (STDP) is particularly well-suited for memristor-based systems because these devices can mimic synaptic behavior through dynamic conductance changes, which are influenced by timing-based inputs like voltage spikes [Burr2017, Du2015, Lee2020]. STDP is an experimentally verified biological learning rule in which the timing, or time difference, between two synaptic spikes, in pre- and post-synaptic neurons, condition the direction and magnitude of change in the synaptic strength [Cai2015, Pedretti2018]. STDP has two distinct plasticity windows: long term potentiation (LTP) and long-term depression (LTD) described next. In LTP, the synapses increase efficiency and the spike activation if the pre-synaptic neuron occurs shortly before the spike in the post-synaptic neuron. In LTD, the synapse decreases efficiency and the spike activation in the post-synaptic neuron spikes shortly before the pre-synaptic neuron. Synaptic plasticity allows to store information and react to different inputs based on the past history. For a visual explanation, a clinical perspective adapted from [Bliss2011] is presented in Fig. 1.12, where both (a) LTP and (b) LTD processes are induced in mice by means of visual stimulation. Both figures represent the % change in synaptic strength over time, which refers to the efficacy of synapses in transmitting signals. The time axis has negative values since the moment where the visual stimulation is performed is set at zero. Notice the figures include the induced LTP and LTD regimes (black symbols) and the control curves (white symbols). For LTP, after the stimulation, the synaptic strength grows (1.12a) and for LTD after the stimulation the synaptic strength decreases (1.12b).

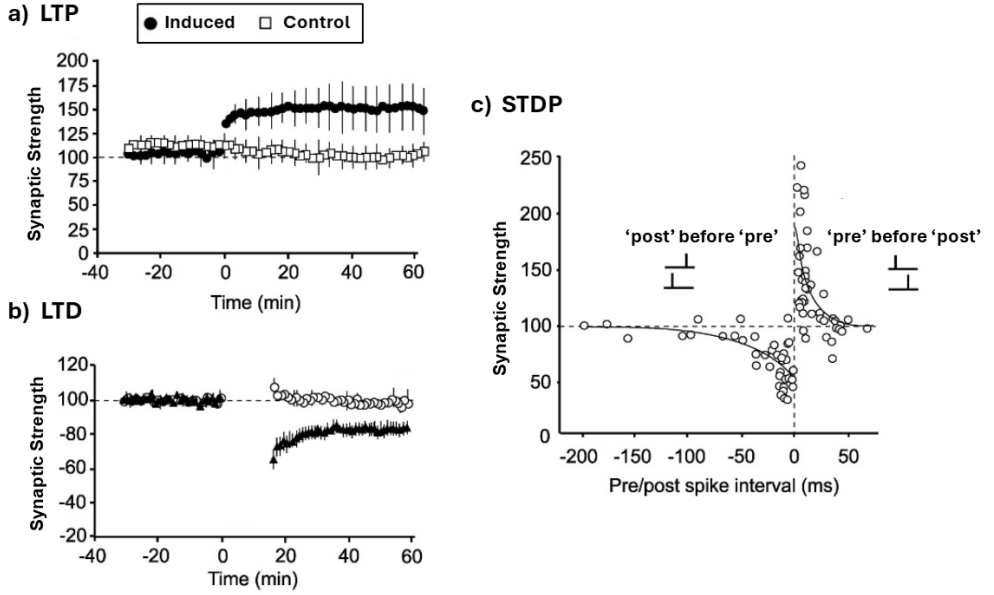


Figure 1.12. Experimental results showcasing induced synaptic plasticity from [Bliss2011]: (a) Long-Term Potentiation (LTP) and (b) Long-Term Depression (LTD) showing the % change in synaptic strength over time. The black and white symbols are induced and control experiments respectively. (c) STDP learning protocol presenting the % change in synaptic strength as a function of the pre/post-synaptic timing. Adapted from [Bliss2011].

In addition, STDP plays a crucial role in the development and well-functioning of neural circuits and contributes to learning and memory processes in the brain. In the specific case of STDP implemented with memristors, memristors are used as the synaptic connections between neurons in neuromorphic systems. The resistance of the device is linked to the synaptic weight. This resistance is changed by means of spikes, in this case voltage spikes, arriving to the device, and occurs when a pre-synaptic voltage spike arrives shortly before the post-synaptic voltage spike or vice versa. In the first case (pre-post pairing) the device conductance is increased, meaning potentiation and in the second case (post-pre pairing) the conductance decreases, meaning depression [Shuai2018]. This is visible in Fig. 1.12c, where the STDP protocol is presented experimentally showing the % change in synaptic strength as a function of the pre- and post-synaptic timing [Bliss2011]. For STDP implemented with memristors, there are other influencing factors in addition to the spike-timing:

the device hysteresis, the initial conductance of the device, the voltage spike waveform, the material properties and variability [Linares-Barranco2009, Elhamdaoui2022]. In recent literature, several investigations regarding the use of memristors to perform the STDP learning rule can be found [Zamarreno-Ramos2011, Camuñas-Mesa2020]. In [Seo2011] a demonstration of the possibility of building artificial synapses in a neuromorphic network using TiO_x based memristors was presented. In [Matveyev2016] the STDP functionality was demonstrated for HfO_2 based memristors. In [Wang2012] the STDP characteristics were studied using voltage pulses at the top and bottom electrodes finding consistent conductance/timing results with the biological synapse behavior. In [Mohan2021] the STDP learning rule is measured experimentally using a silver-chalcogenide based memristor.

In this thesis, we explore how stochastic resonance phenomenon (previously presented in this chapter) can trigger the STDP learning protocol, enhancing learning efficiency in neuromorphic architectures.

1.3.2. Homeostasis

Homeostasis is a pivotal process in living organisms and refers to the ability to maintain the stability of an internal system despite changes in external surroundings [Vergara2019]. It ensures the stability of fundamental variables or magnitudes within certain margins essential for survival. This stability is achieved as a dynamic equilibrium, continuously adjusting to changes while maintaining relatively uniform conditions (steady state) [Davies2016, Davis2006]. Examples of biological homeostatic regulation include body temperature (see Fig. 1.13), fluid balance, blood sugar levels, and pH levels.

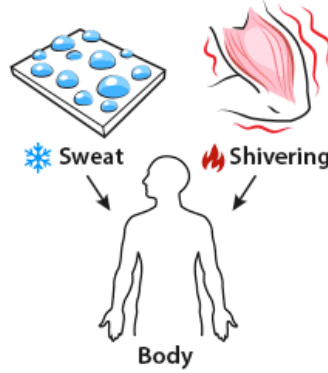


Figure 1.13. Illustration of the homeostasis process in the human body, showing the mechanisms of sweating and shivering in response to extreme temperature variations. Sweating occurs to cool the body down during high temperatures, while shivering generates heat to warm the body in cold conditions, both ensuring the maintenance of a stable internal temperature.

In neuromorphic systems, implementing homeostasis with memristors is not only feasible but effective, as their switching behavior allows for gradual and adaptive adjustments in synaptic weights. This mimicks the biological processes of regulating synaptic strength [Christensen2022, Wang2016, Harnack2015]. In addition, neurons in the brain are subject to diverse varying processes like synaptic plasticity, changes in sensory signals and tissue damage. These processes can lead to under-stimulation (low firing rate) or over-stimulation (continuous spike firing). Both situations are undesired since if maintained in long-term, can be dangerous and energy inefficient. Neural homeostasis role is to prevent both situations maintaining an optimum regime. In case of over-stimulation, excitatory synapses are diminished, inhibitory synapses are increased, and the firing threshold of neurons is increased [Perrinet2010], see Fig. 1.14. In the literature, some works consider the homeostasis in memristor-based neuromorphic systems [Wang2022, Shi2018, Querlioz2011]. In [Sun2022] a memristor-based neural network including memory with emotional homeostasis is designed. In [Yang2021] a training method based in homeostasis was used for pattern recognition. In [Querlioz2013] a spiking neural network implemented with memristive devices immune to device variations is reported. In [Ma2023] a work providing fast inhibitory homeostasis in a circuit with a memristive synapse is presented. Most of the proposals presenting homeostasis in memristor-based systems do not include experimental proof and are only

software based. In a realistic scenario, it would be convenient to include the homeostatic property in the real memristors performance for self-stabilizing the neuron activities. This thesis includes a study on the role of stochastic resonance in regulating neural activity, demonstrating how it enhances system stability by balancing excitatory and inhibitory regimes.

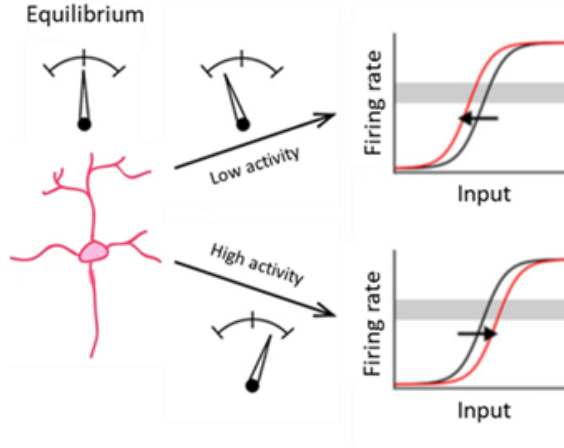


Figure 1.14. Diverse homeostatic plasticity mechanisms stabilize the activity of developing neurons. Adapted from [Tien2018].

1.4. RRAM Modeling

In the recent years, memristors have attracted a lot of interest, but unfortunately not so many new solid and robust memristor models have emerged. This reflects the difficulty of building an accurate model for a non-linear behavior device like a memristor. [Chua2019, Snider2007]. The process for creating a device model reproducing the memristor characteristics involves theoretical analysis, data collection, testing various hypotheses and iterations. Since all models are, in fact, an approximation of a real phenomenon, simplicity becomes a key characteristic to be achieved by any model. However, by increasing simplicity, other qualities can be compromised. These qualities any realistic model should possess consist of:

- Being well-posed, meaning that it should not result in non-physical results.
- To have simulation capability, i.e., a computational solution of the model should be close to the experimental data desired to reproduce or understand.
- Having qualitative similarity to the real device in terms of behavior.
- To have predictive ability for simulations in non-experimented environments.
- Being structurally stable, meaning slight modifications in the model parameters do not lead to hard output properties variation.

Considering these essential characteristics, the following section presents a classification of existing models, highlighting their characteristics, strengths, and limitations.

1.4.1. Classification of RRAM Models

The industrial development of RRAM technology requires different approaches for modeling and predicting device behavior, scaling and reliability. Different simulators can be classified according to their degree of accuracy and computational cost. Three main groups can be discerned: **atomistic simulations** relying on the density function theory (DFT), which are used to calculate fundamental material properties and defect characteristics, **device simulations** which are physically based employing the finite element methods (FEM), and the kinetic Monte Carlo (KMC) models, used to project the material properties into the electrical performances, and **compact models**, or semi-empirical, used in circuit simulations for assessing the system performance starting from isolated device characteristics. Figure 1.15 presents an overview of the types of models for RRAM technology in terms of scale, capabilities and computational cost. This comparison is depicted next in this subsection [Ielmini2017].

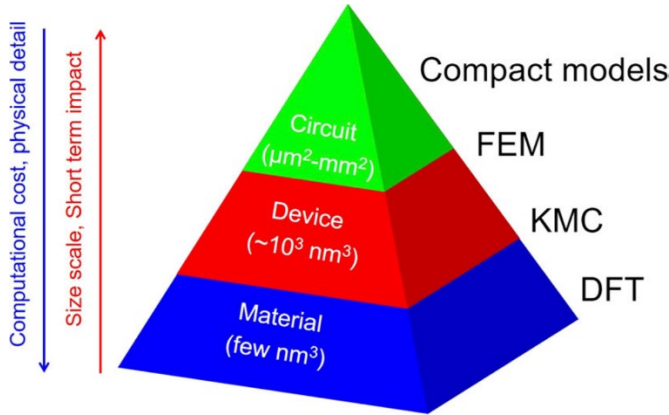


Figure 1.15. Summary of the types of models for RRAM devices highlighting the size scale, the complexity, and computational cost. Adapted from [Ielmini2017].

1. **Atomistic simulators** are the ideal approach for an in-depth study of the phenomenology of the physical processes behind the RS devices. For simulations, ab initio or molecular models (based in DFT) are used. These simulators provide the basis for understanding the materials band structure, the ions or atoms migration, diffusion mechanisms and all the effects rooted to the charge conduction (CF creation and destruction, material structure evolution, heat dissipation). To achieve this goal, the simulators must incorporate structural, phase changes, thermal or optical properties, defects from the materials at the atomic level, etc. The obtained information can be incorporated as inputs for device simulation models. The computational cost of atomistic models is the highest among all the RRAM modeling types [Jiang2016, Onofrio2015].
2. In **device simulation models**, technology computer-aided design (TCAD) techniques allow the simulation of the device conduction and switching characteristics. These techniques provide information about the RS phenomenon in terms of scaling and the impact of geometry on the switching. Device simulation models are interesting for both researchers and industry. TCAD models can be split into two classes: KMC models and FEM models.

The **KMC** modeling approach considers discrete quantities, like position, crystalline structure, vacancies, energy states, and others. In

memristors, generation and recombination of vacancies can be considered as the origin of switching and trap-assisted tunneling as responsible for the conduction. Simulations relating to discrete composition of the CF and its conduction characteristics can be obtained [Yu2011].

In a **FEM** model, generally, the electron transport equations are solved in 2D or 3D geometries where volume is discretized with finite elements. RRAM simulations involve thermal and ionic effects because of their strong link with the RRAM devices functioning. Oxygen vacancies and impurities can be considered for studying changes in the CF [Villena2017, Larentis2012]

Both types of models have been reported to accurately reproduce experimental features of RRAM devices. The FEM models generally describe average device behavior and the KMC can also describe the current fluctuations and switching variability [Larcher2012]. Both FEM and KMC need input parameters calculating using ab initio calculations and must be calibrated using electrical characteristics of devices.

3. **Compact models**, or semi-empirical models, are paramount for developing circuits and systems based on RRAM devices. These models rely on simplification of concepts, i.e. considering the CF of a certain shape, like cylindric or conic. In addition, physical assumptions are based on empirical measurements. In this context, a compact model should be encapsulated in a limited number of simple and robust equations driven by a set of parameters. Usually, these models are implemented in well-known circuit hardware like Spice or Verilog-A. Two different families of models emerge from compact modeling. On the one hand, **physical compact models** aim to capture the physical aspects behind the RRAM phenomenology by means of detailed and complex model equations and extensive parameters. These models can incorporate computational techniques like the previously explained KMC or FEM [Brown2022, Ielmini2011, Huang2013]. On the other hand, in **behavioral compact models**, the pivotal goal is not to perform better than KMC or FEMs in fidelity and accuracy of the device physics,

but to closely match the model outputs and simulations with experimental data. In this regard, behavioral models are built by a few solid equations with a reduced number of parameters. Obtaining an accurate representation of the electron transport for different input signals facilitates the design and control of more complex circuits and enables the identification of connections between the elementary modeling components that lead to the different observed behaviors in the conduction characteristics. In compact modeling, by subtracting complexity, the computational cost of the simulations is harshly reduced, allowing to focus on aspects for circuit designing and simulations and predicting the device behavior within larger circuits. In this way compact behavioral modeling bridges the atomistic, KMC models or FEMs with practical circuit simulations [Cisternas2019, Jiang2014, Li2014, Larcher2014].

1.4.2. Modeling C2C Variability in RRAMs

One of the biggest concerns of RRAM technology lies in its C2C variability, which is intrinsically linked to the resistive switching mechanism. Hence, this variability must be assessed from different scopes, not only experimentally characterized but also in modeling approaches [Chen2011, Dai2015]. Accurately modeling the variability in RRAM devices is crucial for several reasons:

1. By incorporating variability models and simulations in design processes, the development of circuits can be improved in terms of robustness against fluctuations.
2. The performance prediction under different circumstances is essential for system integration. Including variability allows researchers and designers to anticipate the device behavior in real-world applications.
3. Modeling variability helps to understand how it affects reliability and endurance of RRAM devices.
4. Optimizing the fabrication and material selection. Understanding the sources and impact of variability related to the fabrication process allows the engineers to produce more reliable devices.

Different approaches for modeling RRAM devices variability have been reported in the current literature. In [Roldán2023] a review of the most recent advances in this regard is reported, where different strategies are presented to tackle variability from multiple perspectives as well as good practices to assess it. Firstly, **experimental characterization** is key to quantify variability from real devices. It involves detailed experimental studies used to validate the models and understand the physical origins of variability. Microscopy techniques and electrical characterization can be used to determine the statistical distributions of the device parameters [Wouters2019]. Secondly, different types of modeling approaches are necessary for the well-development of this technology. **Physical models** aim to describe the mechanisms behind the resistive switching phenomenon at microscopic level [Guan2012, Chen2015]. **Stochastic models**, which use probabilistic methods to represent the randomness in the switching process. This approach can help physically understanding the intrinsic variability and predicting the device behavior [Joglekar2009, Linn2014]. **Behavioral models**, which focus on the observable behavior of the real devices simplifying complex processes into functional representations [Panda2018, Roldán2023b]. Summarizing, the ideal path for modeling variability in RRAM devices involves **hybrid approaches**. Combining different modeling techniques can enhance the limits of each method, for example, stochastic models can be integrated with behavioral models to improve the understanding and predictive capabilities.

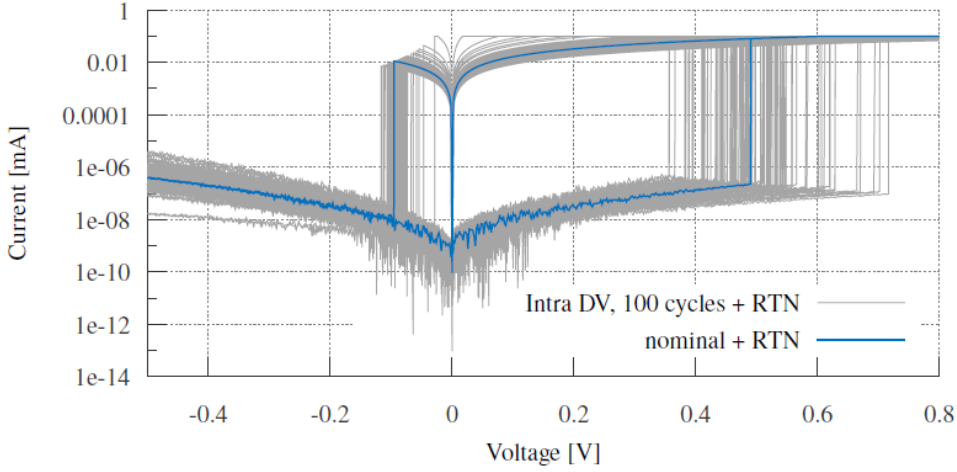


Figure 1.16. 100 Simulated I - V curves of a device exhibiting both RTN and C2C variability. The variability of the conduction mechanisms and switching thresholds varies with the device's cycling and feeding voltage. Adapted from [Garcia-Redondo2017].

More specifically, in [Piccolboni2016], a variability study considering correlation of the HRS and LRS currents for the initial cycles using an analytical model is reported. In [Garcia-Redondo2017], an approach for emulating variability and RTN effects in a Spice memristor model is discussed (Fig. 1.16). In this approach, the variability is included introducing the standard deviations from experimental data or directly including the scattered data in Spice.

In [Li2015], a Monte-Carlo approach to reproduce C2C variability is presented (Fig. 1.17). The variability was included by means of a zero-mean Gaussian function in the definition of the key physical variables of the model: the gap distance (g) and the CF radius (r).

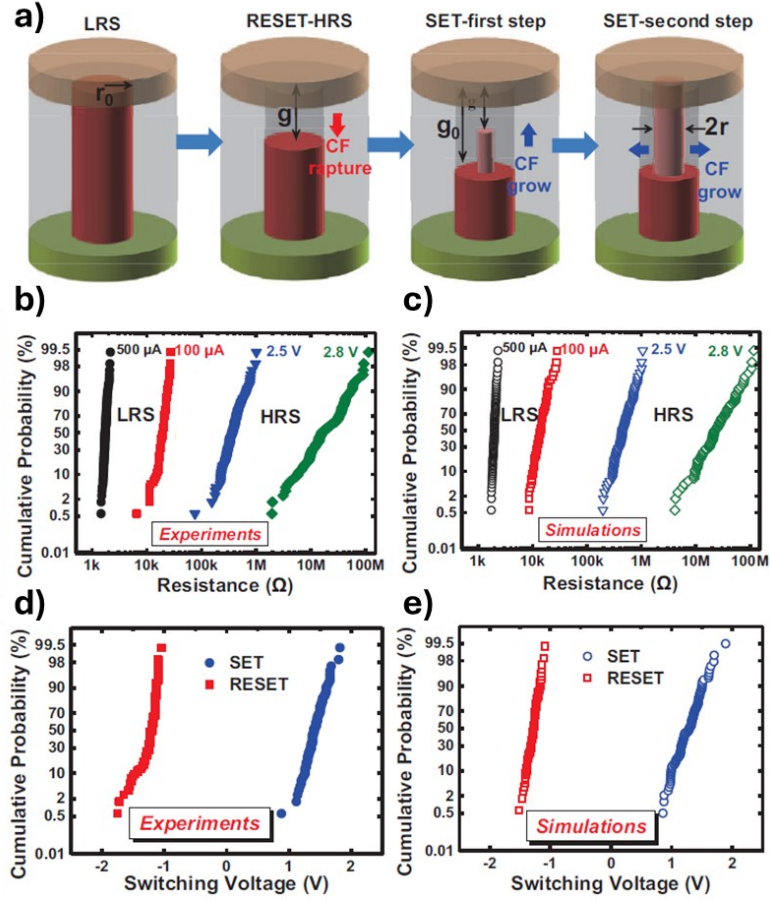


Figure 1.17. a) Schematic of modeling conductive filament (CF) evolution processes during SET and RESET operations on RRAM cell. b) Measured and (c) simulated characteristics with resistance distributions due to cycle-to-cycle variations. d) Measured and e) simulated switching voltage distributions. Adapted from [Li2015]

In [Reuben2020], an algorithm for the inclusion of variability in the Stanford-PKU model is presented. In [Gonzalez-Cordero2016], the connection between the temperature and filament shape with variability is analyzed.

A time series analysis for the evolution of particular observables in RRAMs can also be found in [Alonso2021]. This work presented an approach intended to reproduce the ‘inertia’ the experimental parameters have by defining the set and reset voltages as a function of the previous cycles and the error between experimental and simulated values. This approach required a deep analysis of the experimental features and their autocorrelation (Fig. 1.18).

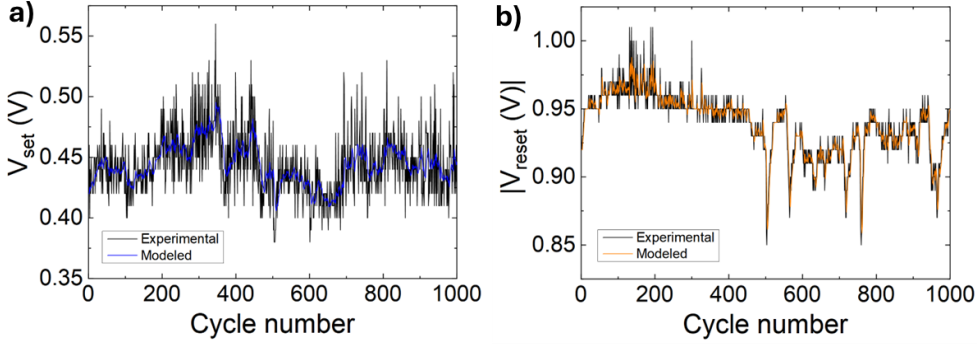


Figure 1.18. a) Set voltage versus cycle number for the switching series under consideration. Measured values are shown in black lines and the modeled ones in blue. b) Vreset versus cycle number for the switching series under consideration. Measured values are shown by black lines and the modelled ones in orange. Figures obtained using the approach in [Alonso2021] and adapted from [Roldán2023].

In this thesis, different methodologies to incorporate variability in RRAM device simulations are examined. These methodologies include thorough analysis of experimental data, development of the modeling approach and valuable tools for comparing experimental and simulated results. The model used in this thesis is the memdiode model for RRAM devices, a behavioral compact model [Miranda2015, Miranda2020, Aguirre2022]. Since this is a model in constant evolution and update, all the sections introducing the different approaches include the description of its version of the model.

1.4.3. Modeling Stochastic Resonance in RRAMs

The study of the beneficial role of SR in the performance of RRAM devices is an emerging topic in recent research. To establish effective methodologies and fully understand this phenomenon, a combination of experimental and modeling techniques is essential. As stated in the previous subsection, to address this issue from a modeling perspective requires the development and integration of various approaches, including physical, stochastic, and behavioral models.

While the modeling methods for RRAM variability have considerably evolved in recent literature, the modeling approaches for stochastic resonance in RRAM

devices remain less developed. Nevertheless, some studies have begun to address this challenge.

For instance, in [Stotland2012], the impact of additive noise in memristors was investigated using a physical model of a memristor. This work solves numerically a simplified version of the model equations and includes Gaussian noise in the input voltage. This study demonstrated that under specific conditions, noise can enhance the memory performance of the device, providing an early theoretical basis for understanding noise-induced effects in resistive switching systems. From Fig. 1.19, it can be observed that for a certain noise sigma (called Γ in Fig. 1.19), there is a maximum in the wideness of the hysteresis lobe area (or window) in the I - V curve and for larger noise intensities the window shrinks again.

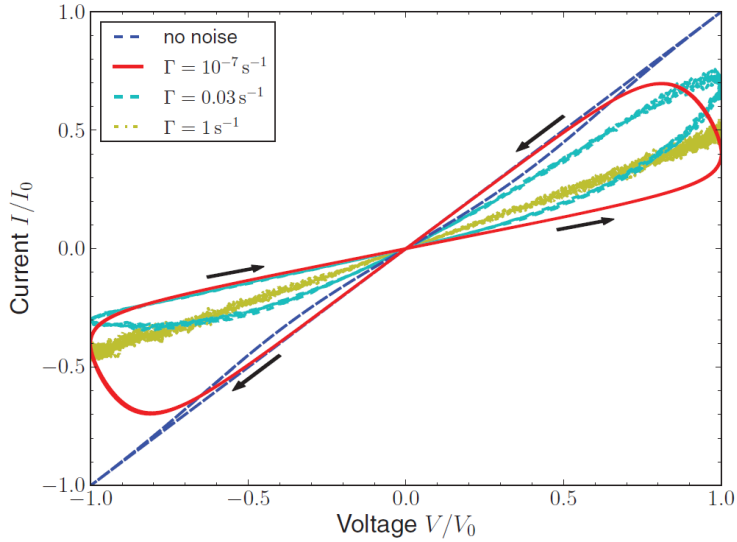


Figure 1.19. Simulated I - V characteristic for different noise intensities (here called Γ). V_0 is the amplitude of the sinusoidal voltage input. $I_0 = V_0/R_{on}$ is the maximum possible current through the system. Adapted from [Stotland2012].

In [Mikhaylov2021], a noisy signal was applied to zirconium and tantalum pentoxide-based memristors, with a detailed analysis from both experimental and theoretical viewpoints. This work included randomness in a physical model equation variable, and also in the external voltage source. The study reported a constructive role of noise in enhancing the switching dynamics, as represented in Fig. 1.20, where experimental and simulated results are compared. The

memory window opens and gets wider by increasing noise until a point where it narrows again with noise excess.

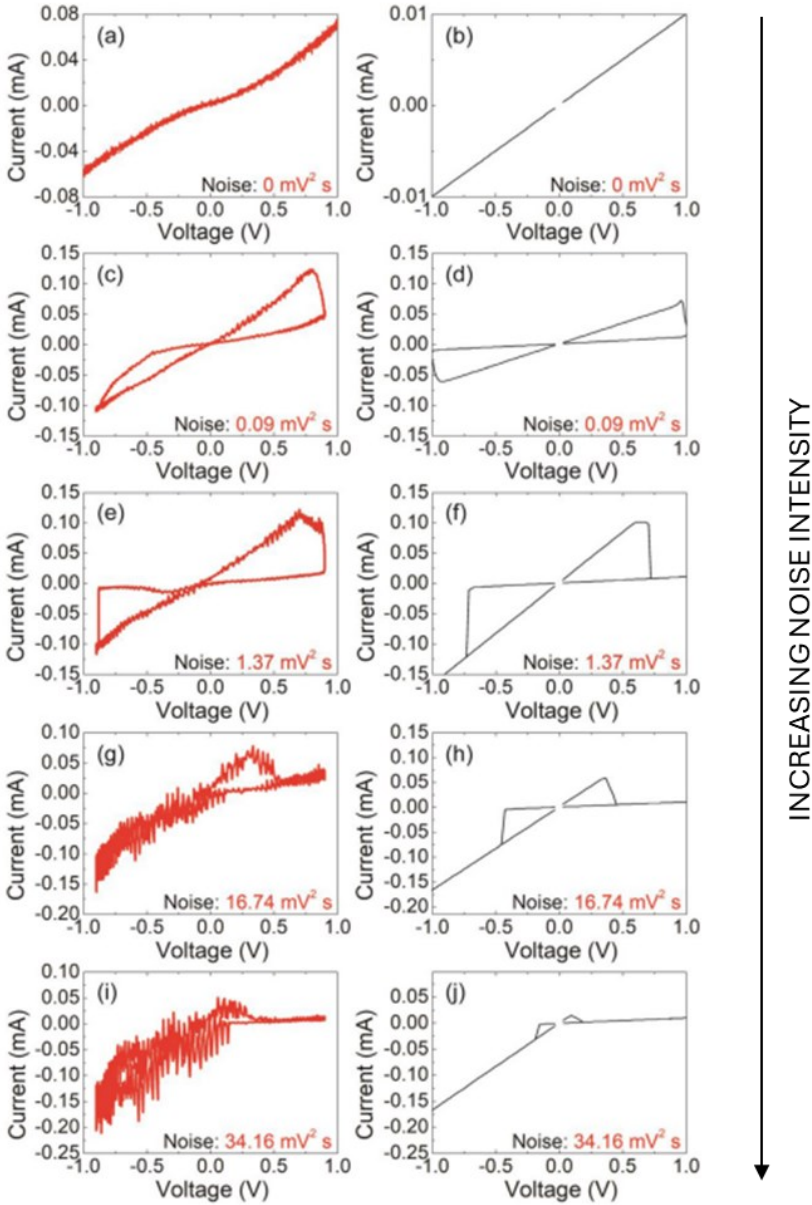


Figure 1.20. I - V characteristics of the memristors under study measured (left panels) and simulated (right panels) under the amplitude of signal 1 V and frequency 10 Hz for the growing intensity of external noise. Adapted from [Mikhaylov2021].

In this thesis, we aim to reproduce experimental findings on the beneficial role of external noise in RRAMs at device level (in both DC and AC regimes) and to investigate the effects of introducing noise into the voltage inputs of RRAM-based neuromorphic systems, using the memdiode model for both cases.

1.5. Highlights

This chapter provided a comprehensive overview of the state of the art of the resistive switching phenomenon, covering its dynamics, properties, and applications. Additionally, the chapter discusses the impact of the stochastic resonance phenomenon on RRAM devices and presents various modeling approaches from recent literature. This chapter provides the necessary background for the discussions and findings presented in the remainder of the thesis. The following chapter details the equipment used for electrical characterization and outlines the key fabrication processes of the investigated memristors, which are essential for the experimental results discussed in later chapters.

Equipment and Fabrication

This chapter is dedicated to present and describe the measurement equipment and setups as well as the fabrication processes for the memristors used for the experimental part reported in this thesis.

2.1 Equipment

The electrical measurements performed during this thesis have been carried out on a multiprobe table, where wafers or wafer fragments are placed and fixed to the chuck using vacuum. An optic microscope is used to contact the probes to the device electrodes. The connectors are plugged into the required instruments according to the required experiment, for example a semiconductor parameter analyzer (SPA), or a signal generator and an oscilloscope. All these instruments are connected to a PC via General Purpose Interface Bus (GPIB bus). The PC is in charge of controlling the GPIB-connected instruments, in our case using Matlab software. The basic principle behind the system's operation is the use of a 'talker' device (the PC) and one or multiple 'listener' devices (instruments). This system sends individual commands to the instruments like setting a voltage and receiving information from the instruments like registering the current. By using Matlab as the controlling software, the input and output data can be stored and analyzed within the same workspace.

Figure 2.1 presents the protocol for the most used setup in this thesis. The main instrument in the setup is the Agilent 4156C (AG-SPA), connected to the PC (a) with a GPIB cable (b) enabling us to perform and analyze the measurements. Since memristors are two terminal devices, the measurements require two probes and two triaxial cables, or source-measurement unit (SMUs) connecting the SPA and the device. In Fig. 2.1, the connections are visible from the AG-SPA (c) to the tips contacted to the device under test (d). After the post-measurement data treatment by means of Matlab software, the results can be presented, for example as a typical I - V curve from a HfO_2 -based memristor (e). The setup presented in Fig. 2.1 was used for measurements like isolated or cycled voltage sweeps for the electrical characterization of memristors presented throughout the following chapters of this thesis.

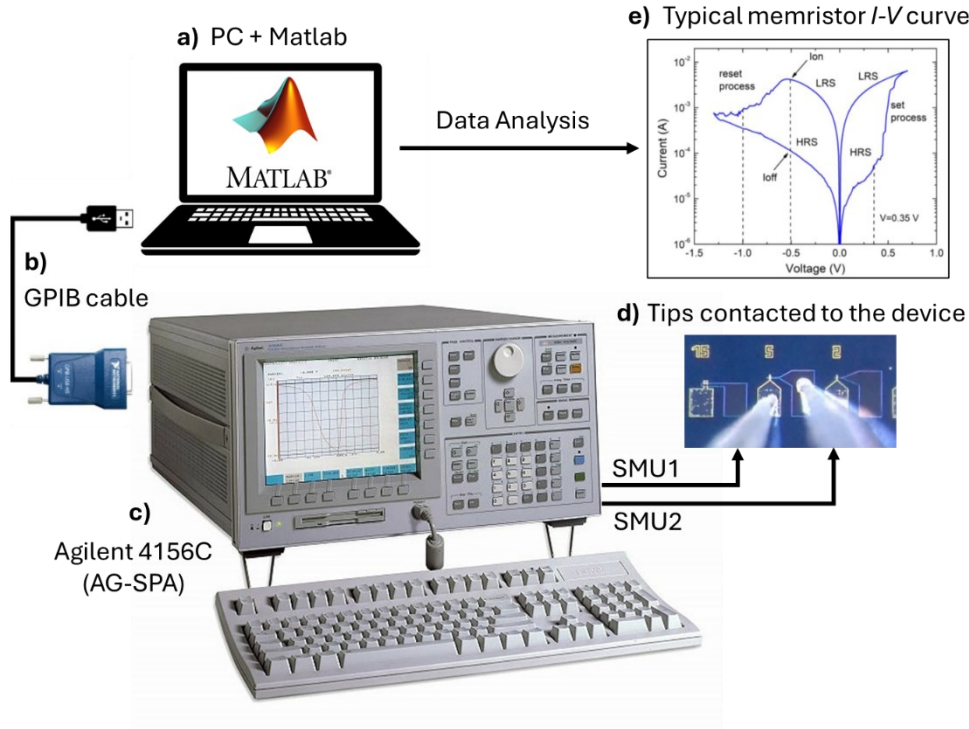


Figure 2.1. Most used setup for electrical characterization of memristors showing the PC (a) connected with a GPIB cable (b) to the AG-SPA (c), the SMU connections to the tip station (d), and an example of a device I - V curve (e).

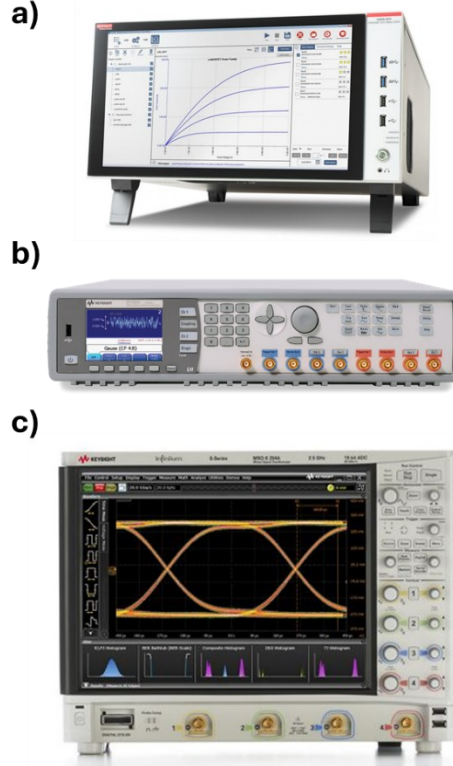


Figure 2.2. Instruments for electrical characterization: a) the Keithley 4200A-SCS semiconductor parameter analyzer, b) the Keysight 81150A pulse and noise generator and c) the Keysight MSOS254A high-definition oscilloscope.

In addition, other setups were used during the thesis for memristor characterization, like the Keithley 4200A-SCS semiconductor parameter analyzer (K-SPA) (Fig. 2.2a). This instrument was used to study the effect of external noise on memristors subjected to AC voltages, since it has a pulsed module which allows the application of pulsed signals with an accurate timing control (pulse width, rise and fall times and period) and register the current simultaneously. This pulsed module is the Keithley 4225-PMU (Pulsed Measure Unit) paired with the Model 4225-RPM (Remote Preamplifier Module). Another instrument that was used for different experimental measurements is the Keysight 81150A, called pulse generator (PG) in this thesis from now on (Fig. 2.2b). This instrument is able to generate pulses or triangular signals and, most important, it can generate a noisy signal, pivotal for the experiments related to the stochastic resonance phenomenon. The PG must be combined

with another instrument for data capturing. In addition, for some electrical measurements, the Keysight MSOS254A which is a high-definition oscilloscope is used to capture the input and output signals to the device (Fig. 2.2c).

The following section deals with the general structure of the devices used in this thesis as well as its fabrication process. It is worth mentioning that different wafers containing a large number of devices were characterized, so that the fabrication process parameters and conditions might slightly change. However, the processes detailed in the next section are common in all the analyzed wafers.

2.2 Fabrication Process of RRAM Devices

The memristors used in this thesis, which were fabricated at the Institut de Microelectrònica de Barcelona (IMB-CNM, CSIC), allowed an in-depth study of the electrical characteristics reaching the results to complete the main goals of the thesis. In this subsection, the fabrication method for two different memristor configurations are described. As previously mentioned, the RRAM device structure consists of a MIM or a MIS structure. One option for these structures is the **cross-point configuration** defined by an intersection of two metal lines, one for each electrode of the device. In between these metallic tracks, the dielectric layer is deposited. The fabrication requires 3 different photolithography masks: one for defining the bottom electrode, one for the top electrode and one to define the openings that will constitute the electrical contact to the bottom electrode. The initial surface is a silicon wafer. The cross-point configuration fabrication sequence is detailed next:

1. Growth of an insulating oxide layer through a thermal oxidation process of silicon.
2. A layer of metal that will form the bottom electrode of the device is deposited by sputtering deposition.
3. First photolithography: Patterns in Mask 1 are defined in the photoresist that are to be transferred to the bottom electrode metal through metal etching.
4. Removal of the photoresist: The metal patterns defined by Mask 1 remain on the wafer surface.

5. A thin layer of dielectric material is deposited using Atomic Layer Deposition (ALD) technique.
6. A layer of metal that will form the top electrode of the device is deposited by sputtering.
7. Second photolithography: Patterns in Mask 2 are defined in the photoresist that are to be transferred to the top electrode metal through metal etching.
8. Removal of the photoresist: The metal patterns defined by Mask 2 are now present on the wafer surface.
9. Third photolithography: Patterns are defined in the photoresist that will form the contact pads to the bottom electrode, which is entirely covered by the dielectric layer.

This process is summarized in Fig. 2.3 where a step-by-step flux diagram and the resulting device schematic cross-section after every fabrication step are presented with an optical microscope view of the final fabricated devices.

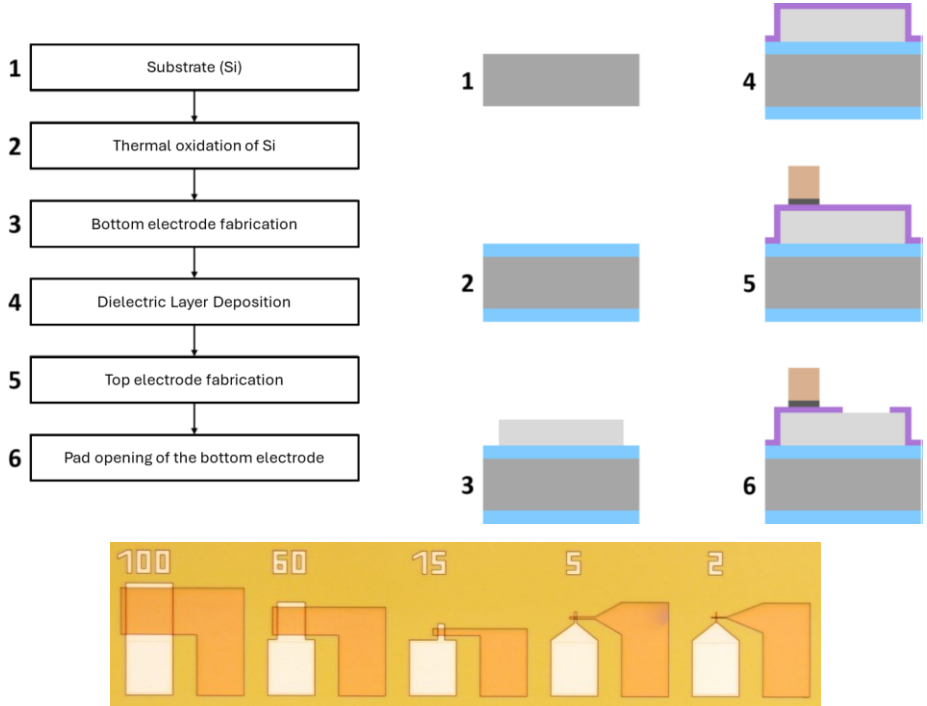


Figure 2.3. Cross-point configuration fabrication diagram, schematic cross section and resulting optical microscope top view of different sized memristors. Adapted from [Poblador2021].

Another option of samples fabrication is the **isolated configuration**, an alternative involving just one etching process and avoiding the two metals crossing. This approach consists of using an oxide layer to define the active area of the device, and a highly doped silicon substrate so that contact to the bottom electrode can be done by contacting the back side of the silicon substrate. Again, the initial surface is a silicon wafer. The isolated configuration fabrication sequence is detailed next:

1. Deposition of the bottom electrode over the entire surface of the silicon wafer is performed using sputtering.

Now there are two options for further steps depending on the moment of deposition of the dielectric thin layer:

Option 1: ALD first

2. Growth of the dielectric layer using Atomic Layer Deposition (ALD).
3. Deposition of a SiO_2 layer using Plasma Enhanced Chemical Vapor Deposition (PECVD).
4. First photolithography: Patterns in the mask defining the active area of the device are transferred to the photoresist and then to the oxide by etching and removal of the photoresist.

Option 2: ALD last

2. Deposition of a SiO_2 layer: Using PECVD.
3. First photolithography: Patterns in the mask defining the active area of the device are transferred to the photoresist and then to the oxide by etching and removal of the photoresist.
4. Growth of the dielectric layer using ALD.

From this point the sequence is the same for both options, structuring the top electrode:

5. Second photolithography transferring the patterns in the mask to the photoresist.
6. Sputtering deposition of the top electrode metal.
7. Removal of the photoresist and structuring the metal via lift-off process.
8. Backside metallization of the wafer by metal sputtering.

This process is summarized in Fig. 2.4 where a step-by-step flux diagram and the resulting device schematic cross-section after every fabrication step are presented with an optical microscope view of the final fabricated devices.

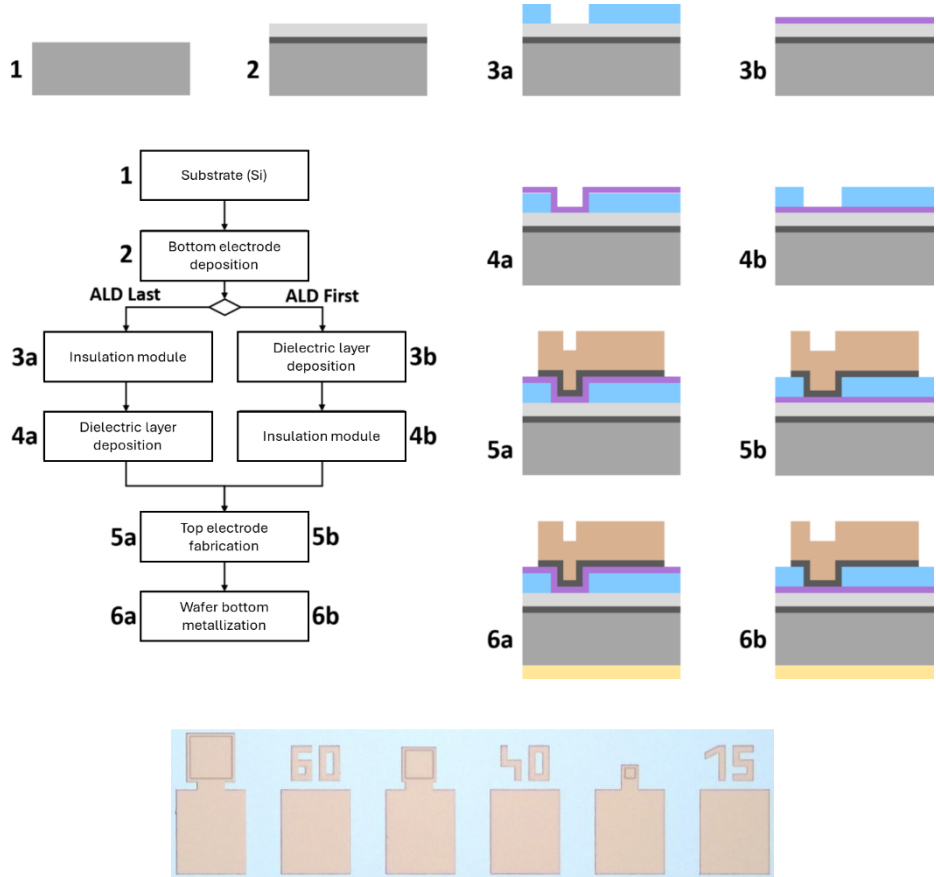


Figure 2.4. Isolated configuration fabrication diagram, schematic cross-sections and resulting optical microscope top view of different sized memristors. Adapted from [Poblador2021].

The isolated configuration presented sequence results in a MIM structure, since the bottom electrode is a metal layer. However, with this fabrication procedure, a MIS structure can also be fabricated, where, instead of the metal layer, the devices can be grown on top of silicon wafers [Poblador2018].

Once the main measurement setup and the general fabrication methods have been detailed, in every further chapter of this thesis, the devices used will

schematically be defined and referred to this subsection specifying the resulting device structure and highlighting any modification of the general fabrication method.

2.3 Typical I - V Curves and Figures of Merit

This section introduces the typical I - V curves obtained by using the AG-SPA setup and highlighting the main figures of merit to be analyzed in the following chapters. The devices used for this section consist of MIM structures with isolated configuration. The active area is $5 \times 5 \mu\text{m}^2$. In this wafer, the bottom electrode is common to all the devices and the electric contact to this electrode is performed by contacting the back side of the wafer, which was metallized with an aluminum layer (see Fig. 2.5a). All the memristors used in this thesis require an initial forming process. During this process the CF is completely created, and the device switches from the pristine state (PS) to the LRS, or ON state. At this point a reset process can be performed to reach the HRS, or OFF state and cycling set/reset processes is enabled. As an example, Fig. 2.5b presents the I - V curve during forming and the subsequent I - V curve is shown in Figs. 2.5c and 2.5d with linear current and logscale current respectively.

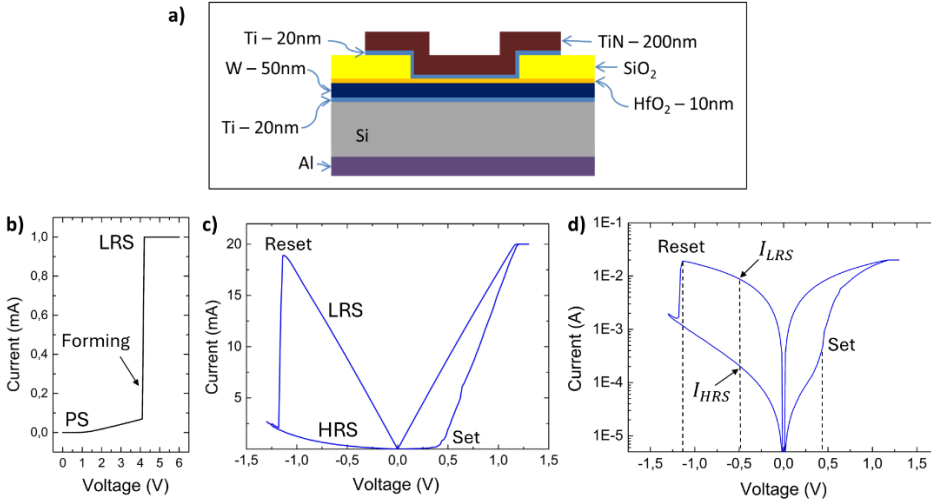


Figure 2.5. a) HfO₂-based memristor structure with an aluminum layer on the back side of the wafer, b) forming process, c) linear current I - V curve, and d) logarithmic current I - V curve after forming using the AG-SPA setup presented in Fig. 2.1.

For the forming process, a voltage sweep from 0 V to 6 V was applied to the memristor using a 1 mA compliance. For the I - V curves, the applied input signal was a DC voltage sweep from 0 V to 1.3 V, from 1.3 V to -1.3 V, and finally from -1.3 V to 0 V with a compliance of 20 mA. In addition, different figures of merit, or observables are highlighted: the set and reset voltages, and the HRS and LRS currents. These four observables will be pivotal for analyzing the memristor behavior under different conditions.

The **HRS** and **LRS currents** are generally extracted by obtaining the current values at a fixed voltage (-0.5 V in this case). The fixed voltage must fulfill two conditions: it must be high enough for differentiating both memristor states and low enough for not being close to the set or reset transitions. The **reset voltage** was defined as the voltage at the maximum current value in the negative region of the curve. There are different methods for obtaining the **set voltage**. Generally, it was obtained by finding the maximum slope change in the first quadrant of the I - V curve. However, some devices present more progressive set events where the maximum slope change is not a good method to select the set voltage. For those devices other approaches need to be followed to define the set voltage, like selecting a current value and obtaining the voltage, or plotting the conductance and selecting the voltage where the conductance is halfway from the HRS to the LRS. The key issue is to select a consistent method for determining the set voltage and proceed equally for all the data used for a certain experiment. Otherwise, the results would be inconclusive. A pivotal figure of merit for characterizing the device conduction is the resistance ratio (R_{OFF}/R_{ON} or R_{Ratio}), defined as the relation between I_{LRS} and I_{HRS} since the voltage value is the same for both extracted current values. The R_{Ratio} indicates the window opening in the I - V curve or the separation of HRS and LRS states.

2.4 Highlights

In this chapter, the equipment, methodologies for the fabrication of memristive devices and a first presentation of the electrical measurements have been detailed. A comprehensive understanding of the setups and devices is crucial for further research, as it lays the basis for interpreting both expected and unexpected results. Hence, this chapter serves as a reference in subsequent chapters, enhancing clarity and avoiding repetition. In addition, the main figures of merit to be analyzed which provide a thorough basis for device evaluation were introduced. The main two research directions of this thesis consist in exploring modeling approaches for the memristor cycle-to-cycle variability and studying the impact on memristor performance of the addition of external noise in the applied signal. These lines of research are discussed thoroughly in Chapters 3 and 4, respectively.

Modeling RRAM Devices and Cycle-to-Cycle Variability

This chapter of the thesis compiles the information, software and model specifications, data analysis tools and the different approaches for a general modeling of RRAM devices and its intrinsic C2C variability. As previously stated in the introduction, the software used for performing the simulations in this thesis is mainly LTspice [Brocard2021] using the memdiode model. The details about the version of the model used for each approach will be presented in the corresponding subsection. The content of this chapter evolves around the following publications: **SSE21**, **SSE23**, **JLPEA24** and **TNANO24** where different approaches to include C2C variability in LTspice and a robust and versatile Matlab implementation of the memdiode model are introduced.

In order to include variability in the LTspice simulator having a robust random number generator (RNG) is imperative. In this regard, a thorough study of the different alternatives to generate random numbers is reported in **TNANO24-SM**. This analysis compares different RNGs in LTspice and presents the implementation of the Monte Carlo Gaussian (MCG) RNG model, using the Box-Muller algorithm [Gentle1998], which ensures Gaussian noise generation. Despite some limitations from the simulator, the MCG function proved close alignment with a normal distribution, as quantile-quantile plots and Lilliefors

test demonstrate [Lilliefors1967]. The resulting MCG RNG was used in articles **EDL24**, **TNANO24** and **TED24**. In addition, **TNANO24-SM** highlights the importance of properly selecting the minimum timestep to prevent glitches in signals with high sampling rates. Visit **TNANO24-SM** in the complementary works section for the complete study.

3.1. Spice Modeling of Uncorrelated C2C Variability

As previously stated in Chapter 1, variability of the conduction characteristics of RRAMs is a hot research topic in academia and industry because it is considered one of the major showstoppers for the successful development and application of this technology. Since variability is always present in the operation of RRAM devices, its inclusion in any compact model is of pivotal importance. In this section, the quasistatic memdiode model (QMM) and the dynamic memdiode model are presented and detailed. A sensitivity analysis of the QMM is also reported and an approach to include uncorrelated cycle-to-cycle (C2C) variability is presented for both QMM and DMM. The contents in this section are extracted from the fundamental articles **SSE21**, **SSE23** and **TNANO24**, the section of the review paper [Roldán23] **AIS23** and the conference paper **MIEL21** included in the complementary works section of the thesis.

3.1.1 Quasistatic Memdiode Model

The quasistatic memdiode model (QMM) is a behavioral compact model that describes the conduction characteristics of bipolar resistive switching devices using a hysteresis operator which keeps track of the memory state of the device. According to the QMM, the I - V characteristic reads [Miranda2015]:

$$I(V) = I_0(\lambda) \sinh\{\alpha(\lambda)[V - (R_S(\lambda) + R_t)I]\} \quad (3.1)$$

where $I_0(\lambda) = I_{0min} + (I_{0max} - I_{0min})\lambda$ is the current amplitude factor, $R_S(\lambda)$ a variable series resistance, and $\alpha(\lambda)$ a fitting parameter. I_{0min} and I_{0max} are minimum and maximum current values (same for R_S and α), respectively. According to (3.1), for low currents, I depends exponentially on V whereas for high currents, I depends linearly on V . Equation (3.2) expresses the relationship

between the memory state λ , a variable ranged from 0 to 1 determining the resistive state (OFF and ON respectively), and the voltage across the filament's constriction $V_c = V - R_i \cdot I$ through the recursive hysteresis operator:

$$\lambda(V_c) = \min\{\Gamma^-(V_c), \max[\lambda(\overline{V_c}), \Gamma^+(V_c)]\} \quad (3.2)$$

where $\lambda(\overline{V_c})$ is the memory value a timestep before (in practice dictated by the simulator timestep). Γ^+ and Γ^- are the so-called positive and negative ridge functions (sigmoidals), respectively, and are expressed as:

$$\Gamma^\pm(V_c) = \frac{1}{1 + \exp[-\eta^\pm \cdot (V_c - V^\pm)]} \quad (3.3)$$

which represent the creation (+) and dissolution (-) processes occurring in the CF. η^\pm (*etas* and *etar* in the model script) are the set (+) and reset (-) transition rates respectively and V^\pm are the threshold voltages for set (+) and reset (-). The model uses other parameters for the fine-tuning of the simulated curves (see the green fragment in the model script in Table 3.1). The model is implemented in LTspice using an equivalent circuit with behavioral current sources and includes the snapback (*isb*) and snapforward (*gam*) effects.

```

.subckt memdiode + - H
.params
+ H0=2E-3 ri=190 rsmin=10
+ etas=50 vs=2 etar=9 vr=-0.57
+ rsmax=8 isb=33E-6 imax=4.5E-3 amax=2.0
+ imin=18E-6 amin=2.0 vt=0.48 gam=0.07
*Memory equation
BH 0 H I=min(R(V(C,-)),max(S(V(C,-)),V(H))) Rpar=1
CH H 0 1E-3 ic={H0}
*I-V
RE + C {ri}
RS C B R=K(rsmin,rsmax)
BD B - I=K(imin,imax)*sinh(K(amin,amax)*V(B,-)) Rpar=1E10
*Auxiliary functions
.func K(min,max)=min+(max-min)*V(H)
.func S(x)=1/(1+exp(-etas*(x- if(x>isb,vt,vs))))
.func R(x)=1/(1+exp(-etar* if(gam==0,1,pow(V(H),gam))*(x-vr)))
.ends

```

Table 3.1 LTspice quasistatic memdiode model script. Colors separate the different parts of the script: green for the parameters, violet for the model equations and blue for the auxiliar functions.

The devices in this section were fabricated using the previously detailed cross-point configuration presented in Chapter 2 and the resulting structure consists of a HfO_2 -based MIM structure with a 10 nm-thick oxide layer and $5 \times 5 \mu\text{m}^2$ active area. The resulting schematics is shown in Fig. 3.1a. More information about the electrical characterization of these devices is available in [Poblador2018]. Figure 3.1b shows the model adjustment to the median curve of 450 experimental voltage sweeping cycles and Fig. 3.1c presents an isolated cycle from the experimental dataset including the snapback (SB) voltage effect (in red). The SB effect occurs during the transition from HRS to LRS, during the creation of the conductive filament. This effect is characterized by a negative slope in the I - V curve dictated by the series resistance R_i (external or internal). By applying an appropriate R_i value and using the voltage correction ($V_{\text{corr}} = V - R_i \cdot I$), the intrinsic characteristics are revealed, showing a sharp current

increase at a voltage called V_T . The current increase after SB is often ascribed to the accumulation of ions or defects in the CF or to its lateral expansion [Karpov2016]. In the reset transition, the filament dissolution triggers at $-V_T$. Hence, V_T represents the minimum voltage required for moving the ions or vacancies [Maldonado2021, Maldonado2022].

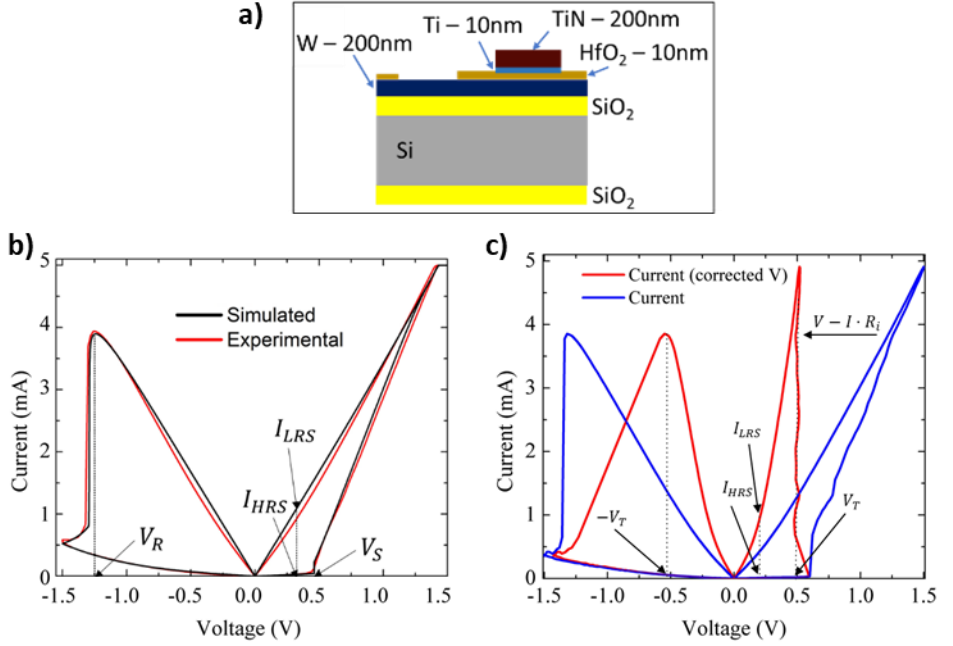


Figure 3.1. a) Schematic cross-section of the experimental devices. b) Simulation (black) results compared to the experimental (red) median I - V curve extracted from 450 cycles of experimental voltage sweeps. c) Isolated experimental cycle in blue and curve applying the snapback voltage correction in red.

A one-way sensitivity analysis was performed using the QMM which relates how uncertainty in the simulation output (observables) can be apportioned to different sources of uncertainty in the model inputs (parameters) [Saltelli2004, Saltelli2008]. In this case, as observables, we selected a figure of merit for every region of the I - V curves: the high resistance state current (I_{HRS}), the low resistance state current (I_{LRS}), the set voltage (V_S) and the reset voltage (V_R). In this sensitivity analysis the parameters were swept one at a time (50 steps each) in a reasonable range (this process does not include C2C variability) and the obtained I - V curves analyzed.

Figure 3.2 shows the relative variation of the observables a) I_{HRS} , b) I_{LRS} , c) V_S and d) V_R as a function of the relative variation of selected model parameters: reset transition rate η_r or $etar$ (in orange), the I - V slope parameter α or $alpha$ (in blue), the maximum current I_{max} (in green), and the minimum current I_{min} (in black). Table 3.2 summarizes the magnitude and trend associated with the variation of each observable in terms of all the modified model parameters (a change of $\pm 30\%$ from its reference value was considered for the analysis). Notice that Table 3.2 uses colors and signs. Red color is associated with almost no dependence between the observable and the model parameter; orange indicates that for a 10% model parameter variation, less than 10% variation is detected in the observable and green corresponds to a variation larger than 10%. (+) or (-) indicate direct or inverse dependence, respectively. Reading the first column of Table 3.2, we can see the impact of all the inputs over the observable I_{HRS} . It is observed for I_{HRS} a strong and positive dependence on $alpha$, $Imin$, and gam . It also exhibits strong and inverse dependence on $Vapp$ and $etar$, weak and positive effect from Vr and $Imax$ and it is scarcely affected by Ri , $etas$, Rs , and Isb . This kind of test is of utmost importance for investigating the sensibility of the considered simulation model when subjected to variability. This helps the readers and potential users of the model to understand the effect of parameters and be able to easily fit their own experimental data to analyze it and predict its behavior in different scenarios. This subsection contains information from article **SSE23**, and the conference paper **MIEL21**.

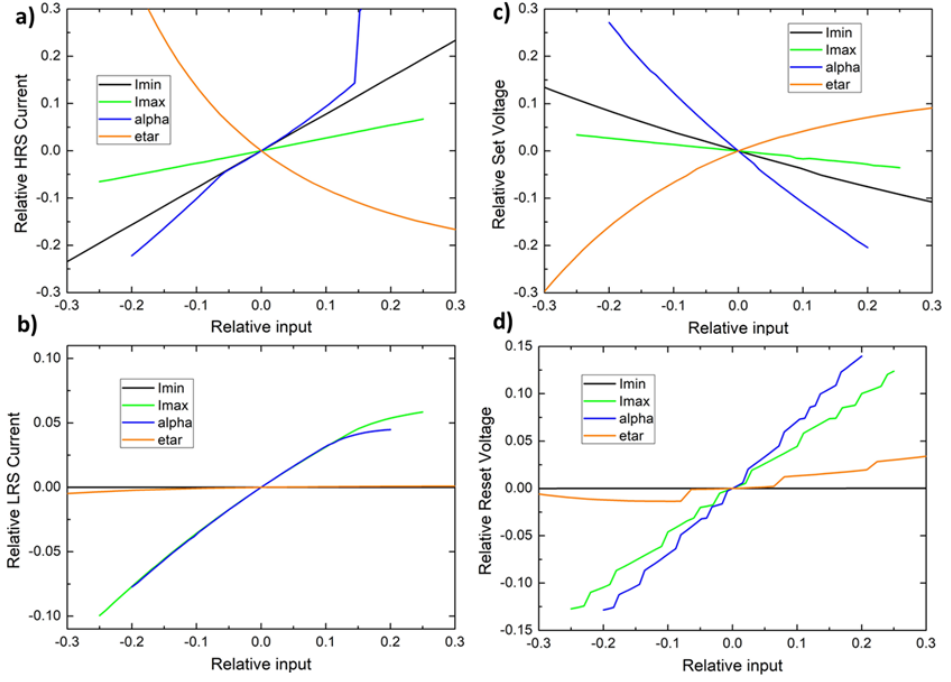


Figure 3.2. One-way sensitivity plots for the relative change of the observables a) I_{HRS} , b) I_{LRS} , c) V_S and d) V_R against the relative change of the model parameters: etar (orange), α (blue), I_{max} (green) and I_{min} (black).

| | I_{HRS} | I_{LRS} | V_S | V_R |
|------------------|-----------|-----------|-------|-------|
| V_{app} | - | 0 | + | 0 |
| R_i | 0 | - | 0 | + |
| etas | 0 | 0 | 0 | 0 |
| etar | - | 0 | + | + |
| α | + | + | - | + |
| V_r | + | 0 | - | + |
| R_s | 0 | - | 0 | - |
| I_{sb} | 0 | 0 | + | 0 |
| I_{max} | + | + | - | + |
| I_{min} | + | 0 | - | 0 |
| gam | + | 0 | - | 0 |

Table 3.2. Sensitivity analysis summary: intensity and sign (direct or opposite) of the four selected observables against all the analyzed parameters. + and - signs for direct and inverse dependence, respectively. Green: $>10\%$, orange: $<10\%$ and red 0%.

3.1.2 Uncorrelated C2C Variability using the QMM

Once the QMM model has been introduced and analyzed, this subsection is dedicated to the inclusion of uncorrelated C2C variability through the random assignment of the model parameters value. Accordingly, the generated I - V cycles are considered independent so that no trends in the low (LRS) or high (HRS) resistance state are expected. This analysis mainly focuses on the spread of the I - V curves around the median characteristic. In this subsection we first investigate the statistical distribution of 450 experimental cycles using the *fitdistrplus* package for the R language [Delignette-Muller2015]. Figure 3.3a presents all the experimental voltage sweep cycles, in this case using memristors as those indicated in Fig. 3.1. Again, the active area is $5 \times 5 \mu\text{m}^2$. The HRS and LRS current histograms are shown in Figs. 3.3b and 3.3c. The measurement procedure was performed using the AG-SPA setup and comprises a forming process occurring at around 4 V limited at 1 mA. During cycling, the applied voltage was swept from 0 V to 1.5 V, from 1.5 V to -1.5 V, and finally from -1.5 V to 0 V with a compliance of 5 mA. Observing the LRS current histogram in Fig. 3.3c, there is a double peak, which suggests that there are two main different configurations of the CF once completely created.

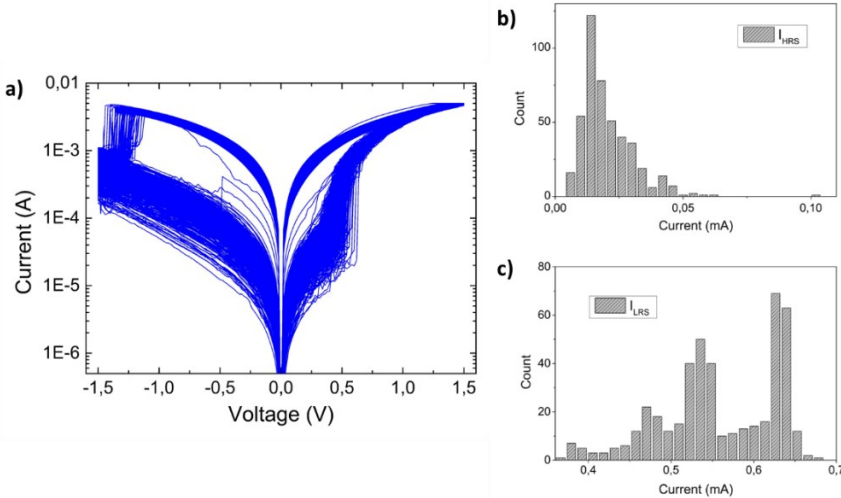


Figure 3.3. I - V curves (a) and HRS and LRS current histograms (b and c respectively) from the HfO_2 -based memristors of $5 \times 5 \mu\text{m}^2$ active area and cross-point configuration.

The information obtained from the statistical analysis of the experimental curves is used to define the model parameters in the QMM LTspice script using the following step list:

1. Measurement, and analysis of the experimental curves to extract the experimental parameters to be reproduced.
2. The best candidate distributions for the observables are found by means of a combination of tools. First, the Cullen and Frey skewness-kurtosis (SK) plot is used as an indicator of the appropriateness of the different candidate distributions. Further analysis is required before concluding which distribution better suits.
3. The different candidate distributions (normal, lognormal, gamma, and Weibull) are fitted and compared with the experimental observables by means of the goodness-of-fit (GoF) statistics (Kolmogorov-Smirnov, Cramer-von Mises, Anderson-Darling) and criteria (Akaike's and Bayesian). In addition, the quantile-quantile (Q-Q) plots graphically compare the experimental distributions with parametric models. This determines the most plausible distributions for experimental parameters.
4. Once the model parameter distributions were established, they were included in the QMM model script for performing simulations including variability.
5. An iterative optimization process was followed to adjust the simulation parameters for obtaining close agreement with the experimental curves. The simulated observables and their variability obtained from a complete simulation run were analyzed first. With this information at hand the parameter values were modified in the appropriate direction (with the help of the one-way SA approach) and the simulation was performed again. This process was repeated until coincidence is achieved, within certain error margins, between the experimental and simulation results.

Figures 3.4a-c show the density plots for V_T , V_R , and R_i , respectively, corresponding to the distributions investigated. In addition, the quantile-quantile (Q-Q) plots, which graphically compare the experimental distributions with the parametric models, are illustrated in Figs. 3.4d-f, for

V_T , V_R , and R_i , respectively. The combination of the information obtained from the GoF statistics and criteria, and the Q-Q plots were used to determine the most plausible distribution for each observable. For the complete study of the candidate distributions, including the SK plots and statistics, read articles SSE21 and SSE23.

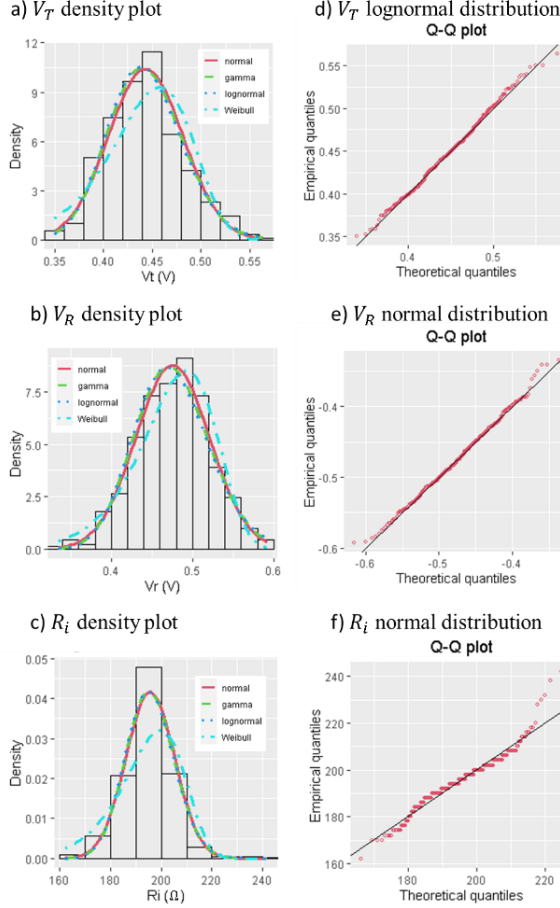


Figure 3.4. a), b) and c) show density plots for V_T , V_R and R_i , respectively, with normal, gamma, lognormal, and Weibull distributions. d), e) and f) show Q-Q plots after selecting the best fitting distribution.

In summary, the analysis carried out indicates that V_T follows a lognormal distribution while V_R and R_i are better described by a normal distribution. The same procedure was followed for the rest of the observables resulting in a normal

distribution for I_{SB} and lognormal distributions for I_{HRS} and I_{LRS} . This information was included in the model parameters section of the QMM script and was used to generate a set of simulated curves with variability.

Table 3.3 presents the parameters section of the model script including variability. The parameters following a normal distribution and a lognormal distribution are represented in red and blue colors respectively. The model equations and auxiliary functions are exactly the same, as in Table 3.1. Some of the model parameters were assumed to be constant to avoid over-randomness in the output curves. The LTspice *gauss* function was used to generate the appropriate parameter values and variability. Simulations were performed taking into account the particular features of the experimental curves, such as the voltage span and the number of cycles. The parameters (including variability) are calculated at the beginning of each cycle and are kept constant until the next cycle. Since ultimately the simulated I - V curves are the result of a sequence of operations in which a number of random parameters are involved, there is always an underlying connection among the mean and dispersion values that need to be considered in order to achieve a consistent set of curves. The goal was to reproduce as close as possible the median curve and the spread of the whole experimental data set.

```
.params
+ H0=2E-3 ri=193+gauss(1) rsmin=10
+ etas=50 vs=2 etar=9 vr=-0.57+gauss(0.028)
+ rsmax=8+gauss(1) isb=33E-6+gauss(2E-6)
+ imax=exp(-5.38+gauss(0.06)) amax=2.0
+ imin=exp(-10.9+gauss(0.68)) amin=2.0
+ vt=exp(-0.733+gauss(0.08)) gam=0.07
```

Table 3.3. Parameters section of the model script. Parameters including variability with a normal and lognormal distribution are represented in red and blue respectively.

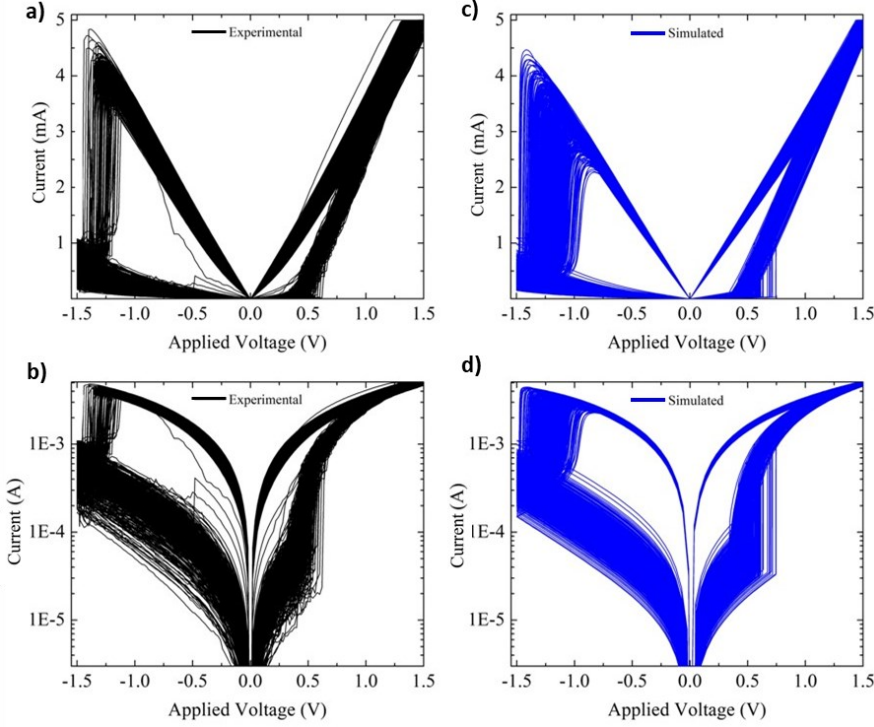


Figure 3.5. Experimental and simulated curves comparison. a, c) I - V curves, and b, d) I - V curves in logscale for experimental and simulated respectively.

In Fig. 3.5, experimental (black) and simulated (blue) curves are compared using two alternative plots for the same set of I - V curves: a) and c) linear-linear axes, and b) and d) log-linear axes. The fitting is reasonably good and simulations reproduce the main features of the experimental curves in all cases. The most conspicuous difference occurs in LRS, mainly because of the peculiarity of the available experimental data. A deeper and fairer comparison between the experimental and simulated observables is presented in Fig. 3.6. This figure shows the statistical distributions corresponding to the four main observables. Aiming to compile information from the different sections of the I - V curves, the following observables were specifically selected: I_{HRS} for the HRS curve, V_T for the SET transition, I_{LRS} for the LRS curve, and V_R for the RESET transition. I_{LRS} exhibits a notable difference. For the case under study, the experimental I_{LRS} histogram shows a double peak which likely corresponds to two different configurations of the CF or different coexisting CFs. Since the approach we report in this subsection only considers a single set of parameters

for each distribution, the simulated curves cannot reproduce the two distributions experimentally observed. For reproducing this double-peak parameter a possible solution would be to include two different distributions and a probability factor for each distribution.

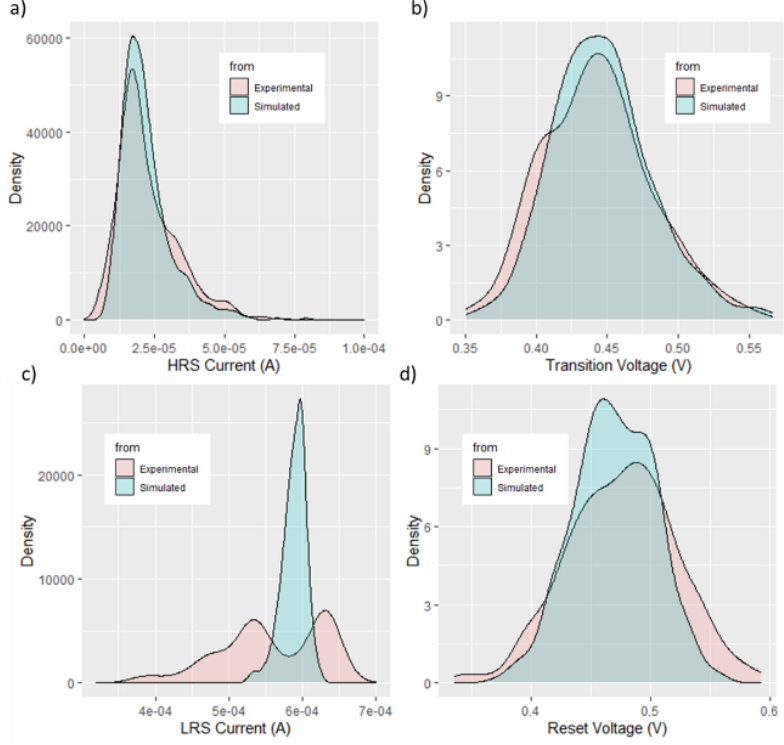


Figure 3.6. Comparison of experimental and simulated parameter distributions: a) I_{HRS} , b) V_{T} , c) I_{LRS} , and d) V_{R} .

3.1.3 Uncorrelated C2C Variability using the DMM

Following the same approach as in Subsection 3.1.2, here we applied the same procedure of experimental curves analysis and parameter distribution determination but now using the dynamic memdiode model (DMM). The contents of this subsection contain information from a section in the [Roldán2023] review, included as **AIS23** in the complementary works section at the end of this manuscript. Before entering the C2C variability inclusion, the DMM will be presented. The DMM describes the conduction characteristics of

RS devices under the application of arbitrary input signals. The origin of the switching behavior is related to the creation and destruction of the CF that spans across the dielectric layer. The DMM reproduces the I - V characteristic of bipolar-type memristive devices using two coupled equations. The first equation (3.4) deals with electron transport while the second equation (3.5) relates to the internal state of the device. According to the DMM, the I - V characteristic reads [Miranda2020, Aguirre2022, Blasco2015]:

$$I(V) = I_0(\lambda) \sinh\{\alpha(\lambda)[V - (R_c(\lambda) + R_i)I]\} \quad (3.4)$$

where V is the applied voltage, I_0 the current amplitude factor, R_c a variable series resistance, and α a fitting parameter. λ runs between 0 and 1 and it is called the memory state of the device. Its purpose is to control the transitions $\text{HRS} \leftrightarrow \text{LRS}$. R_i is a fixed resistance related to the snapback voltage correction. Notice that Equation (3.4) includes three different parameters with λ -dependence. For simplicity, these parameters are assumed to change linearly and in the same way from a minimum (*off*) to a maximum (*on*) value as a function of λ . For instance, $I_0(\lambda) = I_{off} + (I_{on} - I_{off}) \cdot \lambda$, where I_{off} and I_{on} represent the minimum (HRS) and maximum (LRS) current values, respectively. According to Equation (3.4), in HRS, the current depends exponentially on V , while in LRS, the current depends linearly on V because of the potential drop across the series resistances R_i and R_c . λ is described by a balance-type voltage-driven differential equation [Miranda2020]:

$$\frac{d\lambda}{dt} = \frac{1 - \lambda}{\tau_S(\lambda, V_{sb})} - \frac{\lambda}{\tau_R(\lambda, V_{sb})} \quad (3.5)$$

where $\tau_{S,R}$, called TS and TR , respectively in the model script (Table 3.4), are the characteristic times for the set and reset transitions. These characteristic times are expressed as:

$$\tau_S(V) = \exp[-\eta_S(V_{sb} - V_{S,T})] \quad (3.6)$$

$$\tau_R(V) = \exp[\eta_R \lambda^\gamma (V_{sb} - V_R)] \quad (3.7)$$

where $\eta_{S,R}$, also called *etas* and *etar* respectively in the model script, are the transition rates. $V_{S,R}$ are the set and reset switching voltages, respectively. The snapback current (*isb* in the model script in Table 3.4) acts as a threshold current for the snapback effect. The snapforward parameter $\gamma \geq 0$ (called *gam* in

the model script) controls the reset transition rate. Further details about the DMM can be found in [Miranda2020, Aguirre2022].

```
.subckt memdiode + - H
.params
+ H0=0 ri=30 RPP=1E10 etas=20
+ Vr=-0.6+gauss( $\sigma_{vr}$ ) vs=2 etar=20
+ Ion=1E-2+gauss( $\sigma_{ion}$ ) aon=2 ron=1
+ Ioff=1E-5+gauss( $\sigma_{loff}$ ) aoff=2 roff=10
+ Isb=20E-6+gauss( $\sigma_{isb}$ ) vt=0.7 gam=0.2
*Memory Equation
BI 0 H I=if(V(+,-)>=0,(1-V(H))/TS(V(C,-)),-V(H)/TR(V(C,-)))
CH H 0 1 ic={H0}
*I-V
RI + C {ri}
RS C B R=K(ron,roff)
BF B - I=K(Ion,Ioff)*sinh(K(aon,aoff)*V(B,-)) Rpar={RPP}
*Auxiliary functions
.func K(on,off)=off+(on-off)*limit(0,1,V(H))
.func TS(x)=exp(-etas*(x-if(I(BF)>Isb,vt,vs)))
.func TR(x)=exp(etar*pow(V(H),gam)*(x-Vr))
.ends
```

Table 3.4. LTspice DMM script including variability in the most significant parameters. The Gaussian function is added, and the σ is written as a variable for each parameter since different values were applied in this subsection. Colors separate the different parts of the script: green for the parameters, violet for the model equations and blue for the auxiliar functions.

Notice the DMM has similarities with the previously introduced QMM, like the current equations and the building parameters. However, there are key differences between both models. In the QMM the internal state of the device adjusts instantly to changes in the inputs, neglecting the time-dependent dynamics. In contrast, the DMM accounts explicitly the time-dependent evolution of the internal state variable by means of a differential equation. While the QMM is useful for steady-state or low-frequency conditions, the DMM is a better option for understanding higher frequency domains or transient responses.

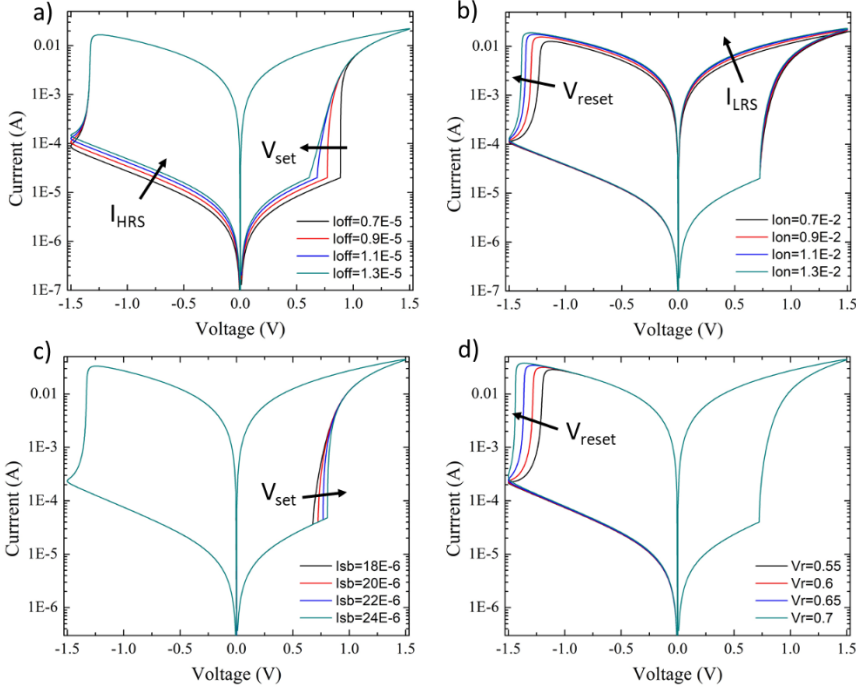


Figure 3.7. Impact of different model parameters on the I - V characteristics: a) I_{off} , b) I_{on} , c) I_{sb} , and d) V_r . The main effects produced by the change of the model parameters is marked with an arrow.

In order to understand model behavior, the effect of changing the key model parameters is evaluated in the model script presented in Table 3.4, Figure 3.7 shows the results of this study. The changes are obtained by iterating 4 different parameters a) I_{off} , b) I_{on} , c) I_{sb} and d) V_r , one at a time. Notice that I_{sb} and V_r changes only produce changes in the output transitions meanwhile I_{off} impacts the HRS current and set transition and I_{on} impacts the LRS current and reset transition. In Fig. 3.7, similarly to the one-way SA in the previous subsection, it is shown that different parameters impact different regions of the output simulations. It is of utmost importance to understand the role of each parameter for not crashing the simulator or generating curves including over-randomness in its parameters in the process of reproducing the variability of a given experimental set of curves.

Once the DMM is introduced, the uncorrelated C2C variability inclusion is discussed. The followed approach is the same as in the previous subsection, by

including variability in the model parameters by means of the *gauss* function in LTspice. However, in this case, the simulations are not reproducing any experimental measurements. In this subsection, only 4 parameters contain the addition of the *gauss* function, hence with these 4 parameters, a simulation containing C2C variability can be performed. In the experimental procedure, three different configurations of variability were selected: A, B and C increasing the σ values for every parameter. For every configuration, a 10-cycle of 1 second simulations were carried out applying the same sinusoidal voltage (1Hz and 1.5V of amplitude). The results are shown in Fig. 3.8 and the σ values for every configuration: a) A in black, b) B in red and C in blue) are collected in Table 3.5 As expected, the simulated results show more dispersion as the chosen σ values are increased. Since DMM is a behavioral compact model, by means of tuning the model parameters value and σ , a suitable configuration to fit an experimental set of measurements can be found.

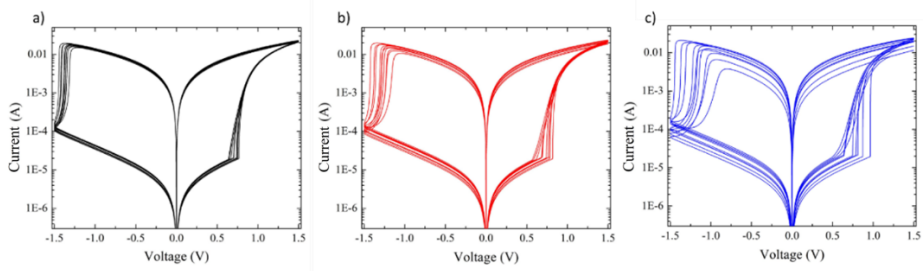


Figure 3.8. I - V curves from 10 cycles simulations including the σ values configuration in Table 3.5; a) A (lower values) in black, b) B (moderate values) in red, and c) C (high values) in blue.

| | A | B | C |
|------------------------|--------|--------|--------|
| σ_{Ioff} | 0.1E-5 | 0.2E-5 | 0.4E-5 |
| σ_{Ion} | 0.1E-2 | 0.2E-2 | 0.4E-2 |
| σ_{Isb} | 1E-6 | 2E-6 | 2E-6 |
| σ_{Vr} | 0.015 | 0.03 | 0.04 |

Table 3.5. Configurations for σ values added to the parameters in the model (Ioff, Ion, Isb and Vr) to obtain the three sets of simulated curves in Fig. 3.8.

In this subsection a first approach to include C2C variability in the DMM was presented. The effect of changing the parameters value was studied and 3

different configurations of variability were presented. The model is able to generate variable I - V curves, and the output simulated curves respond according to changes in the parameters value and σ . The further steps consist in generating a more realistic variability. Since parameters can be affected by themselves as an autoregressive process, by other parameters and by the time evolution, the logic continuation would consist in the addition of the autocorrelation of parameters.

3.2 Modeling Correlated C2C Variability

As stated in the previous section, the inclusion of autocorrelation in the variable parameters is a coherent process. In this section, a method for including correlated C2C variability in the Dynamic Memdiode Model (DMM) [Miranda2020, Aguirre2022] is reported. This section contains information from article **TNANO24** and supplementary material **TNANO24-SM**. The proposed methodology basically consists in introducing correlation and noise in some key model parameters of the DMM. The objective of this work is to show how this new approach is able to generate I - V curves with a degree of dispersion and correlation comparable to what is experimentally observed in HfO_2 -based RRAMs. The devices used in this section were presented in the previous section in Fig. 3.1. The I - V measurements were performed using the AG-SPA. Fresh devices were subjected to a 1 mA current-limited forming process, which in these devices occurs at voltages close to 3.5 V. During cycling, the applied voltage was swept from 0 V to 1.3 V, from 1.3 V to -1.3 V, and finally from -1.3 V to 0 V (100 cycles). Current limitation was included during the set process (20 mA) to avoid an irreversible breakdown of the device. The reset process takes place with no kind of limitation. Figure 3.9a shows 100 I - V cycles for an electroformed memristor. Cycled curves are shown in grey while the median curve is in red. For the analysis, HRS and LRS currents were also evaluated at $V = -0.2$ V. Figure 3.9b shows the resulting I - V curves after applying the snapback (SB) correction to the voltage $V_{sb} = V - R \cdot I$, where R is any internal/external series resistance.

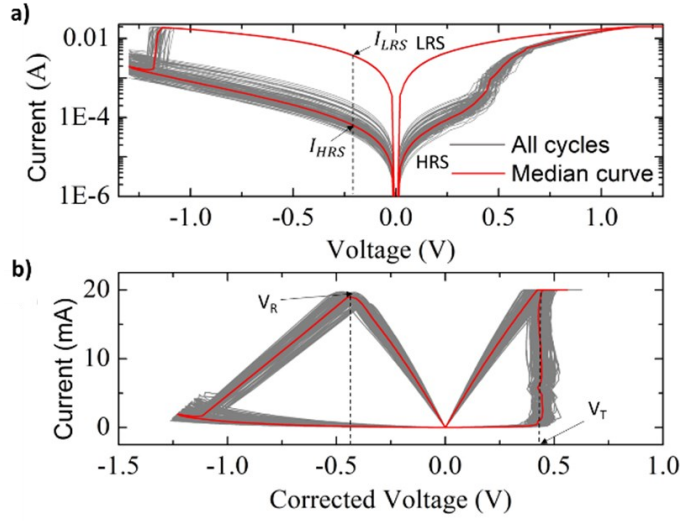


Figure 3.9. a) All cycles and median I - V characteristics for the RRAM devices in logarithmic current axis. b) The same I - V curves using the snapback voltage correction. V_T is the transition voltage and V_R the reset voltage.

Figure 3.10a presents the HRS and LRS current evolution measured at -0.2 V for all the cycles just reported in Figs. 3.9a and 3.9b. Notice that both the LRS and HRS currents exhibit correlated fluctuations, which are clearly detected in the autocorrelation (AC) plots of Fig. 3.10b. Because of this autocorrelated fluctuations, an extension of the approach presented in the previous section was required.

A good candidate function to include correlated variability in the simulations was the Ornstein-Uhlenbeck (OU) process, which fulfils the randomness and autocorrelation effects. The AC of an OU process follows the exponential relationship $AC \sim e^{-\alpha \cdot Lags}$, where α is a constant. We found $\alpha_{HRS} = 0.4$ and $\alpha_{LRS} = 0.17$ for the selected experimental data. Figure 3.10b graphically summarizes the strength of the relationship between the current and past observations (Lags), in our case, the current and past cycles. This approach to include correlated variability in the DMM also includes the experimental analysis for the experimental curves presented in Subsection 3.1.2, where the best distributions for the different experimental observables were obtained using the *fitdistrplus* package for the R language and incorporated into the LTspice model

script. The description of the OU process and the mathematical steps towards the inclusion of the uncorrelated C2C variability are described next.

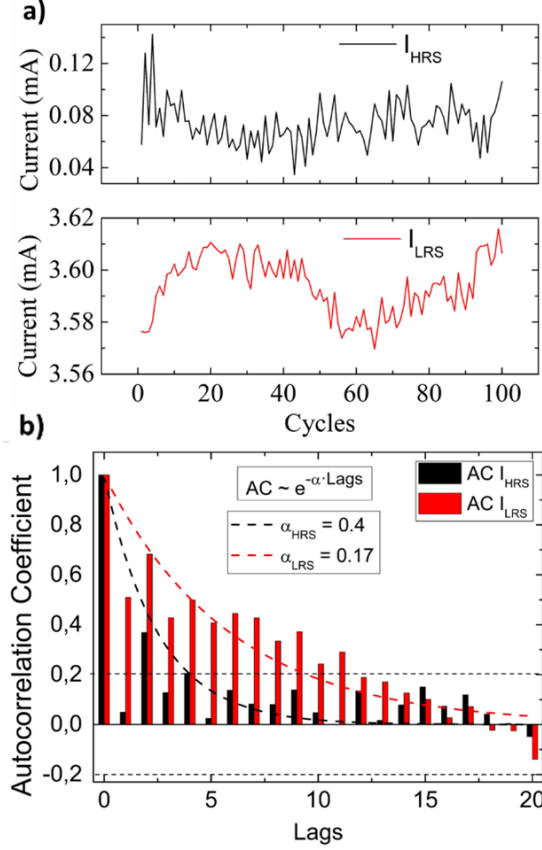


Figure 3.10. a) HRS and LRS current values measured at -0.2V for all the cycles available. b) AC plots for HRS (in black) and LRS (in red) currents. The dash lines are the theoretical exponential decay for AC in an OU process ($AC \sim e^{-\alpha \cdot \text{Lags}}$).

3.2.1 The Ornstein-Uhlenbeck Process

This subsection is dedicated to introducing the Ornstein-Uhlenbeck (OU) process [Uhlenbeck1930] and how to implement it in the LTspice circuit simulator. OU is a widely known stochastic process that comprises a deterministic term for the evolution of the variable of interest plus a noise term which drives the system out of equilibrium. OU processes have a plethora of applications in physics, mathematics, biology, and more, and are the only

stationary Gauss-Markov processes. Because of that, OU plays a central role in the theory of stochastic processes. Since the simulated variable drifts towards its mean value, the OU process is also called mean-reverting. The general expression for the OU process is given by the Itô-type stochastic differential equation (SDE):

$$dx_t = \Theta(\mu - x_t)dt + \sigma dW_t \quad (3.8)$$

where x_t is the value of the variable at time t , μ its central location, Θ the reversion coefficient, dt the time step, σ the volatility coefficient (noise amplitude) and W_t the Wiener process (white noise). The discretized version of (3.8) is expressed as [Gardiner2004]:

$$X_{n+1} = X_n + \Theta(\mu - X_n)\Delta t + \sigma\Delta W_n \quad (3.9)$$

where ΔW_n are independent identically-distributed Wiener increments, or in other words, a normal distribution with zero mean and Δt variance. Hence, $\Delta W_n \sim N(0, \Delta t) = \sqrt{\Delta t} \cdot N(0, 1)$. Accordingly, in practice, Equation (3.9) reads:

$$X_{n+1} = X_n + \Theta(\mu - X_n)\Delta t + \sigma\sqrt{\Delta t} \cdot N(0, 1) \quad (3.10)$$

The implementation of (3.10) requires the use of a Gaussian number generator, a topic thoroughly discussed in TNANO24-SM.

3.2.2 Correlated C2C Variability in LTspice

This subsection is focused on the simulation and characterization of the complete stochastic process. The LTspice tool for generating a controlled recursive process as required by (3.10) is the *delay* function in LTspice. Otherwise, the simulation timestep is always under the control of the simulation engine. The *delay* function considers two parameters: the variable of interest and in our case the time between two consecutive cycles (Δt or *del* in the model script). This Δt considered for simulations needs to be compatible with the experimental data. Subsequently, the model script is presented in Table 3.6 and thoroughly analyzed. $+$ and $-$ are the conventional device terminals, while H is the output terminal for the memory state (not used here). The first section defines the model parameters. *del* specifies the timing of the autoregressive part of the function and corresponds to the period of the measurement cycle. *fps*

(fluctuations per second) is the sampling rate for the random part of the function. $H0$ is the initial memory state and V_t the transition voltage. RPP is a parallel resistance required by the output current generator. The complete circuit is illustrated in Fig. 3.11, which shows the details of the model parameter distributions. To model the correlated variability, a first approximation *pseudo*-OU (p-OU) processes in the definition of 4 DMM parameters were used (see the model script in Table 3.6). The reason for calling the generated processes *pseudo*-OU is the appearance of unexpected points during the simulations because the timestep is not under the user's control in LTspice but only the maximum timestep. However, the time evolution and probability distribution of the LTspice generated signal proved to match an OU signal generated with Matlab. This analysis and further details on the implementation of the p-OU signal in LTspice are reported in TNANO24 and TNANO24-SM.

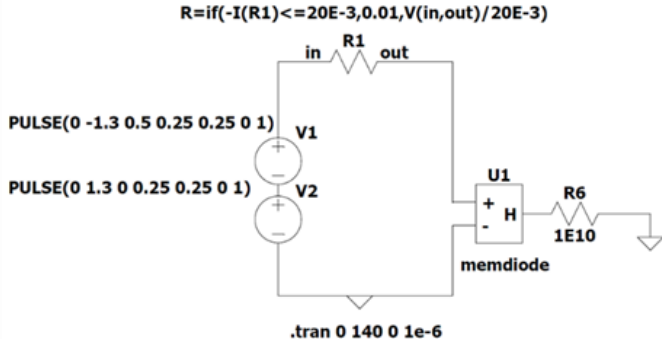


Figure 3.11. LTspice schematics used to perform the simulations. Combining $V1$ and $V2$, the bipolar voltage sweep signal is achieved (from 0 to 1.3 V, to -1.3 V and back to 0). Other signals can be applied if required. $R1$ is used for setting the current compliance at 20 mA. By combining the model script in Table 3.6 and schematics, the simulated I - V curves shown in Fig. 3.12 were obtained.

```

.subckt memdiode + - H
.params
+ H0=0 RPP=1E10 vs=2; initial condition, parallel resistance, set voltage
+ etar=40 del=1 fps=1; reset transition rate, time between cycles, RNG rate
+ gam=0.1; snapforward factor, isb=1/gam=0 no snapback/snapforward
+ th1=0.15 mu1=ln(1.28E-4) s1=0.19 ic1=mu1+gauss((s1**2)/(2*th1)) n1=1; Ioff, HRS current
+ th2=0.45 mu2=20.3E-3 s2=0.7e-3 ic2=mu2+gauss((s2**2)/(2*th2)) n2=2; Ion, LRS current
+ mu3=6e-5 s3=0.2E-5 n3=3; Isb, snapback current
+ th4=0.25 mu4=-0.51 s4=0.009 ic4=mu4+gauss((s4**2)/(2*th4)) n4=4; Vr, reset voltage
+ mu5=27 s5=0.2 n5=5; ri, fix series resistance
+ th6=0.25 mu6=ln(0.415) s6=0.0415 ic6=mu6+gauss((s6**2)/(2*th6)) n6=6; Vt, transition voltage
+ mu7=3.0 s7=0.16 n7=7 mu8=1.9 s8=0.01 n8=8; aoff/aon
+ mu9=20 s9=1.8 n9=9 mu10=5 s10=0 n10=10; roff/ron, variable series resistance
+ mu11=34 s11=3 n11=11; etas, set transition rate
*Memory Equation
BI 0 H I=if(V(+,-)>=0,(1-V(H))/TS(V(C,-)),V(H)/TR(V(C,-))) ; current generator for the memory state
CH H 0 1 ic={H0}; initial state
*I-V
RI + C R=V(P05); fixed series resistance, ri
RS C B R=K(V(P10),V(P09)) ; variable series resistance
BF B - I=K(V(P02),exp(V(P01)))*sinh(K(V(P08),V(P07))*V(B,-)) ; current generator for electron current
RB + - {RPP} ; parallel resistance
*Parameters and variability using pOU process
BP01 0 P01 I=th1*(delay(V(P01),del)-mu1)+delay(V(P01),del)+sqrt(del)*MCG(0,s1,fps,n1) IC=ic1 Rpar=1; Ioff
BP02 0 P02 I=th2*(delay(V(P02),del)-mu2)+delay(V(P02),del)+sqrt(del)*MCG(0,s2,fps,n2) IC=ic2 Rpar=1; Ion
BP03 0 P03 I=mu3+MCG(0,s3,fps,n3) Rpar=1; Isb
BP04 0 P04 I=th4*(delay(V(P04),del)-mu4)+delay(V(P04),del)+sqrt(del)*MCG(0,s4,fps,n4) IC=ic4 Rpar=1; Vr
BP05 0 P05 I=mu5+MCG(0,s5,fps,n5) Rpar=1; ri
BP06 0 P06 I=th6*(delay(V(P06),del)-mu6)+delay(V(P06),del)+sqrt(del)*MCG(0,s6,fps,n6) IC=ic6 Rpar=1; Vt
BP07 0 P07 I=mu7+MCG(0,s7,fps,n7) Rpar=1; aoff
BP08 0 P08 I=mu8+MCG(0,s8,fps,n8) Rpar=1; aon
BP09 0 P09 I=mu9+MCG(0,s9,fps,n9) Rpar=1; roff
BP010 0 P10 I=mu10+MCG(0,s10,fps,n10) Rpar=1; ron
BP011 0 P11 I=mu11+MCG(0,s11,fps,n11) Rpar=1; etas
*Auxiliary functions
.func K(on,off)=off+(on-off)*limit(0,1,V(H)); distribution function
.func TS(x)=exp(-V(P11)*(x-VSB(I(BF))))); characteristic set time
.func TR(x)=exp(etar*ISF(V(H))*(x-V(P04))); characteristic reset time
.func VSB(x)=if(x>V(P03),exp(V(P06)),vs); snapback voltage
.func ISF(x)=if(gam==0,1,pow(limit(0,1,x),gam)); snapbforward effect
.func MCG(x,y,z,n)=x+(y)*sqrt(-2*ln(rand((1E3*n)+time*z)))*cos(2*pi*rand((1E3*n)+time*z+1E5)); Gaussian
generator
.ends

```

Table 3.6. Model script. LTspice DMM script including the parameters (fix, following probability distribution, and p-OU type), the model equations and auxiliary functions for simplicity.

3.2.3 Correlated C2C Variability in the DMM

In this subsection, the simulations including correlated C2C variability using the presented approach are shown and analyzed comparing the simulation results with the experimental curves. It is worth mentioning that simulations were performed using the same timing and voltage conditions as those used for the measurements. The adjustment of the model parameters takes into account the shape of the I - V curves, their statistical distribution and the autocorrelation. The statistical agreement between simulations and experiments is assessed using the Wasserstein's distance (WD) [Villani2009] and comparing the CDF plot for different stages of simulations. The WD is a metric that measures the distance between two probability distributions. In order to find out the best set of parameters, the simulated and experimental curves were subjected to an iterative process in which the global deviation is calculated.

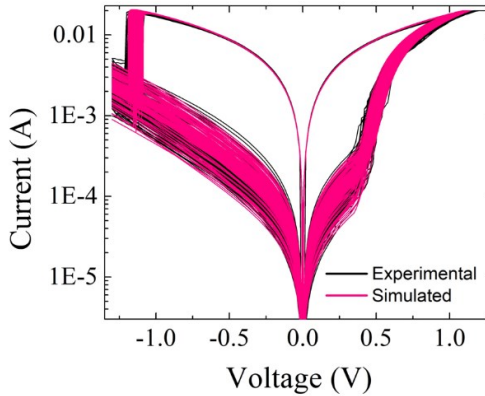


Figure 3.12. Simulated and experimental I - V curves in pink and black respectively in logarithmic axis for the current. The simulated curves were obtained by using the model script and schematics presented in the previous subsection.

The median of the experimental curves is considered as the initial guess for this process. The simulated results, including variability, are compared with the measurements cycle after cycle until a final target is reached. Figure 3.12 shows the final results obtained with the DMM. As can be seen, the main features of the curves are correctly addressed. Fitting the LRS current is by no means straightforward since the corresponding observable is the result of the combination of several model parameters associated with HRS (I_{off} , R_{off} , a_{off}).

In turn, the model parameters associated with the LRS current (I_{on}, R_{on}, a_{on}) directly impact on the voltage location and variability of the reset transition. This is referred to as variability propagation. The complete simulation requires the strict control of some model parameters like I_{off} for example in order not to trigger a simulation error by an improper combination of model parameters.

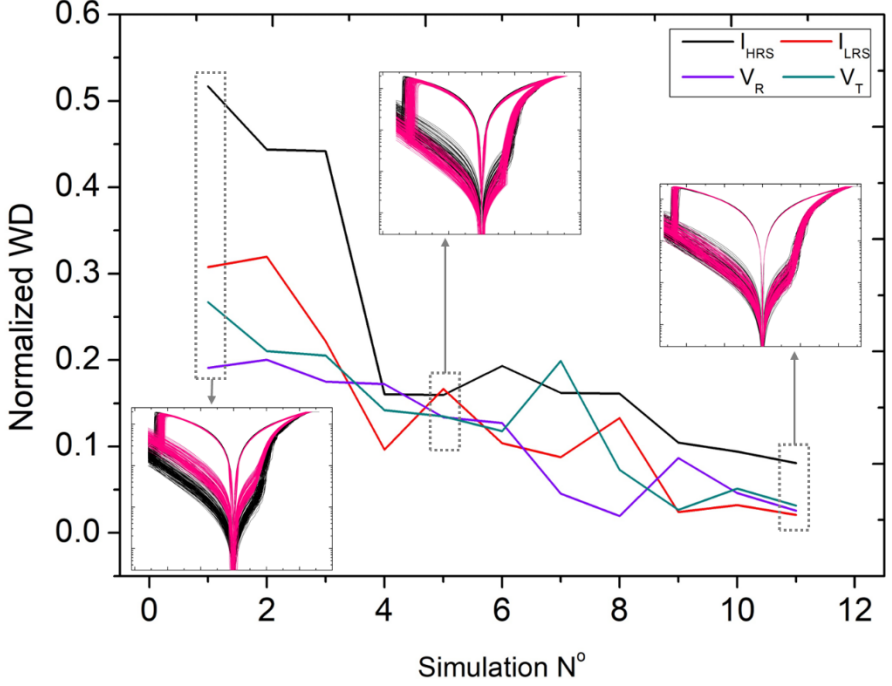


Figure 3.13. Wasserstein distance for the four selected observables in chronologically ordered simulations. For illustrative purposes, the simulated curves are included for initial (S1), intermediate (S5), and final (S11) chronological situations.

More in detail, Fig. 3.13 presents the evolution of the Wasserstein distance for the four selected observables: I_{HRS} (in black), I_{LRS} (in red), V_T (in green) and V_R (in violet) for different stages of the optimization process. Here, we use the WD as a measure of the difference between the simulated and experimental distributions. For the y axis, WD is normalized by the mean value of the experimental observable. This allows plotting the four different observables in the same scale. It is clearly seen that as the optimization process proceeds, WD decreases, which indicates more accurate results in a statistical sense. The

optimization process ends when WD reaches a predefined threshold value. If a given change in the model parameters leads to an increase of WD, this change is rejected. For the sake of clarity, Fig. 3.13 also includes the set of experimental and simulated I - V curves for three different stages of the optimization process: initial (S1), intermediate (S5) and final (S11) situations. The reduction of WD coincides with the improvement of the fitting results. Notice that the selected observables are strategically chosen so as to summarize the information about the complete loop: I_{HRS} for the HRS curve, transition voltage V_T for the SET transition, I_{LRS} for the LRS curve, and V_R for the reset transition. Other selection is also possible. Figure 3.14 shows the cumulative distribution functions for the four selected observables, in black for measurements and in a darkness-fade for simulations (initial-bright, late-dark). In the legends, the simulation numbers (S1, S3, S6, S9, S11) indicate the chronological progression, with S1 representing the first trial and S11 the last. Again, in agreement with the above discussed process, the darker curves are closer to the black ones as optimization proceeds.

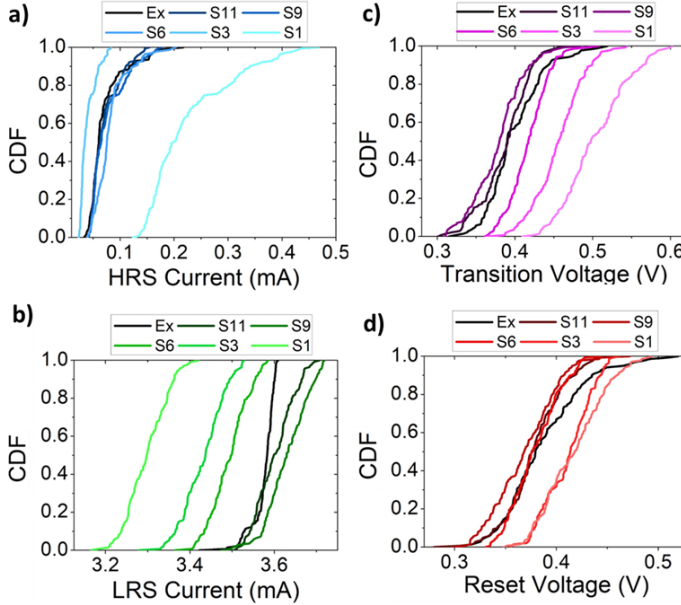


Figure 3.14. Evolution of the CDF plot. Experimental (black) and simulations in a darkness-fade, from initial (lighter) to late (dark). a) for HRS current, b) for LRS current, c) for the transition voltage and d) for the reset voltage.

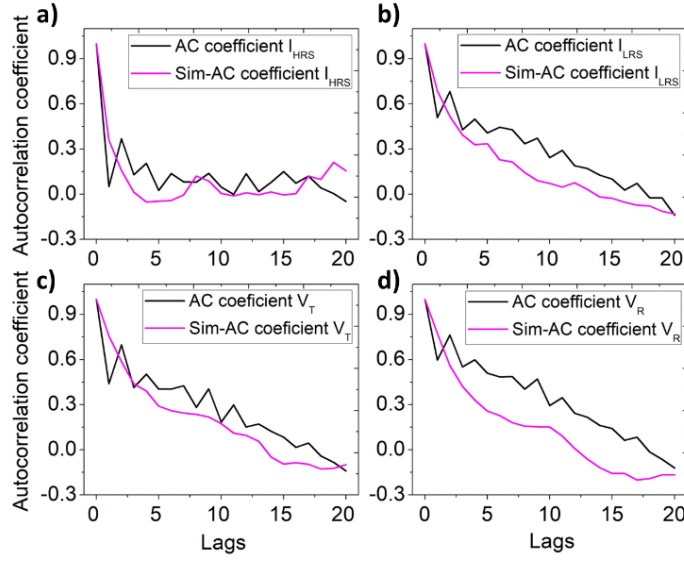


Figure 3.15. Comparison of the autocorrelation coefficients as a function of the Lag (cycle number) for the four selected parameters corresponding to the simulated (pink) and experimental (black) curves. a) for HRS current, b) for LRS current, c) for the transition voltage and d) for the reset voltage.

Figure 3.15 shows the AC plots for the selected observables (experimental in black and simulated in pink) as a function of the measurement cycle for: a) I_{HRS} , b) I_{LRS} , c) V_T and d) V_R . Notably, the AC values of the simulated plots match those of the experimental data.

In summary, the proposed approach to include correlated C2C variability by incorporating p-OU processes in the model parameters was shown to reproduce the experimental data. The adjustment was addressed with a comprehensive evaluation of the Wasserstein distance, the CDFs and the autocorrelation of the different experimental and simulated observables.

3.3. Matlab Version of the Dynamic Memdiode Model

This section presents a fast, simple, robust, and versatile model for RRAM devices built in Matlab. The proposed model is a recursive and discretized version of the DMM, originally implemented in LTspice, as seen in previous sections in this chapter. This section contains information from the article

JLPEA24. Nowadays, a lot of models are implemented in simulators like Spice or Verilog [Ielmini2017]. These simulators are useful for complex architectures involving several devices but also lead to long waiting times for running the simulations and post-processing the data. In this section, a simple and effective tool is presented for reproducing the behavior of single RRAM devices in Matlab, a common and well-known programming language. The advantages of the tool presented consist in easy implementation, straightforward data analysis, short simulating running times, and versatility in terms of parameters definition and input possibilities (applying non-trivial signals like noise). In the current literature there are a few works using Matlab for RRAM modeling. In [Elgabra2012], several existing models were studied using MATLAB simulations. In [Huang2023], a Kinetic Monte Carlo simulation in MATLAB to estimate and optimize the reliability of RRAM devices was reported. In [Mladenov2024], the implementation of a memristor-based neural network using MATLAB, Simulink and LTspice for simulations and analysis was presented.

Here, the modifications in the original DMM Equations (3.4) and (3.5), presented in Section 3.1.3 are discussed. Using the approaches reported in [Miranda2023], the discrete recursive approach for the I - V characteristic in Equation (3.4) now reads:

$$I(V) \approx \frac{1}{\alpha R} \left\{ W \left[\frac{\alpha R I_0}{2} \exp(\alpha V_i) \right] - W \left[\frac{\alpha R I_0}{2} \exp(-\alpha V_i) \right] \right\} \quad (3.11)$$

where W is the Lambert function (*lambertw* in Matlab) and $V_i = V - I \cdot R_i$. Next, the memory state in the DMM in Equation (3.5) is recursively expressed and discretized as follows:

$$\lambda_{t+1} = [\lambda_t - H(V_{it})] \exp \left\{ -\frac{\Delta t}{\tau_{iS,R}} \right\} + H(V_{it}) \quad (3.12)$$

λ_t is the memory state, Δt the selected timestep and H the Heaviside step function. $\tau_{S,R}$ are the characteristic times for the set and reset transitions defined previously in Equations (3.6) and (3.7) respectively. The complete script is reported in Table 3.7, for the reader possibility to copy and use it for its own purposes. In the model script, the first section (in black) builds the input signal. The second section (in green) is dedicated to the model parameters and initial conditions. The third section of the script (in blue) presents the auxiliar

functions required by the model equations. The fourth section (in red) calculates the current $I(t+1)$ and the memory state $l(t+1)$. Finally, (in violet) the simulated currents and voltages are stored in the Im and Vm variables and plotted in the last two lines of the script, in addition the memory state is stored in the lm variable.

```

step=5E-3; V1=0:step:1.2; V2=0:-step:-1.2; V=[V1 flip(V1) V2 flip(V2)]; %Voltage input
aoff=2; aon=2; Ri=40; Roff=30; Ron=30; Ioff=10E-5; Ion=3E-3; %Parameter definition
etas=40; etar=-15; gam=0.1; At=1E-3; Vs=0.5; Vr=-0.3; l(1)=0; I(1)=0;
for t=1:length(V) %Auxiliary functions
Vi=V(t)-Ri*I(t); I0=(Ion-Ioff)*l(t)+Ioff; a=(aon-aoff)*l(t)+aoff; R=(Ron-Roff)*l(t)+Roff;
Tsr =exp(-etas*(Vi-Vs))*(V(t)>0)+exp(-etar*l(t)^gam*(Vi-Vr))*(V(t)<=0);
I(t+1)=(1/(a*R))*(lambertw(a*R*I0/2) *exp(a*Vi)-lambertw(a*R*I0/2*exp(-a*Vi)));
l(t+1)=(l(t)-heaviside(Vi))*exp(-At/Tsr)+heaviside(Vi); %Model Equations
Vm(t)=V(t); Im(t)=I(t); lm(t)=l(t); %Saving variables and plotting
end
semilogy(Vm,abs(Im),'black')
xlabel('Voltage (V)'); ylabel('Current (A)'); title('Current-Voltage Characteristics');

```

Table 3.7. Script for the recursive dynamic DMM implemented in Matlab. In black, the applied voltage. In green, the model. In blue, the auxiliar functions. In red, the model equations. In violet, saving parameters and plotting the I - V curve.

Figure 3.16 shows the simulated results for the script described in Table 3.7, showing the typical memristor current-voltage loop (in black) and the memory state-voltage loop (in blue), highlighting the high/low-resistance states and the set/reset processes.

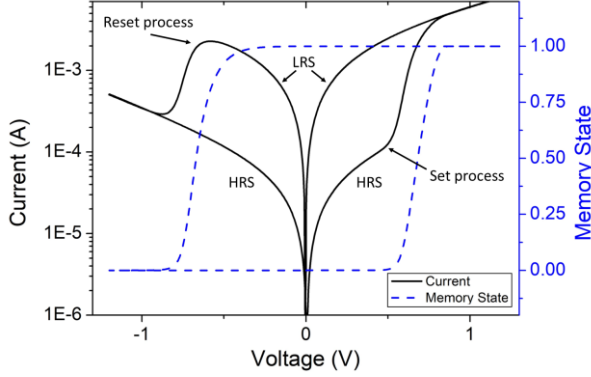


Figure 3.16. Simulated I - V characteristics (black) obtained with the model script in Table 3.7. High and low resistance states, and set and reset processes are highlighted. The memory state voltage loop is represented in the right Y axis (blue).

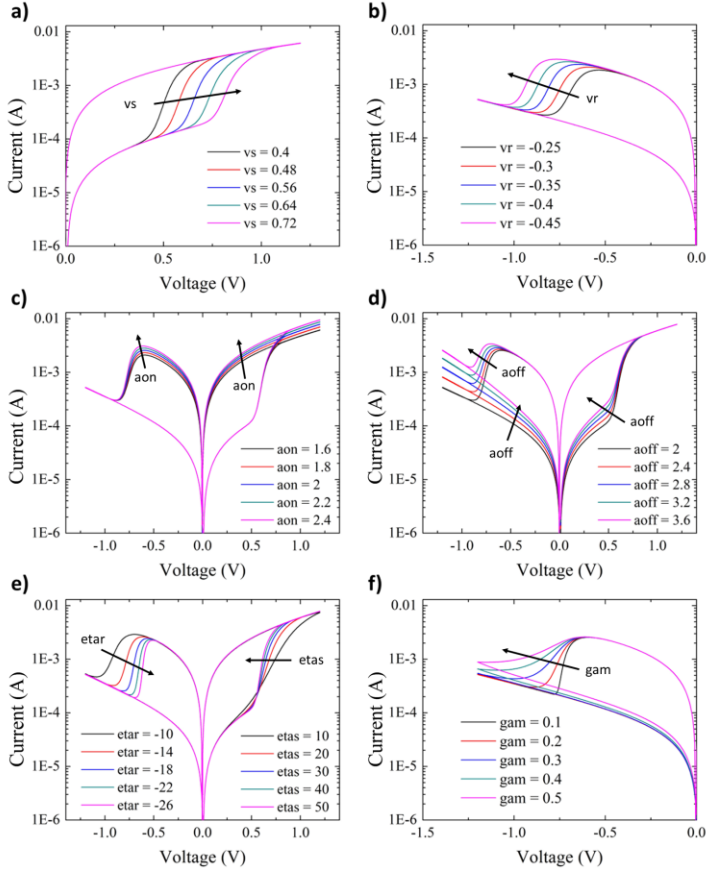


Figure 3.17. Effect of modifying different model parameters on the I - V characteristics. a) vs , b) vr , c) aon , d) $aoff$, e) $etas$ and $etar$, and f) gam .

In Fig. 3.17, a study of the impact of modifying different model parameters on the current-voltage characteristic is presented: a) for vs , b) for vr , c) for aon , d) for $aoff$, e) for $etas$ and $etar$, and f) for gam . This study shows the model sensitivity and is a useful guide for potential users of this version of the dynamic memdiode model.

3.3.1. Matlab Modeling of Uncorrelated C2C Variability

In this subsection the simulations in Section 3.1.2 are performed using the Matlab version of the DMM and compared with the same experimental data (450 cycles of I - V curves measured in HfO_2 -based memristors). Appendix B in article [JLPEA24](#) presents the Matlab script for the simulations in this subsection. As in section 3.1.2, the best distributions for each model parameter were found and incorporated into the model parameters definition. Here two different examples of parameters including variability are reported:

$$Maoff = 2.1; Saoff = 0.13; \mathbf{aoff} = Maoff + Saoff * randn; \quad (3.13)$$

$$\begin{aligned} Mloff &= 3.7E - 5; IoffLN = \log(Mloff); Sloff = 0.06; \\ \mathbf{Ioff} &= \exp(IoffLN + Sloff * randn); \end{aligned} \quad (3.14)$$

Equations (3.13) and (3.14) present two different cases, one following a normal distribution (3.13) and the other following a lognormal distribution (3.14). The variables defined in (3.14): $Maoff$, and $Saoff$ (which represent the mean and standard deviation respectively) are used to define the normally distributed $aoff$ parameter. For a lognormally distributed parameter, like in (3.14), the same $Mloff$, and $Sloff$ are defined, but two extra steps are required: $IoffLN$, which is the logarithm of $Mloff$ and the application of an exponential function in order to generate the lognormal distribution of $Ioff$. The $randn$ function is used for generating a different random number in every cycle. Notice that not all the model parameters include variability and some of them are constant for the sake of simplicity.

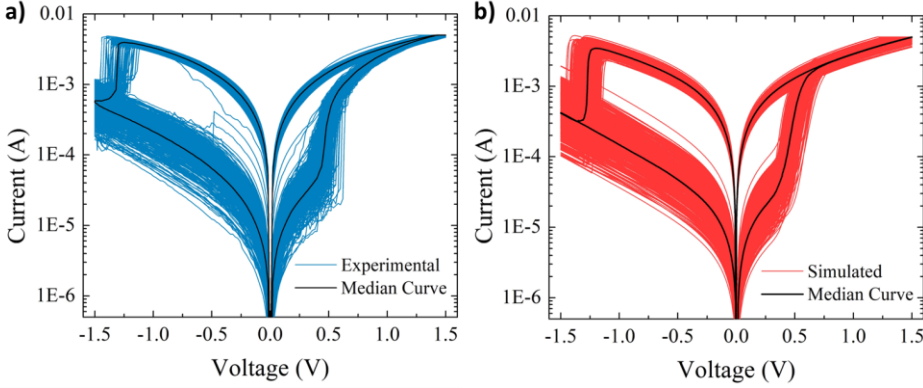


Figure 3.18. Comparison of the 450 I - V cycles. a) From the experimental devices in Section 3.1.2 (in blue) and b), from the simulations (in red) including C2C variability. In both figures, the median curve is shown in black.

In Fig. 3.18, the experimental data reported in Subsection 3.1.2 in blue (Fig. 3.18a), and the simulations obtained using the recursive DMM model in Matlab, in red (3.18b), are compared. The good agreement between experimental and simulated results indicates the ability of the model to reproduce variability in the I - V loops. In addition, Figs. 3.19a, b, c and d present the histograms for the HRS current, LRS current, set voltage, and reset voltage, respectively, both for experiments and simulations. All the histograms are well reproduced except the LRS current case, in which the experimental data exhibits a double peak likely caused by different atomic configurations of the CF. In Subsection 3.1.2, several trials were performed until finding the optimum combination of model parameters for achieving the observed variability. This process is time consuming when performed in LTspice since the obtained results must be analyzed somewhere else. Now, the parameters, model equations and data analysis are carried out with the same Matlab script largely reducing the time consumption, thus easing the possibility of finding better fitting results.

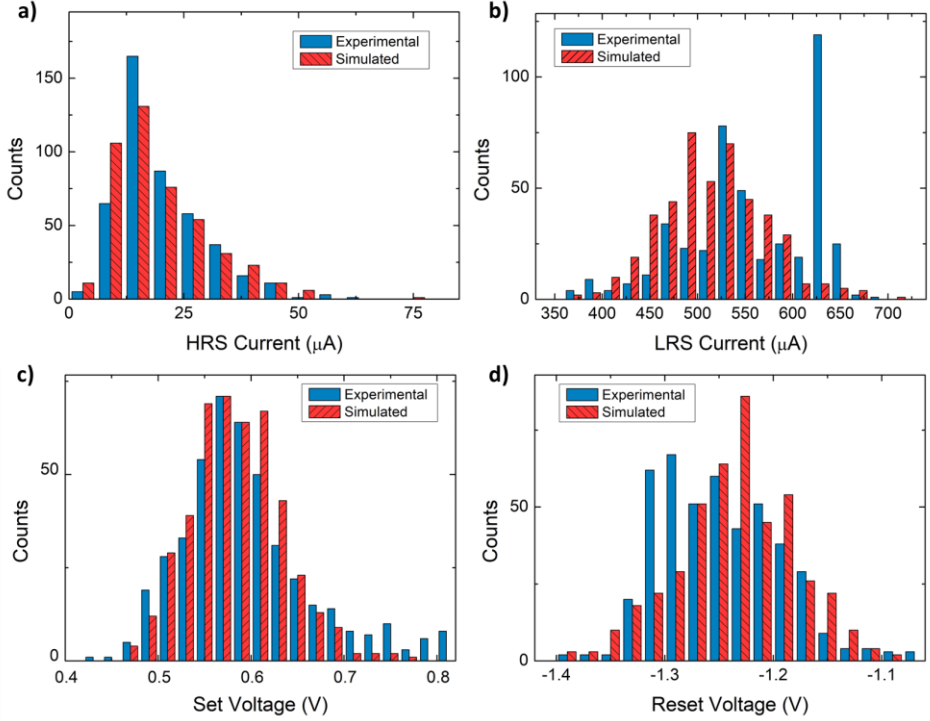


Figure 3.19. Histogram comparison of a) HRS current, b) LRS current, c) set voltage and d) reset voltage for experimental curves (in blue) and simulations (in red).

Moreover, in the **JLPEA24** article, there is a case study dedicated to illustrating the model sensibility to variations in the input signal frequency (for sinusoidal signals) or the ramp rate (for voltage sweeps) performing the simulations with Matlab. In the literature, it is reported that for high frequencies or ramp rates, both the set and reset voltages of bipolar RS devices increase in absolute value, making a wider butterfly shaped I - V curve. A linear relationship between the logarithm of the ramp rate and the set and reset voltages has been reported in the literature [Ostrovskii2022, Rodriguez-Fernandez2017].

3.4. Highlights

This chapter has thoroughly explored various methodologies for incorporating variability into RRAM device simulations, a critical aspect of accurate modeling in this field. Different approaches to model both uncorrelated and correlated cycle-to-cycle (C2C) variability were presented. The chapter also introduced

several powerful tools for analyzing experimental data, such as the *fitdistrplus* package for identifying the best-fitting distributions, as well as Q-Q plots, the Lilliefors test, and others. Finally, it provided valuable methods for comparing experimental results with simulations, including density plots, the Wasserstein distance, and autocorrelation plots.

In addition, the article **SSE24** presents a method for dealing with the time-dependent dielectric breakdown (TDDB) of the oxide layers for MOS and MIM structures using the LTspice software. The TDDB describes the physical phenomenon in which a dielectric material, subjected to an electric field below its intrinsic breakdown strength, progressively degrades the material over time. This process results in a kind of phase transition of the dielectric from an insulating state to a more conductive state, called breakdown, which is one of the major failure mechanisms in integrated circuits [McPherson2012]. The TDDB phenomenon bears notable similarities to the resistive switching mechanism in memristors. Both processes involve the dynamical interaction of electric fields with defects within the oxide layers, ultimately leading to a transition in conductivity. While TDDB is a failure mechanism, resistive switching in memristors exploits similar defect migration processes, such as the movement of oxygen vacancies, to achieve controllable and reversible switching between high and low resistance states. These similarities suggest the approach presented in **SSE24** could be implemented to study time-dependent switching transitions in memristors; however, this remains an open avenue for future research and has yet to be fully explored and validated with memristors.

In conclusion, this chapter presents a comprehensive and open-source framework for modeling variability in RRAM devices, underlining its importance in developing robust and accurate models. By sharing all scripts, the chapter not only facilitates replication but also encourages further advancements in the field. As RRAM technology continues to evolve, the inclusion of variability in models will remain imperative for achieving reliable and predictive simulations. This chapter included information from the following articles and complementary works: **SSE21**, **SSE23**, **SSE24**, **TNANO24**, **TNANO24-SM**, **JLPEA24**, **MIEL21** and **AIS23**.

Stochastic Resonance in RRAM Devices

This chapter of the thesis contains the findings regarding an in-depth study of the stochastic resonance phenomenon in RRAM devices. The analysis begins with a detailed investigation of the manifestation of the SR phenomenon in the I - V characteristics of RRAM devices under test by using DC sweeps. The impact of the SR in these devices was determined by studying the non-linear response of the memristors under different noise intensities. The main studied figures of merit are the resistance ratio and the transition voltages (set and reset). Once the impact of noise in the DC regime was established, the behavior of the devices using inputs of different frequencies was examined. This provided insights about the response of memristors to dynamic inputs and noise.

In addition, this chapter highlights two distinct applications of memristors in neuromorphic systems, with a focus on the experimental influence of external noise. The first application examines the binary STDP learning protocol, where we explore how stochastic resonance can activate the protocol, enhancing learning efficiency in neuromorphic architectures. The second application investigates homeostasis, analyzing the role of SR in regulating neural activity. This mechanism promotes system stability by maintaining a balance between excitatory and inhibitory regimes. While most current studies on memristor-

based neuromorphic applications rely on simulations, the approach in this thesis emphasizes experimental validation, complemented by simulations to reproduce the results using the memdiode model.

This chapter includes contents from the **JLPEA24**, **TED24** and **EDL24** publications and from the **ISCAS22** complementary work.

4.1. Stochastic Resonance Applying DC Voltage Sweeps

This section focuses on introducing measurements and simulations including noise in the voltage inputs and presenting the results of the study of the impact of the SR phenomenon in RRAM devices in a DC regime. This section includes information from articles **EDL24**, **JLPEA24**, and the conference paper **ISCAS22**.

4.1.1. Experimental SR Applying DC Voltage Sweeps

This subsection is dedicated to the experimental study of the SR phenomenon in RRAM devices. The bipolar devices used for the first DC study are from the same wafer previously described in Section 3.1.1 and Fig. 3.1 with an active area of $5 \times 5 \text{ } \mu\text{m}^2$. The measurement setup is the AG-SPA. The instrument was controlled with Matlab software. The input voltage signal was programmed point-by-point to form a voltage sweep. The noise was included in every point of the input signal using the *randn* function from Matlab ($V_{noise} = V_{in} + \sigma_{noise} \cdot \text{randn}$), already presented before in the Section 3.3.1 of this thesis, when generating Gaussian randomness for variability modeling. Firstly, fresh memristors were subjected to a 1mA current-limited forming process that takes place at voltages around 4V. After forming, the memristor *I-V* characteristics were registered during 200 consecutive cycles. To measure the *I-V* curves, the samples were subjected successively to voltage sweeps, sweeping the voltage from 0V to 1.3 V, from 1.3 V to -1.3 V and from -1.3 V to 0 V and the current was registered during the application of voltage. To assess the effect of noise, Gaussian noise with standard deviation (sigma, σ) varying from 50 mV to 150 mV was added to the voltage sweep. The investigation of the effect of noise on

the $R_{\text{OFF}}/R_{\text{ON}}$ ratio was performed by using a fresh memristor for every noise situation. The resistance ratio was obtained directly through Ohm's law by measuring the currents (I_{OFF} and I_{ON}) at a voltage of -0.5 V in the I - V memristor characteristics (see Fig. 4.1a). A typical stochastic resonance curve is found in Fig. 4.1b, which plots the mean ratio value versus the noise sigma. In this figure, every spot represents the mean value of $R_{\text{OFF}}/R_{\text{ON}}$ from the 200 cycles performed for every noise sigma. The cumulative distribution functions (CDFs) for the $R_{\text{OFF}}/R_{\text{ON}}$ ratio measured for the 200 cycles at each noise condition are shown in Fig. 4.1c. The lowest $R_{\text{OFF}}/R_{\text{ON}}$ ratio was measured without including noise, and the incorporation of noise always produces a higher ratio. By increasing the noise σ , a shift to the right of the CDF curves appears meaning a higher resistance ratio. The maximum CDF shift, and so, the maximum resistance ratio was obtained for $\sigma = 90$ mV, also the maximum in the mean resistance ratio plot (Fig. 4.1b). However, from this σ value on, the CDF curves shift back to the left with lower ratios indicating that the stochastic resonance phenomenon was observed in the presence of noise.

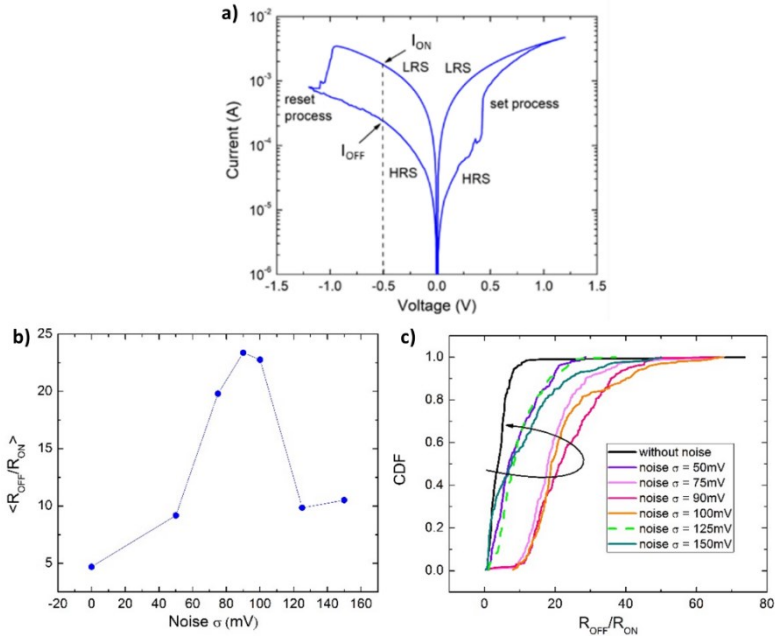


Figure 4.1. (a) I - V characteristic of the devices used in this section. b) $R_{\text{OFF}}/R_{\text{ON}}$ mean values versus noise σ . The peak SR curve is distinguished. c) CDFs of the memristor $R_{\text{OFF}}/R_{\text{ON}}$ for all the noise σ values measured. The maximum resistance ratio is obtained for a σ noise of 90 mV.

For a deeper investigation of the SR effect on the conduction characteristics, Fig. 4.2 shows different I - V curves from the measurements without noise (Fig. 4.2a) and adding the noise that produces the peak of the SR curve ($\sigma = 90$ mV, Fig. 4.2b). From the 200 cycles, three different situations are presented: an early, a mid, and a late cycle (cycles 12, 91, and 193 respectively). Noticeable differences can be observed between both figures in terms of resistance states and transitions between states. The memory window notably increases for noisy measurements, resulting in higher $R_{\text{OFF}}/R_{\text{ON}}$ ratios. We can also observe in each figure that, for late cycles, the memory window is decreased compared with early cycles. This effect was observed for all the experiments and was attributed to the device degradation due to the successive switching [González2019].

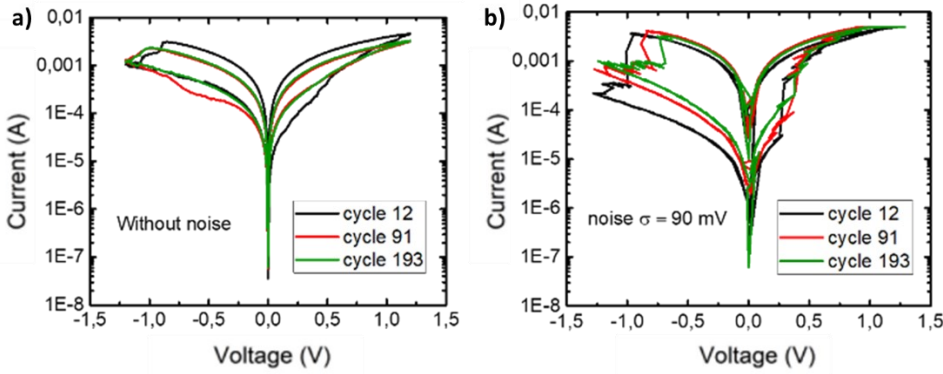


Figure 4.2. Device I - V characteristic for early, mid, and late cycles (12, 91 and 193) a) without noise and b) with a noise $\sigma=90$ mV.

The following experiment introduces a study of the impact of the SR phenomenon in the set and reset transitions voltage in a DC regime. In this regard, the advantage of these unipolar devices with respect to the bipolar devices used in this thesis is the abruptness of the transitions. As previously stated in the introduction, in this type of memristors both set and reset transitions occur at the same voltage polarization. In the case of these devices at negative voltage.

In Fig. 4.3a, the schematic cross-section of the used unipolar memristors is shown and in Fig. 4.3b the I - V curves from 10 voltage sweeping cycles are presented (set and reset processes in black and red respectively). These devices were fabricated with the isolate configuration (introduced in Chapter 2), and

have some distinct characteristics, which are the dielectric layer and the nickel top electrode. In this case, the dielectric layer consists of a stack of HfO_2 and Al_2O_3 : 4 nm HfO_2 – 4 nm Al_2O_3 – 4 nm HfO_2 – 4 nm Al_2O_3 – 4 nm HfO_2 , resulting in a 20 nm-thick dielectric layer. The active area of the devices is $5 \times 5 \mu\text{m}^2$. Further details regarding the fabrication process and device characterization of these unipolar devices can be found in [Maestro-Izquierdo2020]. To trigger the electroforming process, a negative voltage sweep was applied, limiting the current to $1 \mu\text{A}$ to avoid the irreversible breakdown of the device. This electroforming occurs at around -11 V. After, consecutive reset (switching from LRS to HRS) and set (from HRS to LRS) events are performed, through voltage sweeps starting at 0 V and ending when certain conditions are fulfilled. For the reset process, the voltage sweep is halted (reset voltage) when a current decrease of at least one order of magnitude is detected, with a 50 mA compliance limit fixed. The set voltage was defined as the voltage at which the memristor current has increased until $50 \mu\text{A}$.

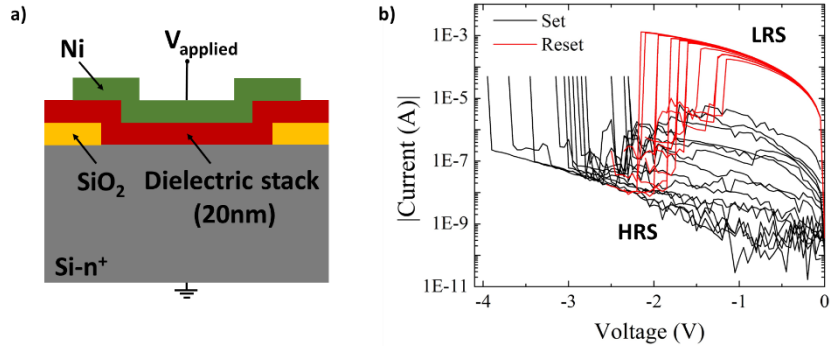


Figure 4.3. a) Schematic cross-section of the unipolar memristors used to study the impact of the SR phenomenon in the set and reset transition voltages in a DC regime and b) typical I - V characteristics after the electroforming of the conductive path.

Using the same measurement process in terms of voltage and current compliance for the electroforming, 500 set-reset cycles were performed. A slight change in the cycling current compliance was employed, now fixed to $90 \mu\text{A}$ for the set process. Figure 4.4a shows the set events (red) and Fig 4.4b presents the reset events (blue). Moreover, a correlation plot between the HRS current and the reset voltage is shown in Fig. 4.4c. It reveals an observable phenomenon: higher (more negative) values for the reset voltage induced lower HRS currents.

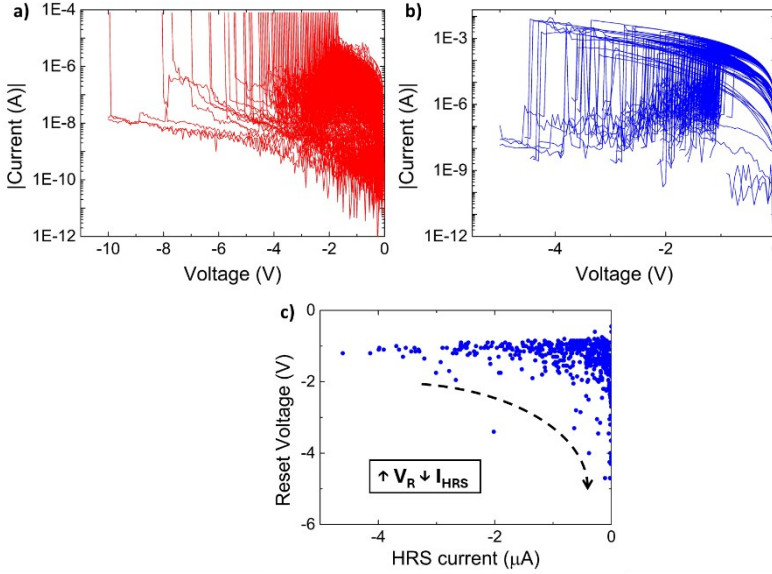


Figure 4.4. I - V curves from 500 set-reset memristor cycles for a) set (red), b) reset processes (blue) and c) correlation plot between the reset voltage and the HRS current.

Once the unipolar devices and their electrical behavior are introduced, the SR impact study is performed. In this experiment, after forming, 100 cycles of consecutive reset (switching from LRS to HRS) and set (from HRS to LRS) events are applied using the same set and reset stop conditions previously defined to obtain the results in Fig. 4.4. Again, the external Gaussian noise was added point-by-point to the bias. Several noise standard deviations (σ) were considered, ranging from 0 mV to 150 mV. In Fig. 4.5, the mean values of the set (a) and reset (b) voltages and their standard deviations (c) were registered and plotted against the applied noise σ . Again, the typical SR curve is observed, with a decrease (in absolute value) of the threshold voltages and a decrease of their σ , in a range of noise σ around 60 mV. The complete picture demonstrates that the threshold voltages of the memristor can be tuned through the action of an external noise source.

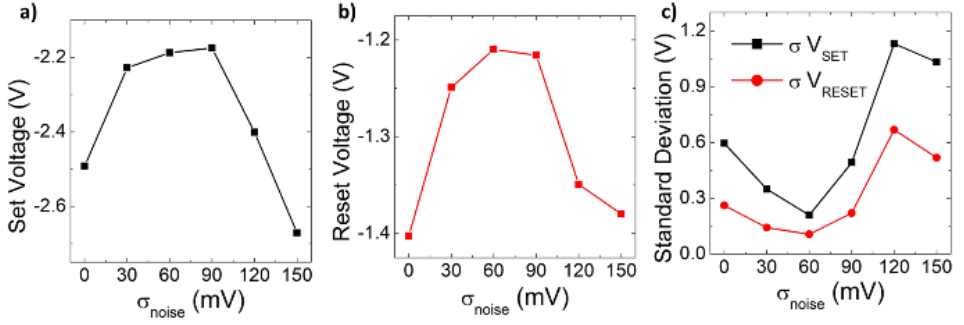


Figure 4.5. Mean a) set, b) reset voltages and c) set (black) and reset (red) voltages standard deviation, versus noise σ .

In addition, Fig. 4.6 presents in red the set process (a, c and e) and in blue the reset process (b, d and f) for three distinct situations: Figures 4.6a and 4.6b for the experiments without noise, Figs. 4.6c and 4.6d for experiments with $\sigma_{noise} = 60$ mV, and Figs. 4.6e and 4.6f for experiments with $\sigma_{noise} = 150$ mV. It is clear that for $\sigma_{noise} = 60$ mV both set and reset transitions occur at lower voltage values than those corresponding to the absence of noise and with $\sigma_{noise} = 150$ mV. In addition, the transitions for $\sigma_{noise} = 60$ mV are less spread, meaning that the set and reset events are shifted to lower and less variable voltage values.

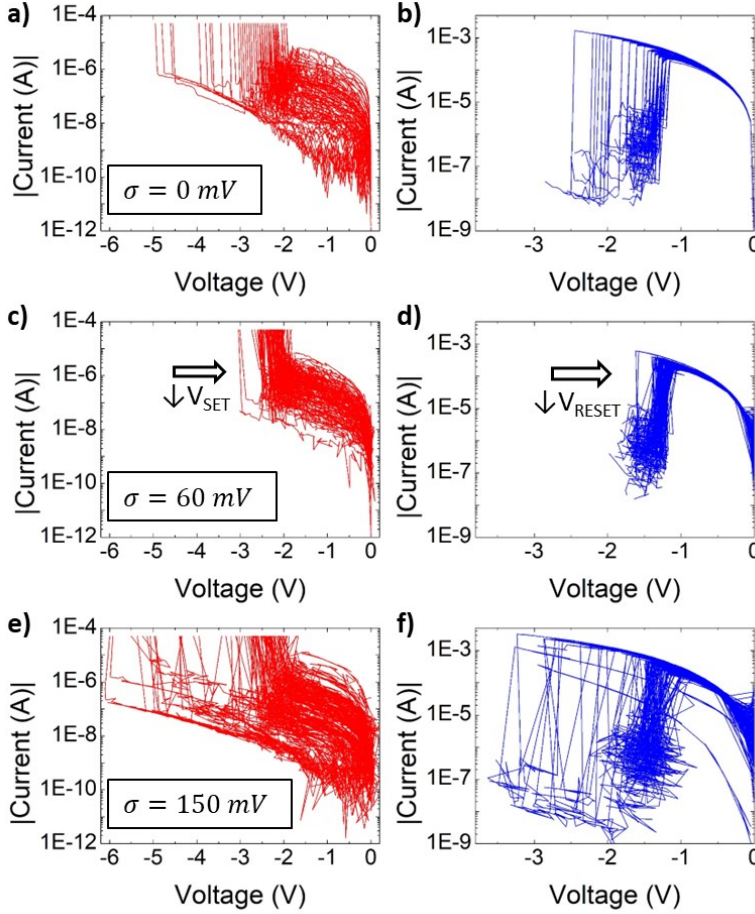


Figure 4.6. I - V curves from the 100 set-reset memristor cycles for set (in red, left column) and reset processes (in blue, right column) for three cases: no noise (a and b), noise addition with $\sigma_{noise} = 60 mV$ (c and d) and $\sigma_{noise} = 150 mV$ (e and f).

4.1.2. Simulating SR Applying DC Voltage Sweeps

In this subsection, the findings in Fig. 4.1b are reproduced using the Matlab version of the DMM presented in Section 3.3. The *randn* function in Matlab is used to generate a normally distributed input voltage signal. The model script used for this study is presented in Appendix C of the **JLPEA24** article, where the main difference with the basic model script shown in Table 3.7 is the addition of noise. Equation (4.1) shows the script line for defining the noise inclusion in the input signal:

$$\text{ampn} = ((g-1)*40)*1\text{E-}3; V(t) = V(t) + \text{ampn} * \text{randn}; \quad (4.1)$$

where ampn is the noise σ , g is an iteration parameter to increase the noise σ after every 200 cycles, $V(t)$ is the input signal updated every time t to include noise using the *randn* function.

The simulation process follows the experimental method described in the previous subsection to obtain the results in Fig. 4.1, which consist of 200 I - V cycles adding different noise values to the applied voltage sweeps. This is carried out with the aim of capturing the real device phenomenology under noisy signals.

Figure 4.7a shows the simulation results without adding noise. The mean resistance ratio extracted from 200 simulated I - V cycles against noise σ is presented in Fig. 4.7b. A maximum in the mean resistance ratio is clearly observed for $\sigma_{\text{noise}} = 240 \text{ mV}$. Even though the experimental (Fig. 4.1b) and simulated curves noticeably differ (a deep investigation about all the model parameter values is required), the model results qualitatively capture the device behavior when an external noise source is added to the input signal. The experimental-simulated coherence in this subsection could be enhanced by adequately modifying the model equations to consider the impact of external noise.

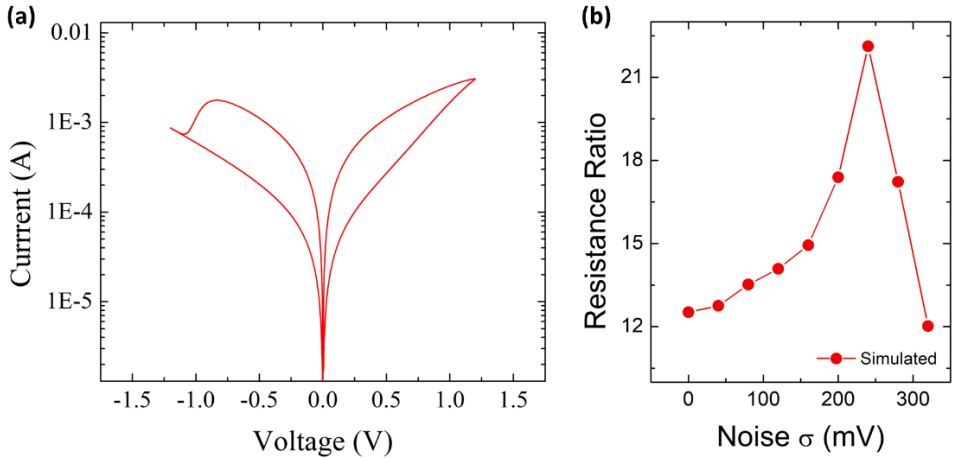


Figure 4.7. a) Simulated I - V curves using the DMM implemented in MATLAB without additional noise. b) Mean resistance ratio evolution versus the applied noise standard deviation in simulations using the DMM.

The results presented in this section motivated further studies presented in the subsequent sections in this chapter. The observed impact of noise, which enhanced the resistance ratio and modulated transition voltages in a DC regime, inspired various new approaches. The findings in DC regime were qualitatively reproduced using the Matlab version of the DMM model. The following sections in this chapter study the memristor responses at different frequencies and explore potential applications considering the stochastic resonance phenomenon in memristors. The chosen applications focused on neuromorphic systems, a field that has gained considerable importance in recent years.

4.2. Stochastic Resonance Applying AC Voltage Inputs

This section is focused on the impact of the SR phenomenon in memristors observed during AC voltage inputs. As stated in Chapter 2, there are different setup possibilities for performing experimental measurements. This section includes results from three different approaches: a setup combining the pulse generator (PG) and the advanced oscilloscope (AC Setup 1), a setup combining the pulse generator and the Agilent SPA (AC Setup 2), and a setup combining the pulse generator and the Keithley SPA (AC Setup 3).

4.2.1. AC Setup 1

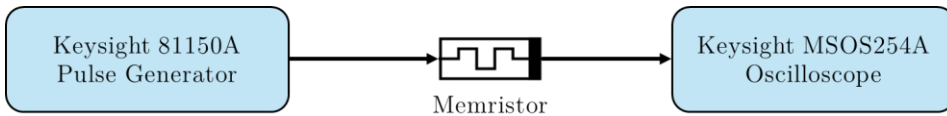


Figure 4.8. Schematic of the AC Setup 1 used for the first approach of the AC stochastic resonance study on memristors. The Keysight 81150A pulse generator is connected to the top electrode of the device sending the input triangular signal and the bottom electrode is connected to the Keysight MSOS254A oscilloscope for collecting the current and voltage data.

The first characterization setup consisted in connecting the PG at the memristor top electrode and the high-definition oscilloscope to its bottom electrode (see Fig. 4.8). The role of the oscilloscope is to capture the input and output voltages, which, by means of the internal resistance of the instrument,

can be converted to current. The devices in this approach were fabricated following the cross-point configuration method introduced in Chapter 2 and have a $5 \times 5 \mu\text{m}^2$ active area. The device structure was presented previously in Fig. 3.1. The PG was programmed to send a triangular signal of 10 Hz frequency and 1.4 V of voltage amplitude (see Fig. 4.9a) emulating the DC voltage sweeps in a low frequency regime. The current for switching was limited to 20 mA. The signal was captured with the oscilloscope. Both instruments were activated and controlled via Matlab programming. Two examples of single current-voltage curves from two different devices of the same wafer are presented, using linear axis for both magnitudes and logscale for the current axis in Figs. 4.9b and 4.9c respectively. In both cases, a previous electroforming event occurring at around 4.5 V limited to 1 mA, and some stabilization cycles were performed.

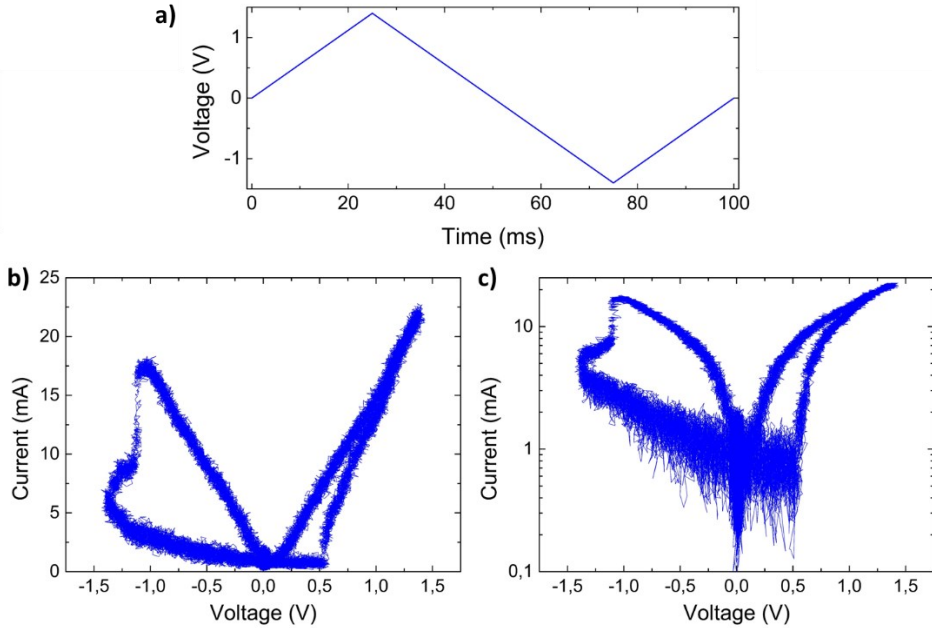


Figure 4.9. a) Input triangular signal with 1.5 V amplitude and 10 Hz frequency. b) Linear and c) logarithmic current I - V curves using the AC Setup 1.

The resulting curves in Fig. 4.9 are notably noisy (notice that these curves do not include external noise in the input signal), with more evidence in the case of low currents for the current logscale figure. The setup responded correctly but the noisy curves could not be improved after several approaches. However,

since it allowed AC measurements, a stochastic resonance study applying different signal frequencies was performed.

Figure 4.10 introduces a stochastic resonance study applying a low frequency triangular signal (10 Hz) using the bipolar devices just presented in Fig. 4.9. The Keysight 81150A (PG) can generate programmable white Gaussian noise with controlled amplitude and crest factor. The crest factor is the ratio of the peak amplitude to the root mean square (RMS) amplitude of a waveform. It measures the peak abundance of the signal compared to its average power. The PG generates the noisy signal by internally adding the noise with a moderate crest factor to the triangular signal. The triangular signal amplitude was programmed to 1.4 V (as in Fig. 4.9a). Each input signal including different noise σ was cycled 100 times using a fresh device for every noise σ value. Figure 4.10a shows the mean resistance ratio evolution for all the noise σ values added to the triangular signal. Again, as in the previous section, a typical SR curve was obtained, with a maximum at $\sigma_{noise} = 90 \text{ mV}$. For a deeper visualization, Fig. 4.10b provides the CDF plots for all the applied noise σ . Notice that all the noisy experiments result in a higher resistance ratio (higher mean value and right shifted in the CDF plots) than the experiment without noise. As a support for understanding the impact of noise, Fig. 4.10c presents an example of a smoothed version from the I - V curve of the experiment without noise (in black) and from the experiment including the noise $\sigma = 90 \text{ mV}$, which resulted in the peak of the SR curve (in red). Notice that the red I - V curve is clearly wider. This experiment proved that the SR phenomenon is occurring using a low-frequency signal.

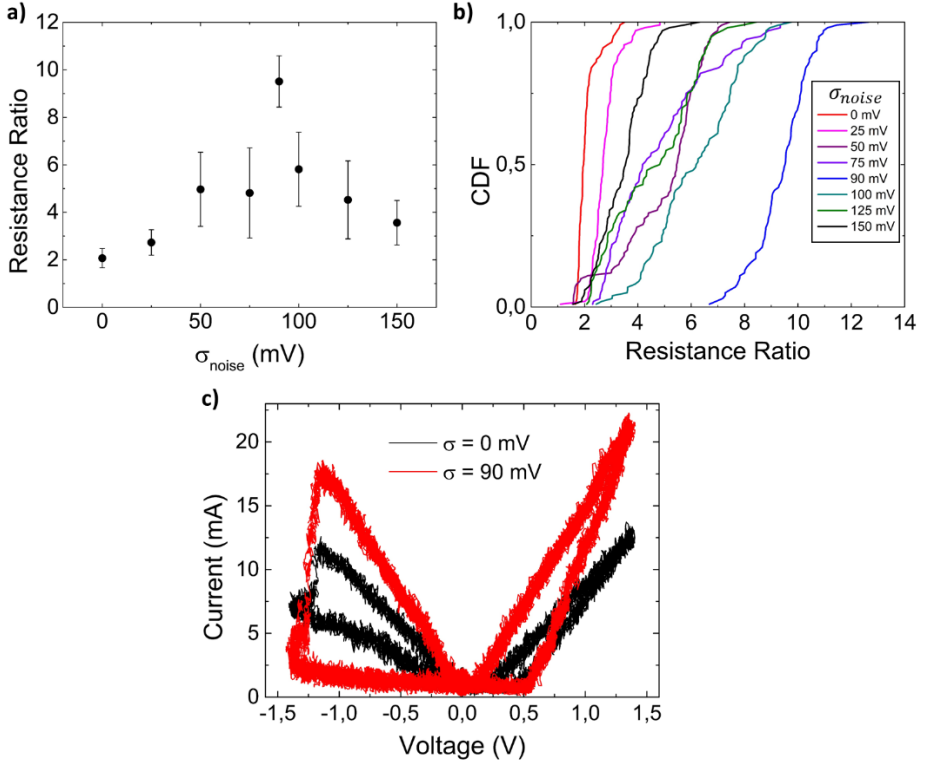


Figure 4.10. Stochastic resonance study using a 10 Hz triangular signal with the AC Setup 1. a) Mean resistance ratio evolution versus noise for different noise σ values, b) CDF plots for all the noise σ values. c) Comparison of an $I-V$ curve without noise (black) in the applied voltage and applying a $\sigma_{noise} = 90$ mV (red).

However, the measurements performed using the AC Setup 1 showed considerable fluctuations for the low current region of the curves, and the information extracted by observing the complete cycling measurements should not be considered as definitive. In this case, the resistance ratio values were obtained by selecting a range of points to exclude outliers and enhance consistency. By only selecting one point at a certain voltage, since these measurements presented a highly noisy regime in the HRS, the extracted resistance ratio would not be precise. Another observation by comparing the SR study in DC (Fig. 4.1) and the 10 Hz AC study is the mean resistance ratio starting point and maximum. On the one hand, in DC, the starting point was 5 and reached 24 at the maximum of the SR curve. On the other hand, in the 10 Hz AC study, the starting point was 2 and reached 10 at the maximum of the SR curve. This result was expected since the time the voltage is applied is

reduced by increasing the frequency and so reducing the impact of the set and reset transitions on the conductive filament. Consequently, this leads to narrower window openings.

4.2.2. AC Setup 2

The following experiment was performed using the second setup option for the stochastic resonance (SR) impact study under AC conditions, which combines the K-SPA with the pulse generator. In this setup, the K-SPA was connected to the top electrode of the device, while the pulse generator was connected to the bottom electrode, acting as a ‘noisy ground’, see the setup schematics in Fig. 4.11. The K-SPA simultaneously sent pulses and measured the device's response with real-time data captured by using the remote pulse module (RPM) of the K-SPA.

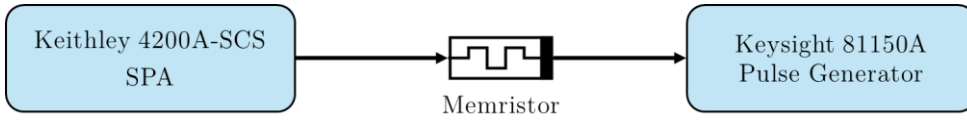
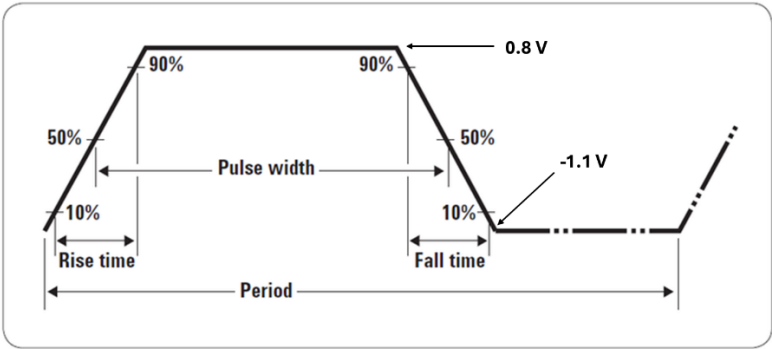


Figure 4.11. Schematic of the AC Setup 2, used for the stochastic resonance study on memristors subjected to AC conditions. The K-SPA is connected to the top electrode of the device both sending the input pulsed signal and receiving the data, and the bottom electrode is connected to the Keysight 81150A pulse generator as a ‘noisy ground’.

The devices used in this experiment were the same as ones used with the AC Setup 1 (introduced in Fig. 3.1). The objective was to study the SR phenomenon using pulsed input signals with different frequencies. In this experiment, the frequency was raised to 50 Hz and 1 kHz, with pulses used as the input signal, and the SR impact was evaluated. The pulses started at -1.1 V, increased to 0.8 V, and then decreased back to -1.1 V. See the pulse schematics of Table 4.1, where the pulses timing is also described. Notably, the aspect ratio (width/rise and fall time ratio) was consistent in both frequency cases.

The experiment consisted of cycling 200 times for every frequency (50 Hz and 1 kHz) and noise σ values (ranging from 0 mV to 300 mV). Figure 4.12 shows

the mean resistance ratio for every noise σ value at the two programmed frequencies: 50 Hz (black) and 1 kHz (red). In this case, the HRS and LRS currents were directly extracted at -0.5 V from the measurement datapoints. The devices responded as expected to the noise inclusion, and stochastic resonance curves were obtained for both frequencies. Again, higher frequencies produced lower resistance ratio values. This setup enabled a successful SR impact study at frequencies up to 1 kHz. However, programming and response issues arose at higher frequencies.



| Frequency | Period (ms) | Width (ms) | Rise/Fall time (μ s) |
|-----------|-------------|------------|---------------------------|
| 50 Hz | 0.02 | 0.01 | 1 |
| 1 kHz | 1 | 0.5 | 50 |

Table 4.1. Input pulse timing (period, width and rise/fall times) for the two frequencies applied in the experiment in Fig. 4.12. The above pulse schematics shows the meaning of the timing terms.

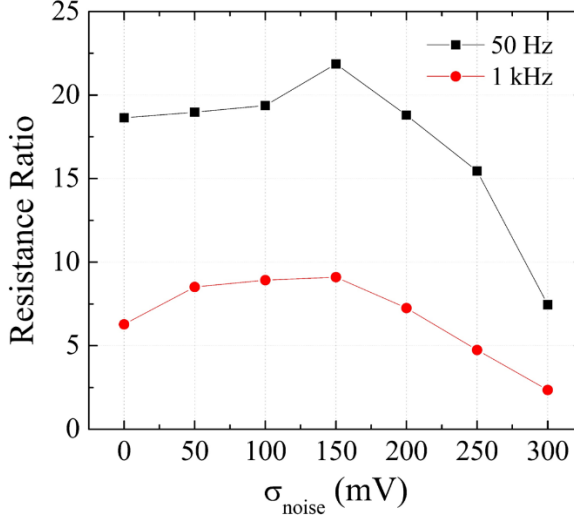


Figure 4.12. Mean resistance ratio evolution versus noise σ when pulses of 50 Hz (black) and 1 kHz (red) frequency are applied with the AC Setup 2.

4.2.3. AC Setup 3

The third approach (AC Setup 3) consisted in combining the pulse generator (at the memristor top electrode) and the AG-SPA (at the memristor bottom electrode), as shown in Fig. 4.13.

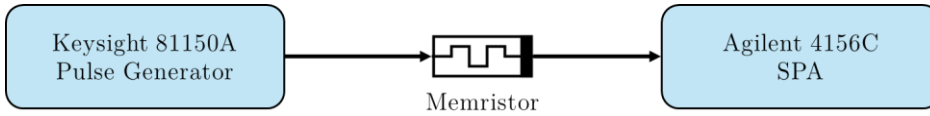


Figure 4.13. Schematic of the AC Setup 3 for the stochastic resonance study on memristors subjected to AC conditions. The Keysight 81150A pulse generator is connected to the top electrode of the device applying the input pulsed signal and the bottom electrode is connected to the Agilent 4156C SPA to read the resistance state of the device.

The AG-SPA is not capable of measuring the real-time current and voltage coming from an external instrument. Hence, a strategy to measure the resistance state after every pulse is required. In this case, the set and reset pulses are performed by the PG and the reading pulses after every transition are applied with the AG-SPA (see Fig. 4.14a and the list below). The reading

pulses consist in a negative voltage that is not affecting the memory state. The devices used in this experiment are the same as the ones previously presented in Fig. 2.5 with the aluminum layer as the common bottom electrode.

The following list introduces the complete measurement procedure:

1. Forming + 20 stabilizing DC I - V cycles performed with the AG-SPA.
 2. Set process conducted with the PG. The connection to the AG-SPA is grounded.
 3. The connection to the PG is grounded. The AG-SPA sends a read pulse of -0.5 V amplitude.
 4. Reset process performed with the PG. The connection to the AG-SPA is grounded.
 5. The connection to the PG is grounded. The AG-SPA sends a read pulse of -0.5 V amplitude.
- * Cycling is performed by iterating steps 2 to 5.

Figure 4.14b shows the HRS (blue) and LRS (red) currents from a 200 cycles measurement without including noise, following the procedure in the previous list.

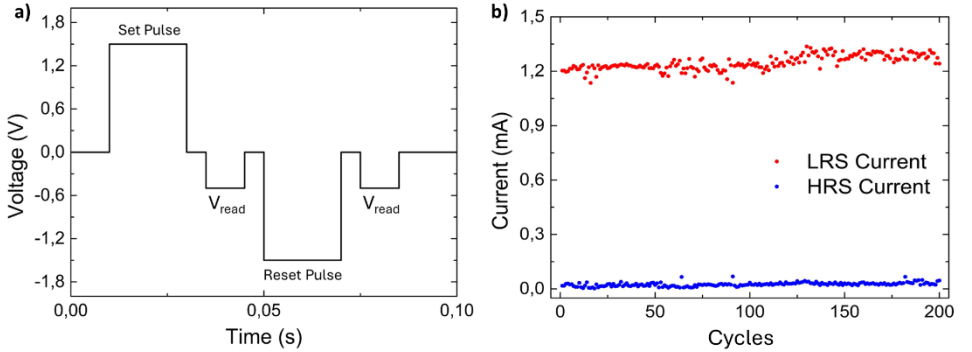


Figure. 4.14. Pulsed measurements performed with the AC Setup 3 using a $5 \times 5 \mu\text{m}^2$ active area memristor. a) Complete time evolution of the applied signal. b) HRS (blue) and LRS (red) currents for 200 applied signal cycles.

Once the measurement procedure is introduced, Fig. 4.15 presents the comparison of experiments of 200 resistive switching cycles with (red) and without (black) noise performed applying pulses of four different frequencies: 1 Hz, 1 kHz, 10 kHz and 100 kHz. Every experiment was carried out using a fresh

device. The set and reset pulses consisted in a ± 1.2 V pulse respectively. Now, the set and reset pulses include noise, whereas the read pulses do not. After considering different values, the selected noise σ was 150 mV, which resulted suitable for the different frequency values. The device-to-device variability was altering the output results, so the initial resistance ratio from the initial stabilization cycles (R_0) was extracted to perform a normalization and defined the relative resistance ratio. This consisted in the measured resistance ratio for every experiment (noise σ and frequency) divided by the R_0 from each device. Figure 4.15 represents the mean value of the relative resistance ratio as a function of the pulse frequency. If the relative resistance ratio is 1, it means the resistance ratio from the experiment is the same as the ones obtained in the initial voltage sweeping cycles from the device. Upon closer analysis, it can be observed that at 1 Hz, the noisy experiment results in a ratio exceeding R_0 , while all other experiments show ratios below R_0 . This result is expected, since as the frequency increases, the memristor is exposed to the input signal for a shorter duration, thereby reducing the impact of noise. At 100 kHz, there is no discernible difference between the noisy and noise-free experiments, illustrating the minimal effect of noise at such high frequencies.

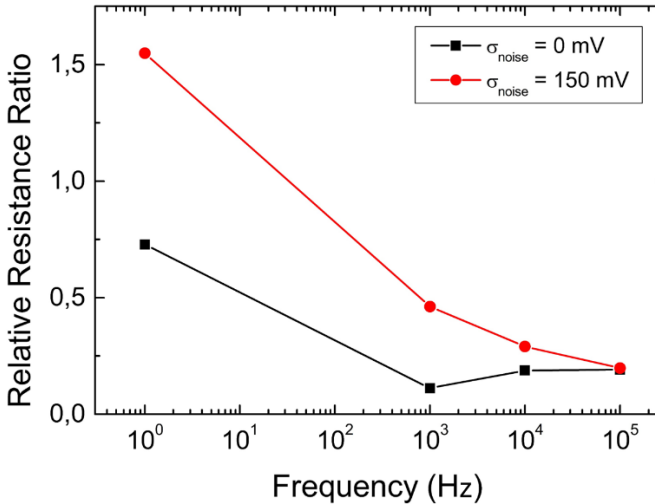


Figure 4.15. Mean relative resistance ratio evolution versus pulse frequency. In red, the experiments without noise, and in red the experiments with a noise σ of 150 mV.

This third approach to study the impact of external noise on memristor performance proved to be the most stable. The results are promising, suggesting that the noise influence drops as the frequency increases. However, none of the setups used was ideal, leaving room for methodological improvements.

While the current findings are significant, several limitations in the experimental setup must be addressed to obtain more robust results. The first concern comes from the transition voltages shift observed for different frequencies (as discussed in article **JLPEA24**), which introduces a double-variable effect: the stochastic resonance (SR) phenomenon and the frequency-dependent transition voltage shift. This dual effect complicates the interpretation of results, highlighting the need for more refined methodologies.

To address these challenges, future experiments should incorporate more stable setups capable of remote control and precise pulse application. A good potential option is using the Keysight B1500A, which includes a pulsed module and Matlab integration. This system would introduce noise in the input signal using the *randn* function in Matlab and simultaneously registering the current. Additionally, to account for the frequency-dependent transition voltage shift, future studies should consider varying pulse amplitudes for different frequencies to ensure that all experiments begin from a similar start point in terms of resistance ratio. For higher frequencies, higher pulse amplitudes are required to obtain the same resistance ratio.

These improvements in both experimental setup and methodology could lead to more solid and reproducible results, enhancing the reliability of conclusions regarding the impact of external noise on memristor performance. Once these optimizations are implemented and with a more rigorous approach, these results could help the advance in understanding the memristor performance under the influence of the stochastic resonance phenomenon and the input signal frequency.

The findings in this section provided deep insights into the AC stochastic resonance phenomenon and also opened the door to potential applications in the memristor-based neuromorphic systems field, like the spike timing-dependent plasticity (STDP) learning rule and the homeostasis.

4.3. Impact of External Noise on the Binary STDP Protocol

The results obtained in the previous sections in this chapter motivated the analysis of the SR effect in a more sophisticated biasing configuration. In this section, we will focus on the SR effect on memristor-based neuromorphic computing, and in particular, on the binary STDP learning rule implementation. This effect was studied both experimentally and complemented with LTspice simulations. As previously stated in the Introduction, STDP is a fundamental learning rule that updates the synaptic weight based on the timing between pre- and post-synaptic spikes. In binary STDP, where synaptic weights are constrained to discrete states (in this case HRS and LRS), the introduction of noise can help to activate the learning process. Even though artificial neural networks are assumed to work with no noise, neurobiological systems are known to operate in noisy environments. Thus, noise can tune the activation threshold of neurons, enhancing the response of nonlinear circuits. This section includes information from the **TED24** article.

4.3.1. Experimental Noise-Induced Binary STDP

The devices used for the experimental study of the impact of noise in the binary STDP learning protocol are the same isolated configuration devices from the previously presented wafer with aluminum as a common bottom electrode (see Fig. 2.5 in Section 2.3). The electrical setup consisted of one SMU from the AG-SPA connected to the top electrode of the device and another SMU to the bottom electrode. The noise was added to the input signal by means of the *randn* function in Matlab. In this case, to analyze the external noise impact on binary STDP, under the absence of noise, the memristor state does not change. However, the application of noise allows the memristor to switch, activating the occurrence of the set and/or reset processes.

We study binary STDP via the SR phenomenon following three different approaches: A) activating the set process, B) activating the reset process and C) activating both set and reset processes simultaneously.

To provoke binary STDP the memristors were subjected to set and reset pulses to reach ON and OFF states respectively. Firstly, all the set and reset pulses are formed from a pre-synaptic pulse (V_{pre}) applied to the top electrode of the device and a post-synaptic pulse (V_{post}) applied to the bottom electrode. The resultant voltage drop at the memristor reads: $V_{tot} = V_{pre} - V_{post}$ as illustrated in Fig 4.16a. The width of the pre- and post-synaptic pulses was always 150 ms. Also, we consider two different types of set and reset pulses: fixed and variable. The fixed ones consist of a constant pulse with voltage amplitude high enough to ensure the memristor state transition. The more complicated variable pulses follow an adaptive pulse-width scheme that is detailed next, in each approach. Depending on each investigated case, the set and reset pulses can be fixed or variable, and with or without noise addition. After completing every transition pulse (set or reset), the memristor conductance state was determined by means of a read voltage pulse ($V_{read} = -0.5 V$) of 150 ms duration applied to the top electrode of the device and grounding the bottom one. The complete sequence of applied signals will be presented in each corresponding approach. A fresh device was used for each experiment (one for measuring without noise and one for the noisy measurement).

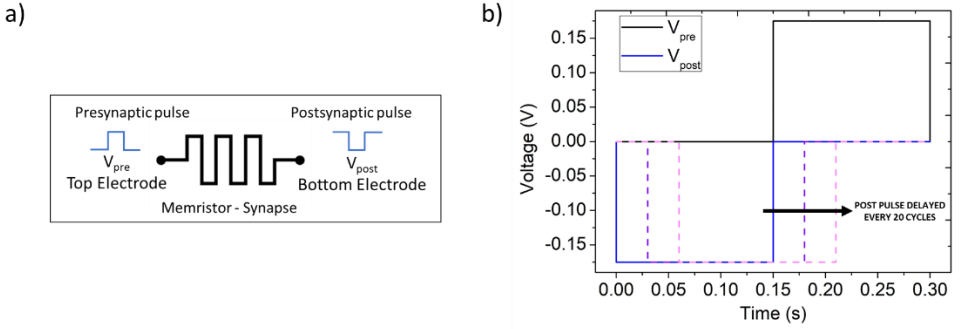


Figure 4.16. a) Memristor schematics presenting the applied pulses (pre- and post-synaptic) at the top and bottom electrodes respectively. b) Initial situation of the applied pre- and post-synaptic pulses (no overlap) is represented with continuous lines. Different situations with delay of the post-synaptic pulse are presented in dash lines.

The added noise, for all the different considered test conditions, was Gaussian ($\sigma_{noise} = 150 mV$), which was found to be the suitable value for the SR observation in these samples, after analyzing different values. The resistance ratio is calculated as follows: $R_{ON}/R_{OFF} = (\frac{R_{Reset}}{R_{Set}}) = (\frac{V_{Read}/I_{Reset}}{V_{Read}/I_{Set}}) = (\frac{I_{Set}}{I_{Reset}})$, where

I_{Set} and I_{Reset} consist in the registered currents during the read pulse after the set and reset pulses, respectively. In what follows, the information about the complete applied signal and the results corresponding to the three different approaches is introduced.

A. Set Process Activation

In this first approach, the focus is to improve the binary STDP with the addition of Gaussian noise to the pulse that provokes the set transition. We ensure that the memristor remains in the HRS state by selecting appropriate amplitudes for the pre- and post-synaptic pulses without external noise. For this reason, we selected a set voltage, $V_{tot} = V_{set}$, slightly below the voltage required to activate the set transition. This ensures that once noise is added, there is a probability of overcoming the set threshold voltage. In this study, we set the maximum voltage to $V_{set} = V_{tot} = 0.35 \text{ V}$.

To induce a change from LRS to HRS, a reset pulse was generated by applying -0.5 V at the top electrode and 0.5 V at the bottom electrode. Thus, the reset pulse consists of $V_{reset} = V_{tot} = -1 \text{ V}$ during 150 ms . However, generating the set pulse, V_{set} , is more challenging because the post-synaptic pulse must allow for adaptive time-shifting to generate different overlap situations between the pre- and the post-synaptic pulses. This overlap induces changes in the maximum values of V_{set} . In Fig. 4.16b the initial situation of the pre- and post-synaptic pulses is illustrated. Notice that initially there is no delay between pulses. The dash lines in the figure represent the successive delays of the post-synaptic pulse. For a better understanding, we describe the details of a variable set pulse generation. The duration of the set pulse at maximum voltage (0.35 V) starts at 0 ms , goes up to 150 ms and drops back to 0 ms following 15 ms steps. Figure 4.17 illustrates three cases for a variable set process: in a) the pre- and post-synaptic pulses are not overlapped, that produces a 300 ms pulse of $V_{set} = V_{tot} = 0.175 \text{ V}$; in b), a partial overlap situation that generates a 3-level voltage pulse. In this situation, the maximum $V_{set} = V_{tot} = 0.35 \text{ V}$ was during approx. 60 ms ; in c), a complete pulse overlap, where $V_{set} = V_{tot} = 0.35 \text{ V}$ pulse that lasts 150 ms .

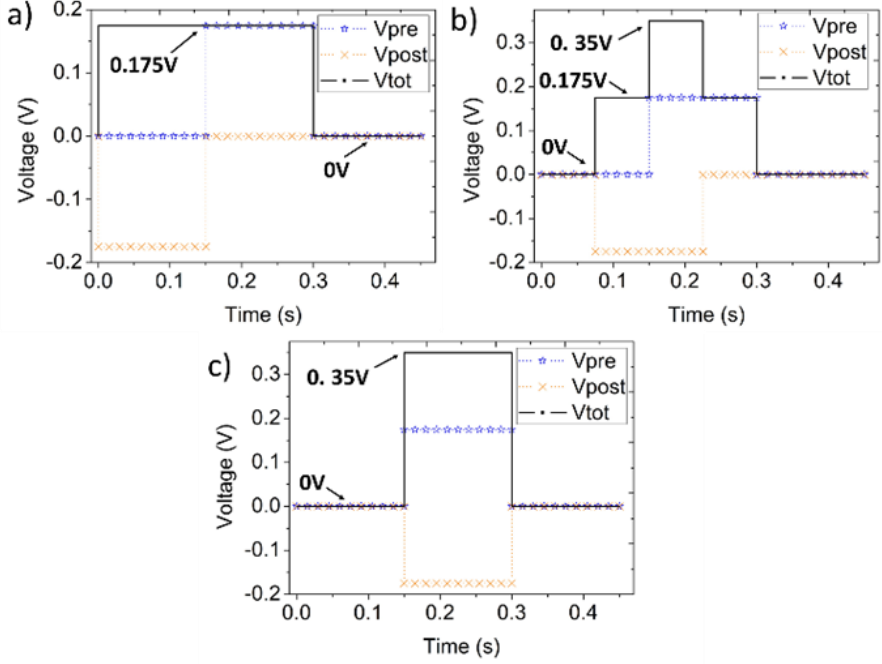


Figure 4.17. Total set voltage (V_{tot}) in continuous lines. Pre- and post-synaptic pulses in dashed lines for three different overlap cases: a) no overlap, b) intermediate, and c) complete.

In Fig 4.18a, the complete measurement sequence for this first approach is reported. In every post-synaptic pulse delay (Δt), the sequence is cycled 20 times to allow for statistical analysis. At the beginning of the measurement sequence, the pre- and post-synaptic pulses do not overlap, and the 20 cycles are performed. The post-synaptic pulse is then delayed 15 ms, and again the 20 cycles are executed. This process is repeated for each shift. $\Delta t = n * 15 \text{ ms}$ where n starts at 0 and grows until 21. Focusing again on Fig. 4.17: a) presents the initial situation where $n=0$. As Δt increases, the overlap grows until a maximum situation in c) for $n=11$. After the maximum overlap situation, n keeps growing until there is no overlap again, for $n=21$.

The currents for the 20 cycles after each set and reset processes in all the previously mentioned iterations are illustrated in Figs. 4.18b and 4.18c against Δt for experiments without considering noise and including it respectively. Orange symbols represent the read currents after a set transition and the blue ones after a reset transition. In addition, in the figures, the mean value of the

read current is shown with a solid line of the same color of the respective symbols. The comparison of both figures reveals that noise addition is crucial in identifying resistive states. Without noise, there is no state separation (see Fig. 4.18b). However, with noise, both ON and OFF states are separated because the set transition is enhanced. This state separation is proportional to the overlap between pre- and post-synaptic pulses. It is important to highlight that the maximum overlap situation is shown at $\Delta t = 150 \text{ ms}$. Figure 4.18d displays the mean resistance ratio as a function of Δt for the measurements without (in blue) and with noise (in orange). The dash grey line in Fig. 4.18d represents the overlap as a function of Δt , which supports the analysis reported in Figs. 4.18b and 4.18c. about the proportionality between pre- and post-synaptic pulses overlap and the resistance ratio. In conclusion, the addition of noise to the set transition improves the resistance ratio.

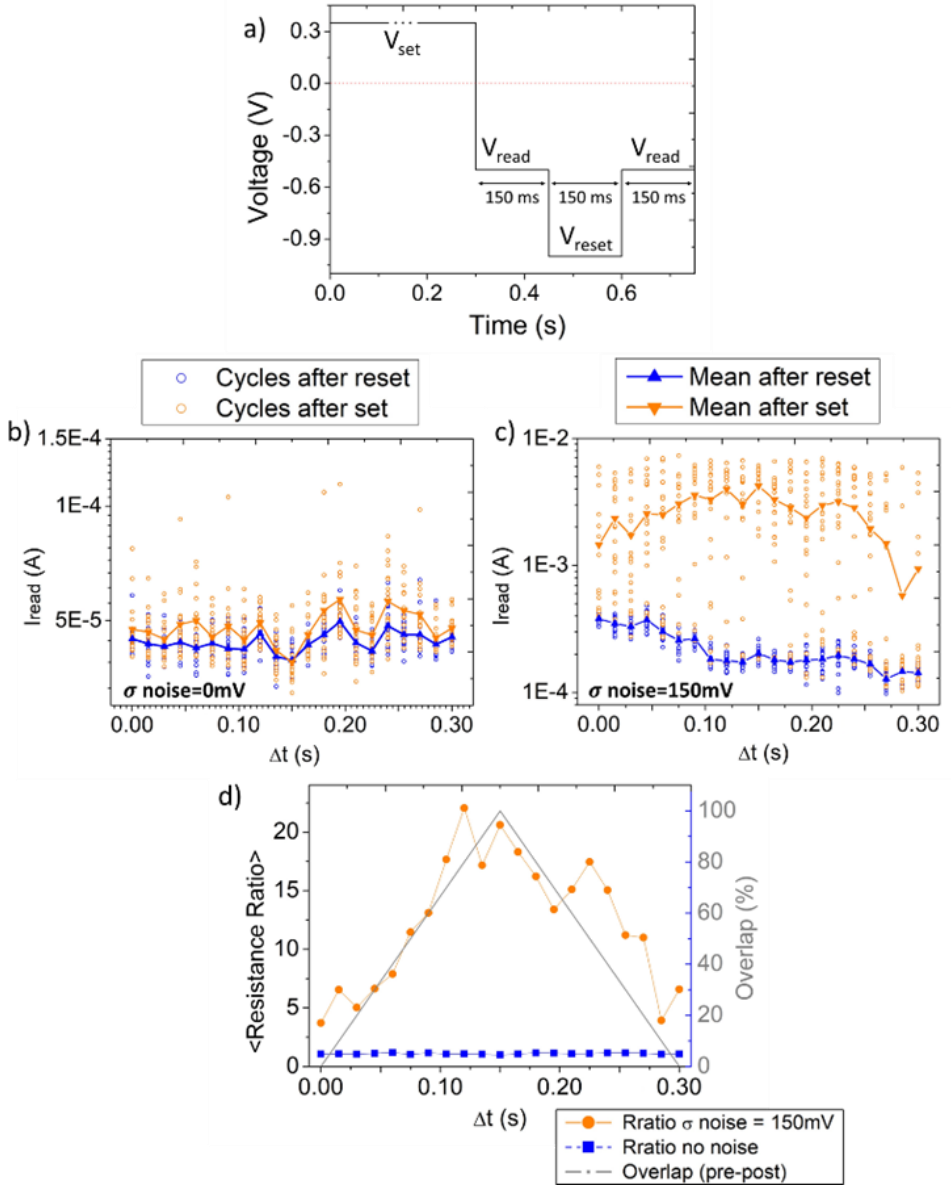


Figure 4.18. Set process activated via noise addition. a) Complete applied signal for this study during one cycle. The maximum value timespan of V_{set} pulse varies every 20 cycles. The current during the 20 cycles for each Δt and mean current evaluated after a set transition, in orange, and after a reset in blue is presented in b) for the measurements without noise and in c) including noise ($\sigma = 150\text{mV}$). In d) the mean value of R_{Ratio} against Δt is presented. For the measurements without including noise, in blue, and with noise, in orange.

B. Reset Process Activation

This approach presents the opposite situation to the previous case. Set pulses are fixed while reset pulses are variable. Now, it is the reset process the one intended to be activated via noise addition. Hence, the applied voltages have the opposite sign with respect to case A. The set pulses maximum voltage is fixed to a voltage high enough to ensure the transition to the LRS. Now, the pre- and post-synaptic pulses consist in 0.3 V and -0.3 V pulses respectively, resulting in a 150ms pulse of $V_{set} = V_{tot} = 0.6\text{V}$, which is always applied (the same in all cycles and iterations). However, the complexity appears now in the reset voltage, but the methodology used for its generation is the same as that considered in the previous approach resulting, in this case, in a negative voltage pulse with a maximum value $V_{reset} = V_{tot} = -0.55\text{V}$. This value is low enough to activate the reset process. The noise intensity is the same as in the previous approach ($\sigma_{noise} = 150\text{mV}$). Here, the delay is in the post-synaptic pulse for the reset process, what generates a different overlap condition every 20 identical cycles. In this approach, the noise is applied during the reset process.

As reported in the previous approach, Fig. 4.19a shows one cycle of the applied signal for this reset process activation, where the set process is a fixed pulse and the reset pulse is variable, changing every 20 cycles, as mentioned above. Figure 4.19b illustrates an example of a medium overlap situation between the pre- and post-synaptic pulses to form the reset pulses in this approach and highlights the resulting voltage values. Figures 4.19c and 4.19d show the currents measured after every transition and cycle as a function of Δt for the experiments without and with noise, respectively. Again, the noise allows the device to switch, but in this case from LRS to HRS with a switching probability proportional to the overlap. This trend is confirmed by the results shown in Fig 4.19e, where the R_{Ratio} of the two different situations (with and without noise inclusion) is shown as a function of the post-synaptic pulse delay. The figure includes the dash gray line showing the overlap evolution as a function of the delay as well. Once it is demonstrated that both set and reset processes can be activated separately with the addition of noise, the key part of this work is to combine both activations simultaneously. This study is presented in the following approach.

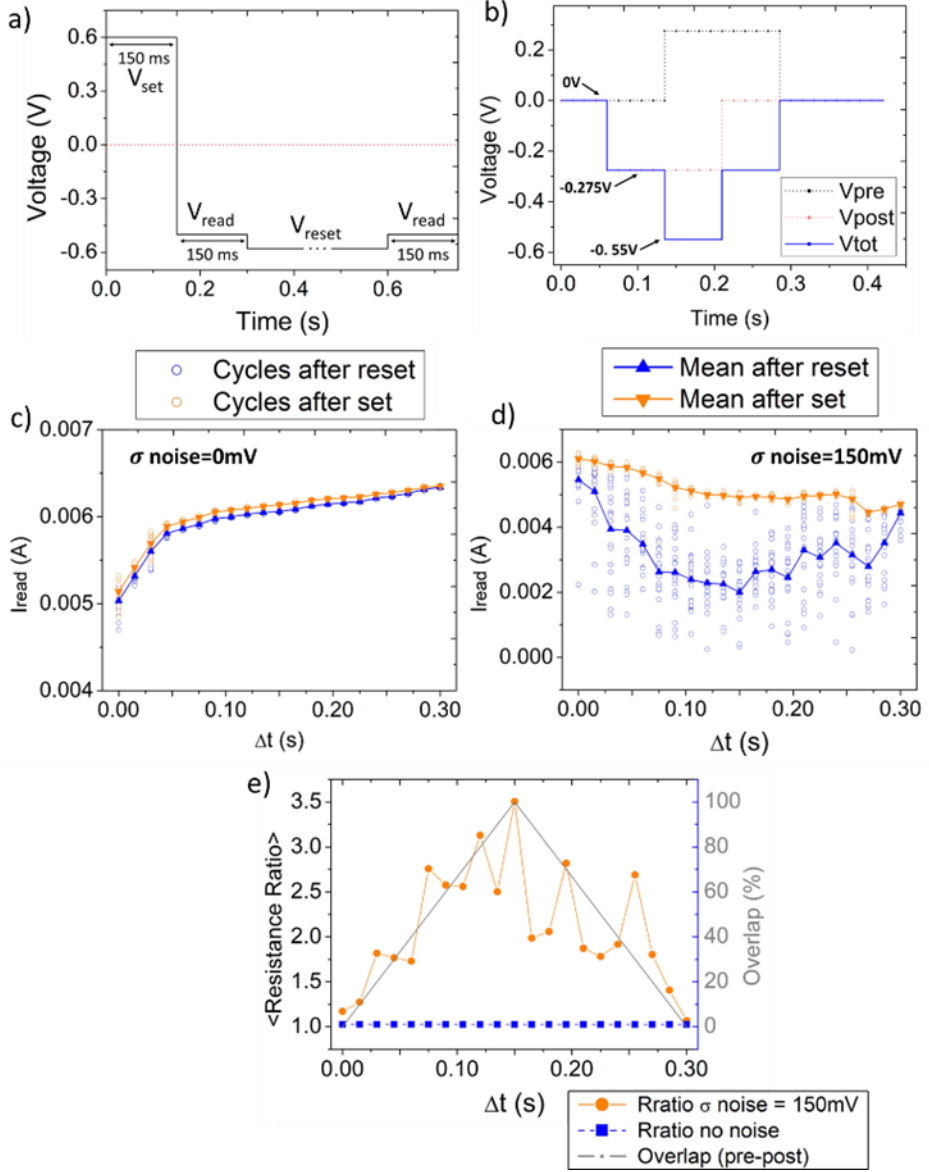


Figure 4.19. Reset process activated via noise addition. a) Complete applied signal for this study during one cycle. b) medium overlap situation between the pre- and post-synaptic pulses to build the variable reset pulse. The maximum value timespan of V_{set} pulse varies every 20 cycles. The current during the 20 cycles for each Δt and mean current evaluated after a reset transition, in orange, and after a reset in blue is presented in c) for the measurements without noise and in d) including noise ($\sigma = 150 \text{ mV}$). In e) the mean value of R_{ratio} against Δt is presented. For measurements without including noise, in blue, and with noise, in orange.

C. Complete Switching Activation

In this approach, the combination of the two previous studies is presented. This is the most realistic situation where a system is always driven by a noisy signal. Hence, both set and reset processes will be under noise influence. The applied voltages are $V_{set} = V_{tot} = 0.38 \text{ V}$ and $V_{reset} = V_{tot} = -0.58 \text{ V}$. Both values are not sufficient to activate the switching. The same noise ($\sigma_{noise} = 150 \text{ mV}$) was applied. The slight set and reset voltage values differences with respect to the previous approaches are a consequence of the inherent device-to-device (D2D) variability. These particular values were selected so as to achieve an initial condition as similar as possible for all the experiments. From the results in several devices (~ 25), we identified the optimal voltage ranges to be: V_{set} from 0.35 V to 0.4 V and V_{reset} from -0.55 V to 0.6 V . In the same line as in the previous approaches, Fig 4.20 summarizes the experimental study carried out. Figure 4.20a illustrates the applied voltage signal where both set and reset durations are variable. A key point for the set and reset pulses timing in this approach is that the evolution of the pre- and post-synaptic pulses duration is synchronized. This means that the timespan of the maximum value in both set and reset pulses is the same (i.e., the same overlap), for all the cycles.

Figures 4.20b and 4.20c present the measured current after every set and reset transition against Δt for the experiments without noise and including it, respectively. The added noise enables both transitions simultaneously. In this approach, the overlap between pre- and post-synaptic pulses evolves equally in both set and reset transitions.

It is worth mentioning that there are differences in the resistance ratio values obtained with the three approaches (see Figs 4.18d, 4.19e and 4.20d) described above. In the first approach, where the set process is activated by noise, the maximum resistance ratio value is approximately equal to 20. In the second approach, where the reset process is activated, the maximum value is around 3.5, and in the third approach, with both transitions activated, the maximum value is 9.

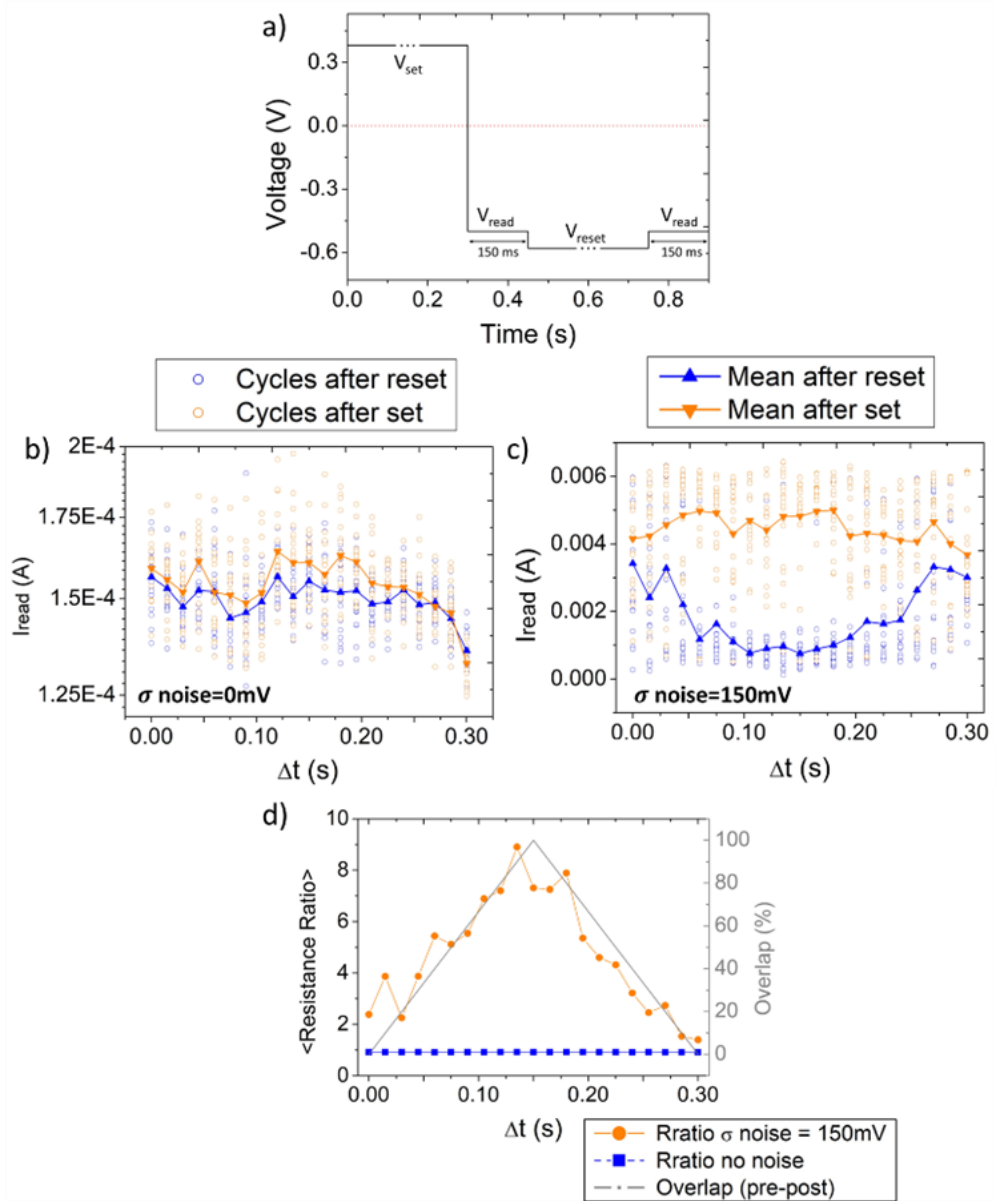


Figure 4.20. Set and reset processes activated via noise. a) Presents the complete applied signal during one cycle. The duration of the maximum values of V_{set} and V_{reset} is the same. The current during the 20 cycles for each Δt and mean current evaluated after a set transition, in orange, and after a reset in blue is presented in b) for the measurements without noise and in c) including noise ($\sigma = 150 \text{ mV}$). In d) the mean value of R_{ratio} against Δt is presented. For the measurements without including noise, in blue, and with noise, in orange.

The resistance ratio differences observed in the three approaches can be ascribed to the widely known intrinsic memristor variability, the selection of noise sigma, and the voltage values for the constant pulses for reset and set transitions in approaches A and B respectively. The predominant factor is the different abruptness of the set and reset processes in the used memristors. Regarding the last issue, in the typical HfO_2 -based memristors I - V curves, the set process is notably more abrupt than the reset process, which is more gradual. Hence, the noise activation of the set (approach A) allows a high resistance ratio after a complete reset process. However, for approach B, the resistance ratio values are lower because of the progressiveness of the reset process, therefore noise does not allow a large resistance state change during this process.

In this subsection, a comprehensive investigation into the SR effect within neuromorphic systems utilizing memristors was presented. The study highlighted the positive impact of noise on the binary STDP protocol. Through the strategic introduction of noise in either the set pulse, reset pulse, or both simultaneously, we demonstrated the switching activation. The experiments detailed in this study were replicated using other devices from the same wafer to verify consistency and reproducibility of results.

4.3.2. Simulating STDP Activation via SR

As part of this study, this subsection reports simulation results using the LTspice simulator. The goal is to reproduce the same input signal used for the third and more complex approach presented and to analyze the response of the memristor provided by the considered model. For the simulations we have used the already presented DMM model for RRAM devices (see Subsection 3.1.3 in this thesis). In this subsection, the model will be tested with complex and noisy signals.

Before the simulations, setting the model parameters is a necessary step. The procedure consisted in selecting the model parameters that reproduce the behavior of the devices used in this work, which are obtained by fitting the experimental data to the model equations. The result of this fitting process is shown in Fig 4.21a, where the I - V curves corresponding to 10 experimental

cycles (in grey) are compared to a simulated curve (in red). In addition, Fig 4.21b presents the schematics of the LTspice circuit used for the simulations containing 4 voltage sources: the pre- and post-synaptic pulses (V_{pre} and V_{post}), and the noise sources for the set and reset processes ($SetVn$ and $ResetVn$, respectively). The complex signals were generated in LTspice using the Piecewise linear (PWL) function, where time and voltage can be programmed point by point, while the white gaussian noise signal is added externally. Once the pulsed signals are generated, the noise is included in the transitions, the simulations run, and the results externally compiled and analyzed in Matlab.

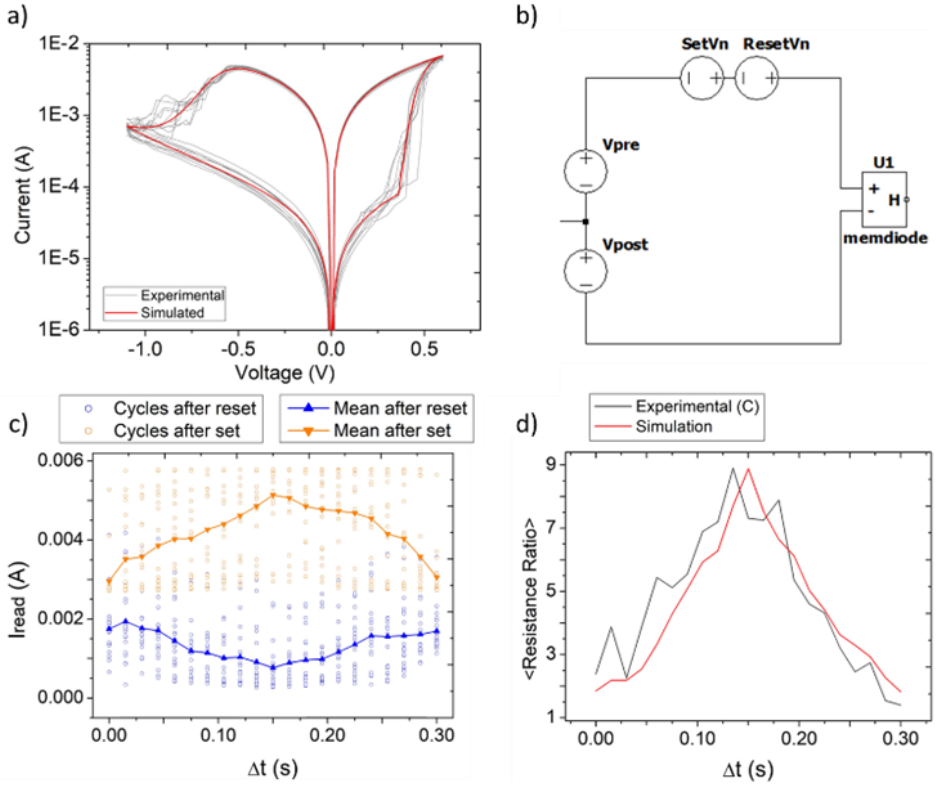


Figure 4.21. a) Comparison of the experimental (grey) and fitted (red) I - V characteristic. b) LTspice circuit schematics used to simulate STDP activation via SR. c) Simulated current during the 20 cycles for each Δt and mean current evaluated after a set transition, in orange, and after a reset transition in blue including noise obtained using the LTspice simulator and the DMM model. d) Experimental (grey) and simulated (red) resistance ratio against Δt showing a good agreement between both curves.

The results reported in Fig. 4.21c (symbols) show the reading current after every set (in orange) and reset (in blue) transitions versus the Δt for a simulation including noise. The continuous line corresponds to the mean value of the LTspice simulation. The HRS and LRS reading current values and dependence on the post-synaptic pulse delay obtained through simulation show that the model is able to reproduce the experimental behavior.

Figure 4.21d compares the experimental and simulated resistance ratio against Δt . The simulations demonstrate that the binary STDP protocol can be activated through external noise addition in LTspice, showing a good agreement between experimental and simulated results.

In this section, a complete experimental study of the SR in STDP protocol implemented with memristors, showing the beneficial role of additive noise on the binary STDP protocol was reported. This study analyzes the SR phenomenon in a scenario where the memristor's HRS and LRS was not distinguishable. Nevertheless, we have demonstrated that by including noise to the set pulse, reset pulse or both pulses simultaneously, the resistive switching was activated. These findings showed that as the duration of the maximum noise-activated transitions (set, reset, or both) increases, the resistance ratio also increases. The results obtained from the simulations using the DMM well reproduce the experimental observations. The presented results are promising and offer a potential avenue for further exploration of the stochastic resonance phenomenon in more complex neuromorphic systems.

4.4. Homeostasis in Memristor-Based Neuromorphic Systems

In this section, the capability of noise to emulate the biological homeostatic properties of neurons within memristor-based neuromorphic systems is demonstrated. As previously detailed in Subsection 1.3.1, homeostasis is a critical feature in biological neural networks, ensuring stability and adaptability in response to external stimuli. Inspired by this biological principle, in this section, it is shown how controlled noise injection into the bias applied to memristors enables the regulation of their performance when functioning as

artificial neurons. Specifically, the addition of external noise facilitates the modulation of memristor threshold voltages and switching times, effectively controlling the firing process of the artificial neuron. This approach leverages the stochastic resonance phenomenon to achieve noise-induced homeostasis, mimicking key aspects of neuronal behavior. Such regulation is particularly relevant for neuromorphic systems that require adaptability and robustness, like biological networks.

In this section, noise-induced homeostasis in memristors is studied by observing the effect of noise on the spike time of a single memristor operating as a neuron. We focus on the simplest memristor neuron, where the spike time is defined as the time to trigger a memristor set event. In this sense, on the one hand, if the presence of external noise reduces the time required for a set event (spike), the system exhibits increased excitability, termed potentiation regime. On the other hand, if noise prolongs set event times, the system experiences decreased excitability, known as depression regime. Both potentiation and depression regimes are previously illustrated in the Introduction, and visible in Fig. 1.12. In this case, in the following subsections two different results are presented using distinct devices from the same wafer. In the first one, noise-induced potentiation is demonstrated and in the second one it is proved that both potentiation and depression regimes can be induced via noise.

To validate the proposed approaches, extensive experimental characterizations were conducted and supported by simulations. The experimental results were obtained using the unipolar type devices previously presented in Section 4.1, where the external noise modulated both set and reset voltages (see Figs. 4.3 and 4.4) and were reproduced using the LTspice simulator, employing the dynamic memdiode model (DMM). The electrical measurements in this section were carried out with the AG-SPA setup and the noise was included via software with the *randn* function in Matlab. This combination of empirical and simulated data highlights the consistency and reliability of the findings. Parts of the content in this section were published in the **EDL24** article.

4.4.1. Noise-Induced Potentiation

This subsection is dedicated to demonstrating the noise-induced potentiation effect on memristors acting as neurons. To reach that goal, the memristor initial state was the HRS and the memristor spike time is defined as the cumulative time needed to produce a set event when a staired constant voltage is applied (i.e., a sequence of constant voltages of a certain duration, whose value was increased in steps in a given voltage range, see Fig. 4.22a). The staired voltage started at -1.2 V adding -100 mV every 1.5 seconds; the sweep is stopped once the set event occurs (i.e., when the current abruptly increases and reaches 50 μ A). To ensure the memristor was at the HRS, the reset process was induced with voltage sweeps as the ones applied in Fig. 4.6. The staired constant voltage is applied to accelerate the set transition and to ensure that the device switches to the LRS in an acceptable time window. The voltage increase is clearly slower than when a voltage sweep is applied. This procedure (reset with a voltage sweep and set with a staired constant voltage) was repeated 100 times (i.e., cycles). The best noise sigma for modulating the set transition was found to be $\sigma_{noise} = 120$ mV after testing different values. The ideal noise sigma depends on the device and the raw input signal.

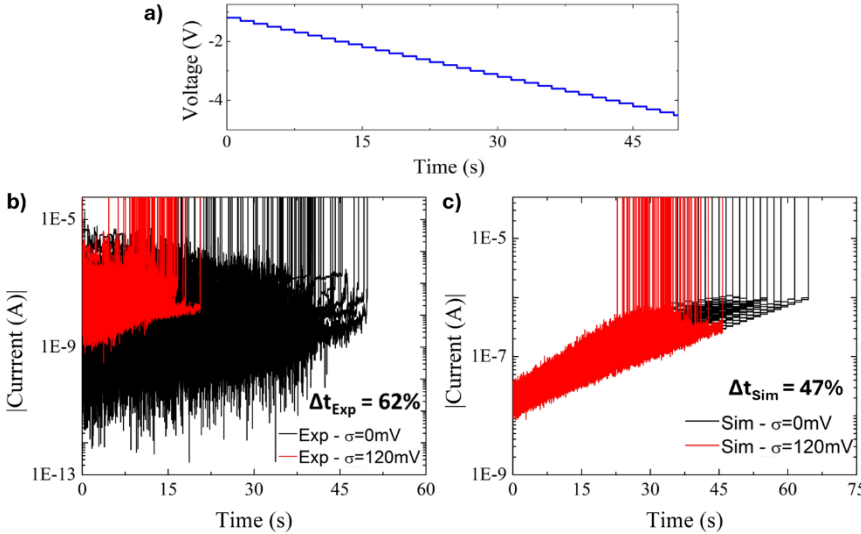


Figure 4.22. a) Time evolution of the staired constant voltage. Current versus time evolution without noise (black) and with $\sigma_{noise} = 120$ mV (red) obtained b) experimentally and c) in simulations.

The experimental results are visible in Figure 4.22b, where the memristor current versus time without (black) and with noise (red) for the 100 measured cycles respectively is presented. The abrupt increase of the current means the occurrence of the memristor spike. It is clearly observable at first sight that the noise inclusion induces lower set event times, and consequently, meaning a decrease of the spike time. This emulates the biological neuron behavior and modulates the neuron performance increasing its activity (potentiation regime). For a more detailed evaluation, Fig. 4.23a presents the experimental set event time along the 100 experimental cycles without noise (black) and with noise (red). Again, it is clearly observed that noise impacts reducing the set event times. The previous experimental results were compared with LTspice simulations carried out with the DMM memristor model. The DMM relies on two key equations, one governing the current-voltage characteristic and the other dictating the memristor memory state. Cycle-to-cycle variability was included in the model parameters related to the HRS current and set voltage, following the method presented in Subsection 3.1.2. The calibration of the model parameters was performed by reproducing the experimental median I - V behavior using standard voltage sweeps. After calibration, the same input signal was reproduced including Gaussian noise in the applied signal. The reduction of the set event times is also clearly observed in the simulations, see Fig. 4.22c and Fig. 4.23b. This result proves the well-functioning of the DMM in terms of versatility since it can qualitatively reproduce the experimental behavior of different types of memristors under the influence of different input signals.

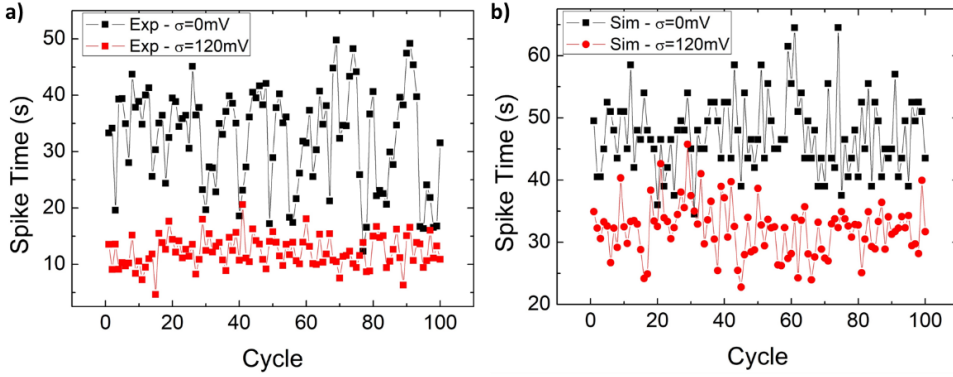


Figure 4.23. a) Set times for every cycle without noise (black) and with $\sigma_{noise} = 120 \text{ mV}$ (red) obtained a) experimentally and b) in simulations.

After this experiment on the noise-induced potentiation regime, a more complete approach was performed to reach modulation in both potentiation and depression regimes. By inducing these two regimes using different noise values, the homeostatic regulation could be emulated. This approach is presented in the following subsection.

4.4.2. Noise-Induced Homeostasis

This subsection extends the findings in the previous one, where a demonstration of the noise-induced potentiation on single memristors acting as a neuron was presented. In this subsection, in order to induce both potentiation and depression regimes, firstly, the same unipolar memristors were subjected to larger σ_{noise} values following the same method as the one used in the previous subsection to obtain a typical stochastic resonance curve. The results of this experiment are shown in Fig. 4.24, where we observe a stochastic resonance curve depicting the evolution of mean set time (or spike time) versus σ_{noise} . Notice that different points are highlighted. Assuming brain as a noisy system, for instance, B point can be interpreted as an equilibrium point. When σ_{noise} is increased, shorter set times are obtained leading to a potentiation regime, meanwhile a decrease in σ_{noise} results in a depression regime. The dynamics are reversed if D is interpreted as the equilibrium point. The impact of noise on the memristor spike time has been analyzed in detail for three

different noise σ values: 160mV, 200 mV and 240 mV (points A, B, and C respectively in Fig. 4.24).

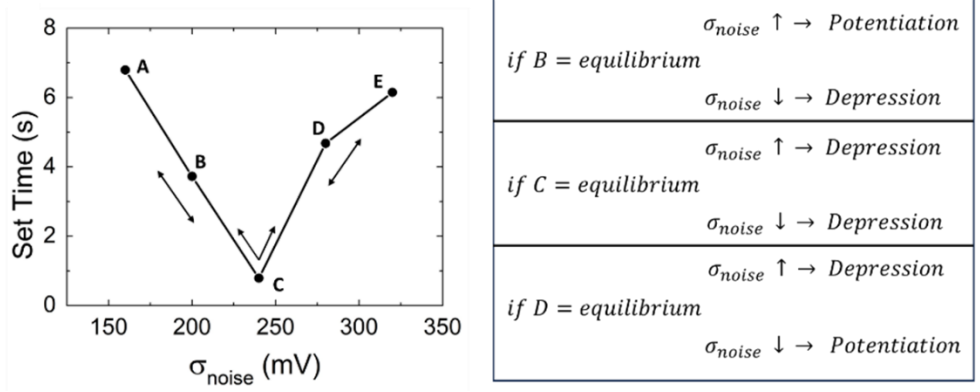


Figure 4.24. Stochastic resonance curve in the set event time against the noise σ . Schematic of homeostatic regulation possibilities for different equilibrium situations.

Fig. 4.25a shows the experimental memristor current as a function of time for $\sigma_{noise} = 160 \text{ mV}$ (red curves) and $\sigma_{noise} = 200 \text{ mV}$ (black curves). The abrupt increase in current means the occurrence of the memristor spike. A depression regime is observed, being the spike time increased by reducing σ_{noise} . On the contrary, Fig. 4.25b shows the memristor current as a function of time for the experiments with $\sigma_{noise} = 200 \text{ mV}$ (black curves) and with $\sigma_{noise} = 240 \text{ mV}$ (blue curves). Now, a potentiation regime emerges, demonstrating reduced spike time with increased noise σ . Thus, modifying the σ_{noise} , memristor spike times are modulated, thereby regulating the neuron activity to maintain homeostasis.

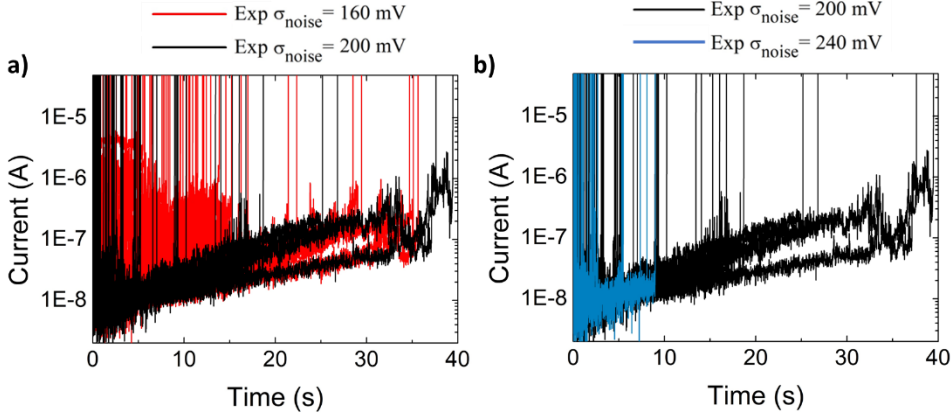


Figure 4.25. a) Experimental current versus time evolution during a staired constant voltage for $\sigma_{noise} = 160 \text{ mV}$ (black curves) and $\sigma_{noise} = 200 \text{ mV}$ (red curves). b) for $\sigma_{noise} = 200 \text{ mV}$ (black curves) and $\sigma_{noise} = 240 \text{ mV}$ (blue curves).

The previous experimental results were again compared with LTspice simulations carried out with the DMM memristor model following exactly the same process as in the previous subsection, but with different σ_{noise} values. LTspice simulated results in Fig. 4.26 are qualitatively the same as the experimental results of Fig. 4.25 observing the spike time modulation in both depression (Figs. 4.25a and 4.26a) and potentiation (Figs. 4.25b and 4.26b) regimes. This result demonstrates the suitability of the DMM for simulating the noise impact on the spike time.

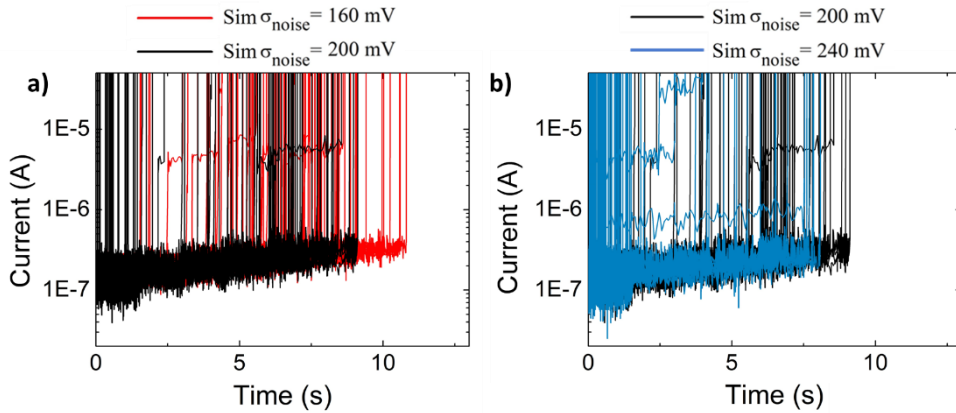


Figure 4.26. a) Simulated current versus time evolution during a staired constant voltage for $\sigma_{noise} = 160 \text{ mV}$ (black curves) and $\sigma_{noise} = 200 \text{ mV}$ (red curves). b) for $\sigma_{noise} = 200 \text{ mV}$ (black curves) and $\sigma_{noise} = 240 \text{ mV}$ (blue curves).

The work in this section presented a first experimental demonstration of noise-induced modulation of the spike time in memristor-based SNNs. The stochastic resonance phenomenon was previously observed in both memristor set and reset voltages and their respective standard deviations earlier in this chapter. The inclusion of noise can modulate the memristor spike times, thereby facilitating both potentiation and depression of neural activity, crucial for maintaining system homeostasis. The experimental results were correctly reproduced in LTspice using the DMM. The results highlight the pivotal role of noise in SNNs, thereby paving the way for further research of next generation computing systems.

4.5. Highlights

This chapter explored the findings related to the stochastic resonance phenomenon in RRAM devices. First, the effect of noise on these devices under DC regime was investigated through voltage sweeps. Then, the behavior under AC signals, including pulses and triangular waveforms, was analyzed. Additionally, the impact of stochastic resonance on the binary STDP learning protocol was examined. Finally, a noise-induced homeostasis study was carried out using memristors as neurons.

In conclusion, this chapter presents a comprehensive study of the positive impact of noise on the performance of isolated RRAM devices. While most of the results presented are experimental, the reproduction of these findings using the DMM model highlights the significance of noise. In the field of memristor-based neuromorphic systems, noise was shown to enhance performance in applications such as the STDP learning protocol and homeostasis. These findings open the door to further research, including exploring different types of memristors and materials, achieving higher frequencies in AC experiments, establishing more stable and innovative setups, and performing more complex measurements and simulations with multiple memristors to approach more realistic scenarios in artificial neural networks. This chapter included information from the following articles and complementary works: **ISCAS22**, **JLPEA24**, **TED24** and **EDL24**.

Conclusions and Future Work

Conclusions

In this thesis RRAM devices were characterized, modeled and simulated focusing on the cycle-to-cycle variability and the impact of the stochastic resonance phenomenon. Most of the findings in the thesis are reported in different publications and conference papers carried out during the thesis period.

The content of this thesis was divided into four chapters (excluding the current chapter with conclusions and future lines). Once the motivation and general objectives were exposed, the most relevant aspects discussed in each chapter are pointed out below:

An overview of the state of the art regarding RRAM devices was reported in **Chapter 1**. In that chapter it was briefly explained the general switching mechanisms of RRAM devices, their properties and applications.

The description of the measurement instruments and its combinations to build different setups for characterization, the main fabrication processes and the electrical characterization of memristors were presented in **Chapter 2**.

Chapter 3 discussed various methodologies for incorporating variability into RRAM devices simulations, a critical aspect of accurate modeling in this field:

- Uncorrelated C2C variability was included in simulations using different versions of the memdiode model: the QMM in LTspice, the DMM in LTspice and the discretized DMM in Matlab.
- Correlated C2C variability was included in simulations using the DMM in LTspice reproducing the features from experimental data.
- Several powerful tools for analyzing experimental data were introduced, such as the *fitdistrplus* package for identifying the best-fitting distributions, as well as Q-Q plots, the Lilliefors test, and others.
- Valuable methods for comparing experimental results with simulations were also provided, including density plots, the Wasserstein distance, and autocorrelation plots.

This chapter presented a comprehensive and open-source framework for modeling variability in RRAM devices, highlighting the importance of this aspect in developing robust and accurate models. By sharing all the associated methods and model scripts, this chapter not only facilitated replication but also encouraged further advancements in the field. As RRAM technology continues to evolve, the inclusion of variability in models will remain imperative for achieving reliable and predictive simulations.

An examination of the findings related to the stochastic resonance phenomenon in RRAM devices was presented in **Chapter 4**.

- The effect of noise in RRAM devices under a DC and AC regimes was investigated through voltage sweeps, pulses and triangular waveforms.
- The beneficial role of external noise was proved for DC and AC regimes enhancing the resistance ratio of the devices. The typical SR curves were obtained for both regimes.
- The positive impact of the SR phenomenon on the binary STDP learning protocol was demonstrated. By strategically introducing noise in the set pulse, the reset pulse or both simultaneously, the STDP protocol was activated via noise. In addition, the resulting resistance ratio of the devices was directly related to the overlap between pre- and post-synaptic pulses.
- A noise-induced homeostasis mechanism was explored using memristors operating as a neuron. By controlling the noise inclusion, the memristor

spike time was modulated in both directions facilitating potentiation and depression of neural activity, essential for maintaining the system homeostasis.

Summarizing, this chapter presented a thorough study of the positive impact of noise on the performance of isolated RRAM devices. While most of the results included in this chapter were experimental, the reproduction of these findings using the DMM model highlighted the significance of noise and proved the versatility of the model.

Future Work

Several potential research avenues have emerged from this thesis which are worth highlighting:

- In the modeling research line, future work could involve testing the proposed approaches for incorporating cycle-to-cycle (C2C) variability in different materials and device types. Additionally, these approaches could be further developed by increasing their complexity, such as introducing trends in the simulations or considering multivariate correlations. However, greater complexity may lead to slower and more computationally demanding simulations. Since this thesis focused on device-level variability modeling, extending the inclusion of C2C variability to systems involving multiple memristors would be a logical next step.
- For the research line related to the stochastic resonance phenomenon, the findings open the door to further research, including exploring different types of memristors and materials, higher frequency AC experiments, the development of more stable and innovative experimental setups, and conducting more complex measurements and simulations involving multiple memristors to approximate more realistic scenarios in neuromorphic systems.

References

- [Aguirre2022] F. Aguirre, J. Suñé, E. Miranda, “SPICE Implementation of the Dynamic Memdiode Model for Bipolar Resistive Switching Devices”, *Micromachines*, vol. 13, 330, 2022.
- [Aguirre2024] F. Aguirre, A. Sebastian, M. Le Gallo, et al., “Hardware implementation of memristor-based artificial neural networks,” *Nature Communications*, vol. 15, 1974, 2024.
- [Alonso2021] F.J. Alonso, D. Maldonado, A. M. Aguilera, and J. B. Roldán, “Memristor variability and stochastic physical properties modeling from a multivariate time series approach”, *Chaos, Solitons and Fractals*, vol. 143, 110461, 2021.
- [Anderson2000] J.S. Anderson, I. Lampl, D. C. Gillespie, D. Ferster, “The contribution of noise to contrast invariance of orientation tuning in cat visual cortex”, *Science*, vol. 290, 5498, 2000.
- [Arumi2023] D. Arumi, S. Manich, Á. Gómez-Pau, R. Rodríguez-Montañés, M. Gonzalez, F. Campabadal, “True Random Number Generator Based on RRAM-Bias Current Starved Ring Oscillator,” *IEEE Journal on Exploratory Solid-State Computational Devices and Circuits*, vol. 9, no. 2, pp. 92-98, 2023.
- [Aziza2020] H. Aziza, J. Postel-Pellerin, H. Bazzi, P. Canet, M. Moreau, V. Della Marca, A Harb, “True Random Number Generator Integration in a

REFERENCES

Resistive RAM Memory Array Using Input Current Limitation”, *IEEE Transactions on Nanotechnology*, vol. 19, pp. 214-222, 2020.

[Benzi1981] R. Benzi, A. Sutera and A. Vulpiani, “The mechanism of stochastic resonance”, *Journal of Physics A: Mathematical and General*, vol. 14, no. 11, L453, 1981.

[Blasco2015] J. Blasco, N. Ghenzi, J. Suñé, P. Levy, and E. Miranda, “Equivalent circuit modeling of the bistable conduction characteristics in electroformed thin dielectric films,” *Microelectronics Reliability*, vol. 55, no. 1, pp. 1–14, 2015.

[Bliss2011] T. V. Bliss, S. F. Cooke, “Long-term potentiation and long-term depression: a clinical perspective,” *Clinics (Sao Paulo)*, vol. 66, no. Suppl 1, pp. 3–17, 2011.

[Brocard2021] G. Brocard, “The LTspice XVII Simulator: Commands and Applications”, *Adolf Würth GmbH & Co. KG*, 2021.

[Brown2022] T.D. Brown, S. Kumar, R.S. Williams, “Physics-based compact modeling of electro-thermal memristors: Negative differential resistance, local activity, and non-local dynamical bifurcations,” *Applied Physics Reviews*, vol. 9, no. 1, 011308, 2022.

[Burr2017] G. W. Burr et al., “Neuromorphic computing using non-volatile memory,” *Advances in Physics: X*, vol. 2, no. 1, pp. 89–124, 2017.

[Cagli2008] C. Cagli, D. Ielmini, F. Nardi, and A. L. Lacaita, “Evidence for threshold switching in the set process of NiO-based RRAM and physical modeling for set, reset, retention and disturb prediction,” in *2008 IEEE International Electron Devices Meeting*, pp. 1–4, 2008.

[Cai2015] W. Cai, F. Ellinger, and R. Tetzlaff, “Neuronal synapse as a memristor: Modeling pair- and triplet-based STDP rule,” *IEEE Transactions on Biomedical Circuits and Systems*, vol. 9, no. 1, pp. 87–95, 2015.

[Camuñas-Mesa2020] L. A. Camuñas-Mesa, B. Linares-Barranco and T. Serrano-Gotarredona, “Implementation of a tunable spiking neuron for STDP with memristors in FDSOI 28nm,” *2nd IEEE International Conference on*

Artificial Intelligence Circuits and Systems (AICAS), Genova, Italy, pp. 94-98, 2020.

[Carboni2019] R. Carboni, D. Ielmini, “Stochastic Memory Devices for Security and Computing”, *Advanced Electronic Materials*, vol. 5, 1900198, 2019.

[Celano2016] U. Celano, “Metrology and Physical Mechanisms in New Generation Ionic Devices”, *Springer International Publishing, Cham*, 2016.

[Chae2008] S. C. Chae, J. S. Lee, S. Kim, S. B. Lee, S. H. Chang, C. Liu, B. Kahng, H. Shin, D.-W. Kim, C. U. Jung, S. Seo, M.-J. Lee, and T. W. Noh, “Random Circuit Breaker Network Model for Unipolar Resistance Switching,” *Advanced Materials*, vol. 20, pp. 1154–1159, 2008.

[Chanthbouala2016] A. Chanthbouala, V. Garcia, R.O. Cherifi, K. Bouzehouane, S. Fusil, X. Moya, S. Xavier, H. Yamada, C. Deranlot, N.D. Mathur, M. Bibes, A. Barthélémy, J. Grollier, “A ferroelectric memristor”, *Nature Materials*, vol. 11, 860–864, 2012.

[Chen2011] A. Chen and M. R. Lin, “Variability of resistive switching memories and its impact on crossbar array performance”, *IEEE International Reliability Physics Symposium*, pp. 843-846, 2011.

[Chen2015] P.-Y. Chen, S. Yu, “Compact Modeling of RRAM Devices and Its Applications in 1T1R and 1S1R Array Design,” *IEEE Transactions on Electron Devices*, vol. 62, no. 12, pp. 4022-4028, Dec. 2015.

[Cheng2010] C. H. Cheng, A. Chin, and F. S. Yeh, “Novel ultra-low power RRAM with good endurance and retention,” in *2010 Symposium on VLSI Technology, VLSIT 2010 (Digest of Technical Papers - Symposium on VLSI Technology)*, pp. 85–86, 2010.

[Christensen2022] D. V. Christensen et al., “2022 roadmap on neuromorphic computing and engineering,” *Neuromorphic Computing and Engineering*, vol. 2, 022501, 2022.

[Chua1971] L. O. Chua, “Memristor – The missing element”, *IEEE Transactions on Circuit Theory*, vol. 18, no. 5, pp. 507-519, 1971.

REFERENCES

- [Chua2019] L. Chua, G. Ch. Sirakoulis, A. Adamatzky, “*Handbook of Memristor Networks*”, Springer, 2019.
- [Cisternas2019] A. Cisternas Ferri, A. Rapoport, P.I. Fierens, G.A. Patterson, E. Miranda, J. Suñé, “On the Application of a Diffusive Memristor Compact Model to Neuromorphic Circuits,” *Materials*, vol. 12, no. 14, p. 2260, 2019.
- [Coll2019] M. Coll *et al.*, “Towards Oxide Electronics: a Roadmap,” *Applied Surface Science*, vol. 482, pp. 1–93, 2019.
- [Dai2015] Y. Dai, Y. Zhao, J. Wang, J. Xu and F. Yang, “First principle simulations on the effects of oxygen vacancy in HfO₂-based RRAM,” *AIP Advances*, vol. 5, 017133, 2015.
- [Davies2016] K. J. Davies, “Adaptive homeostasis,” *Molecular Aspects of Medicine*, vol. 49, pp. 1–7, 2016.
- [Davis2006] G. W. Davis, “Homeostatic control of neural activity: from phenomenology to molecular design,” *Annual Review of Neuroscience*, vol. 29, pp. 307–323, 2006.
- [De-Benito2019] C. de Benito, M. M. Al Chawa, M. Roca, R. Picos, S. G. Stravinides, “Self-learning perceptron using a digital memristor emulator”, *2019 8th International Conference on Modern Circuits and Systems Technologies (MOCAST)*, 2019.
- [Delignette-Muller2015] M. L. Delignette-Muller, C. Dutang, “fitdistrplus: An R package for fitting distributions”, *Journal of Statistical Software*, vol. 64, pp. 1–34, 2015.
- [Dozortsev2018] A. Dozortsev, I. Goldshtein, and S. Kvatinsky, “Analysis of the row grounding technique in a memristor-based crossbar array,” *International Journal of Circuit Theory and Applications*, vol. 46, pp. 122–137, 2018.
- [Du2015] Z. Du, D. D. Ben-Dayana Rubin, Y. Chen, L. He, T. Chen, L. Zhang, C. Wu, and O. Temam, “Neuromorphic accelerators: a comparison between neuroscience and machine-learning approaches,” in *Proceedings of the 48th International Symposium on Microarchitecture (MICRO-48)*, Association for Computing Machinery, New York, NY, USA, 2015.

- [Elgabre2012] H. Elgabre, I. A. H. Farhat, A. S. A. Hosani, D. Homouz, and B. Mohammad, “Mathematical modeling of a memristor device,” in *2012 International Conference on Innovations in Information Technology (IIT)*, Abu Dhabi, United Arab Emirates, pp. 156-161, 2012.
- [Elhamdaoui2022] M. Elhamdaoui, F. O. Rzig, K. Mbarek, et al., “Spike-time-dependent plasticity rule in memristor models for circuit design,” *Journal of Computational Electronics*, vol. 21, pp. 1038–1047, 2022.
- [Fan2017] Z. Fan, H. Fan, L. Yang, P. Li, Z. Lu, G. Tian, Z. Huang, Z. Li, J. Yao, Q. Luo, C. Chen, D. Chen, Z. Yan, M. Zeng, X. Lu, X. Gao, J.-M. Liu, “Resistive switching induced by charge trapping/detrapping: a unified mechanism for colossal electroresistance in certain Nb:SrTiO₃-based heterojunctions,” *Journal of Materials Chemistry C*, vol. 5, pp. 7317–7327, 2017.
- [Fujiwara2008] K. Fujiwara, T. Nemoto, M. J. Rozenberg, Y. Nakamura, and H. Takagi. “Resistance Switching and Formation of a Conductive Bridge in Metal/Binary Oxide/Metal Structure for Memory Devices.” *Japanese Journal of Applied Physics*, vol. 47, no. 8R, 6266, 2008.
- [Garcia-Redondo2017] F. García-Redondo, M. López-Vallejo, C. L. Barrio, “Advanced integration of variability and degradation in RRAM SPICE compact models,” *2017 14th International Conference on Synthesis, Modeling, Analysis and Simulation Methods and Applications to Circuit Design (SMACD)*, pp. 1-4, 2017.
- [Gardiner2004] C. Gardiner, “Handbook of Stochastic Methods”, *Springer Series in Synergetics*, vol. 13, 2004.
- [Gentle1998] J. E. Gentle, “Random Number Generation and Monte Carlo Methods”, *Statistics and Computing*, 1998.
- [Gerstner1993] W. Gerstner, R. Ritz, J. L. Hemmen. “Why spikes? Hebbian learning and retrieval of time-resolved excitation patterns,” *Biological Cybernetics*, vol. 69, pp. 503–515, 1993.
- [González2019] M. B. González, J. Martín-Martínez, M. Maestro-Izquierdo, M. C. Acero, M. Nafria, and F. Campabadal, “Investigation of Filamentary Current Fluctuations Features in the High-Resistance State of Ni/HfO₂-Based

REFERENCES

RRAM”, *IEEE Transactions on Electron Devices*, vol. 63, no. 8, pp. 3116-3122, 2016.

[Gonzalez-Cordero2016] G. González-Cordero et al., “A new compact model for bipolar RRAMs based on truncated-cone conductive filaments-a Verilog-A approach”, *Semiconductor Science and Technology*, vol. 31, 115013, 2016.

[Gopal2015] B. G. Gopal, “ImPLY Logic Implementation of Carry Save Adder Using Memristors,” *International Journal of Engineering Research and Applications*, vol. 5, pp. 2248–9622, 2015.

[Guan2012] X. Guan, S. Yu, H.-S. P. Wong, “A SPICE Compact Model of Metal Oxide Resistive Switching Memory With Variations,” *IEEE Electron Device Letters*, vol. 33, no. 10, pp. 1405-1407, Oct. 2012.

[Harmer2002] G.P. Harmer, B. R. Davis, D. Abbot, “A review of stochastic resonance: circuits and measurement”, *IEEE Transactions on Instrumentation and Measurements*, vol. 31, no. 2, pp. 299-309, 2002.

[Harnack2015] D. Harnack, M. Pelko, A. Chaillet, Y. Chitour, and M. C. van Rossum, “Stability of Neuronal Networks with Homeostatic Regulation,” *PLOS Computational Biology*, vol. 11, no. 7, e1004357, 2015.

[Huang2023] L. Huang and A. Mosleh, “A Physics of Failure, Kinetic Simulation Model for Reliability of RRAM,” in *2023 Annual Reliability and Maintainability Symposium (RAMS)*, Orlando, FL, USA, pp. 1-6, 2023.

[Hickmott1962] T. W. Hickmott, "Low-Frequency Negative Resistance in Thin Anodic Oxide Films," *Journal of Applied Physics*, vol. 33, no. 9, pp. 2669–2682, 1962.

[Hui2017] F. Hui, E. Grustan-Gutierrez, S. Long, Q. Liu, A. K. Ott, A. C. Ferrari, M. Lanza,” Graphene and Related Materials for Resistive Random Access Memories”, *Advanced Electronic Materials*, vol. 3, 1600195, 2017.

[Ielmini2011] D. Ielmini, “Modeling the universal set/reset characteristics of bipolar RRAM by field- and temperature-driven filament growth,” *IEEE Trans. Electron Devices*, vol. 58, no. 12, 4309–4317, 2011.

- [Ielmini2012] D. Ielmini, F. Nardi, and S. Balatti, “Evidence for voltage-driven set/reset processes in bipolar switching RRAM,” *IEEE Transactions on Electron Devices*, vol. 59, no. 8, pp. 2049–2056, 2012.
- [Ielmini2017] D. Ielmini and V. Milo, “Physics-based modeling approaches of resistive switching devices for memory and in-memory computing applications,” *Journal of Computational Electronics*, vol. 16, pp. 1121–1143, 2017.
- [Ielmini2018] D. Ielmini, S. H. P. Wong, “In-memory computing with resistive switching devices”, *Nature Electronics*, vol. 1, pp. 333–343, 2018.
- [Im2020] I. H. Im, S. J. Kim, H. W. Jang, “Memristive Devices for New Computing Paradigms”. *Advanced Intelligent Systems*, vol. 2, no. 11, 2000105, 2020.
- [Inoue2008] I. H. Inoue, S. Yasuda, H. Akinaga, and H. Takagi, “Nonpolar resistance switching of metal/binary-transition-metal oxides/metal sandwiches: Homogeneous/inhomogeneous transition of current distribution,” *Physical Review B*, vol. 77, no. 3, pp. 035105, 2008.
- [Jeong2010] H. Y. Jeong, J. Y. Kim, J. W. Kim, J. O. Hwang, J.-E. Kim, J. Y. Lee, T. H. Yoon, B. J. Cho, S. O. Kim, R. S. Ruoff, and S.-Y. Choi, “Graphene oxide thin films for flexible nonvolatile memory applications,” *Nano Letters*, vol. 10, no. 11, pp. 4381–4386, 2010.
- [Jeong2011] D. S. Jeong, B. Cheong, and H. Kohlstedt, “Pt/Ti/Al₂O₃/Al tunnel junctions exhibiting electroforming-free bipolar resistive switching behavior,” *Solid-State Electronics*, vol. 63, no. 1, pp. 1–4, 2011.
- [Jiang2014] Z. Jiang, S. Yu, Y. Wu, J.H. Engel, H.-S.P. Wong, “Verilog-a compact model for oxide-based resistive random access memory (RRAM),” in *International Conference on Simulation of Semiconductor Processes and Devices (SISPAD)*, pp. 41–44, 2014.
- [Jiang2016] H. Jiang, D.A. Stewart, “Enhanced oxygen vacancy diffusion in Ta₂O₅ resistive memory devices due to infinitely adaptive crystal structure,” *Journal of Applied Physics*, vol. 119, 134502, 2016.

REFERENCES

- [Joglekar2009] Y. N. Joglekar, S. J. Wolf, “The elusive memristor: properties of basic electrical circuits,” *European Journal of Physics*, vol. 30, no. 4, p. 661, May 2009.
- [Karpov2016] V. Karpov, D. Niraula, I. Karpov, “Thermodynamic analysis of conductive filaments”, *Applied Physics Letters*, vol. 109, pp. 1–5, 2016.
- [Kasai2014] S. Kasai, “Stochastic resonance and related phenomena in nonlinear electron nanodevices”, *IEEE International Nanoelectronics Conference (INEC)*, 2014.
- [Kim2012] H. Kim, M. P. Sah, C. Yang, T. Roska and L. O. Chua, “Neural Synaptic Weighting With a Pulse-Based Memristor Circuit,” *IEEE Transactions on Circuits and Systems I: Regular Papers*, vol. 59, no. 1, pp. 148–158, Jan. 2012.
- [Koeberl2013] P. Koeberl, Ü. Kocabaş and A. -R. Sadeghi, “Memristor PUFs: A new generation of memory-based Physically Unclonable Functions,” *2013 Design, Automation & Test in Europe Conference & Exhibition (DATE)*, Grenoble, France, 2013
- [Kozicki2016] M. N. Kozicki and H. J. Barnaby, “Conductive bridging random access memory—materials, devices and applications,” *Semiconductor Science and Technology*, vol. 31, no. 11, 113001, 2016.
- [Krauss2017] P. Krauss, M. Schilling, S. Schulz, and K. Tziridis, “Adaptive stochastic resonance for unknown and variable input signals,” *Scientific Reports*, vol. 7, 2450, 2017.
- [Lanza2019] M. Lanza et al., “Recommended Methods to Study Resistive Switching Devices”, *Advanced Electronic Materials*, vol. 5, 1800143, 2019.
- [Lanza2021] M. Lanza et al., “Standards for the Characterization of Endurance in Resistive Switching Devices,” *ACS Nano*, vol. 15, no. 11, pp. 17214–17231, 2021.
- [Larcher2012] L. Larcher, A. Padovani, O. Pirrotta, L. Vandelli, G. Bersuker, “Microscopic understanding and modeling of HfO₂ RRAM device physics,” *IEDM Technical Digest*, pp. 474–477, 2012.

- [Larcher2014] L. Larcher, F.M. Puglisi, P. Pavan, A. Padovani, L. Vandelli, G. Bersuker, “A compact model of program window in HfOx RRAM devices for conductive filament characteristics analysis,” *IEEE Transactions on Electron Devices*, vol. 61, no. 8, pp. 2668–2673, 2014.
- [Larentis2012] S. Larentis, F. Nardi, S. Balatti, D.C. Gilmer, D. Ielmini, “Resistive switching by voltage-driven ion migration in bipolar RRAM—Part II: Modelling,” *IEEE Transactions on Electron Devices*, vol. 59, no. 9, pp. 2468–2475, 2012.
- [Lee2011] M. J. Lee, C. B. Lee, D. Lee, S. R. Lee, M. Chang, J. H. Hur, Y. B. Kim, C. J. Kim, D. H. Seo, S. Seo, U. I. Chung, I. K. Yoo, and K. Kim, “A fast, high-endurance and scalable non-volatile memory device made from asymmetric Ta₂O_(5-x)/TaO_(2-x) bilayer structures,” *Nature Materials*, vol. 10, no. 8, pp. 625–630, 2011.
- [Lee2015] J. S. Lee S. Lee, and T. W. Noh, “Resistive switching phenomena: A review of statistical physics approaches”. *Applied Physics Reviews*, vol. 2, no. 3, 031303, 2015.
- [Lee2020] S.H. Lee, X. Zhu, W. D. Lu, “Nanoscale resistive switching devices for memory and computing applications”, *Nano Research*, vol. 13, pp. 1228–1243, 2020.
- [Li2014] H. Li, P. Huang, B. Gao, B. Chen, X. Liu, J. Kang, “A SPICE model of resistive random access memory for large-scale memory array simulation,” *IEEE Electron Device Letters*, vol. 35, no. 2, pp. 211–213, 2014.
- [Li2015] H. Li et al., “Variation-aware, reliability-emphasized design and optimization of RRAM using spice model”, *2015 Design, Automation Test in Europe Conf. Exhibition*, pp. 1425–1430, 2015.
- [Li2021] X. Li, T. Zanotti, T. Wang, K. Zhu, F. M. Puglisi, and M. Lanza, “Random Telegraph Noise in Metal-Oxide Memristors for True Random Number Generators: A Materials Study,” *Advanced Functional Materials*, vol. 31, 2102172, 2021.

REFERENCES

- [Lilliefors1967] H. W. Lilliefors, “On the Kolmogorov-Smirnov Test for Normality with Mean and Variance Unknown”, *Journal of the American Statistical Association*, vol. 62, no. 318, 1967.
- [Linares-Barranco2009] B. Linares-Barranco, T. Serrano-Gotarredona, “Memristance can explain spike-time-dependent-plasticity in neural synapses,” *Nature Precedings*, 2009.
- [Linn2014] E. Linn, A. Siemon, R. Waser, S. Menzel, “Applicability of Well-Established Memristive Models for Simulations of Resistive Switching Devices,” *IEEE Transactions on Circuits and Systems I: Regular Papers*, vol. 61, no. 8, pp. 2402–2410, Aug. 2014.
- [Longtin1997] A. Longtin, “Autonomous stochastic resonance in bursting neurons”, *Physical Review E*, vol. 55, no. 1, pp. 868–876, 1997.
- [Lv2021] S. Lv, J. Liu, and Z. Geng, “Application of Memristors in Hardware Security: A Current State-of-the-Art Technology,” *Advanced Intelligent Systems*, vol. 3, 2000127, 2021.
- [Ma2023] G. Ma, M. Man, Y. Zhang, and S. Liu, “A Fast Homeostatic Inhibitory Plasticity Rule Circuit with a Memristive Synapse,” *Electronics*, vol. 12, no. 3, 490, 2023.
- [Maestro-Izquierdo2019] M. Maestro-Izquierdo, F.J. Romero, P. Solis-Fernandez, A. Fernandez, E. Perez, F. Jimenez-Molinos, J.B. Roldán, “Experimental Verification of Memristor-Based Material Implication NAND Operation,” *IEEE Transactions on Emerging Topics in Computing*, vol. 7, no. 4, pp. 545–552, 2019.
- [Maestro-Izquierdo2020] M. Maestro-Izquierdo, M. B. González, F. Jiménez-Molinos, E. Moreno, J. B. Roldán, F. Campabadal, “Unipolar resistive switching behavior in Al₂O₃/HfO₂ multilayer dielectric stacks: Fabrication, characterization and simulation,” *Nanotechnology*, vol. 31, no. 13, 135202, 2020.
- [Maldonado2021] D. Maldonado, F. Aguirre, G. González-Cordero, A. M. Roldán, M. B. González, F. Jiménez-Molinos, F. Campabadal, E. Miranda, J. B. Roldán, “Experimental study of the series resistance effect and its impact on

the compact modeling of the conduction characteristics of HfO₂-based resistive switching memories”, *Journal of Applied Physics*, vol. 130, no. 5, 054503, 2021.

[Maldonado2022] D. Maldonado, F. Jiménez–Molinos, J. B. Roldán, M. B. González and F. Campabadal, “An enhanced Verilog-A compact model for bipolar RRAMs including transient thermal effects and series resistance,” *2022 37th Conference on Design of Circuits and Integrated Circuits (DCIS)*, Pamplona, Spain, 2022.

[Maldonado2023] D. Maldonado, A. Cantudo, E. Perez, R. Romero-Zaliz, E. Perez-Bosch Quesada, M. K. Mahadevaiah, F. Jimenez-Molinos, C. Wenger, J. B. Roldán, “TiN/Ti/HfO₂/TiN Memristive Devices for Neuromorphic Computing: From Synaptic Plasticity to Stochastic Resonance,” *Frontiers in Neuroscience*, vol. 17, 1271956, 2023.

[Matveyev2016] Y. Matveyev, R. Kirtaev, A. Fetisova, S. Zakharchenko, D. Negrov, A. Zenkevich, “Crossbar nanoscale HfO₂-based electronic synapses,” *Nanoscale Research Letters*, vol. 11, 147, 2016.

[McCulloch1943] W. S. McCulloch and W. Pitts, “A logical calculus of the ideas immanent in neurons activity,” *Bulletin of Mathematical Biophysics*, vol. 5, pp. 115–133, 1943.

[McDonnell2009] M. D. McDonnell, D. Abbott, “What Is Stochastic Resonance? Definitions, Misconceptions, Debates, and Its Relevance to Biology,” *PLOS Computational Biology*, vol. 5, no. 5, e1000348, 2009.

[McPherson2012] J.W. McPherson, “Time dependent dielectric breakdown physics – Models revisited,” *Microelectronics Reliability*, vol. 52, no. 9–10, pp. 1753–1760, 2012.

[Mikhaylov2021] A.N. Mikhaylov, D.V. Guseinov, A.I. Belov, D.S. Korolev, V.A. Shishmakova, M.N. Koryazhkina, D.O. Filatov, O.N. Gorshkov, D. Maldonado, F.J. Alonso, J.B. Roldan, A.V. Krichigin, N. V. Agudov, A.A. Dubkov, A. Carollo, B. Spagnolo, “Stochastic resonance in a metal-oxide memristive device”, *Chaos, Solitons & Fractals*, vol. 144, 110723, 2021.

REFERENCES

- [Miranda2015] E. Miranda, “Compact Model for the Major and Minor Hysteretic I–V Loops in Nonlinear Memristive Devices”, *IEEE Transactions Nanotechnology*, vol. 14, 787–789, 2015.
- [Miranda2020] E. Miranda, J. Suñé, “Memristive State Equation for Bipolar Resistive Switching Devices Based on a Dynamic Balance Model and its Equivalent Circuit Representation”, *IEEE Transactions Nanotechnology*, vol. 19, pp. 837–840, 2020.
- [Miranda2023] E. Miranda *et al.*, “Simulation of Bipolar-Type Resistive Switching Devices Using a Recursive Approach to the Dynamic Memdiode Model,” *IEEE Electron Device Letters*, vol. 44, no. 9, pp. 1551–1554, 2023.
- [Mladenov2024] V. Mladenov and S. Kirilov, “A Memristor Neural Network Based on Simple Logarithmic-Sigmoidal Transfer Function with MOS Transistors,” *Electronics*, vol. 13, p. 893, 2024.
- [Mohammad2016] B. Mohammad, M. Abi Jaoudé, V. Kumar, D.M. Al Homouz, H.A. Nahla, M. Al-Qutayri, N. Christoforou, "State of the Art of Metal Oxide Memristor Devices," *Nanotechnology Reviews*, vol. 5, no. 3, pp. 311–329, 2016.
- [Mohan2021] C. Mohan, L. A. Camuñas-Mesa, J. M. de la Rosa, T. Serrano-Gotarredona, B. Linares-Barranco, “Implementation of Binary Stochastic STDP Learning Using Chalcogenide-Based Memristive Devices,” in *2021 IEEE International Symposium on Circuits and Systems (ISCAS)*, 2021.
- [Naprstek2017] J. Naprstek and C. Fischer, “Stochastic resonance and related topics,” in *Resonance, InTech*, Nov. 2017.
- [Ntinas2019] V. Ntinas, A. Rubio, G. Ch. Sirakoulis, R. Rodriguez, M. Nafria, “Experimental Investigation of Memristance Enhancement”, *IEEE/ACM International Symposium on Nanoscale Architectures (NANOARCH)*, 2019.
- [Ntinas2021] V. Ntinas, A. Rubio, G. Ch. Sirakoulis, E. Salvador, M. Pedro, A. Crespo-Yepes, J. Martin-Martinez, R. Rodriguez, M. Nafria, “Power-Efficient Noise-Induced Reduction of ReRAM Cell’s Temporal Variability Effects”, *IEEE Transactions on Circuits and Systems II: Express Briefs*, vol. 68, no. 4, pp. 1378–1382, 2021.

- [Ogban2007] F. Ogban, I. Arikpo, and I. Eteng, “Von Neumann Architecture and Modern Computers,” *Global Journal of Mathematical Sciences*, vol. 6, no. 2, p. 97, 2007.
- [Onofrio2015] N. Onofrio, D. Guzman, A. Strachan, “Atomic origin of ultrafast resistance switching in nanoscale electrometallization cells,” *Nature Materials*, vol. 14, no. 4, pp. 440–446, 2015.
- [Ostrovskii2022] V. Ostrovskii, P. Fedoseev, Y. Bobrova, D. Butusov, “Structural and parametric identification of Known memristors”. *Nanomaterials*, vol. 12, 63, 2022.
- [Padovani2015] A. Padovani, L. Larcher, O. Pirrotta, L. Vandelli and G. Bersuker, “Microscopic Modeling of HfOx RRAM Operations: From Forming to Switching,” *IEEE Transactions on Electron Devices*, vol. 62, no. 6, pp. 1998–2006, 2015.
- [Pal2020] S. Pal, S. Bose, W.-H. Ki, and A. Islam, “Reliable write assist low power SRAM cell for wireless sensor network applications,” *IET Circuits, Devices & Systems*, vol. 14, no. 2, pp. 162–169, 2020.
- [Panda2018] D. Panda, P.P. Sahu, T.Y. Tseng, “A Collective Study on Modeling and Simulation of Resistive Random Access Memory,” *Nanoscale Res. Lett.*, vol. 13, no. 8, 2018.
- [Patterson2013] G. A. Patterson, P. I. Fierens, D. F. Grosz, “On the beneficial role of noise in resistive switching”, *Applied Physics Letters*, vol. 103, 074102, 2013.
- [Pedretti2018] G. Pedretti, V. Milo, S. Ambrogio, R. Carboni, S. Bianchi, A. Calderoni, N. Ramaswamy, A. S. Spinelli, D. Ielmini, “Stochastic learning in neuromorphic hardware via spike timing dependent plasticity with RRAM synapses”, *IEEE Journal on Emerging and Selected Topics in Circuits and Systems*, vol. 8, pp. 77-85, 2018.
- [Perez2019] E. Pérez, D. Maldonado, C. Acal, J. E. Ruiz-Castro, F. J. Alonso, A. M. Aguilera, F. Jiménez-Molinos, Ch. Wenger, and J. B. Roldán, “Analysis of the statistics of device-to-device and cycle-to-cycle variability in

REFERENCES

TiN/Ti/Al:HfO₂/TiN RRAMs,” *Microelectronic Engineering*, vol. 214, pp. 104–109, 2019.

[Perrinet2010] L. U. Perrinet, “Role of homeostasis in learning sparse representations,” *Neural Computation*, vol. 22, no. 7, pp. 1812–1836, 2010.

[Piccolboni2016] G. Piccolboni et al., “Investigation of Cycle-to-Cycle Variability in HfO₂-Based OxRAM”, *IEEE Electron Device Letters*, vol. 37, pp. 721–723, 2016.

[Poblador2018] S. Poblador, M. Gonzalez, and F. Campabadal, “Investigation of the multilevel capability of TiN–Ti–HfO₂–W resistive switching devices by sweep and pulse programming”, *Microelectronic Engineering*, vol. 187, pp. 148–153, 2018.

[Poblador2021] S. Poblador, ‘Diseño, fabricación y caracterización de dispositivos de conmutación resistiva basados en estructuras TiN/Ti/HfO₂/W’, PhD Thesis, Universitat Autònoma de Barcelona, 2021.

[Querlioz2011] D. Querlioz, O. Bichler, and C. Gamrat, “Simulation of a memristor-based spiking neural network immune to device variations,” *2011 International Joint Conference on Neural Networks (IJCNN)*, pp. 1775–1781, 2011.

[Querlioz2013] D. Querlioz, O. Bichler, P. Dollfus, and C. Gamrat, “Immunity to Device Variations in a Spiking Neural Network with Memristive Nanodevices,” *IEEE Transactions on Nanotechnology*, vol. 12, no. 3, pp. 288–295, 2013.

[Rahma2019] F. Rahma, S. Muneam, “Memristive nonlinear electronic circuits: dynamics, synchronization and applications”, *Springer*, 2019.

[Reuben2020] J. Reuben, M. Biglari, D. Fey, “Incorporating Variability of Resistive RAM in Circuit Simulations Using the Stanford–PKU Model”, *IEEE Transactions on Nanotechnology*, vol. 19, pp. 508–518, 2020.

[Rodriguez-Fernandez2017] A. Rodriguez-Fernandez, C. Cagli, L. Perniola, J. Suñé, E. Miranda, “Effect of the voltage ramp rate on the set and reset voltages of ReRAM devices”. *Microelectronic Engineering*, vol. 178, pp. 61–65, 2017.

- [Roldán2023] J. B. Roldán et al., “Variability in resistive memories”, *Advanced Intelligent Systems*, vol. 5, 2200338, 2023.
- [Roldán2023b] J.B. Roldán, D. Maldonado, C. Aguilera-Pedregosa, F.J. Alonso, Y. Xiao, Y. Shen, W. Zheng, Y. Yuan, M. Lanza, “Modeling the Variability of Au/Ti/h-BN/Au Memristive Devices,” *IEEE Transactions on Electron Devices*, vol. 70, no. 4, pp. 1533–1539, 2023.
- [Roldán2024] J. B. Roldán, A. Cantudo, J. J. Torres, D. García, M. López-García, and P. Fernández, “Stochastic resonance in 2D materials based memristors,” *npj 2D Materials and Applications*, vol. 8, no. 7, pp. 1–9, 2024.
- [Saltelli2004] A. Saltelli S. Tarantola, F. Campolongo, and M. Ratto, “Sensitivity Analysis in Practice”, *John Wiley & Sons, Ltd*, 2004.
- [Saltelli2008] A. Saltelli, M. Ratto, T. Andres, F. Campolongo, J. Cariboni, D. Gatelli, M. Saisana and S. Tarantola, “Global Sensitivity Analysis. The Primer”, *John Wiley & Sons, Ltd*, 2008.
- [Sawa2004] A. Sawa, T. Fujii, M. Kawasaki, and Y. Tokura, “Nanoscale resistive switching in SrTiO₃ thin films,” *Applied Physics Letters*, vol. 85, pp. 4073, 2004.
- [Seo2004] S. Seo, M. J. Lee, D. H. Seo, E. J. Jeoung, D.-S. Suh, Y. S. Joung, I. K. Yoo, I. R. Hwang, S. H. Kim, I. S. Byun, J.-S. Kim, J. S. Choi, and B. H. Park, “Reproducible resistance switching in polycrystalline NiO films,” *Applied Physics Letters*, vol. 85, no. 23, pp. 5655–5657, 2004.
- [Seo2011] K. Seo, I. Kim, S. Jung, M. Jo, S. Park, J. Park, et al., “Analog memory and spike-timing-dependent plasticity characteristics of a nanoscale titanium oxide bilayer resistive switching device,” *Nanotechnology*, vol. 22, 254023, 2011.
- [Shao2022] Z. Shao, R. Zhao, S. Yuan, M. Ding, and Y. Wang, “Tracing the evolution of AI in the past decade and forecasting the emerging trends,” *Expert Systems With Applications*, vol. 209, 118221, 2022.
- [Shen2020] Z. Shen, C. Zhao, Y. Qi, et al., “Advances of RRAM Devices: Resistive Switching Mechanisms, Materials and Bionic Synaptic Application,” *Nanomaterials (Basel)*, vol. 10, no. 8, 1437, 2020.

REFERENCES

- [Shi2018] X. Shi, Z. Zeng, L. Yang, and Y. Huang, “Memristor-Based Circuit Design for Neuron with Homeostatic Plasticity,” *IEEE Transactions on Emerging Topics in Computational Intelligence*, vol. 2, no. 5, pp. 359–370, 2018.
- [Shuai2018] Y. Shuai, X. Pan, and X. Sun, “Spike-Timing-Dependent Plasticity in Memristors”, *Memristor and Memristive Neural Networks*, *InTech*, Apr. 2018.
- [Singh2019] J. Singh, B. Raj, “An accurate and generic window function for nonlinear memristor models”, *Journal of Computational Electronics*, vol. 18, pp. 640–647, 2019.
- [Snider2007] G.S. Snider, “Self-organized computation with unreliable, memristive nanodevices,” *Nanotechnology*, vol. 18, no. 36, 365202, 2007.
- [Stotland2012] A. Stotland, M. Di Ventra, “Stochastic memory: Memory enhancement due to noise”, *Physical Review E*, vol. 85, 011116, 2012.
- [Strukov2008] D. Strukov, G. Snider, D. Stewart, et al., “The missing memristor found,” *Nature*, vol. 453, pp. 80–83, 2008.
- [Su2022] K. Su, et al., “Design of Memristor-based XOR Logic Gate and Half Adder,” *Journal of Physics: Conference Series*, 2221 012001, 2022.
- [Sun2022] J. Sun, J. Han, and Y. Wang, “Memristor-Based Neural Network Circuit of Memory with Emotional Homeostasis,” *IEEE Transactions on Nanotechnology*, vol. 21, pp. 204–212, 2022.
- [Tetzlaff2004] R. Tetzlaff, “*Memristors and Memristive Systems*”, *Springer*, 2014.
- [Tien2018] N. W. Tien, D. Kerschensteiner, “Homeostatic plasticity in neural development,” *Neural Development*, vol. 13, no. 9, 2018.
- [Uhlenbeck1930] G. E. Uhlenbeck, L. S. Ornstein, “On the theory of Brownian Motion”, *Physical Review*, vol. 36, no. 5, pp. 823–841, 1930.
- [Vaidyanathan2024] S. Vaidyanathan and C. Volos, “*Advances in Memristors, Memristive Devices, and Systems*. Springer,” 2017.

- [Valov2011] I. Valov, R. Waser, J. R. Jameson, and M. N. Kozicki, “Electrochemical metallization memories—fundamentals, applications, prospects,” *Nanotechnology*, vol. 22, no. 25, 254003, 2011.
- [Vergara2019] R. C. Vergara, S. Jaramillo-Riveri, A. Luarte, C. Moënné-Loccoz, R. Fuentes, A. Couve, and P. E. Maldonado, “The Energy Homeostasis Principle: Neuronal Energy Regulation Drives Local Network Dynamics Generating Behavior,” *Frontiers in Computational Neuroscience*, vol. 13, 2019.
- [Villani2009] C. Villani, "Optimal transport", *Grundlehren der Mathematischen Wissenschaften [Fundamental Principles of Mathematical Sciences]*, vol. 338, 2009.
- [Villena2017] M.A. Villena, J.B. Roldán, F. Jiménez-Molinos, E. Miranda, J. Suñé, M. Lanza, “SIM2RRAM: a physical model for RRAM devices simulation,” *Journal of Computational Electronics*, vol. 16, no. 4, pp. 1095–1120, Dec. 2017.
- [Wang2012] Z. Q. Wang, H. Y. Xu, X. H. Li, H. Yu, Y. C. Liu, X. J. Zhu, “Synaptic learning and memory functions achieved using oxygen ion migration/diffusion in an amorphous InGaZnO memristor,” *Advanced Functional Materials*, vol. 22, pp. 2759–2765, 2012.
- [Wang2016] L. Wang et al., “Long-Term Homeostatic Properties Complementary to Hebbian Rules in CuPc-Based Multifunctional Memristor,” *Scientific Reports*, vol. 6, 35273, 2016.
- [Wang2022] Y. Wang, X. Xu, E. Wang, X. Zhang, Z. Wu, R. Gu, Q. Li, and Q. Liu, “A Configurable Artificial Neuron Based on a Threshold-Tunable TiN/NbO_x/Pt Memristor,” *IEEE Electron Device Letters*, vol. 43, no. 4, pp. 631-634, 2022.
- [Wang2023] C. Wang, G. Shi, F. Qiao, R. Lin, S. Wu, and Z. Hu, “Research progress in architecture and application of RRAM with computing-in-memory,” *Nanoscale Advances*, vol. 5, no. 6, pp. 1559–1573, 2023.
- [Wang2023] S. Wang, L. Song, W. Chen, G. Wang, E. Hao, C. Li, Y. Hu, Y. Pan, A. Nathan, G. Hu, S. Gao, “Memristor-Based Intelligent Human-Like Neural Computing,” *Advanced Electronic Materials*, vol. 9, 2200877, 2023.

REFERENCES

- [Waser2007] R. Waser, M. Aono, “Nanoionics-based resistive switching memories”, *Nature Materials*, vol. 6, pp. 833–840, 2007.
- [Wiesenfeld1995] K. Wiesenfeld, F. Moss,” Stochastic resonance and the benefits of noise: from ice ages to crayfish and SQUIDS”, *Nature*, vol. 373, pp. 33–36, 1995.
- [Wong2012] H.-S. P. Wong, L. Lai, M. Yang, M. R. Stan, P. D. Ye, and A. A. Tseng, “Metal–oxide RRAM,” *Proc. IEEE*, vol. 100, no. 6, pp. 1951–1970, 2012.
- [Wouters2015] D.J. Wouters, R. Waser, M. Wuttig, “Phase-Change and Redox-Based Resistive Switching Memories,” *Proc. IEEE*, vol. 103, no. 8, pp. 1274–1288, 2015.
- [Wouters2019] D.J. Wouters, S. Menzel, J.A.J. Rupp, T. Hennen, R. Waser, “On the universality of the I–V switching characteristics in non-volatile and volatile resistive switching oxides”, *Faraday Discuss*, vol. 213, pp. 183–196, 2019.
- [Wu2011] W. Wu, Z.L. Wang, “Piezotronic Nanowire-Based Resistive Switches As Programmable Electromechanical Memories,” *Nano Letters*, vol. 11, no. 7, pp. 2779–2785, 2011.
- [Yang2013] J. J. Yang, D. B. Strukov, and D. R. Stewart, “Memristive devices for computing,” *Nature Nanotechnology*, vol. 8, no. 1, pp. 13–24, 2013.
- [Yang2021] G. Yang, D. Yu, S. Jia, X. Cui, and Y. Wang, “A Homeostasis-based Enhanced Training Method in Spiking Neural Networks for Pattern Recognition,” *2021 China Semiconductor Technology International Conference (CSTIC)*, pp. 1-3, 2021.
- [Ye2022] L. Ye, Z. Gao, J. Fu, W. Ren, C. Yang, J. Wen, X. Wan, Q. Ren, S. Gu, X. Liu, X. Lian, and L. Wang, “Overview of Memristor-Based Neural Network Design and Applications,” *Frontiers in Physics*, vol. 10, 839243, 2022.
- [Yu2011] S. Yu, X. Guan, H.-S.P. Wong, “On the stochastic nature of resistive switching in metal oxide RRAM: physical modeling, Monte Carlo simulation, and experimental characterization,” *IEDM Technical Digest*, pp. 413–416, 2011.

- [Yu2016] S. Yu and P. Y. Chen, “Emerging Memory Technologies: Recent Trends and Prospects”, *IEEE Solid State Circuits Magazine*, vol. 8, no. 2, pp. 43-56, 2016.
- [Yuan2019] G. Yuan, X. Ma, C. Ding, S. Lin, T. Zhang, Z. S. Jalali, Y. Zhao, L. Jiang, S. Soundarajan, and Y. Wang, “An Ultra-Efficient Memristor-Based DNN Framework with Structured Weight Pruning and Quantization Using ADMM,” in *2019 IEEE/ACM International Symposium on Low Power Electronics and Design (ISLPED)*, 2019.
- [Zahoor2020] F. Zahoor, T. Z. Azni Zulkifli, and F. A. Khanday, “Resistive random access memory (RRAM): an overview of materials, switching mechanism, performance, multilevel cell (MLC) storage, modeling, and applications,” *Nanoscale Research Letters*, vol. 15, no. 90, pp. 1–26, 2020.
- [Zamarreno-Ramos2011] C. Zamarreno-Ramos et al., “On spike-timing-dependent-plasticity, memristive devices, and building a self-learning visual cortex,” *Frontiers in Neuroscience*, vol. 5, no. 26, 2011.
- [Zhang2023] Z. Zhang, C. Li, W. Zhang, J. Zhou, and G. Liu, “An FPGA-based memristor emulator for artificial neural network,” *Microelectronics Journal*, vol. 131, 105639, 2023.
- [Zheng2015] L. Zheng, S. Shin and S. M. S. Kang, “Memristor-based synapses and neurons for neuromorphic computing,” *2015 IEEE International Symposium on Circuits and Systems (ISCAS)*, Lisbon, Portugal, pp. 1150-1153, 2015.

REFERENCES

Articles in this Ph.D. Thesis

Article SSE21

*SPICE modeling of cycle-to-cycle variability in
RRAM devices*

E. Salvador, M.B. Gonzalez, F. Campabadal, J. Martin-
Martinez, R. Rodriguez, E. Miranda



Contents lists available at ScienceDirect

Solid State Electronics

journal homepage: www.elsevier.com/locate/sse

SPICE modeling of cycle-to-cycle variability in RRAM devices

E. Salvador^{a,*}, M.B. Gonzalez^b, F. Campabadal^b, J. Martin-Martinez^a, R. Rodriguez^a, E. Miranda^a^a Departament d'Enginyeria Electrònica, Universitat Autònoma de Barcelona, 08193 Cerdanyola del Valles, Spain^b Institut de Microelectrònica de Barcelona, IMB-CNM, CSIC, 08193 Cerdanyola del Valles, Spain

ARTICLE INFO

Keywords:
 RRAM
 Variability
 Modeling
 LTSpice
 Fittidistrplus

ABSTRACT

In this work, we investigated how to include uncorrelated cycle-to-cycle (C2C) variability in the LTSpice quasi-static memdiode model for RRAM devices. Variability in the I - V curves is first addressed through an in-depth study of the experimental data using the *fittidistrplus* package for the R language. This provides a first approximation to the identification of the most suitable model parameter distributions. Next, the selected candidate distributions are incorporated into the model script and used for carrying out Monte Carlo simulations. Finally, the experimental and simulated observables (set and reset currents, transition voltages, etc.) are statistically compared and the model estimands recalculated if it is necessary. Here, we put special emphasis on describing the main difficulties behind this seemingly simple procedure.

1. Introduction

Memristors or Resistive RAMs (RRAMs) are electroformed metal-oxide-metal devices that can alter their resistance states in a non-volatile fashion. They are currently considered not only for memory arrays but also for a plethora of applications including neuromorphic computing, logic circuits, cryptography, etc. [1–3]. Nevertheless, one of the major drawbacks that this technology currently faces concerns with its inherent variability, which is associated with the alternate formation and destruction of the filamentary conducting structure at atomic scale [4,5]. Since variability is at the heart of RRAM operation, inclusion of this phenomenon in any compact model intended for circuit simulation environments would be of utmost importance. In this work, we explore the introduction of uncorrelated cycle-to-cycle (C2C) variability in the quasi-static memdiode model (QMM) for RRAM devices [6]. Correlated C2C variability involving time series dependence (simulation results for cycle i depend on simulation results for cycle $i-1$) and chained parameter simulations involving multivariate regression (parameter value i explicitly depends on parameter value j within cycle k) are the following logical steps to investigate after this first attempt. However, before entering into the subject, it is important to understand how variability affects the simulation results. Uncorrelated C2C variability does not mean that the parameter estimands can be independently chosen within a certain cycle. Since the generated I - V curve is the result of a sequence of operations in which multiple parameters intervene, there is an

underlying connection among their average and dispersion values. This interdependence must be addressed in order to obtain realistic simulated curves. In this work, we adopt a simplistic approach which consists in estimating first the most suitable distribution functions for the experimental observables and then attributing these functions to the corresponding most relevant model parameters in each part of the I - V curve. However, recall that the final simulated curve is the result of a combination of nonlinear functions with random parameters. In order to obtain acceptable results under this scheme, we follow a kind of recursive approach in which the model parameters are at the end selected according to the statistical results they generate.

2. Devices and experimental results

HfO₂-based MIM structures [7] were investigated in this work. The oxide thickness is 10 nm and the area of the devices 5x5μm². The bottom electrode is a 200 nm-thick W layer and the top electrode is a 200 nm-thick TiN layer on top of a 10 nm-thick Ti layer acting as oxygen getter material [8]. Simulations are compared with experimental data obtained from applying 450 voltage sweeps to the devices described previously. The complete set of experimental I - V curves and the median curve are shown in Fig. 1.a. High (I_{HRS}) and low (I_{LRS}) resistance state currents are extracted at $V = 0.2$ V. The snapback (SB) correction is calculated as $V_{SB} = V_{applied} - R_i I_{measured}$, where R_i is a series resistance (internal). R_i is chosen so as to achieve a current increase at a constant

* Corresponding author.

E-mail address: emili.salvador@uab.cat (E. Salvador).<https://doi.org/10.1016/j.sse.2021.108040>

Available online 29 May 2021

0038-1101/© 2021 The Author(s). Published by Elsevier Ltd. This is an open access article under the CC BY license (<http://creativecommons.org/licenses/by/4.0/>).

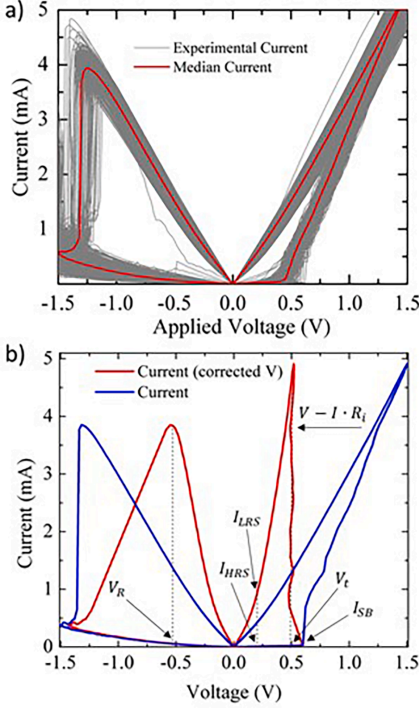


Fig. 1. a) Experimental I-V curves: 450 cycles and median curve. b) Voltage correction illustrating the snapback effect in a single cycle and parameter specification.

transition voltage V_t (see Fig. 1.b) [9]. This correction is calculated for all the cycles using a different R_t value. The RESET voltage V_R is the voltage corresponding to the maximum current reached at negative bias. The SB current I_{SB} is found from the last data point before the occurrence of the SET jump. The parameter extraction was carried out using MATLAB. The extracted parameters for the whole set of curves were analyzed using the tools available in the *fitdistplus* package for the R language [10]. Different distributions (normal, lognormal, gamma, and Weibull) were fitted to the data and compared. The goodness of fit and criteria (minimum values in Table 1) in combination with the quantile-quantile (Q-Q) plots are illustrated in Fig. 2, which graphically compare the experimental distributions with the parametric models. This information is used to determine the best candidate distributions.

Fig. 2.a, .b and .c show the density plots for V_t , V_R and R_t corresponding to the four distributions investigated. According to this analysis, V_t follows a lognormal distribution while V_R and R_t are better described by a normal one. The same analysis was carried out for the rest of the above mentioned parameters resulting in: normal distribution for I_{SB} , and lognormal distributions for I_{HRS} and I_{LRS} . This prior information will be used to define the distribution of the leading model parameters in the device script.

Table 1

Goodness-of-fit statistics (Kolmogorov-Smirnov, Cramer-von Mises, Anderson-Darling) and criteria (Akaike's and Bayesian) for a) V_t , b) for V_R and c) for R_t .

| a) | | | | | |
|-------|--------|-----------------|------------------|----------|----------|
| | Method | Normal | Lognormal | Gamma | Weibull |
| Stat. | K-S | 0.0375 | 0.0295 | 0.0298 | 0.0856 |
| | C-vM | 0.1289 | 0.0576 | 0.0696 | 0.9333 |
| | A-D | 0.9495 | 0.3944 | 0.5076 | 6.343 |
| Cri. | AIC | -1654.55 | -1662.72 | -1661.04 | -1585.18 |
| | BIC | -1646.34 | -1654.501 | -1652.82 | -1576.96 |
| b). | | | | | |
| | Method | Normal | Lognormal | Gamma | Weibull |
| Stat. | K-S | 0.0275 | 0.0449 | 0.0393 | 0.046 |
| | C-vM | 0.045 | 0.1709 | 0.1149 | 0.2497 |
| | A-D | 0.2707 | 1.043 | 0.6944 | 1.858 |
| Cri. | AIC | -1500.53 | -1487.75 | -1493.46 | -1480.1 |
| | BIC | -1492.32 | -1479.532 | -1485.25 | -1471.89 |
| c). | | | | | |
| | Method | Normal | Lognormal | Gamma | Weibull |
| Stat. | K-S | 0.0954 | 0.0986 | 0.1003 | 0.1532 |
| | C-vM | 0.7561 | 0.7826 | 0.8059 | 3.077 |
| | A-D | 4.819 | 4.991 | 5.137 | 18.919 |
| Cri. | AIC | -3315.67 | -3313.39 | -3313.25 | -3463.92 |
| | BIC | -3323.89 | -3321.62 | -3321.46 | -3472.14 |

3. QMM with variability

Once the model parameter distributions are established, they are included in the header of the QMM model script as shown in Table 2. Some model parameters are assumed to be constant in order to avoid over-randomness. The LTSpice *gauss* function and its transformations are used to generate the appropriate parameter values and variability. According to the QMM [2] the I-V characteristic reads:

$$I(V) = I_0(\lambda) \sinh\{\alpha(\lambda)[V - (R_S(\lambda) + R_t)I]\} \quad (1)$$

where $I_0(\lambda) = I_{\min} + (I_{\max} - I_{\min}) \cdot \lambda$ is the current amplitude factor, R_S a series resistance, α a fitting parameter and I_{\min} and I_{\max} , minimum and maximum current values, respectively. Equation (2) relates the memory state λ to the voltage across the filament's constriction V_C through the recursive hysteresis operator:

$$\lambda(V_C) = \min\left\{\Gamma^-(V_C), \max\left[\lambda(\tilde{V}_C), \Gamma^+(V_C)\right]\right\} \quad (2)$$

where Γ^+ and Γ^- are the so-called ridge functions, which represent the ion/vacancy movement for SET and RESET, respectively. $\lambda(\tilde{V}_C)$ is the memory value a timestep before (dictated by the simulator). The model includes other parameters for the fine-tuning of the simulated curves.

4. Comparison between experimental and simulation results

The next step consists in performing Monte Carlo simulations using the QMM model discussed in the previous Section. In Fig. 3, experimental (grey) and simulated (red) curves are compared using three

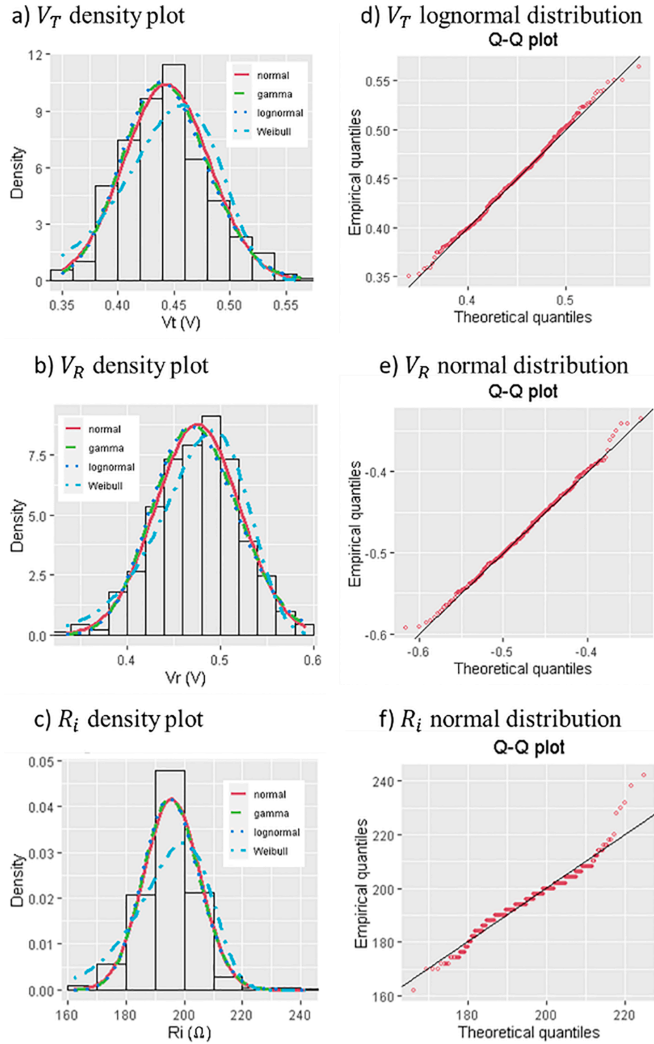


Fig. 2. a), b) and c) show density plots for V_T , V_R and R_i , respectively, with normal, gamma, lognormal, and Weibull distributions. d), e) and f) show Q-Q plots after selecting the best fitting distribution.

different plots for the I - V curves: a) linear-linear, b) log-linear, and c) linear-linear (with SB correction). Although the fitting is not perfect, the simulations reproduce the main features of the experimental curves in all the cases. The most conspicuous difference occurs in LRS, mainly because of a peculiarity of the experimental data. This will be discussed in detail next.

In order to make a fair comparison, the statistical distributions of the four observables is considered in Fig. 4. These observables were

specifically selected so as to compile information from the entire set of the I - V curves in the different regimes: I_{HRS} for the HRS curve, V_T for the SET transition, I_{LRS} for the LRS curve and V_R for the RESET transition. This compilation was performed without considering the SB correction and for a direct evaluation of I_{HRS} and I_{LRS} . As shown in Fig. 4, simulation results for I_{HRS} , V_T , and V_R are consistent with the experimental data. However, I_{LRS} exhibits a notorious discrepancy. The reason is clear, for the particular case under study, the experimental I_{LRS} histogram presents

Table 2

LTSpice QMM script including variability in the most significant parameters taking into account the previously extracted best candidate distributions. In red the Gaussian distribution and in blue the lognormal distributions.

```
.subckt memdiode + - H
.params
+ H0=2E-3 ri=193+gauss(1)
+ etas=50 vs=2 etar=9 vr=-0.57+gauss(0.028)
+ rsmx=8+gauss(1) rsmin=10
+ imax=exp(-5.38+gauss(0.06)) amax=2.0
+ imin=exp(-10.9+gauss(0.68)) amin=2.0
+ vt=exp(-0.733+gauss(0.08)) isb=33E-6+gauss(2E-6)
+ CH0=1E-3 gam=0.07 RPP=1E10
*Memory equation
BH 0 H I=min(R(V(C,-)),max(S(V(C,-)),V(H))) Rpar=1
CH H 0 {CH0} ic={H0}
*I-V
RE + C {ri}
RS C B R=RS(V(H))
BD B - I=I0(V(H))*sinh(A(V(H))*V(B,-))
RB + - {RPP}
*Auxiliary functions
.func I0(x)=imin+(imax-imin)*x
.func A(x)=amin+(amax-amin)*x
.func RS(x)=rsmin+(rsmx-rsmin)*x
.func VSB(x)=if(x>isb,vt,vs)
.func ISF(x)=if(gam==0,1,pow(x,gam))
.func S(x)=1/(1+exp(-etas*(x-VSB(I(BD))))))
.func R(x)=1/(1+exp(-etar*ISF(V(H))*(x-vr)))
.ends
```

two peaks which likely corresponds to two different configurations of the filamentary path or to competing filaments. The simulated curves are unable to capture this feature because of the use of a single distribution function. This single distribution is responsible for the large central peak shown in Fig. 4.c. This inconsistency illustrates that caution should be exercised when unexpected deviations in the experimental data occur.

Finally, Fig. 5 illustrates the importance of C2C correlations in the experimental curves [11]. Experimental and simulated data corresponding to the time evolution of two parameters (high resistance state current I_{HRS} and reset voltage V_R) are compared. Notice that our approach is unable to generate a trend since the LTSpice simulations considered in this work are uncorrelated. These issues will be further investigated in the future.

5. Conclusions

In this work, we explored how uncorrelated C2C variability can be included in the QMM model for resistive switching devices. The experimental I - V curves obtained from HfO_2 -based devices were analyzed and the main parameters extracted. The best candidate distributions for the experimental parameters were determined using the *fitdistrplus* package from the R language and this information was included in the model script. We showed that the model results reproduce reasonably well the

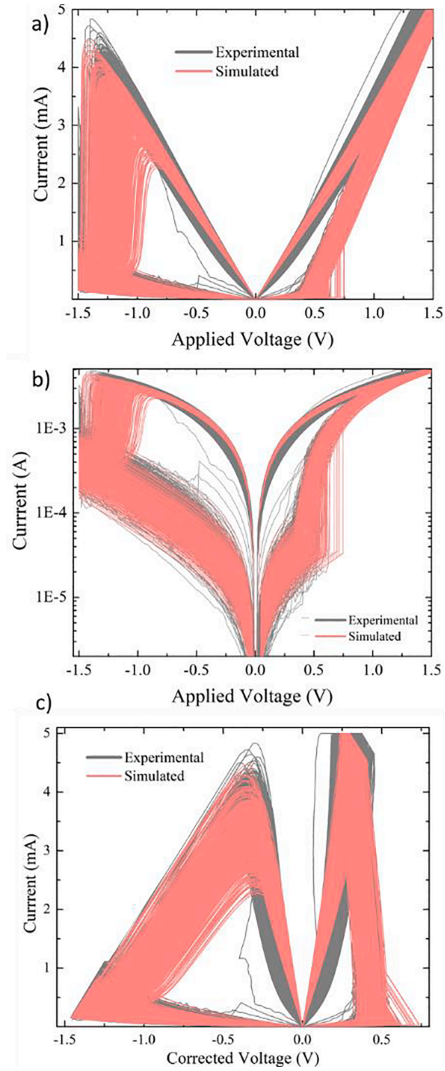


Fig. 3. Experimental and simulated curves comparison. a) I - V curves, b) I - V curves in logscale and c) I - V curves applying the SB voltage correction.

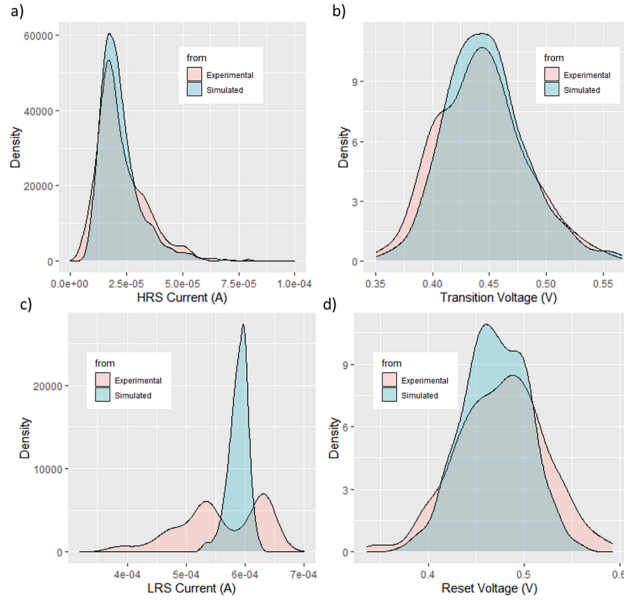


Fig. 4. Comparison of experimental and simulated parameter distributions: a) I_{HRS} , b) V_T , c) I_{LRS} , and d) V_R .

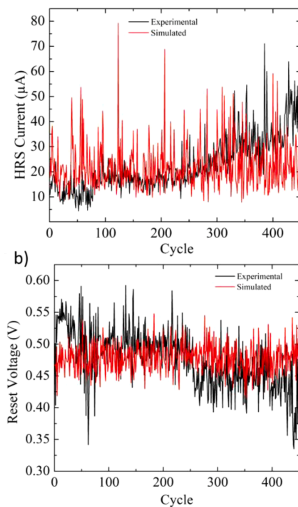


Fig. 5. Time evolution of experimental and simulated parameters for: a) HRS current and b) reset voltage.

main features exhibited by the experimental curves. Future investigations will include time series and chained-parameter analysis for correlated C2C variability simulations.

Declaration of Competing Interest

The authors declare that they have no known competing financial interests or personal relationships that could have appeared to influence the work reported in this paper.

Acknowledgements

This work was supported by the Spanish Ministry of Science, Innovation and Universities through projects TEC2017-84321-C4-1-R, TEC2017-84321-C4-4-R, and PID2019-103869RB-C32.

References

- [1] Yu S, et al. IEEE Solid State Circuits Magazine 2016;8(2):43–56.
- [2] Lee JS, Appl., et al. Phys. Rev. 2015;2(3):031303.
- [3] Jo Sung Hyun, et al. Nano Lett 2010;10(4):1293–301.
- [4] Chen A, et al. IEEE IRPS 2011;843–846.
- [5] Bargallo M, et al. IEEE Trans. Electron Devices 2016;63(8):3116–22.
- [6] Miranda E. IEEE TNano 2015;14:787–9.
- [7] Piccolboni G, et al. IEEE Electron Device Lett. 2016;37(6):721–3.
- [8] Poblador S, et al. Microelectron. Eng. 2018;187–188:148–53.
- [9] Karpov V, et al. Appl. Phys. Lett. 2015;109:1–5.
- [10] Delignette-Muller ML, et al. J. Stat. Softw. 2015;64:1–34.
- [11] Alonso FJ, et al. Chaos. Solitons and Fractals 2021;143:110461.



Emili Salvador Aguilera is a PhD student at the Electronical Engineering department from the Universitat Autònoma de Barcelona under the supervision of Enrique Alberto Miranda and Rosana Rodríguez, from the same department. Prior to the PhD, coursed my Bachelor degree in Nanoscience and Nanotechnology and Master degree in Advanced Nanoscience and Nanotechnology at the Universitat Autònoma de Barcelona. He carried out my Master thesis at the Institut Català de Nanociència i Nanotecnologia (ICNZ) working in the graphene transistors field.



Javier Martin-Martinez received the M.S. degree in physics from the Universidad de Zaragoza, Zaragoza, Spain, in 2004, and the Ph.D. degree from the Universitat Autònoma de Barcelona (UAB), Bellaterra, Spain, in 2009. He was with the Università degli Studi di Padova, Padua, Italy, and IMEC, Leuven, Belgium. He is currently an Associate Professor with UAB. His main research interests include the characterization and modeling of failure mechanisms in MOSFETs and also RRAM characterization and modeling for neuromorphic applications.



Mireia Bargallo Gonzalez received the degree in physics from the University of Barcelona, Barcelona, Spain, and the Ph.D. degree on the topic of stress analysis and defect characterization techniques of semiconductor materials and devices, from Katholieke Universiteit Leuven, Leuven, Belgium, in 2011. She pursued her Ph.D. thesis with the Interuniversity Microelectronics Center (imec), Leuven, Belgium. In 2011, she joined the Institut de Microelectrònica de Barcelona (IMB-CNM, CSIC). Her current research interests include electrical characterization, modeling and applications of resistive switching devices.



Rosana Rodriguez received the Ph. D. in Electrical Engineering from Universitat Autònoma de Barcelona (UAB) in 2000. Funded by the Fulbright program, she worked on devices and circuits reliability at the IBM Thomas J. Watson Research Center (USA). Currently, she is associate professor at the UAB. Her research is focused on the variability and reliability of advanced CMOS devices. She is interested in the electrical characterization and modeling of process-related and time-dependent variability sources as Random Telegraph Noise (RTN) and aging mechanisms as Bias Temperature instability (BTI) and Hot Carrier Injection (HCI). Her research includes the study of the variability impact on the performance of single devices and digital and analogical circuits. She is also interested

in the characterization of resistive switching devices (memristors) and their application for non-volatile memories, computing and neuromorphic applications.



Francesca Campabadal received the Ph.D. degree in physics from the Universitat Autònoma de Barcelona, Bellaterra, Spain, in 1986. She joined the Institut de Microelectrònica de Barcelona, Consejo Superior de Investigaciones Científicas, Barcelona, Spain, in 1987, where she is currently a Research Professor. Her current research interests include the deposition of high-k dielectric layers, their electrical characteristics, and the resistive switching phenomena in RRAM devices.



Enrique Miranda is Professor at the Universitat Autònoma de Barcelona (UAB), Spain. He has a PhD in Electronics Engineering from the UAB (1999) and a PhD in Physics from the Universidad de Buenos Aires, Argentina (2001). He received numerous scholarships and awards including: RAMON y CAJAL (UAB), DAAD (Technical University Hamburg-Harburg), MATSUMAE (Tokyo Institute of Technology, Japan), TAN CHIN TUAN (Nanyang Technological University, Singapore), WALTON award from Science Foundation Ireland (Tyndall National Institute), Distinguished Visitor Award (Royal Academy of Engineering, UK), CESAR MILSTEIN (CNEA, Argentina), Visiting Professorships from the Abdus Salam International Centre for Theoretical Physics, Slovak Academy of Sciences,

Politecnico di Torino, Leverhulme Trust (University College London, UK), and Nokia Foundation (University of Turku, Finland). He serves as member of the Distinguished Lecturer program of the Electron Devices Society (EDS-IEEE) since 2001 and as Associate Editor of Microelectronics Reliability since 2003. He has authored and co-authored around 250 peer-review journal papers.

Article SSE23

Assessment of the variability of the I-V characteristic of HfO₂-based resistive switching devices and its simulation using the quasi-static memdiode model

E. Salvador, M.B. Gonzalez, F. Campabadal, J. Martin-Martinez, R. Rodriguez, E. Miranda



Contents lists available at ScienceDirect

Solid State Electronics

journal homepage: www.elsevier.com/locate/sse

Assessment of the variability of the I - V characteristic of HfO_2 -based resistive switching devices and its simulation using the quasi-static memdiode model

E. Salvador^{a,*}, M.B. Gonzalez^b, F. Campabadal^b, J. Martin-Martinez^a, R. Rodriguez^a, E. Miranda^a

^a Departament d'Enginyeria Electrònica, Universitat Autònoma de Barcelona, 08193 Cerdanyola del Valles, Spain

^b Institut de Microelectrònica de Barcelona, IMB-CNM, CSIC, 08193 Cerdanyola del Valles, Spain

ARTICLE INFO

Keywords:

Memristor
Variability
Resistive switching
 HfO_2

ABSTRACT

Variability of the conduction characteristics of filamentary-type resistive switching devices or resistive RAMs (RRAMs) is a hot research topic both in academia and industry because it is currently considered one of the major showstoppers for the successful development and application of this technology. In this work, we thoroughly investigate the statistics of the cycle-to-cycle (C2C) variability observed in the experimental current–voltage (I - V) curves of HfO_2 -based memristive structures using the *fitdistplus* package for the R language. This exploratory analysis allows us to identify which parametric probability distributions are the most suitable candidates for describing our data. This study involves graphical tools such as the density, skewness-kurtosis (S-K), and quantile–quantile (Q-Q) plots. The analysis is completed with the aid of goodness-of-fit statistics (Kolmogorov-Smirnov, Cramer-von Mises, Anderson-Darling) and criteria (Akaike's and Bayesian). The selected distributions are incorporated into the SPICE script of the quasi-static memdiode model for resistive switching devices and used for simulating uncorrelated C2C variability. Finally, a one-way sensitivity analysis is carried out in order to test the impact of the model parameters variation in the output characteristics of the device.

1. Introduction

Filamentary-type resistive switching devices or resistive random-access memories (RRAMs) are electroformed metal-oxide-metal structures that can alter their resistance state upon the application of an external stimulus (voltage, current, light, etc.). In these structures, a localized vacancy or ion conducting bridge spans the oxide layer and connects or disconnects the opposite electrodes in a non-volatile fashion. This means that when power is turned off, the last resistance state of the device remains unaltered. Nowadays, this kind of structure is considered a promising candidate for a plethora of applications including information storage, neuromorphic computing, logic circuits, cryptography, and many more. [1–3] Nevertheless, one of the major drawbacks that this technology must face concerns with its intrinsic variability linked to morphologic changes of the conducting filament occurring at the atomic scale [4,5]. This is particularly important for the high resistance state where a few atoms participate in the conduction process. Since variability is always present in RRAM operation, its inclusion in any

compact model for such devices would be of utmost importance. In this work, uncorrelated cycle-to-cycle (C2C) variability is introduced in the quasi-static memdiode model (QMM) [6–7] through the random assignment of the model parameter values. We consider here the QMM because we are only interested in simulating the devices when subjected to ramped voltage with fixed ramp rate. For pulsed measurements, where switching times are of utmost importance, a dynamical approach is required. Uncorrelated C2C means in this context that the generated cycles are considered independent so that no trends in the low (LRS) or high (HRS) resistance state are expected. Trends can be included by adding the appropriate wearout rules in the definition of the model parameters. The analysis reported here mainly focuses on the spread of the I - V curves around the median characteristic. It is worth mentioning that for specific applications, the model should be recalibrated since the parameter values may be affected by the device state history if it involves any kind of irreversible effect. After the inclusion of variability in the model parameters, the attention concentrates on the general behavior of the QMM. We have investigated how sensitive the model is

* Corresponding author.

E-mail address: emili.salvador@uab.cat (E. Salvador).

<https://doi.org/10.1016/j.sse.2023.108667>

Received 10 January 2022; Received in revised form 15 March 2023; Accepted 2 May 2023

Available online 11 May 2023

0038-1101/© 2023 The Author(s). Published by Elsevier Ltd. This is an open access article under the CC BY license (<http://creativecommons.org/licenses/by/4.0/>).

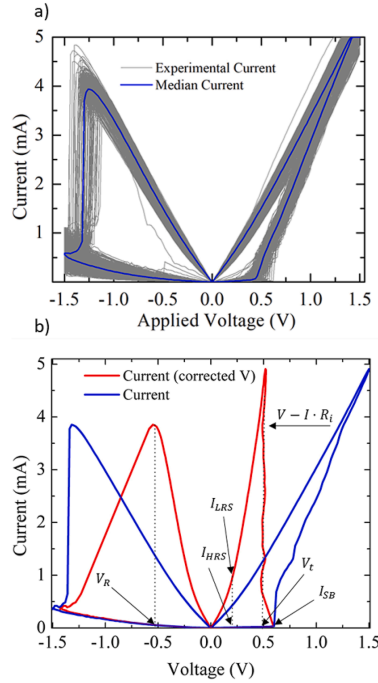


Fig. 1. A) experimental i-v curves: 450 cycles and median curve. b) voltage correction illustrating the snapback effect in a single cycle and parameter specification.

to systematic modifications of the parameter values. The approach followed is also valid for any other model and it is technically referred to as a one-way sensitivity analysis (SA). To be more precise, the sensitivity we are discussing relates to how uncertainty in the simulation output can be apportioned to different sources of uncertainty in the model inputs [8,9]. This paper is organized as follows: in Section 2, the fabrication process of the devices under investigation and the preparation of the experimental data are described. In Section 3, the experimental observations are statistically analyzed. In Section 4, the quasi-static memristive model is presented. The inclusion of variability in the model script is discussed in Section 5. In Section 6, experimental and simulated results are compared and, in Section 7, the one-way SA is performed. Section 8 reports the conclusions of this work.

2. Devices and preparation of experimental data

The devices studied in this work are HfO_2 -based metal-oxide-metal structures [10]. The oxide thickness is 10 nm and the active area of the devices is $5 \times 5 \mu\text{m}^2$. The bottom electrode consists in a 200 nm-thick W layer and the top electrode is a 200 nm-thick TiN layer on top of a 10 nm-thick Ti layer acting as oxygen receiver material [11]. After the electroforming process, the devices are cycled 450 times with a bipolar voltage sweep with limits ± 1.5 V. The electrical measurements were performed using the Semiconductor Parameter Analyzer (SPA) Agilent 4156C. The equipment was controlled via GPIB bus and programmed with Matlab software. The measured I - V curves are plotted in grey in Fig. 1.a. The median curve is plotted in blue. In Fig. 1.b, the snapback (SB) correction for a single cycle extracted from the set of experimental

curves is illustrated. The snapback voltage is defined as $V_{SB} = V_{\text{applied}} - R_i \cdot I_{\text{measured}}$ where R_i is an internal series resistance (it can also include any external series resistance). The value of R_i is selected so as to provide an almost vertical increase of the current after the SET event. This vertical increase occurs at a constant voltage called the transition voltage V_t . [12] Both R_i and V_t are obtained individually for each cycle in the measurement set. A number of *observables* are indicated in Fig. 1.b: the high (I_{HRS}) and low (I_{LRS}) resistance state currents are obtained by extracting the current values at a fixed voltage, $V = 0.2$ V, the RESET voltage V_R is obtained from the voltage corresponding to the maximum current reached for negative bias. The last current data point before the SET event is the SB current I_{SB} . All these observables are extracted from the experimental curves using Matlab coding. In the following Section, the statistical distribution of these observables is investigated.

3. Analysis of the experimental results

In this Section, we investigate the statistical distribution of the observables mentioned in Section 2 using the *fitdistplus* package for the R language [13]. The obtained results will be used to define the model parameters in the QMM SPICE script. First, the Cullen and Frey skewness-kurtosis (SK) or Pearson plot is used as an indicator of the appropriateness of the different candidate distributions (normal, lognormal, gamma, Weibull, logistic, etc.). This plot compares the kurtosis and the squared skewness corresponding to the available data. For some specific distributions (normal, uniform, logistic, exponential), there is only one possible value for the skewness and kurtosis. Thus, the

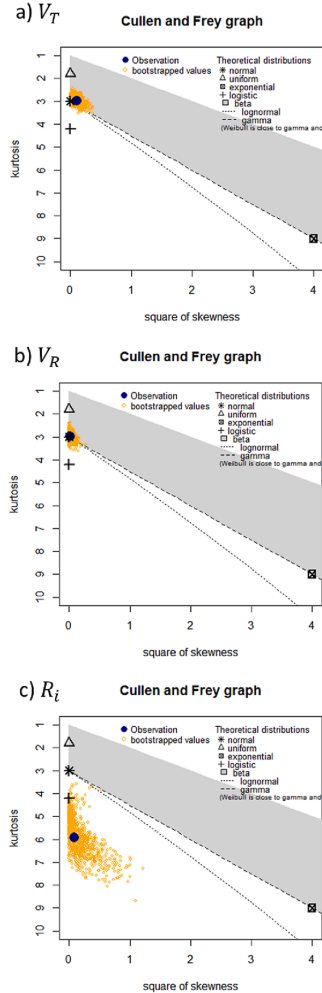


Fig. 2. A), b) and c) show the cullen and frey plots for V_T , V_R and R_i respectively.

distribution is represented by a single point on the plot. For other distributions, areas of possible values are represented, consisting in lines (as for the gamma and lognormal distributions), or shaded areas (as for the beta distribution). Notice the location of the observation (blue dot) with respect to the theoretical symbols and lines. The yellow points are bootstrapped data (random sampling with replacement). Fig. 2.a-c show the SK plot for V_T , V_R , and R_i , respectively. For V_T and V_R , the figures show that the experimental observations are close to the star symbol (normal distribution). Nevertheless, the V_T observation as well as the bootstrapping cloud are slightly shifted almost coinciding with the dashed line representing the lognormal distribution. In contrast, for R_i ,

Table 1

Goodness-of-fit statistics (Kolmogorov-Smirnov, Cramer-von Mises, Anderson-Darling) and criteria (Akaike's and Bayesian) for a) V_T , b) for V_R and c) for R_i .

| a) | | | | | |
|-------|--------|----------|------------------|----------|----------|
| | Method | Normal | Lognormal | Gamma | Weibull |
| Stat. | K-S | 0.0375 | 0.0295 | 0.0298 | 0.0856 |
| | C-vM | 0.1289 | 0.0576 | 0.0696 | 0.9333 |
| | A-D | 0.9495 | 0.3944 | 0.5076 | 6.343 |
| Cri. | AIC | -1654.55 | -1662.72 | -1661.04 | -1585.18 |
| | BIC | -1646.34 | -1654.501 | -1652.82 | -1576.96 |

| b). | | | | | |
|-------|--------|-----------------|-----------|----------|----------|
| | Method | Normal | Lognormal | Gamma | Weibull |
| Stat. | K-S | 0.0275 | 0.0449 | 0.0393 | 0.046 |
| | C-vM | 0.045 | 0.1709 | 0.1149 | 0.2497 |
| | A-D | 0.2707 | 1.043 | 0.6944 | 1.858 |
| Cri. | AIC | -1500.53 | -1487.75 | -1493.46 | -1480.1 |
| | BIC | -1492.32 | -1479.532 | -1485.25 | -1471.89 |

| c). | | | | | |
|-------|--------|-----------------|-----------|----------|----------|
| | Method | Normal | Lognormal | Gamma | Weibull |
| Stat. | K-S | 0.0954 | 0.0986 | 0.1003 | 0.1532 |
| | C-vM | 0.7561 | 0.7826 | 0.8059 | 3.077 |
| | A-D | 4.819 | 4.991 | 5.137 | 18.919 |
| Cri. | AIC | -3315.67 | -3313.39 | -3313.25 | -3463.92 |
| | BIC | -3323.89 | -3321.62 | -3321.46 | -3472.14 |

the blue dot and the bootstrapped data show a large kurtosis (leptokurtic behavior) which means that the tails of the distribution are heavier than those corresponding to a normal distribution. Since the SK plot must only be used as a first indicator, further analysis is required before concluding which distribution better suits. Next, the different candidate distributions (normal, lognormal, gamma, and Weibull) are fitted and compared with the experimental observables. The goodness-of-fit (GoF) statistics (Kolmogorov-Smirnov, Cramer-von Mises, Anderson-Darling) and criteria (Akaike's and Bayesian) are shown in Table 1. Fig. 3.a-c show the density plots for V_T , V_R , and R_i , respectively, corresponding to the distributions investigated. The quantile-quantile (Q-Q) plots, which graphically compare the experimental distributions with the parametric models, are illustrated in Fig. 3.d-f, for V_T , V_R , and R_i , respectively. The combination of the information obtained from the GoF statistics and criteria, and the Q-Q plots were used to determine the most plausible distribution for each observable. In summary, the analysis carried out indicates that V_T follows a lognormal distribution while V_R and R_i are better described by a normal distribution. The same procedure was followed for the rest of the observables resulting in: normal distribution for I_{SB} and lognormal distributions for I_{HRS} and I_{LRS} . This information will be included in the model parameters of the QMM script and will be used to generate a set of simulated curves with variability.

4. Brief introduction to the QMM

As mentioned in Section 1, variability simulations and sensitivity analysis were performed with the QMM model [7]. This model describes the conduction characteristics of bipolar resistive switching devices

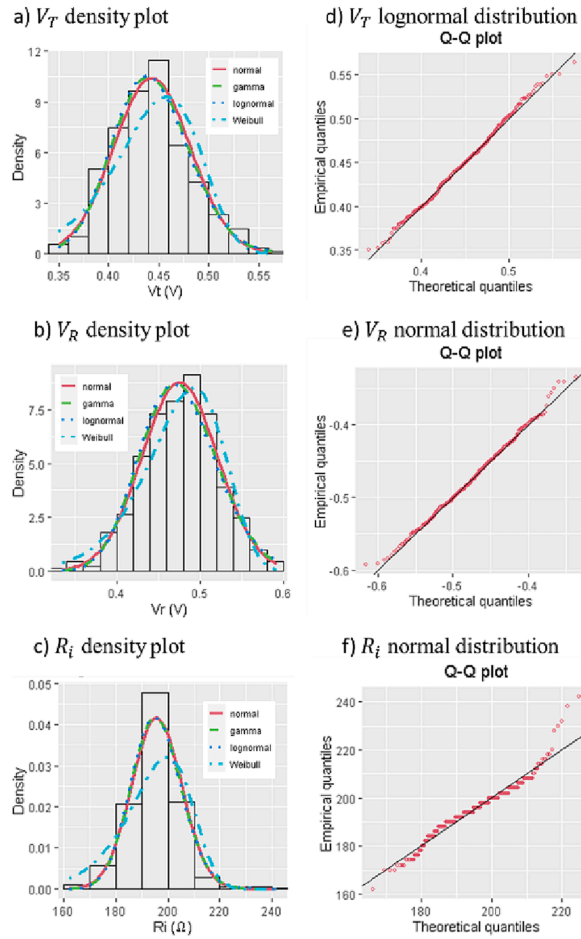


Fig. 3. A), b) and c) show density plots for V_T , V_R and R_i , respectively, with normal, gamma, lognormal, and Weibull distributions. d), e) and f) show Q-Q plots after selecting the best fitting distribution.

Table 2

LTSpice QMM script including variability in the most significant parameters taking into account the previously extracted best candidate distributions. In red the Gaussian distributions and in blue the lognormal distributions.

```
.subckt memdiode + - H
.params
+ H0=2E-3 ri=193+gauss(1) rsmin=10
+ etas=50 vs=2 etar=9 vr=-0.57+gauss(0.028)
+ rsmax=8+gauss(1) isb=33E-6+gauss(2E-6)
+ imax=exp(-5.38+gauss(0.06)) amax=2.0
+ imin=exp(-10.9+gauss(0.68)) amin=2.0
+ vt=exp(-0.733+gauss(0.08)) gam=0.07
*Memory equation
BH 0 H I=min(R(V(C,-)),max(S(V(C,-)),V(H))) Rpar=1
CH H 0 IE-3 ic={H0}
*I-V
RE + C {ri}
RS C B R=K(rsmin,rsmax)
BD B - I=K(imin,imax)*sinh(K(amin,amax)*V(B,-)) Rpar=1E10
*Auxiliary functions
.func K(min,max)=min+(max-min)*V(H)
.func S(x)=1/(1+exp(-etas*(x- if(x>isb,vt,vs))))
.func R(x)=1/(1+exp(-etar* if(gam==0,1,pow(V(H),gam))*(x-vr)))
.ends
```

using a hysteresis operator which keeps track of the memory state of the device. The origin of the switching is related to the formation of a conducting filament (CF) spanning the dielectric film caused by the application of an external field (SET process for the transition HRS to LRS). The CF is created as a consequence of the displacement and accumulation of metal ions or oxygen vacancies (depending on the device type). The CF can be ruptured by the application of a field with opposite sign (RESET process for the transition LRS to HRS). According to the QMM, the I - V characteristic reads:

$$I(V) = I_0(\lambda) \sinh\{\alpha(\lambda)[V - (R_S(\lambda) + R_i)I]\} \quad (1)$$

where $I_0(\lambda) = I_{0min} + (I_{0max} - I_{0min})\lambda$ is the current amplitude factor, $R_S(\lambda)$ a variable series resistance, and $\alpha(\lambda)$ a fitting parameter. I_{0min} and I_{0max} are minimum and maximum current values (same for R_S and α), respectively. According to (1), for low currents, I depends exponentially on V whereas for high currents, I depends linearly on V . Equation (2) expresses the relationship between the memory state λ and the voltage across the filament's constriction $V_C = V - R_i I$ through the recursive hysteresis operator:

$$\lambda(V_C) = \min\left\{\Gamma^-(V_C), \max\left[\lambda\left(\tilde{V}_C\right), \Gamma^+(V_C)\right]\right\} \quad (2)$$

where $\lambda\left(\tilde{V}_C\right)$ is the memory value a timestep before (in practice dictated by the simulator timestep). Γ^+ and Γ^- are the so-called positive and negative ridge functions (sigmoidals), respectively, and are expressed as:

$$\Gamma^\pm(V_C) = \frac{1}{1 + \exp[-\eta^\pm(V_C - V^\pm)]} \quad (3)$$

which represent the creation (+) and dissolution (-) processes of the CF. η^\pm ($etas$ and $etar$ in the model script) are the set (+) and reset (-) transition rates and V^\pm are the threshold voltages for set (+) and reset (-). The model uses other parameters for the fine-tuning of the simulated curves (see the script in Table 2). The model is implemented in LTSpice using an equivalent circuit with behavioral current sources and includes the snapback (isb) and snapforward (gam) effects.

5. Simulation with variability using the QMM

Once the model parameter distributions were established (see Section 3), they were included in the QMM model script (see Table 2). Some of the model parameters were assumed to be constant to avoid over-randomness in the output curves. The LTSpice gauss function and its transformation were used to generate the appropriate parameter values and variability. Simulations were performed having in mind the particular features of the experimental curves, such as the voltage span and the number of cycles. The parameters (including variability) are calculated at the beginning of each cycle and are kept constant until the next cycle. The goal was to reproduce as close as possible the median curve and the spread of the experimental data set. Since ultimately the simulated I - V curves are the result of a sequence of operations in which a number of random parameters are involved, there is always an underlying connection among the mean and dispersion values that need to be considered in order to achieve a consistent set of curves. To control this interdependence an iterative optimization process was followed to adjust the simulation parameters for obtaining close agreement with the experimental curves. The simulated observables and their variability obtained from a complete simulation run were analyzed first. With this information at hand the parameter values were modified in the appropriate direction (with the help of the one-way SA approach) and the simulation was performed again. This process was repeated until coincidence is achieved, within certain error margins, between the experimental and simulation results. Notice we included variability in 7 out of 15 model parameters, this combination was found to be reasonable for reproducing the experimental curves. For other devices, less variable parameters might be enough to reproduce their behavior, in fact a basic variable set of curves can be obtained by including the 'gauss' LTSpice function in 4 parameters ($imin$, $imax$, isb and vr).

6. Comparison between experimental and simulation results

Simulations using the QMM model were performed taking into account the iterative optimization process discussed in the previous Section. In Fig. 4, experimental (black) and simulated (blue) curves are

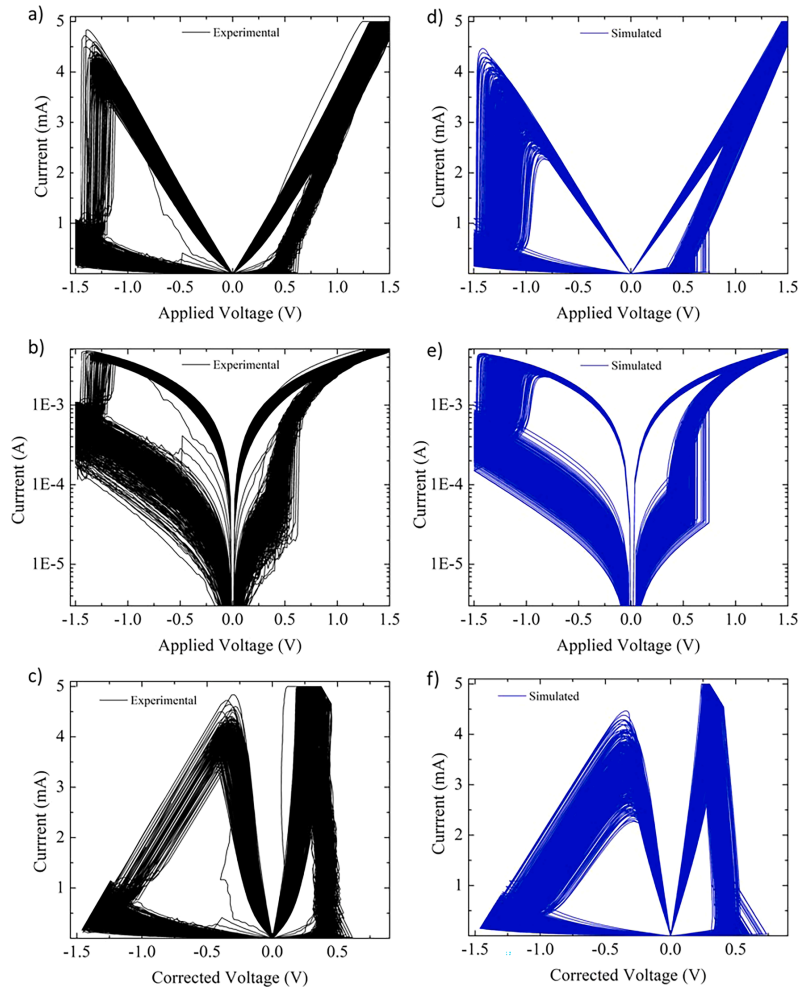


Fig. 4. Experimental and simulated curves comparison. a, d) I-V curves, b, e) I-V curves in logscale and c, f) I-V curves applying the SB voltage correction for experimental and simulated respectively.

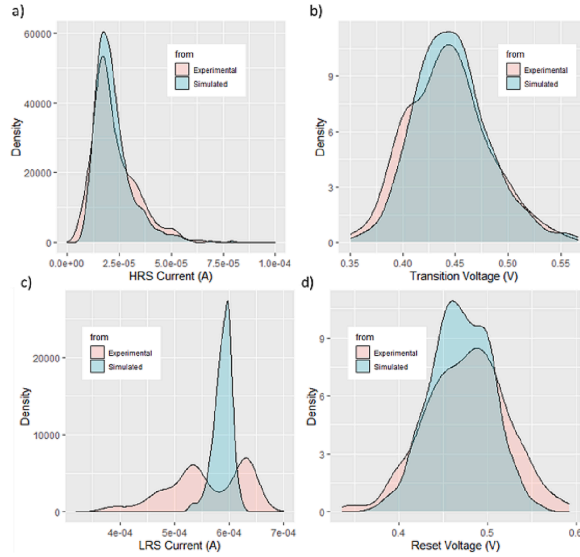


Fig. 5. Comparison of experimental and simulated parameter distributions: a) I_{HRS} , b) V_T , c) I_{LRS} , and d) V_R .

compared using three alternative plots for the same set of I - V curves: a) and d) linear-linear axes, b) and e) log-linear axes, and c) and f) linear-linear axes (with SB correction). The fitting is reasonably good and simulations reproduce the main features of the experimental curves in all the cases. The most conspicuous difference occurs in LRS, mainly because of a peculiarity of the available experimental data. This will be discussed later. A deeper and fairer comparison between the experimental and simulated observables is presented in Fig. 5. This figure shows the statistical distributions corresponding to the four main observables. Aiming to compile information from the different sections of the I - V curves, the following observables were specifically selected: I_{HRS} for the HRS curve, V_T for the SET transition, I_{LRS} for the LRS curve, and V_R for the RESET transition. This compilation was performed using the corrected I - V curves for V_T and V_R , and the raw I - V curves, i.e. without applying the SB correction for a direct evaluation of I_{HRS} and I_{LRS} . As shown in Fig. 5, the density plots corresponding to the experimental and simulated data, I_{HRS} and V_T are reproduced correctly. V_R presents a curious effect: taking a closer view at the raw I - V curves, the dispersion in the simulations is clearly higher than in the experimental case, but for the corrected I - V curves, the dispersion is well reproduced. Instead, I_{LRS} exhibits a big difference. The reason is clear, for the case under study, the experimental I_{LRS} histogram shows a double peak which likely corresponds to two different configurations of the CF or different coexisting CFs. Since the approach we are reporting here only considers a single set of parameters for each distribution, the simulated curves cannot reproduce the two distributions experimentally observed. Our parameters are only able to generate a single peak as illustrated in Fig. 5.c. This inconsistency illustrates that caution should be exercised when unexpected deviations in the experimental data occur and additional features are required to simulate them appropriately.

As an indicator of the importance of considering the time series evolution and the correlation among parameters, Fig. 6 shows experimental and simulated data corresponding to the C2C variability of two

parameters: the high resistance state current a) I_{HRS} and the RESET voltage b) V_R [14]. Both figures show the presence of a trend in the experimental observables. Notice that our approach is unable to generate this trend since the LTspice simulations considered in this work do not include cross-correlation among parameters. Aiming to compare the fluctuation of the observables without trends, Fig. 6 c) and d) illustrate the difference in the observable between cycle $k + 1$ and cycle k both for I_{HRS} and V_R , defined as ΔI_{HRS} and ΔV_R , respectively. As expected, the plots show that the experimental and model fluctuations are of the same order of magnitude regardless the cycle number. In order to quantify this fluctuation, different indicators are presented in Table 3: the mean value μ , i.e. the first moment of the distribution, the standard deviation (σ), i.e. the second moment of the distribution, the inter-quartile range (IQR), a measures of the data spread, and the mean absolute deviation (MAD), which represents the average distance between each point and the mean value. Table 3 compares the four indicators (experimental and simulated), for the four different observables indicated in Fig. 6. It can be seen that the indicators are similar for all the observable which points out that the fluctuations are correctly captured.

7. One-way sensitivity analysis of the output curves

As mentioned in Section 1, a one-way sensitivity analysis (SA) was also carried out as part of this study. This analysis was performed considering a voltage sweep high enough to achieve the full SET and RESET states of the I - V curves without introducing irreversible damage to the devices. To understand why the applied voltage is an important issue for this analysis, Fig. 7 illustrates the role played by the maximum applied voltage (V_{app}) on the simulations. The figure includes indicators for the trends of the four different observables as the maximum applied voltage is increased. Notice that if the voltage is set to 1.5 V (black curve), the simulated curve does not reach the full HRS, which means that the RESET process is not complete. Therefore, if the referred voltage

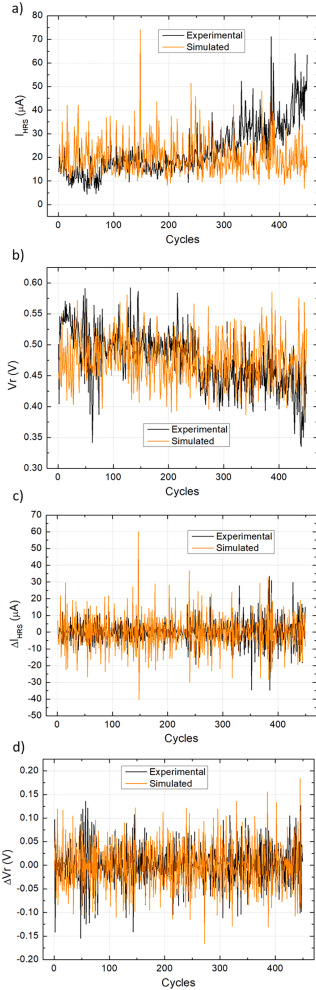


Fig. 6. Time evolution of experimental and simulated parameters for: a) HRS current, b) reset voltage, c) and d) the difference in the observable between cycle $k + 1$ and cycle k for I_{HRS} and V_R (ΔI_{HRS} and ΔV_R).

is not high enough, it will seriously affect the sensitivity studies performed on the rest of observables. This is an important point to consider within this analysis.

In what follows, we will only take into account complete SET and RESET processes. This can be achieved with a maximum applied voltage of ± 2.5 V (see Fig. 7 in green). The parameters were swept one at a time (50 steps each) in a reasonable range (this process does not include C2C variability) and the obtained I - V curves analyzed. Fig. 8 shows the relative variation of the observables as a function of the relative variation of selected model parameter: a) η , or etar (reset transition rate), b) α

Table 3

Different indicators for studying the fluctuations of: HRS current, reset voltage, and the difference in the observable between cycle $k + 1$ and cycle k for I_{HRS} and V_R (ΔI_{HRS} and ΔV_R).

| | V_R | I_{HRS} | ΔV_R | ΔI_{HRS} |
|--------------|--------|-----------|--------------|------------------|
| Exp σ | 0.0455 | 1.08e-05 | 0.0458 | 7.63e-06 |
| Sim σ | 0.0381 | 7.84e-06 | 0.0541 | 1.12e-05 |
| Exp IQR | 0.0624 | 1.29e-05 | 0.0555 | 7.53e-06 |
| Sim IQR | 0.0523 | 8.96e-06 | 0.0784 | 1.29e-05 |
| Exp MAD | 0.0455 | 1.08e-05 | 0.0458 | 7.63e-06 |
| Sim MAD | 0.0381 | 7.84e-06 | 0.0541 | 1.12e-05 |

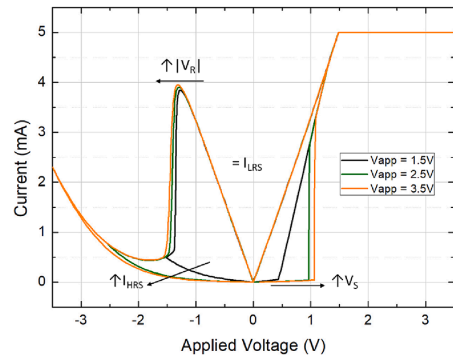


Fig. 7. Simulated I - V curves for different applied voltages. The change in the observables is indicated.

or α (I - V slope parameter), c) I_{max} , and d) I_{min} (maximum and minimum currents). Table 4 summarizes the magnitude and trend associated with the variation of each observable in terms of all the modified model parameters (a change of $\pm 30\%$ from its reference value was considered for the analysis). The reference parameters are those obtained from the fitting of the median I - V curve (see Fig. 1). Notice that Table 4 uses colors and signs. Red color is associated with almost no dependence between the observable and the model parameter; orange indicates that for a 10% model parameter variation, less than 10% variation is detected in the observable and green corresponds to a variation larger than 10%. (+) or (-) indicate direct or inverse dependence, respectively. Reading the first column of Table 4, we can see the impact of all the inputs over the observable I_{HRS} . It is observed for I_{HRS} a strong and positive dependence on α , I_{min} , and gam . It also exhibits strong and inverse dependence on V_{app} and etar , weak and positive effect from V_r and I_{max} and it is scarcely affected by R_t , etas , R_s , and I_{sb} . This kind of test is of utmost importance for investigating the sensibility of the considered simulation model when subjected to variability.

8. Conclusions

In this work, we investigated uncorrelated C2C variability in RRAM devices using the QMM model. The analysis consisted in comparing experimental I - V curves, obtained from HfO_2 -based devices with SPICE simulations. First, the experimental curves were analyzed and the main observables extracted. By means of the different tools available in the *fudistplus* package from the *R* language, the best candidate distributions for the experimental observables were determined. The obtained information was included in the model script. Simulations indicate that the QMM model can reproduce reasonably well the main features exhibited by the experimental curves in terms of mean value and variability. It was

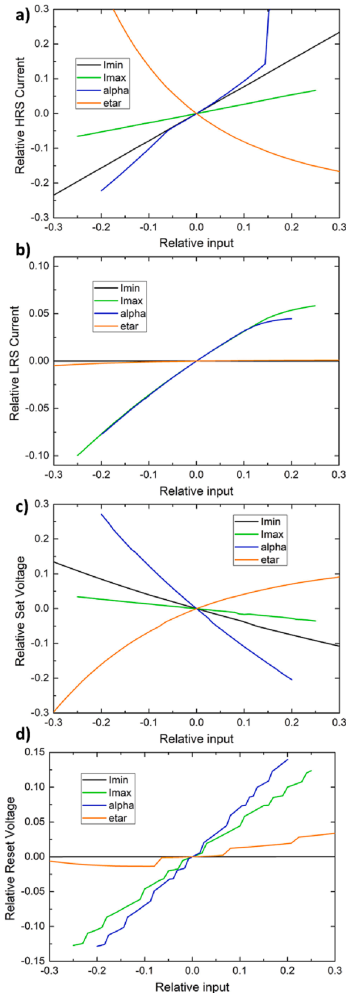


Fig. 8. One-way sensitivity plots for the relative change of the observables a) I_{HRS} , b) I_{LRS} , c) V_S and d) V_R against the relative change of the model parameters: etar , α , I_{\max} and I_{\min} .

also shown that the study of time series and chained-parameter analysis for correlated C2C variability simulations is a required action. We also investigated the impact that variations in the model inputs (parameters) have in the model outputs (observables) using a one-way sensitivity analysis. The role of each model parameter was assessed and presented graphically summarizing the intensity and detected trend between parameter and observable (direct or inverse).

Table 4

Intensity and sign (direct or opposite) of four observables against all the analyzed parameters. + and - signs for direct and inverse dependence, respectively. Green: greater than 10%, orange: less than 10% and red 0%.

| | I_{HRS} | I_{LRS} | V_S | V_R |
|---------------|-----------|-----------|-------|-------|
| V_{app} | - | 0 | + | 0 |
| R_i | 0 | - | 0 | + |
| etas | 0 | 0 | 0 | 0 |
| etar | - | 0 | + | + |
| α | + | + | - | + |
| V_r | + | 0 | - | + |
| R_s | 0 | - | 0 | - |
| I_{sb} | 0 | 0 | + | 0 |
| I_{\max} | + | + | - | + |
| I_{\min} | + | 0 | - | 0 |
| gam | + | 0 | - | 0 |

Declaration of Competing Interest

The authors declare that they have no known competing financial interests or personal relationships that could have appeared to influence the work reported in this paper.

Data availability

Data will be made available on request.

Acknowledgements

This work was supported by the Spanish Ministry of Science, Innovation and Universities through project PID2019-103869RB-C32. 'Departament de Recerca i Universitats de la Generalitat de Catalunya' is acknowledged for the 2020 FISDU 00261 grant.

References

- [1] Yu S, Chen PY. *IEEE Solid State Circuits Magazine* 2016;8(2):43–56.
- [2] J. S. Lee S. Lee, and T. W. Noh, *Appl. Phys. Rev.*, vol. 2, no. 3, 031303 (2015).
- [3] Jo SH, Chang T, Ebong I, Bhadviya BB, Mazumder P, Lu W. *Nano Lett* 2010;10(4):1293–301.
- [4] Chen A, Lin MR. *IEEE IRPS* 2011;843–846.
- [5] A. Saltelli S. Tarantola, F. Campolongo, and M. Ratto, *John Wiley & Sons, Ltd*, (2004).
- [6] Salvador E, Gonzalez MB, Campabadal F, Martín-Martínez J, Rodríguez R, Miranda E. *Solid State Electron* 2021;185:108040.
- [7] Miranda E. *IEEE TNano* 2015;14:787–9.
- [8] A. Saltelli, M. Ratto, T. Andres, F. Campolongo, J. Cariboni, D. Gatelli, M. Saisana and S. Tarantola, *John Wiley & Sons, Ltd*, (2008).
- [9] Bargallo M, Martín-Martínez J, Maestro MC, Acero MC, Nafria M, Campabadal F. *IEEE Trans Electron Devices* 2016;63(8):3116–22.
- [10] Piccolboni G, Molas G, Garbin D, Vianello E, Cueto O, Cagli C, et al. *IEEE Electron Device Lett* 2016;37(6):721–3.
- [11] Poblador S, Gonzalez MB, Campabadal F. *Microelectron Eng* 2018;187–188:148–53.
- [12] Karpov V, Niraula D, Karpov I. *Appl Phys Lett* 2015;109:1–5.
- [13] Delignette-Muller ML, Dutang C. *J Stat Softw* 2015;64:1–34.
- [14] Alonso FJ, Maldonado D, Aguilera AM, Roldán JB. *Chaos. Solitons and Fractals* 2021;143:110461.



Emili Salvador Aguilera is a PhD student at the Electronical Engineering department from the Universitat Autònoma de Barcelona under the supervision of Enrique Alberto Miranda and Rosana Rodríguez, from the same department. Prior to the PhD, coursed my Bachelor degree in Nanoscience and Nanotechnology and Master degree in Advanced Nanoscience and Nanotechnology at the Universitat Autònoma de Barcelona. He carried out my Master thesis at the Institut Català de Nanociència i Nanotecnologia (ICNZ) working in the graphene transistors field.



Javier Martin-Martinez Javier Martin-Martinez received the M.S. degree in physics from the Universidad de Zaragoza, Zaragoza, Spain, in 2004, and the Ph.D. degree from the Universitat Autònoma de Barcelona (UAB), Bellaterra, Spain, in 2009. He was with the Università degli Studi di Padova, Padua, Italy, and IMEC, Leuven, Belgium. He is currently an Associate Professor with UAB. His main research interests include the characterization and modeling of failure mechanisms in MOS-FETs and also RRAM characterization and modeling for neuromorphic applications.



Mireia Bargallo Gonzalez received the degree in physics from the University of Barcelona, Barcelona, Spain, and the Ph.D. degree on the topic of stress analysis and defect characterization techniques of semiconductor materials and devices, from Katholieke Universiteit Leuven, Leuven, Belgium, in 2011. She pursued her Ph.D. thesis with the Interuniversity Microelectronics Center (imec), Leuven, Belgium. In 2011, she joined the Institut de Microelectrònica de Barcelona (IMB-CNM, CSIC). Her current research interests include electrical characterization, modeling and applications of resistive switching devices.



Rosana Rodriguez received the Ph. D. in Electrical Engineering from Universitat Autònoma de Barcelona (UAB) in 2000. Funded by the Fulbright program, she worked on devices and circuits reliability at the IBM Thomas J. Watson Research Center (USA). Currently, she is associate professor at the UAB. Her research is focused on the variability and reliability of advanced CMOS devices. She is interested in the electrical characterization and modeling of process-related and time-dependent variability sources as Random Telegraph Noise (RTN) and aging mechanisms as Bias Temperature instability (BTI) and Hot Carrier Injection (HCI). Her research includes the study of the variability impact on the performance of single devices and digital and analogical circuits. She is also interested in the characterization of resistive switching devices (memristors) and their application for non-volatile memories, computing and neuromorphic applications.



Francesca Campabadal received the Ph.D. degree in physics from the Universitat Autònoma de Barcelona, Bellaterra, Spain, in 1986. She joined the Institut de Microelectrònica de Barcelona, Consejo Superior de Investigaciones Científicas, Barcelona, Spain, in 1987, where she is currently a Research Professor. Her current research interests include the deposition of high-k dielectric layers, their electrical characteristics, and the resistive switching phenomena in RRAM devices.



ENRIQUE MIRANDA is Professor at the Universitat Autònoma de Barcelona (UAB), Spain. He has a PhD in Electronics Engineering from the UAB (1999) and a PhD in Physics from the Universidad de Buenos Aires, Argentina (2001). He received numerous scholarships and awards including: RAMON y CAJAL (UAB), DAAD (Technical University Hamburg-Harburg), MATSUMAE (Tokyo Institute of Technology, Japan), TAN CHIN TUAN (Nanyang Technological University, Singapore), WALTON award from Science Foundation Ireland (Tyndall National Institute), Distinguished Visitor Award (Royal Academy of Engineering, UK), CESAR MILSTEIN (CNEA, Argentina), Visiting Professorships from the Abdus Salam International Centre for Theoretical Physics, Slovak Academy of Sciences, Politecnico di Torino, Leverhulme Trust (University College London, UK), and Nokia Foundation (University of Turku, Finland). He serves as member of the Distinguished Lecturer program of the Electron Devices Society (EDS-IEEE) since 2001 and as Associate Editor of Microelectronics Reliability since 2003. He has authored and co-authored around 250 peer-review journal papers.

Article SSE24

*SPICE simulation of the time-dependent
clustering model for dielectric breakdown*

E. Salvador, R. Rodriguez, E. Miranda



Contents lists available at ScienceDirect

Solid State Electronics

journal homepage: www.elsevier.com/locate/sse

SPICE simulation of the time-dependent clustering model for dielectric breakdown

E. Salvador^{*}, R. Rodriguez, E. Miranda

Departament d'Enginyeria Electrònica, Universitat Autònoma de Barcelona, 08193 Cerdanyola del Valles, Spain

ARTICLE INFO

The review of this paper was arranged by Prof. Sorin Cristoloveanu

Keywords:
clustering
breakdown
reliability
SPICE
Weibull

ABSTRACT

In this letter, a method for dealing with the time-dependent dielectric breakdown (TDDB) of oxide layers in MOS and MIM structures in the framework of SPICE simulations is reported. In particular, we focus the attention on the clustering model (Burr's XII distribution) for dielectric breakdown which can be considered an extension of the well known Weibull model. The oxide time-to-breakdown for both models is calculated using the inversion method for the cumulative distribution function. For the sake of completeness, the proposed approach includes uncorrelated variability both in the initial and final resistance states. For illustrative purposes, it is also shown how voltage acceleration, progressive breakdown or any other correlation factor can be introduced in the simulation parameters. As an application example, the proposed method is used to simulate the simplest case of a gate-to-drain dielectric breakdown of a NMOS-based inverter circuit.

1. Introduction

Because of the stochastic nature of the dielectric breakdown (BD) phenomenon in metal–oxide–semiconductor (MOS) and metal–insulator–metal (MIM) devices, its statistical features need to be addressed in terms of probability distributions. The most widely used distribution representing the time-to-BD statistics for constant or ramped voltage/current stress is the Weibull distribution [1]. This is a very flexible distribution able to capture different failure rate regimes, the most relevant one in the context of oxide reliability being the wearout phase (increasing failure rate). In previous studies, Monte Carlo simulations were used to investigate compound Weibull distributions [2] as well as the deviations caused by the oxide thickness variation and series resistance effect [3]. However, in recent years, oxide failure data have been shown to follow in many cases the so-called time-dependent clustering (TDC) model, from which the Weibull distribution can be derived as one of its limits [4]. Weibull and TDC coincide at the lowest percentiles but they notoriously differ at the highest ones. Importantly, TDC not only applies to failure data but also to the set and reset voltages of memristive devices based on the resistive switching (RS) mechanism [5,6]. TDC is a member of the Burr's family of distributions (Burr XII) and it can be regarded as a superposition of Weibull distributions with different scale factors [7]. This distribution of scale factors can arise for instance from a nonuniform gate oxide thickness from device to device

which reflects in a wider spread of the BD times. In the case of RS devices, the distribution of scale factors can be attributed to the different current capacities of the generated filamentary structures. In any case, TDC involves some kind of additional variability in the analyzed data (detectable or undetectable) other than the weakest link character of dielectric BD. Monte Carlo simulations were also used to investigate TDC in the context of Bayesian inference [8] and non-uniform BD [7,9,10]. In this work, TDC is implemented in the LTspice XVII circuit simulator from Analog Devices [11] with the aim of simulating the oxide failure event occurring during a constant voltage stress. This is the typical experiment considered for qualifying a given MOS or MIM technology and is often referred to as Time-Dependent Dielectric Breakdown (TDDB). The proposed methodology can be adapted to more complex situations in which device area, stress voltage and temperature acceleration or correlation effects across model parameters and/or in between the initial and final resistance states of the device need to be considered. In the general case, to accomplish these objectives one can make use of feedback signals (current or voltage) acting on the behavioral electric components provided by the simulator or by adding new elements to the basic circuit. Here, we will concentrate on the simplest case, *i.e.* when the applied voltage directly drops across the device under test but series resistance effects can be easily included in the simulations. Once the simulation ends, measurement directives allow extracting the target information for further analysis or just for the generation of

^{*} Corresponding author.

E-mail address: emili.salvador@uab.cat (E. Salvador).

<https://doi.org/10.1016/j.sse.2024.108895>

Available online 7 March 2024
0038-1101/© 2024 Published by Elsevier Ltd.

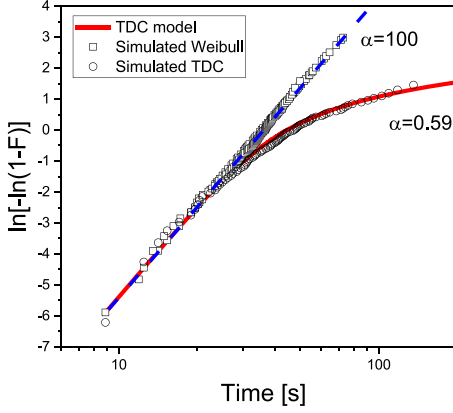


Fig. 1. Simulated data using the LTspice model (symbols) and calculated curves (lines) using Eqs. (1) and (4). The blue dashed line corresponds to the Weibull model. (For interpretation of the references to colour in this figure legend, the reader is referred to the web version of this article.)

statistical reports. The method is extended to the case of progressive breakdown of the oxide layer. A simple example consisting in a biased MOS transistor with a gate-to-drain dielectric BD working as an inverter is used to illustrate how the proposed approach operates in a circuit environment.

2. Theoretical considerations

According to the TDC model, the cumulative distribution function for the BD events reads:

$$F_c(t) = 1 - \left[1 + \frac{1}{\alpha} \left(\frac{t}{\tau} \right)^\beta \right]^{-\alpha} \quad (1)$$

where α is the clustering factor, β the shape factor, and τ the scale factor (characteristic time). τ corresponds to the 63rd percentile value of the failure time. Following [8], expression (1) can be rewritten as:

$$F(t) = 1 - \exp \left\{ -\alpha \ln \left[1 + \frac{1}{\alpha} \left(\frac{t}{\tau} \right)^\beta \right] \right\} \quad (2)$$

so that considering a series expansion results:

$$F(t) = 1 - \exp \left\{ -\alpha \left[\frac{1}{\alpha} \left(\frac{t}{\tau} \right)^\beta - \frac{1}{2} \left(\frac{1}{\alpha} \left(\frac{t}{\tau} \right)^\beta \right)^2 + \frac{1}{3} \left(\frac{1}{\alpha} \left(\frac{t}{\tau} \right)^\beta \right)^3 - \dots \right] \right\} \quad (3)$$

For $\alpha \rightarrow \infty$, the Weibull distribution is obtained:

$$F_w(t) = 1 - \exp \left[- \left(\frac{t}{\tau} \right)^\beta \right] \quad (4)$$

It can be demonstrated that expression (4) coincides with expression (1) at the lowest percentiles. In Fig. 1, the corresponding Weibull functions W calculated as $W = \ln[-\ln(1-F)]$ are plotted. In order to generate BD times consistent with Eq. (1) and therefore with Eq. (4) in the appropriate limit, Eq. (1) is inverted for a uniform random number $u \sim \text{Unif}[0,1]$ so that the BD time reads:

$$t = \tau \left\{ \alpha \left[u^{\frac{1}{\alpha}} - 1 \right] \right\}^{\frac{1}{\beta}} \quad (5)$$

```
.tran 0 200 0 1e-3
.step param run 1 200 1
.param R0=10Meg+gauss(1Meg) RBD=10K+gauss(1K)
.param a=0.592 b=4.258 t0=4.2E2 gam=3.61E-1
.param seed=1000 t=t0*exp(-gam*Vs) Vs=7
.param tbd=t*((a*(rand(run+seed)**(-1/a)-1))**(1/b))
```

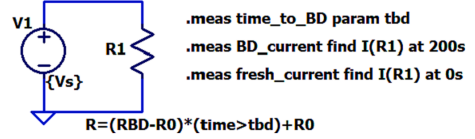


Fig. 2. Complete schematic in LTspice for the time-dependent clustering and Weibull models for dielectric breakdown. The complete explanation about the expressions and commands used in this script is provided in Section 3.

Notice that since u is uniformly distributed, $1-u$ is also uniformly distributed. As reported in [12], for the model parameters considered in this work, τ is a voltage-dependent parameter which in the framework of the E -model (voltage acceleration) [7,13] is expressed as:

$$\tau = \tau_0 \exp[-\gamma(V - I \cdot R_s)] \quad (6)$$

where τ_0 and γ are constants, V the applied voltage, I the current flowing through the device and R_s a series resistance. Eq. (6) illustrates how the potential drop in a series resistance can be introduced in the characteristic failure time as a feedback or correction term. This kind of effect has been reported in [3].

It is also worth mentioning that alternative expressions for the voltage acceleration factor in Eq. (6) such as the V^0 -model [14], $1/E$ -model [7] or $E^{1/2}$ -model [2] can be considered as well.

3. SPICE model and simulation results

Simulations were carried out using the LTspice XVII simulator. This is a free downloadable circuit solver with a powerful simulation engine. For the sake of simplicity, the clustering parameters reported in [12] for the first BD event in $\text{Al}_2\text{O}_3/\text{HfO}_2$ -based devices are considered. This is not relevant in the context of this work since we are not focusing neither on a particular device nor technology. We are presenting a computational method for its use in a circuit simulator which can be easily adapted to the user's particular needs. Since we will not analyze here the case of multiple failure events, the potential drop in Eq. (6) caused by the current flowing through the device can in principle be neglected. The proposed circuit schematic is illustrated in Fig. 2. After the definition of the total simulation time (200 s) and maximum timestep (1 ms), the parameter *run* (from 1 to 200 in unity steps) determines the number of independent simulations to be generated. Then, parameters α (a), β (b), τ_0 (t_0), and γ (gam) are specified. *seed* (1000) is a parameter used to alter the random number generator output. *tbd* computes the BD time using Eqs. (5) and (6) with uniform random numbers generated by the stepped parameter *run*. V_s (7 V) is the stress voltage. R specifies the device resistance before (R_0) and after (R_{BD}) the BD event. *time > tbd* is a logic expression whose value is 1 for *time > tbd* and 0 for *time < tbd*. For simplicity, pre- and post-BD resistance values with Gaussian variability were assumed here but notice that these component can be easily edited so as to represent the current flowing through the fresh device (tunneling, Schottky, Poole-Frenkel, etc.) and the BD current (soft or hard BD, quantum point contact: $R = h/(2e^2N)$, etc.). R abruptly changes as the simulation proceeds according to *tbd*. Finally post-processing directives (*.meas*) provide the required outcomes as a function of the simulation run. In this particular case, the BD time is stored in the variable called *time_to_BD*. The current flowing through the device at the

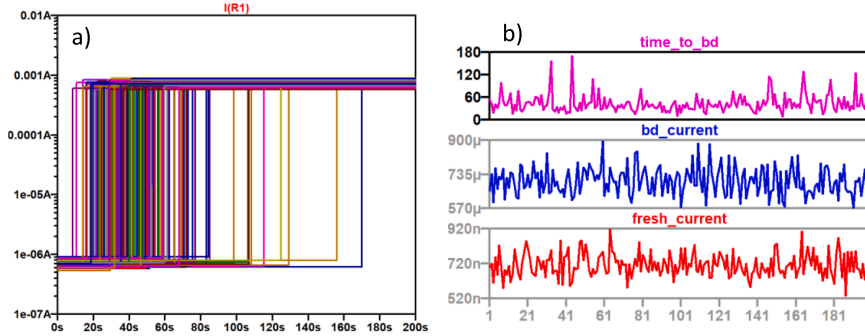


Fig. 3. A) Itspice simulations of the bd process using tdc. b) the time-to-bd, post-bd current and initial current as a function of the simulation number are also reported.

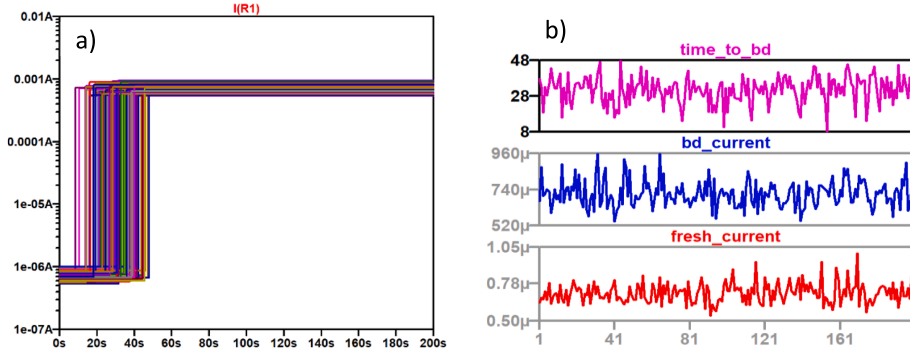


Fig. 4. A) Itspice simulations of the bd process using weibull. b) the time-to-bd, post-bd current and initial current as a function of the simulation number are also reported.

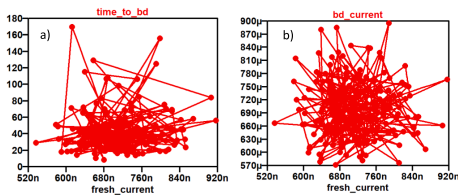


Fig. 5. Correlation plots among generated variables using TDC: a) time-to-BD as a function of the fresh current magnitude, b) post-BD current as a function of the fresh current magnitude. In this case, no specific correlations are expected.

onset (0 s) and end time (200 s) of the simulation are also recorded for further analysis. All these results can be viewed using the *Plot.step'ed.meas data* option (right click on the mouse) in the *VIEW* → *SPICE Error Log* tag. Notice that the BD times generated in this way can exceed the chosen simulation time window. In this case a redefinition of the total simulation time is required in order to avoid censoring. Average

quantities or specific circuit values at a given time or condition can also be achieved using similar directives.

Fig. 1 shows the Weibit plot for the simulated BD times according to the TDC (see Fig. 3.a) and Weibull (see Fig. 4.b) approaches. Notice the close agreement between the simulated data and the theoretical curves calculated using Eqs. (1) and (4). As expected, both distributions coincide at the lowest percentiles and differ for the longest BD times. For completeness, Fig. 3.b and 4.b show the BD times and the initial and final current values as a function of the simulation run. Correlation plots are provided for the TDC model in Fig. 5. In the present case, currents are straightforwardly linked to the resistance values so that no correlations across calculated variables are expected. These plots are just for illustrating the kind of analysis that can be performed using the post-processing tools (*.meas* in Fig. 2) the simulator offers.

In addition, Fig. 6 illustrates how the proposed approach can deal with voltage acceleration (see Eq. (6)). As the applied voltage is reduced ($V_g = 9, 7, \text{ and } 3 \text{ V}$), longer BD times are statistically observed. This is equivalent to the addition of a series resistance in the circuit mesh. The acceleration law appears as a multiplicative factor in Eq. (6) and this affects both the average value and dispersion of the BD times.

The proposed approach also allows modeling progressive breakdown of the oxide layer. If a sigmoidal evolution [15] is assumed for the

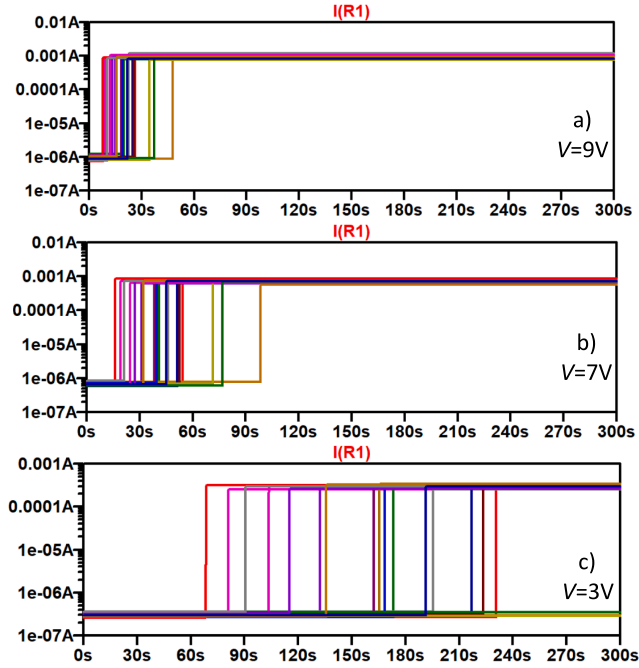


Fig. 6. Simulated curves using the TDC model with applied voltages: a) $V_g = 9$ V, b) 7 V, and c) 3 V.

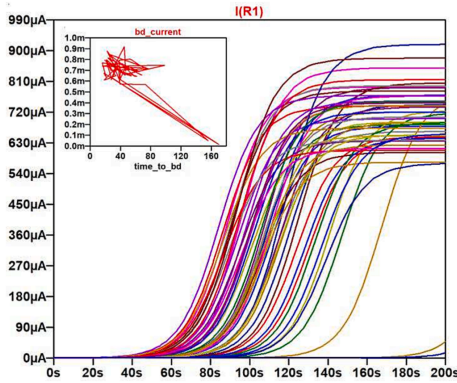


Fig. 7. Simulated curves using the TDC model and the progressive breakdown resistance (see Eq. (7)). The inset shows the final current magnitude as a function of the time to breakdown. Curves were obtained using the script shown in Fig. 2 with $k = 0.1 \text{ s}^{-1}$.

breakdown resistance R in Fig. 2:

$$R = (RBD - R0) \{1 - \exp[-k(\text{time} - \text{tbd})]\} \cdot (\text{time} > \text{tbd}) + R0 \quad (7)$$

the results shown in Fig. 7 are obtained. k is a constant referred to as the degradation rate and depends on the applied voltage [16]. In this case, progressive breakdown and clustering/weibull models are combined in a single approach. As expected, the final state of the device depends on the total simulation time, the time-to-BD, and the initial and final distributions of resistances. As is clearly seen in Fig. 7's inset, the final breakdown current is no longer gaussian-distributed, i.e. degradation time matters.

4. Application to circuit simulations

The simulation of a failure event in SPICE or in any other simulator is important not only for the effects occurring in the device itself but also for the consequences this event can generate in the rest of a circuit [17,18,19,20,21]. As an application example, Fig. 8 shows the effects of a severe gate-to-drain dielectric BD occurring in transistors. Only the TDC case is investigated here for a simple NMOS inverter circuit. The same parameter values as in the previous sections were used just for illustrative purposes but they actually need to be tuned for the pulsed stress (dead times need to be considered). As shown in Fig. 8.a a pulsed signal (0–5 V) with duty cycle 0.5 is applied to the gate of the transistor (2 N7002). At ~ 35 s, according to the TDC distribution, the oxide breaks down establishing a direct path between gate and drain. A simple resistor (hard BD) was considered here but a power-law (soft BD) for the current-voltage characteristic can also be assumed [13,18,22]. From

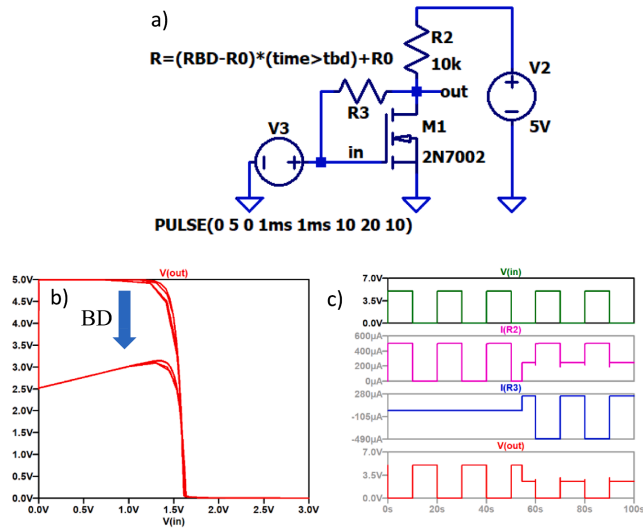


Fig. 8. A) application of the tdc model to a nmos inverter circuit. b) transfer curve for the circuit shown in a) before and after the bd event. c) input and output characteristics of the transistor as a function of time before and after the bd event ($t_{bd} \sim 35$ s).

this point on, the circuit does no longer work as expected. Fig. 8.b shows the transfer function before and after the BD event. The channel current cannot be switched off and the gate current reaches positive and negative values as reported in [20]. The bottom panel in Fig. 8.c illustrates that, though the device still operates as an inverter, the output voltage excursion becomes limited. In [23], a similar problem was addressed in SPICE but considering the contribution of several independent voltage-controlled current sources in the gate-drain circuit. The authors analyzed the impact of a successive BD events on the performance of a ring oscillator. In this case, Monte Carlo simulations were carried out in combination with the Weibull distribution. Successive BDs in a CMOS inverter and their impact on the frequency drift of a ring oscillator were also investigated in [24] but again in the context of Weibull distribution. For the case of a gate-to-channel short, a model consisting in third order polynomial sources at the drain and source with a third current source in between drain and source with value proportional to the channel current was proposed in [25]. In none of the cases, the script used for generating the oxide BD data was provided.

5. Conclusions

A SPICE approach for simulating the breakdown time of the oxide layer in MOS and MIM structures was reported. We show how the clustering model for dielectric breakdown can be implemented using the inversion method for the cumulative distribution function. The Weibull distribution is included as a limiting case. Most of the paper is devoted to abrupt breakdown events, but it has also been shown how the equations can be adapted to the progressive breakdown case. A simple example (NMOS inverter with a gate-to-drain hard breakdown) showing how the proposed approach applies in a circuit environment was also presented.

CRedit authorship contribution statement

E. Salvador: Conceptualization, Formal analysis, Investigation,

Supervision, Writing – original draft, Writing – review & editing. R. Rodríguez: Conceptualization, Funding acquisition, Investigation, Supervision, Writing – original draft, Writing – review & editing. E. Miranda: Conceptualization, Formal analysis, Investigation, Supervision, Writing – original draft, Writing – review & editing.

Declaration of competing interest

The authors declare the following financial interests/personal relationships which may be considered as potential competing interests: Enrique Miranda reports financial support was provided by EMPIR programme, project MEMQuD, code 20FUN06.

Data availability

Data will be made available on request.

Acknowledgements

E.M. acknowledges the support provided by the European project MEMQuD, code 20FUN06, which has received funding from the EMPIR programme co-financed by the Participating States and from the European Union's Horizon 2020 research and innovation programme. This work has been partially developed under Grant PID2022-139586NB-CB41 funded by MCIN/AEI/10.13039/501100011033 and by "ERDF A way of making Europe". The Spanish MCIN/AEI/10.13039/501100011033 under grant PID2019-103869RB-C32 and the 'Departament de Recerca i Universitats de la Generalitat de Catalunya' for the 2020 FISDU 00261 scholarship are also acknowledged.

References

- [1] Wu E. Facts and myths of dielectric breakdown processes—Part II: post-breakdown and variability. *IEEE Trans Electron Devices* 2019;66:4535.

- [2] Chen F, Graas C, Shinosky M, Zhao K, Narasimha S, Liu X, et al. Breakdown data generation and in-die deconvolution methodology to address BEOL and MOL dielectric breakdown challenges. *Mic Rel* 2015;55:2727.
- [3] Roy D, Bruyere S, Vincent E, Monsieur F. Series resistance and oxide thickness spread influence on weibull breakdown distribution: new experimental correction for reliability projection improvement. *Mic Rel* 2002;42:1497.
- [4] Wu E, Li B, Stathis J. Modeling of time-dependent non-uniform dielectric breakdown using a clustering statistical approach. *Appl Phys Lett* 2013;103:152907.
- [5] Raghavan N. Failure of weibull distribution to represent switching statistics in OxRAM. *Mic Eng* 2017;178:230.
- [6] Sun H, Zhang M, Li Y, Long S, Liu Q, Lv H, et al. A cell-based clustering model for the reset statistics in RRAM. *App Phys Lett* 2017;110:123503.
- [7] Shimizu T, Suzumura N, Ohgata K, Tsuchiya H, Aono H, Osagawara M. "A new aspect of time-dependent clustering model for non-uniform dielectric TDDB", 2016 IEEE International Reliability Physics Symposium (IRPS), Pasadena, CA, USA, 2016, pp. 3A-4-1-3A-4-10.
- [8] Kunii K, Endo S, Yokozawa S. Bayesian inference of a lifetime distribution parameter on the time-dependent dielectric breakdown with clustering defects. *Jap J App Phys* 2019;58. SHHG02.
- [9] Wu E, Li B, Stathis J, Achanta R, Filippi R, McLaughlin P. "A time-dependent clustering model for non-uniform dielectric breakdown", 2013 IEEE International Electron Devices Meeting, Washington, DC, USA, 2013, pp. 15.3.1-15.3.4.
- [10] Mei S, Raghavan N, Bosman M, Pey KL. "Statistical basis and physical evidence for clustering model in FinFET degradation", 2017 IEEE International Reliability Physics Symposium (IRPS), Monterey, CA, USA, 2017, pp. 3C-1.1-3C-1.6.
- [11] <https://www.analog.com/en/design-center/design-tools-and-calculators/tspice-simulator.html>.
- [12] Muñoz J, Gonzalez MB, Campabadal F, Suñé J, Miranda E. Application of the clustering model to time-correlated oxide breakdown events in multilevel antifuse memory cells. *IEEE Elect Dev Lett* 2020;41:1770.
- [13] Li X, Qin J, Bernstein J. Compact modeling of MOSFET wearout mechanisms for circuit-reliability simulation. *IEEE Trans Dev Mat Rel* 2008;8:98.
- [14] Wu EY, Nowak EJ, Vayshenker A, Lai WL, Harmon DL. CMOS scaling beyond the 100-nm node with silicon-dioxide-based gate dielectrics. *IBM J Res Develop* 2002; 46:287.
- [15] Miranda E, Jiménez D, Suñé J. Progressive breakdown dynamics and entropy production in ultrathin SiO₂ gate oxides. *Appl Phys Lett* 2011;98:253504.
- [16] Aguirre F, Rodriguez-Fernandez A, Pazos S, Suñé J, Miranda E, Palumbo F. Study on the connection between the set transient in RRAMs and the progressive breakdown of thin oxides. *IEEE Trans Electron Dev* 2019;66:3349.
- [17] Rodriguez R, Stathis J, Linder B, Kowalczyk S, Chuang C, Joshi R, et al. The impact of gate-oxide breakdown on SRAM stability. *IEEE Elect Dev Lett* 2002;23:559.
- [18] Rodriguez R, Stathis J, Linder B. A model for gate-oxide breakdown in CMOS inverters. *IEEE Elect Dev Lett* 2003;24:114.
- [19] Kaczer B, Degraeve R, Roussel Ph, Groeseneken G. Gate oxide breakdown in FET devices and circuits: from nanoscale physics to system-level reliability. *Mic Rel* 2007;47:559.
- [20] Nicollan P, Cakici R, Krishnan A, Reddy V, Seshadri A. Device characteristics and equivalent circuits for NMOS gate-to-drain soft and hard breakdown in polysilicon/SiON gate stacks. *IEEE Trans Electron Dev* 2011;58:1170-5.
- [21] Miranda E, Kawanago T, Kakushima K, Suñé J, Iwai H. Analysis and simulation of the postbreakdown I-V characteristics of n-MOS transistors in the linear response regime. *IEEE Elect Dev Lett* 2013;34:798.
- [22] Fang J, Sapatnekar S. Scalable methods for analyzing the circuit failure probability due to gate oxide breakdown. *IEEE Trans Very Large Scale Int Sys* 2012;20:1960.
- [23] Panagopoulos G, Ho C, Kim S, Roy K. "Physics-based compact modeling of successive breakdown in ultrathin oxides. *IEEE Trans Nano* 2015;14:7.
- [24] Saliva M, Cacho F, Huard V, Angot D, Federspiel X, Durand M, Parra M, Bravaix A, Anghel L. "New insights about oxide breakdown occurrence at circuit level," 2014 IEEE International Reliability Physics Symposium, Waikoloa, HI, USA, 2014, pp. 2D.5.1-2D.5.6.
- [25] Chehade S, Chehab A, Kayssi A. "Modeling of gate oxide short defects in MOSFETS", 2009 4th International Design and Test Workshop (IDT), Riyadh, Saudi Arabia, 2009, pp. 1-4.

Article JLPEA24

*A Simple, Robust, and Versatile MATLAB
Formulation of the Dynamic Memdiode Model
for Bipolar-Type Resistive Random Access
Memory Devices*

E. Salvador, R. Rodriguez, E. Miranda



A simple, robust, and versatile MATLAB formulation of the dynamic memdiode model for bipolar-type RRAM devices

Emili Salvador, Rosana Rodriguez, Enrique Miranda

Departament d'Enginyeria Electrònica, 08193 Cerdanyola del Valles, Universitat Autònoma de Barcelona.

• Correspondence: emili.salvador@uab.cat

Abstract: Modeling in an emerging technology like RRAM devices is one of the pivotal concerns for its well-development. In the current bibliography, most of the models face difficulties to implement or simulate unconventional scenarios, particularly when dealing with complex input signals. In addition, circuit simulators like SPICE require long running times for high resolution results because of their internal mathematical implementation. In this work, a fast, simple, robust, and versatile model for RRAM devices built in MATLAB is presented. The proposed model is a recursive and discretized version of the dynamic memdiode model (DMM) for bipolar-type resistive switching devices originally implemented in LTspice. The DMM model basically consists in two coupled equations: one for the current (non-linear current generator) and a second one for the memory state of the device (time-dependent differential equation). This work presents an easy-to-use tool for researchers to reproduce the experimental behavior of their devices and predicting the outcome from non-trivial experiments. Three study cases are reported aimed at capturing different phenomenologies: a frequency effect study, a cycle-to-cycle variability fit, and a stochastic resonance impact analysis.

Keywords: RRAM, memristor, MATLAB, Stochastic Resonance, Variability

1. Introduction

In recent years, the scientific community in the microelectronics field has expressed huge interest in RRAM (Resistive Random Access Memory) devices due to their unique properties such as low power consumption, high scalability, endurance, and CMOS compatibility, among others [1]. As the switching material, these devices can be based on metal oxides like TiO₂ or HfO₂, chalcogenide glasses, lower dimensional materials like nanowires or nanodots as well as other novel materials like metal-oxide frameworks [2–4]. Their application range include logic circuits, neuromorphic systems, cryptology, and information storage [5–9]. Since RRAM devices are still an emerging technology, device level characterization and powerful modeling tools are key for enhancing its evolution to a massive commercialization. Up to the date, a lot of models are implemented in simulators like Spice or Verilog [10]. These simulators are useful for complex architectures involving several devices but also lead to long waiting times for running the simulations and post-processing the data. In this work, a simple and effective tool is presented for reproducing the behavior of single RRAM devices in MATLAB, a common and well-known programming language. The advantages of the tool presented consist in easy implementation (since the script is openly included in the manuscript), straightforward data analysis, short simulating running times, and versatility in terms of parameters definition and input possibilities (applying non-trivial signals like noise). In the current literature, a few works using MATLAB for RRAM modeling are discussed. In [11], different existing models were studied using MATLAB simulations. In [12], a Kinetic Monte Carlo simulation in MATLAB to estimate and optimize the reliability of RRAM devices was reported. In [13], the implementation of a memristor-based neural network using MATLAB, Simulink and LTspice for simulations and analysis was presented. In this work, the presented

Citation: To be added by editorial staff during production.

Academic Editor: Firstname Last-name

Received: date

Revised: date

Accepted: date

Published: date



Copyright: © 2024 by the authors. Submitted for possible open access publication under the terms and conditions of the Creative Commons Attribution (CC BY) license (<https://creativecommons.org/licenses/by/4.0/>).

tool consists in a recursive version of the dynamic memdiode model (DMM) for RRAM devices, which was originally built for LTspice [14]. Its main features and the corresponding script are introduced in Section 2. In Section 3, a study about the effect of the input signal frequency is shown. Section 4 disserts a method for incorporating cycle-to-cycle variability in the model. Finally, a stochastic resonance impact study is presented in Section 5.

2. Dynamic Memdiode Model

This section introduces the DMM, which is defined by means of mainly two coupled equations, one for the current conduction and another for the memory state. The DMM is a compact behavioral model built under the idea that the current flows through a conductive filament (CF) running across the insulating layer of a metal-insulator-metal/semiconductor structure. The CF is created and destroyed as the consequence of the application of an external field, and this is the origin of the switching behavior [15–16]. For a bipolar-type resistive switching device, the DMM reads:

$$I(V) = I_0(\lambda) \sinh \{ \alpha(\lambda) [V - (R_i + R(\lambda))] \} \quad (1)$$

where $I_0(\lambda) = (I_{on} - I_{off})\lambda + I_{off}$ is the current amplitude and λ the memory state (I in the model script) which ranges from 0 to 1. $\alpha(\lambda)$ (a in the model script) and $R(\lambda)$ are defined in the same way as I_0 . ‘off’ and ‘on’ terms are linked to the high and low-resistance states (HRS and LRS), respectively. V is the input voltage and R_i is a constant series resistance [14]. After some considerations thoroughly discussed in [17], the discrete recursive approach for the I - V characteristic reads:

$$I(V) \approx \frac{1}{\alpha R} \left\{ W \left[\frac{\alpha R I_0}{2} \exp(\alpha V_i) \right] - W \left[\frac{\alpha R I_0}{2} \exp(-\alpha V_i) \right] \right\} \quad (2)$$

where W is the Lambert function (*lambertw* in MATLAB) and $V_i = V - I \cdot R_i$. Next, the evolution of the memory state in the DMM is written as the following balance equation:

$$\frac{d\lambda}{dt} = \frac{1 - \lambda}{\tau_S} - \frac{\lambda}{\tau_R} \quad (3)$$

(3) is the general equation for a redox process and is a nondimensional differential equation. $\tau_{S,R}$ are the characteristic switching times for the set and reset transitions, respectively. According to our convention, the set occurs at positive bias and the reset at negative bias. Again, after some approaches discussed in [17], the recursively expressed and discretized version of (3) reads:

$$\lambda_{t+1} = [\lambda_t - H(V_{it})] \exp \left\{ -\frac{\Delta t}{\tau_{IS,R}} \right\} + H(V_{it}) \quad (4)$$

λ_t is the memory state, Δt the selected timestep and H the Heaviside step function.

$$\tau_{IS}(V_{it}) = \exp [-\eta_S(V_{it} - V_S)] \quad (5)$$

$$\tau_{IR}(V_{it}) = \exp [-\eta_R \lambda^{\gamma} (V_{it} - V_R)] \quad (6)$$

where $\eta_{S,R}$ and $V_{S,R}$ (*vs* and *vr* in the model script) are the transition rates ($\eta_S > 0$, $\eta_R < 0$, *etas* and *etar* in the model script respectively) and reference switching voltages ($V_S > 0$, $V_R < 0$). Physically, these dependences are linked to the movement of metal ions or oxygen vacancies. γ or *gam*, in the model script, controls the reset transition rate. The model is ruled by equations (2) and (4). (5) and (6) are auxiliar functions. The complete script is reported in Table 1, for the reader possibility to copy and use it for its own purposes. In the model script, the first section (in black) builds the input signal. The second section (in green) is dedicated to the model parameters and initial conditions. The third section of the script (in blue) presents the auxiliar functions required by the model equations. The fourth section (in red) calculates the current $I(t+1)$ and the memory state $I(t+1)$. Finally, (in violet)

the simulated currents and voltages are stored in the I_m and V_m variables and plotted in the last two lines of the script, in addition the memory state is stored in the lm variable. The same color pattern is followed in Appendixes A, B and C where the scripts for the case studies in the following Sections 3, 4 and 5 are presented. In the Appendixes, the violet fragment includes the data analysis. Figure 1 shows the model results for the script described in Table 1, showing the typical memristor current-voltage loop (in black) and the memory state-voltage loop (in blue), highlighting the high/low-resistance states and the set/reset processes.

In Figure 2, a study of the impact of modifying different model parameters on the current-voltage characteristic is presented: a) for vs , b) for vr , c) for aon , d) for $aoff$, e) for $etas$ and $etar$, and f) for gam . This study shows the model sensitivity and is a useful guide for potential users of the model.

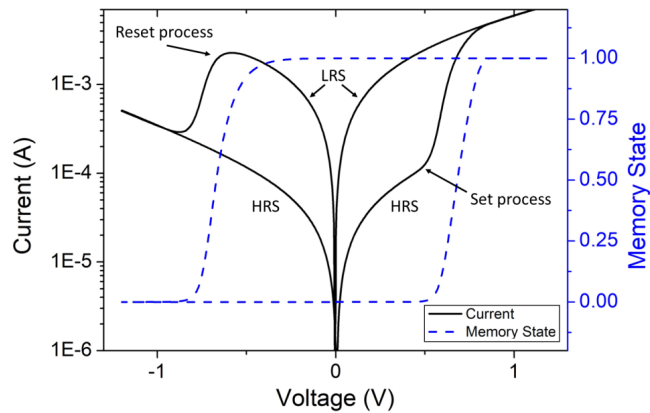


Figure 1. Simulated I - V characteristics obtained with the model script in Table 1. High and low resistance states, and set and reset processes are highlighted. The right Y axis, in blue, represents the memory state.

| Dynamic Memdiode Model in MATLAB | |
|---|--|
| <code>step=5E-3; V1=0:step:1.2; V2=0:-step:-1.2; V=[V1 flip(V1) V2 flip(V2)]; %Voltage input</code> | |
| <code>aoff=2; aon=2; Ri=40; Roff=30; Ron=30; Ioff=10E-5; Ion=3E-3; %Parameter definition</code> | |
| <code>etas=40; etar=-15; gam=0.1; At=1E-3; Vs=0.5; Vr=-0.3; l(1)=0; l(1)=0;</code> | |
| <code>for t=1:length(V) %Auxiliary functions</code> | |
| <code>Vi=V(t)-Ri*I(t); I0=(Ion-Ioff)*l(t)+Ioff; a=(aon-aoff)*l(t)+aoff; R=(Ron-Roff)*l(t)+Roff;</code> | |
| <code>Tsr=exp(-etas*(Vi-Vs))*(V(t)>0)+exp(-etar*l(t)^gam*(Vi-Vr))*(V(t)<=0);</code> | |
| <code>I(t+1)=1/(a*R)*(lambertw(a*R*I0/2)*exp(a*Vi)-lambertw(a*R*I0/2*exp(-a*Vi))); % Model equations</code> | |
| <code>l(t+1)=(l(t)-heaviside(Vi))*exp(-At/Tsr)+heaviside(Vi);</code> | |
| <code>Vm(t)=V(t); Im(t)=I(t); lm(t)=l(t); %Saving variables and plotting</code> | |
| <code>end</code> | |
| <code>semilogy(Vm,abs(Im),'black')</code> | |
| <code>xlabel('Voltage (V)'); ylabel('Current (A)'); title('Current-Voltage Characteristics');</code> | |

Table 1. Script for the recursive dynamic memdiode model implemented in MATLAB. In black, the applied voltage. In green, the model. In blue, the auxiliar functions. In red, the model equations. In violet, saving parameters and plotting the I - V curve.

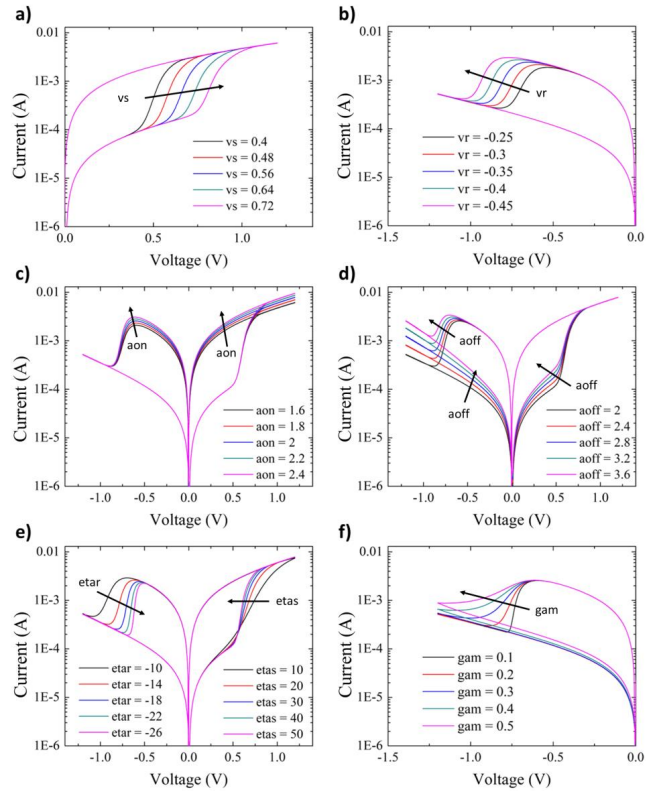


Figure 2. Effect of modifying different model parameters on the I - V characteristics. a) vs , b) vr , c) aon , d) $aoff$, e) $etas$ and $etar$, and f) gam .

3. First case study: Modeling of frequency and ramp rate effects

This section is dedicated to illustrate the model sensibility to variations in the input signal frequency (for sinusoidal signals) or the ramp rate (for voltage ramps). In the literature, it is reported that for high frequencies or ramp rates, both the set and reset voltages of bipolar RS devices increase in absolute value, making a wider butterfly shaped I - V curve. A linear relationship between the logarithm of the ramp rate and the set and reset voltages has been reported [18–19]. For ramped input voltages, the magnitude for expressing the timing is the ramp rate (RR), which is directly related to the signal frequency. Figure 3 presents the evolution of the conduction characteristic for a typical experiment as reported in [19], using a voltage ramp as the input with different RRs of 50 V/s (red), 500 V/s (orange), 5000 V/s (light green) and 50000 V/s (dark green). On the one hand, in Figure 3a, the study is focused on the set evolution when the reset ramp rate is kept fixed. On the other hand, Figure 3b focuses on the reset evolution when the ramp rate for the set event is kept unaltered. Figure 3c shows the evolution of the set and reset voltages as a function of the ramp rate for these cases. Notice that the experimental curves are affected by a series transistor (current limitation during set). Further details about the devices and the

measurement setup can be found in [19]. Simulations are reported in Figure 4 and they do not include the transistor effect. Here, the focus is on the frequency phenomenology. The dependence of the set and reset voltages as a function of the ramp rate is shown in Figure 4a, including I - V curves using as the input signal a voltage ramp with identical ramp rates and colors used in Figure 3a. In Figure 4b, the dependence of the set and reset voltages as a function of the signal frequency is illustrated, including I - V curves using as the input signal a sinusoidal voltage with frequencies of 1 Hz (red), 10 Hz (orange), 100 Hz (light green), and 1000 Hz (dark green). The insets in Figure 4a and 4b show the set and reset voltage evolution as a function of the logarithm of the ramp rate (4a) or the logarithm of the frequency (4b). A linear dependence is found in both cases. The required modifications in the model script to achieve these results can be found in Appendix A. Notice that some parts are omitted, identified with %Ramp Rate, or %Frequency at the end of the line, since in one script the two kind of evaluations (RR or frequency) can be performed. The Appendix A corresponds to the frequency study. For the RR study, delete the lines ending with %Frequency and activate the lines ending with %Ramp Rate. The model parameters RR and Δt (Δt in the model script), included in Appendix A, are modified accordingly to set the desired input signal ramp rate or frequency.

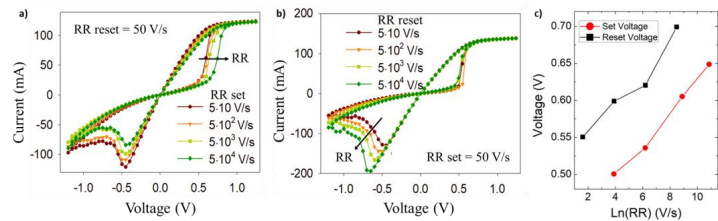


Figure 3. Experimental ramp rate study impact study in [19]. In a) and b) I - V curves for studying the set and reset voltage evolution with the RR respectively. c) Shows the linear evolution of set and reset voltages against the logarithm of RR. Data from [19].

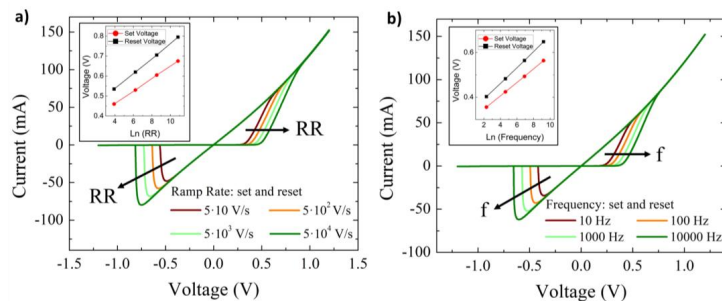


Figure 4. Simulated impact of the ramp rate (a) and frequency (b) on the set and reset voltages: a) I - V curves using as input signal a voltage ramp with a ramp rate of 50 V/s (red), 500 V/s (orange), 5000 V/s (light green) and 50000 V/s (dark green). b) I - V curves using as input signal a sinusoidal voltage with a frequency of 1 Hz (red), 10 Hz (orange) and 100 Hz (light green) and 1000 Hz (dark green). The insets show the linear dependence of the set (red) and reset (black) voltage with the logarithm of the ramp rate (a) or the frequency (b).

4. Second case study: Modeling cycle-to-cycle variability

In RRAM devices, the most significant challenge relates to its inherent C2C variability linked to atomic scale changes in the CF across the dielectric layer [20–21]. The inclusion

of C2C variability is of utmost importance for any comprehensive model intended to reproduce the real device behavior. In the literature, different approaches for including variability in compact modeling can be found [22–24]. This section reproduces the experimental results reported in [25], where uncorrelated C2C variability is included in a previous version of the memdiode model. The experimental data comes from 450 cycles of *I*-*V* curves measured in HfO₂-based memristors. Additional information about the electrical characterization and fabrication process of the devices can be found in [26]. Before the incorporation of the C2C variability in the model, a study of the experimental features of the *I*-*V* curves involving the *fitdistrplus* package for the R language was carried out [27]. The best distributions for each model parameter were found and incorporated into the model parameters definition. Appendix B presents the MATLAB model script used for the simulations discussed in this Section. Here two different examples of parameters including variability are reported:

$$Maoff = 2.1; Saoff = 0.13; aoff = Maoff + Saoff * randn; \quad (7)$$

$$Mloff = 3.7E - 5; loffLN = \log(Mloff); Sloff = 0.06; \quad (8)$$

$$loff = \exp(loffLN + Sloff * randn);$$

In (7) and (8) (see Appendix B), two cases are presented, one following a normal distribution (7) and one following a lognormal distribution (8). The variables defined in (7): *Maoff*, and *Saoff* (which represent the mean and standard deviation respectively) are used to define the normally distributed *aoff* parameter. For a lognormally distributed parameter, like in (8), the same *Mloff*, and *Sloff* are defined, but two extra steps are required: *loffLN*, which is the logarithm of *Mloff* and the application of an exponential function in order to generate the lognormal distribution of *loff*. The *randn* function is used for generating a different random number in every cycle. Notice that not all the model parameters include variability and some of them are constant for the sake of simplicity.

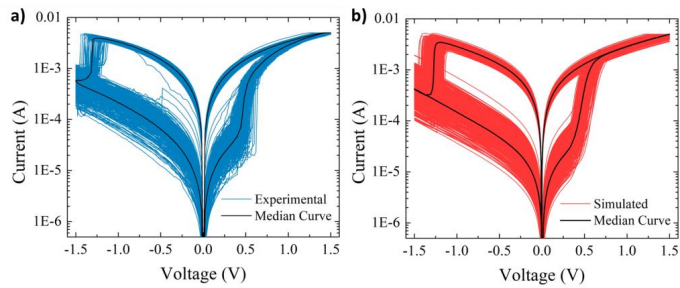


Figure 5. Comparison of the 450 *I*-*V* cycles. a) From the experimental devices in [25] (in blue) and b), from the simulations (in red) including C2C variability. In both figures, the median curve is shown in black. Experimental data from [25].

In Figure 5, the experimental data reported in [25] in blue (5a), and the simulations obtained using the recursive DMM model in MATLAB, in red (5b), are compared. The good agreement between experimental and simulated results indicates the ability of the model to reproduce variability in the *I*-*V* loops. In addition, Figures 6a, 6b, 6c and 6d present the histograms for the HRS current, LRS current, set voltage, and reset voltage, respectively, both for experiments and simulations. All the histograms are well reproduced except the LRS current case, in which the experimental data exhibits a double peak likely caused by different atomic configurations of the CF. In [25], several trials were performed until finding the optimum combination of model parameters for achieving the observed

variability. This process is time consuming when performed in LTspice since the obtained results must be analyzed somewhere else. Now, the parameters, model equations and data analysis are carried out with the same MATLAB script largely reducing the spent time, thus easing the possibility of finding better fitting results.

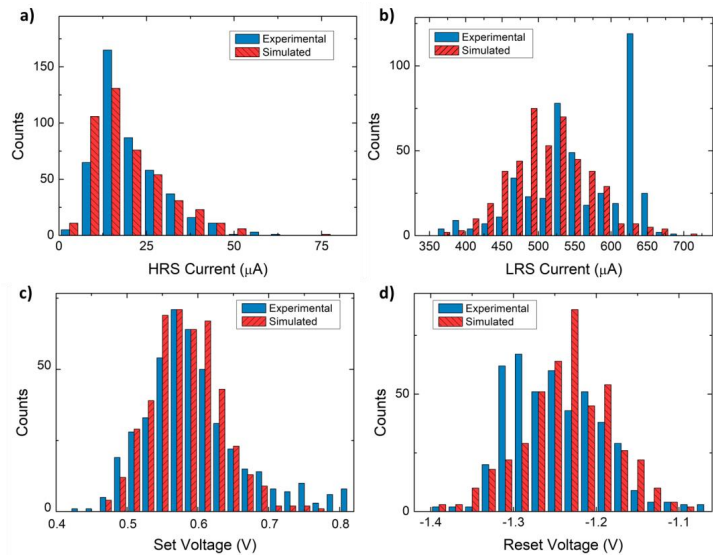


Figure 6. Histogram comparison of a) HRS current, b) LRS current, c) set voltage and d) reset voltage for experimental curves (in blue) and simulations (in red). Experimental data from [25].

5. Third case Study: Modeling the stochastic resonance impact on RRAM devices

Very often in electronics, noise is considered an undesired factor that needs to be eliminated. However, for certain non-linear systems, noise can play a beneficial role in terms of device performance [28]. This phenomenon is referred to as stochastic resonance (SR), and is present in a plethora of research fields like biology, physics, engineering and many more [29–30]. Since RRAM devices are non-linear components, some works in the recent literature have studied the inclusion of external noise as a beneficial aspect for their performance [31–35]. In this section, noise is added to the applied voltage ramp. Again, the *randn* function in MATLAB is used to generate a normally distributed input voltage signal. The model script used for this study is presented in Appendix C, where the main difference with the basic model script shown in Table 1 is the following line:

$$\text{ampn} = ((g - 1) * 40) * 1\text{E} - 3; V(t) = V(t) + \text{ampn} * \text{randn}; \quad (9)$$

In (9) *ampn* controls the noise standard deviation (σ) added to the input signal *V* by means of the *randn* MATLAB function, *g* is a variable controlling the noise σ (every 200 cycles it increases 40 mV). The simulation process follows the experimental method reported in [36], consisting in 200 *I-V* cycles adding different noise values to the applied voltage ramps. This is carried out with the aim of capturing the real device phenomenology under noisy signals. Appendix C presents the script for the simulations described in this Section. Figure 7a shows the simulation results without added noise. The figure of merit that is analyzed here to determine the noise impact on RRAM devices is the separation between HRS and LRS, in particular the resistance ratio extracted at a fixed voltage

($V = -0.3$ V) as illustrated in Figure 7a. Figures 7b and 7c show the time evolution of the applied voltage and the simulated current, respectively, for a single simulated cycle using a noise amplitude $\sigma=200$ mV. The resistance ratio evolution as a function of σ is illustrated in Figure 8. The experimental results extracted from [36] are shown in Figure 8a and represent the mean resistance ratio of 200 I - V cycles for different σ values. The mean resistance ratio of 200 simulated I - V cycles against noise σ is presented in Figure 8b, where an evident maximum is found for $\sigma=240$ mV. Even though the experimental and simulated curves noticeably differ (a deep investigation about all the model parameter values is required), the model results qualitatively capture the device behavior when an external noise source is added to the input signal. The experimental-simulated coherence in this case study could be enhanced by modifying the model equations to consider the impact of external noise.

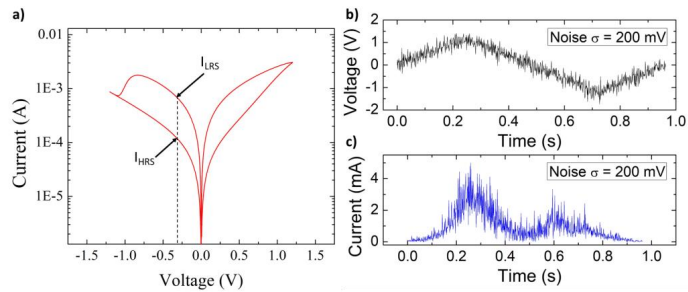


Figure 7. a) Simulated I - V curves using the DMM implemented in MATLAB without noise addition. b) and c) time evolution of applied voltage and simulated current respectively, of one simulated cycle using a noise sigma of 200 mV.

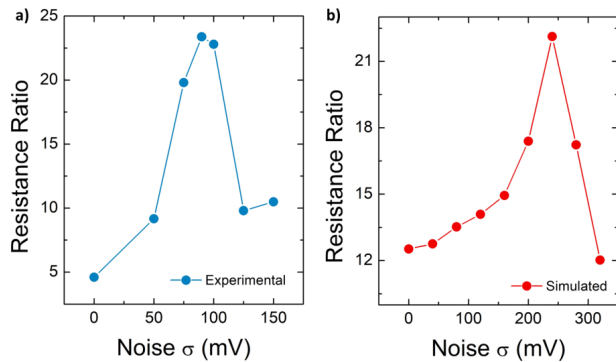


Figure 8. Mean resistance ratio evolution versus the applied noise standard deviation in simulations using the DMM in MATLAB. a) Experimental data of 200 cycles each noise sigma in [36] and b) simulated data from 200 cycles each noise sigma.

6. Conclusions

In this work a versatile and useful tool for modeling RRAM devices is presented. The model is a recursive version of the dynamic memdiode model (DMM) implemented in MATLAB software. This work includes the model script for the easiness and freely usage of the reader. This model has proven to be frequency sensitive, to reproduce the cycle-to-

cycle variability of experimental devices, and to predict the impact of an external noise source in RRAM devices, where the resistance ratio against the noise amplitude follows the typical stochastic resonance curve. Comparing with the DMM version implemented in LTspice, the time needed to modify parameters, simulate and analyze the results is largely reduced. Because of these reasons, this tool could be of interest for researchers working in the RRAM field at device level.

Author Contributions:

Conceptualization, E.S., R.R., and E.M.; Data curation, E.S. and E.M.; Formal analysis, E.S., R.R., and E.M.; Funding acquisition, R.R. and E.M.; Investigation, E.S., R.R., and E.M.; Methodology, E.S., R.R., and E.M.; Project administration, R.R.; Resources, R.R. and E.M.; Software, E.S. and E.M.; Supervision, E.M.; Validation, E.S., R.R., and E.M.; Writing, review & editing, E.S., R.R., and E.M. All authors have read and agreed to the published version of the manuscript.

Funding: This work was supported in part by Spanish MCIN/AEI/10.13039/501100011033/FEDER under projects PID2019-103869RB-C32, PID2022-139586NB-C41. E.S. acknowledges the Departament de Recerca i Universitats de la Generalitat de Catalunya for the 2020FISDU00261 scholarship.

Data Availability Statement: The data is not uploaded anywhere but the authors will provide it under request.

Conflicts of Interest: The authors declare no conflicts of interest.

Appendix A

```

Frequency Effect - DMM in MATLAB
ncyc=4;
for n=1:ncyc
V= 1.2 * sin(linspace(0, 2*pi, 10000));%Frequency
% step=0.005; V1=0:step:1.2; V2=0:-step:-1.2; V=[V1 flip(V1) V2 flip(V2)];%Ramp Rate
aoff=2; aon=2; Ri=3; Roff=30; Ron=10; Ioff=10E-5; Ion=150E-3;
etas=40; etar=-40; gam=0; Vs=0.35; Vr=-0.35; l(1)=0; I(1)=0;
RR(n)=1; At(n)=1/(10^n); f(n)=1/At(n);%Frequency
% At(n)=1; RR(n)=5*10^(n); %Ramp Rate
for t=1:length(V)
Vi=V(t)-(Ri*I(t)); I0=(Ion-Ioff)*I(t)+Ioff; a=(aon-aoff)*I(t)+aoff; R=(Ron-Roff)*I(t)+Roff;
Tsr=exp(-etas*(Vi-(Vs+log(RR(n))/etas)))*(V(t)>0)+exp(-etar*I(t)^gam*(Vi-
(Vr+log(RR(n))/etar)))*(V(t)<=0);
I(t+1)=(1/(a*R))*(lambertw((a*R*I0)/2).*exp(a*Vi)-lambertw((a*R*I0)/2).*exp(-a*Vi));
I(t+1)=(l(t)-heaviside(Vi))*exp(-(At(n)/Tsr))+heaviside(Vi);
Vm(t,n)=V(t); Im(t,n)=I(t);lm(t,n)=I(t);
end
pos=find(lm(:,n)>=0.5);
reset(n)=Vm(pos(end),n);
set(n)=Vm(pos(1));
end
subplot(2, 1, 1); plot(Vm,Im); title('I-V - Frequency effect');%Frequency
subplot(2, 1, 2); plot(log(f),set,log(f),abs(reset)); title('Log F VS |S/R Voltage|'); %Frequency
% subplot(2, 1, 1); plot(Vm,Im); title('I-V - Ramp Rate effect'); %Ramp Rate
% subplot(2, 1, 2); plot(log(RR),set,log(RR),abs(reset)); title('Log RR VS |S/R Voltage|'); %Ramp Rate

```

Appendix A. Script used for obtaining the simulations in Section 3, where a frequency effect study was performed in the recursive dynamic memdiode model implemented in MATLAB.

Appendix B

```

Cycle-to-Cycle Variability - DMM in MATLAB
ncyc=450;
for n=1:ncyc
step=0.005; V1=0:step:1.5; V2=0:-step:-1.5; V=[V1 flip(V1) V2 flip(V2)];%for applied voltage

```

```

Maoff=2.1; Saoff=0.13; aoff=Maoff+Saoff*randn;%M=mean S=standard deviation
Maon=1.25; Saon=0.06; aon=Maon+Saon*randn;
Mloff=3.7E-5;lloffLN=log(Mloff);Sloff=0.6; loff=exp(lloffLN+Sloff*randn);%lognormal
Mlon=2.4E-3; lonLN=log(Mlon);Slon=0.12; lon=exp(lonLN+Slon*randn);
MVs=0.38;VsLN=log(MVs);SVs=0.12; Vs=exp(VsLN+SVs*randn);%lognormal
MVR=0.86; SVr=0.035; Vr=MVR+SVr*randn;
Metas=32; Setas=3.1; etas=Metas+Setas*randn;
etar=-27; Ri=60; gam=0; At=1E-3; Roff=50; Ron=20; IC=5E-3; l(1)=0; I(1)=0;
for t=1:length(V)
Vi=V(t)-(Ri)*I(t); I0=(lon-loff)*I(t)+loff; a=(aon-aoff)*I(t)+aoff; R=(Ron-Roff)*I(t)+Roff;
Tsr=exp(-etas*(Vi-Vs))*(V(t)>0)+exp(-etar*I(t)^gam*(Vi-Vr))*(V(t)<=0);
if I(t)>IC
I(t)=IC; % Compliance current
end
I(t+1)=(1/(a*R))*(lambertw(a*R*I0/2)*exp(a*Vi)-lambertw(a*R*I0/2*exp(-a*Vi)));
I(t+1)=(I(t)-heaviside(Vi))*exp(-At/Tsr)+heaviside(Vi);
Vm(t,n)=V(t); Im(t,n)=I(t);Im(t,n)=I(t);
end
pos=find(Im(:,n)>=0.5);
posl=find(Vm(:,n)>=0.2);
ihrs(n)=Im(posl(1),n);
reset(n)=Vm(pos(end),n);
end
subplot(2, 1, 1); semilogy(Vm,abs(Im),'r'); title('I-V + C2C Variability');
subplot(2, 2, 3); hist(ihrs,15); title('Histogram Ihrs');
subplot(2, 2, 4); hist(reset,15); title('Histogram VReset');

```

Appendix B. Script used for obtaining the simulations in Section 4, where a C2C variability study was performed in the recursive dynamic memdiode model implemented in MATLAB.

Appendix C

Stochastic Resonance - DMM in MATLAB

```

for g=1:9 %g iterates the noise sigma
ncyc=200;
for n=1:ncyc
step=0.005; V1=0;step:1.2; V2=0;-step:-1.2; V=[V1 flip(V1) V2 flip(V2)];%applied voltage
aoff=1.9;aon=1.3;Roff=30; Ron=50;loff=19E-5;lon=6.5E-3; %Parameters
Vs=0.55;Vr=-0.45; etas=4; etar=-9; Ri=0; gam=0; L0=0; At=1E-3;l(1)=0; I(1)=0;
for t=1:length(V)%calculating current
ampn=((g-1)*40)*1E-3; V(t)=V(t)+ampn*randn;%noise inclusion
Vi=V(t)-(Ri)*I(t); I0=(lon-loff)*I(t)+loff; a=(aon-aoff)*I(t)+aoff; R=(Ron-Roff)*I(t)+Roff;
Tsr=exp(-etas*(Vi-Vs))*(V(t)>0)+exp(-etar*I(t)^gam*(Vi-Vr))*(V(t)<=0);
I(t+1)=(1/(a*R))*(lambertw(a*R*I0/2)*exp(a*Vi)-lambertw(a*R*I0/2*exp(-a*Vi)));
I(t+1)=(I(t)-heaviside(Vi))*exp(-At/Tsr)+heaviside(Vi);
Im(t,n,g)=I(t); Vm(t,n,g)=V(t); %Saving I and V variables
end
nn=1; pos=find(Vm(:,1)>=0.3);%Data analysis
Rl=mean((Im(pos(end)-nn:pos(end)+nn,,:g))); Rh=mean((Im(pos(1)-nn:pos(1)+nn,,:g)));
rat=(Rl/Rh); RRatio(g,1)=mean(rat);
end
end
subplot(2,1,1); semilogy(Vm(:,1),abs(Im(:,1)), 'r'); title('I-V without noise');
subplot(2,1,2); plot(RRatio); title('RRatio VS Noise sigma');

```

Appendix C. Script used for obtaining the simulations in Section 5, where a stochastic resonance impact study was performed in the recursive dynamic memdiode model implemented in MATLAB.

References

1. Im, I. H.; Kim, S. J.; Jang, H. W. Memristive Devices for New Computing Paradigms. *Advanced Intelligent Systems*. 2020, 2(11), 2000105. doi: 10.1002/aisy.202000105. 346
2. Nagashima, K.; Yanagida, T.; Oka, K.; Taniguchi, M.; Kawai, T.; Kim, J.; Park, B.H. Resistive Switching Multistate Nonvolatile Memory Effects in a Single Cobalt Oxide Nanowire. *Nano Letters*. 2010, 10, 1359–1363. doi: 10.1021/nl9042906. 347
3. Ishibe, T.; Maeda, Y.; Terada, T.; Naruse, N.; Mera, Y.; Kobayashi, E.; Nakamura, Y. Resistive switching memory performance in oxide hetero-nanocrystals with well-controlled interfaces. *Science and Technology of Advanced Materials*, 2020, 21, 195–204. doi: 0.1080/14686996.2020.1736948. 348
4. Shu, F.; Chen, X.; Yu, Z.; Gao, P.; Liu, G. Metal–Organic Frameworks–Based Memristors: Materials, Devices, and Applications. *Molecules* 2022, 27, 8888. doi: 10.3390/molecules27248888. 349
5. Lee, S.H.; Zhu, X.; Lu, W. D. Nanoscale resistive switching devices for memory and computing applications. *Nano Research*. 2020, 13, 1228–1243. doi: s12274-020-2616-0. 350
6. Ielmini, D.; Wong, S. H. P. In-memory computing with resistive switching devices. *Nature Electronics*. 2018, 1, 333–343. doi: s41928-018-0092-2. 351
7. Pedretti, G.; Milo, V.; Ambrogio, S.; Carboni, R.; Bianchi, S.; Calderoni, A.; Ramaswamy, N.; Spinelli, A. S.; Ielmini, D. Stochastic learning in neuromorphic hardware via spike timing dependent plasticity with RRAM synapses. *IEEE Journal on Emerging and Selected Topics in Circuits and Systems*. 2018, 8, 77–85. doi: 10.1109/JETCAS.2017.2773124. 352
8. Li, C.; Hu, M.; Li; et al. Analogue signal and image processing with large memristor crossbars. *Nature Electronics*. 2018, 7, 52–59. doi: 10.1038/s41928-017-0002-z. 353
9. Aziza, H.; Postel-Pellerin, J.; Bazzi, H.; Canet, P.; Moreau, M.; Della Marca, V.; Harb, A. True Random Number Generator Integration in a Resistive RAM Memory Array Using Input Current Limitation. *IEEE Transactions on Nanotechnology*. 2020, 19, 214–222. doi: 10.1109/TNANO.2020.2976735. 354
10. Ielmini, D.; Milo, V. Physics-based modeling approaches of resistive switching devices for memory and in-memory computing applications. *J. Comput. Electron.* 2017, 16, 1121–1143. doi: 10.1007/s10825-017-1101-9. 355
11. Elgabra, H.; Farhat, I. A. H.; Hosani, A. S. A.; Homouz, D.; Mohammad, B. Mathematical modeling of a memristor device. 2012 International Conference on Innovations in Information Technology (IIT). Abu Dhabi, United Arab Emirates, 2012, 156–161, doi: 10.1109/INNOVATIONS.2012.6207722. 356
12. Huang, L.; Mosleh, A. A Physics of Failure, Kinetic Simulation Model for Reliability of RRAM. 2023 Annual Reliability and Maintainability Symposium (RAMS), Orlando, FL, USA, 2023, 1–6, doi: 10.1109/RAMS51473.2023.10088177. 357
13. Mladenov, V.; Kirilov, S. A Memristor Neural Network Based on Simple Logarithmic-Sigmoidal Transfer Function with MOS Transistors. *Electronics*. 2024, 13, 893. https://doi.org/10.3390/electronics13050893 358
14. Aguirre, F. L.; Suñé, J.; Miranda, E. SPICE Implementation of the Dynamic Memdiode Model for Bipolar Resistive Switching Devices. *Micromachines*. 2022, 13, 330. doi: 10.3390/mi13020330. 359
15. Karpov, V.; Niraula, D.; Karpov, I. Thermodynamic analysis of conductive filaments. *Appl. Phys. Lett.* 2016, 109, 1–5. doi: 10.1063/1.4962136. 360
16. Wouters, D.J.; Menzel, S.; Rupp, J.A.J.; Hennen, T.; Waser, R. On the universality of the I–V switching characteristics in non-volatile and volatile resistive switching oxides. *Faraday Discuss.* 2019, 213, 183–196. doi: 10.1039/C8FD000116B. 361
17. Miranda, E.; et al. Simulation of Bipolar-Type Resistive Switching Devices Using a Recursive Approach to the Dynamic Memdiode Model. *IEEE Electron Device Letters*. 2023, 44(9), 1551–1554. doi: 10.1109/LED.2023.3298023 362
18. Ostrovskii, V.; Fedoseev, P.; Bobrova, Y.; Butusov, D. Structural and parametric identification of Known memristors. *Nano-materials*. 2022, 12, 63. doi: 10.3390/nano12010063. 363
19. Rodríguez-Fernández, A.; Cagli, C.; Perniola, L.; Suñé, J.; Miranda, E. Effect of the voltage ramp rate on the set and reset voltages of ReRAM devices. *Mic. Eng.* 2017, 178, 61–65. doi: 10.1016/j.mee.2017.04.039. 364
20. Chen, A.; Lin, M. R. Variability of resistive switching memories and its impact on crossbar array performance. *IEEE IRPS*. 2011, 843–846. doi: 10.1109/IRPS.2011.5784590. 365
21. Piccolboni, G.; et al. Investigation of Cycle-to-Cycle Variability in HfO₂-Based OxRAM. *IEEE Electron Device Lett.* 2016, 37, 721–723. doi: 10.1109/LED.2016.2553370. 366
22. García-Redondo, F.; López-Vallejo, M.; Barrio, C. L. Advanced integration of variability and degradation in RRAM SPICE compact models. 2017 14th International Conference on Synthesis, Modeling, Analysis and Simulation Methods and Applications to Circuit Design (SMACD). 2017. 367
23. Roldán, J. B.; et al. Variability in resistive memories. *Advanced Intelligent Systems*. 2023, 5, 2200338. doi: 10.1002/aisy.202200338. 368
24. Reuben, J.; Biglari, M.; Fey, D. Incorporating Variability of Resistive RAM in Circuit Simulations Using the Stanford–PKU Model. *IEEE Transactions on Nanotechnology*. 2020, 19, 508–518. doi: 10.1109/TNANO.2020.3004666. 369
25. Salvador, E.; Gonzalez, M. B.; Campabadal, F.; Martín-Martínez, J.; Rodríguez, R.; Miranda, E. Assessment of the variability of the I–V characteristic of HfO₂-based resistive switching devices and its simulation using the quasi-static memdiode model. *Solid State Electronics*. 2023, 206, 108667. doi: 10.1016/j.sse.2023.108667 370
26. Poblador, S.; Gonzalez, M. B.; Campabadal, F. Investigation of the multilevel capability of TiN/Ti/HfO₂/W resistive switching devices by sweep and pulse programming. *Microelectron. Eng.* 2018, 187–188, 148–153. doi: 10.1016/j.mee.2017.11.007. 371

-
27. Delignette-Muller, M. L.; Dutang, C. *fitdistrplus: An R Package for Fitting Distributions*. *Journal of Statistical Software*. 2015, 64(4), 1–34. doi: 10.18637/jss.v064.i04. 404
28. Benzi, R.; Sutera, A.; Vulpiani, A. The mechanism of stochastic resonance. *Journal of Physics A: Mathematical and General*. 1981, 14(11), L453. doi: 10.1088/0305-4470/14/11/006. 405
29. Wiesenfeld, K.; Moss, F. Stochastic resonance and the benefits of noise: from ice ages to crayfish and SQUIDS. *Nature*, 1995, 373, 33–36. doi: 10.1038/373033a0 407
30. Harmer, G.P.; Davis, B. R.; Abbot, D. A review of stochastic resonance: circuits and measurement *IEEE Transactions on Instrumentation and Measurements*. 2002, 31(2), 299–309. doi: 10.1109/19.997828. 408
31. Kasai, S. Stochastic resonance and related phenomena in nonlinear electron nanodevices. *IEEE International Nanoelectronics Conference (INEC)*. 2014. 409
32. Scotland, A.; Di Ventra, M. Stochastic memory: Memory enhancement due to noise. *Physical Review E*. 2012, 85, 011116. doi: 10.1103/PhysRevE.85.011116. 410
33. Patterson, G. A.; Fierens, P. I.; Grosz, D. F. On the beneficial role of noise in resistive switching. *Appl. Phys. Lett.* 2013, 103, 074102. doi: 10.48550/arXiv.1307.0143 411
34. Roldán, J.B.; Cantudo, A.; Torres, J. J.; Maldonado, D.; Shen, Y.; Zhen, W.; Yuan, Y.; Lanza, M. Stochastic resonance in 2D materials based memristors. *npj 2D Materials and Applications*. 2024, 8, 7. doi: 10.1038/s41699-024-00444-1. 412
35. Mikhaylov, A.N.; Guseinov, D.V.; Belov, A.I.; Korolev, D.S.; Shishmakova, V.A.; Koryazhkina, M.N.; Filatov, D.O.; Gorshkov, O.N.; Maldonado, D.; Alonso, F.J.; Roldan, J.B.; Krichigin, A.V.; Agudov, N. V.; Dubkov, A.A.; Carollo, A.; Spagnolo, B. Stochastic resonance in a metal-oxide memristive device. *Chaos, Solitons & Fractals*. 2021, 144, 110723. doi: 10.1016/j.chaos.2021.110723 413
36. Rodriguez, R.; Martin-Martinez, J.; Salvador, E.; Crespo-Yepes, A.; Miranda, E.; Nafria, M.; Rubio, A.; Ntinav, V.; Sirakoulis, G. Ch. Beneficial Role of Noise in Hf-based Memristors. 2022 *IEEE International Symposium on Circuits and Systems (ISCAS)*. 2022. 414
- 415
- 416
- 417
- 418
- 419
- 420
- 421
- 422
- 423
- 424
- 425
- 426

Article EDL24

Noise-induced homeostasis in memristor-based neuromorphic systems

E. Salvador, R. Rodriguez, E. Miranda,
J. Martin-Martinez, A. Rubio, A. Crespo-Yepes, V. Ntinis,
G. Ch. Sirakoulis, M. Nafria

Noise-induced homeostasis in memristor-based neuromorphic systems

E. Salvador¹, R. Rodriguez¹, E. Miranda¹, J. Martin-Martinez¹, A. Rubio², A. Crespo-Yepes¹, V. Ntinis², G. Ch. Sirakoulis³, M. Nafria¹

Abstract—In this work, it is experimentally demonstrated that noise can be used to emulate the biological homeostatic neuron property in memristor-based neuromorphic systems. The addition of an external noise to the bias allows regulating the memristor performance when used as an artificial neuron, controlling the firing process through the modulation of the memristor threshold voltages. Experimental results have been correctly addressed using the Dynamic Memdiode Model (DMM) for memristors in the framework of SPICE simulation.

Index Terms—Memristor, RRAM, resistive switching, stochastic resonance, homeostasis, spike neural networks, SPICE.

I. INTRODUCTION

POST Von-Neuman computing architectures, such as neuromorphic systems, have attracted the attention of the scientific community in the last years because of their enormous possibilities in several application fields [1,2]. Neuromorphic systems try to emulate the brain performance, forming the computation and memory units a single operational structure. The development of hardware implementations of these new architectures using emerging devices such as memristors offers beneficial features in terms of energy consumption and computational efficiency. In case of biological neurons, they receive, process and transfer information through the gap in between them called synapse. Since memristors are nonvolatile memory devices exhibiting nonlinearity, good scalability and programming capabilities, they are considered excellent candidates for the implementation of both artificial neurons and synapses in neuromorphic circuits [2, 3].

In Spike Neural Networks (SNN), excitatory and inhibitory neuron operations are fundamental processes of synaptic activities, and they mutually coordinate each other. However, neuron operation can lead to excessive excitatory or inhibitory processes [4], causing some neurons to continuously fire spikes (having a dominant role in the training process), while others

cannot learn because of the low firing frequency [5]. However, biological neurons present a configurable performance capable of adapting to changing conditions maintaining the neural system homeostasis [6]. The homeostatic mechanism is necessary to balance neuron activities and reach more stable neural performances, resilient to different types of unstable neuron behavior [7, 8]. Then, the inclusion of homeostasis in artificial neural networks becomes mandatory for regulating the activity of neurons [9] and optimize learning [10].

Some previous works in the literature consider the homeostasis in memristor-based neuromorphic systems. In [5], the training of a SNN is enhanced through the flexible adjustment of the synaptic weight update frequency based on homeostasis. In [11], a memristive neural network circuit that can implement memory with emotional homeostasis is designed. In [12,13] homeostasis also plays a relevant role to avoid device variations in SNNs. Most of these proposals include homeostasis through software implementation. In a more realistic scenario, it would be convenient to include the homeostatic property in the memristor performance for self-adjusting the neuron activities and enhance the neuron ability of self-stabilizing.

Because of the non-linear properties of memristors, their performance can be improved through the exploitation of the so-called stochastic resonance (SR) phenomenon, which is the beneficial use of an external noise, in this case, to enhance memristor functionality (a detailed description of SR can be found in [14]). Some previous works have observed the increase of the memristor resistance ratio (R_{OFF}/R_{ON}) [15] and the improvement of the spike-time-dependent plasticity (STDP) learning protocol [16] through the addition of an external noise. In this work, we demonstrate that, by adding external noise to the device bias, the homeostasis property can be implemented in memristor-based SNNs. The impact of noise on the regulation of the spiking neuron operation, through the modulation of the memristor threshold voltages (set and reset voltages), is described. Experimental results were reproduced using the LTspice simulator and the dynamic memdiode model (DMM), which has demonstrated high versatility for different materials and input signals [17-20].

II. DEVICES AND MEASUREMENT METHODOLOGY

The devices used in this work were Ni/insulator/Si-n⁺ metal-insulator-semiconductor (MIS) square structures with a 15x15 μm^2 active area. These devices were fabricated on highly doped N-type (100) silicon wafers. The insulator layer was deposited via Atomic Layer Deposition (ALD) at 225 °C using as precursors trimethylaluminum and H₂O for Al₂O₃, and tetrakis

This research was funded by the Spanish MCIN/AEI/10.13039/501100011033 and Project PID2019-103869RB and PID2022-136949OB-C22 funded by MCIN/AEI/10.13039/501100011033/FEDER, UE. The authors acknowledge the Instituto de Microelectrónica de Barcelona (IMB-CNM, CSIC) for sample fabrication. E.S. acknowledges the Departament de Recerca i Universitats de la Generalitat de Catalunya for the 2020FISDU00261 scholarship.

¹Electronic Engineering Department, Universitat Autònoma de Barcelona, 08193 Bellaterra, Spain

²Electronic Engineering Department, Universitat Politècnica de Catalunya, 08034, Barcelona, Spain

³Dept. of Electrical & Computer Engineering, Democritus University of Thrace, 67100, Kimmeria, Xanthi, Greece
email: emili.salvador@uab.cat

(dimethylamido)-hafnium and H_2O for HfO_2 . N_2 was used as carrier and purge gas. The Ni top electrode was deposited by magnetron sputtering and patterned by lift-off. The dielectric film of the characterized devices consisted of a stack of HfO_2 and Al_2O_3 : 4 nm HfO_2 – 4 nm Al_2O_3 – 4 nm HfO_2 – 4 nm Al_2O_3 – 4 nm HfO_2 , resulting in a 20 nm-thick dielectric layer. The device structure is presented in Fig. 1a. Further details regarding the fabrication process and device characterization can be found in [21]. Fig. 1b illustrates the unipolar non-volatile memristor behavior operating at negative voltages, showing the memristor high resistance state (HRS) and low resistance state (LRS).

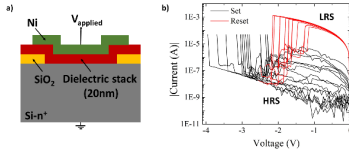


Fig. 1. a) Schematics of the unipolar memristors used in this work and b) typical I - V characteristics after the electroforming of the conductive path.

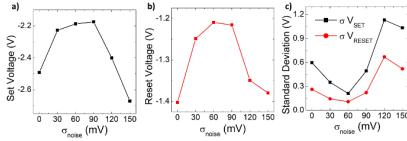


Fig. 2. a) Mean set and b) reset voltages and c) set (black) and reset (red) voltages standard deviation, versus noise σ .

The Semiconductor Parameter Analyzer (SPA) Agilent 4156C was used to carry out the electrical measurements. The experiments were programmed, launched and analyzed in MATLAB software. To trigger the electroforming process, a negative voltage sweep was applied, limiting the current to 1 μA to avoid the irreversible breakdown of the device. This electroforming occurs at around -11 V. In the experiments described in section III, after forming, 100 cycles of consecutive reset (switching from LRS to HRS) and set (from HRS to LRS) events are applied, through voltage ramps starting at 0V and ending when certain conditions are fulfilled. For the reset process, the ramp voltage is halted (reset voltage) when a current decrease of at least one order of magnitude is detected, with a 50mA compliance limit fixed. The set voltage was defined as the voltage at which the memristor current has increased until 50 μA . An external Gaussian noise was added point-by-point to the bias voltage; several noise standard deviations (σ) were considered, ranging from 0 mV to 150 mV. The set and reset voltages and their standard deviations have been registered and analyzed. In section IV, after forming, staired constant voltages (i.e., a sequence of constant voltages of a certain duration, whose value was increased in steps in a given voltage range) were applied on different samples. The set transition modulation was studied by computing the time needed to switch the device. The experiments detailed in this work were repeated in other devices from the same wafer to ensure consistency and reproducibility of outcomes.

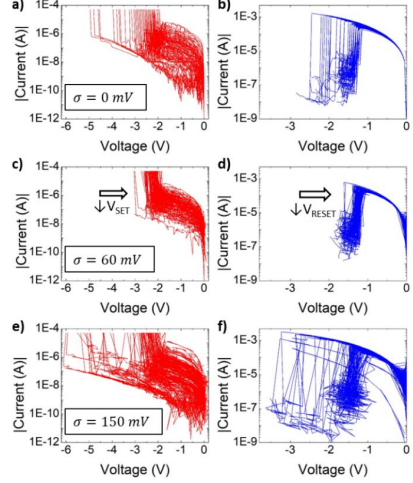


Fig. 3. I - V curves from the 100 set-reset memristor cycles for set (in red, left column) and reset processes (in blue, right column) for three cases: no noise (a and b), noise addition with $\sigma=60\text{mV}$ (c and d) and $\sigma=150$ mV (e and f).

III. NOISE IMPACT IN THE SET AND RESET TRANSITIONS

In this section, the impact of an external noise in the set and reset voltages of a memristive device is evaluated. The mean set and reset voltages obtained for different noise amplitudes σ are shown in Figs. 2a and 2b, respectively; the standard deviation of these voltages is presented in Fig. 2c. The typical SR curve is observed, with a decrease (in absolute value) of the threshold voltages and a decrease of their σ , in a range of noise σ around 60 mV. The complete picture demonstrates that the threshold voltages of the memristor can be tuned through the action of an external noise source. Fig. 3 presents the set (in red, Fig. 3 a, c and e) and reset processes (in blue, in Fig. 3b, d and f) for three distinct situations: Figures 3a and 3b for the experiments without noise, Figures 3c and 3d for experiments with $\sigma_{noise} = 60$ mV, and Figures 3e and 3f for experiments with $\sigma_{noise} = 150$ mV. It is clear that for $\sigma_{noise} = 60$ mV both set and reset transitions occur at lower voltage values than those corresponding to the absence of noise and with $\sigma_{noise} = 150$ mV. In addition, the transitions for $\sigma_{noise} = 60$ mV are less spread, meaning that the set and reset events are modulated to lower and less variable voltage values.

IV. NOISE IMPACT ON MEMRISTOR SPIKE TIME

In this section, noise-induced homeostasis in memristors is studied by observing the effect of noise on the spike time of a single memristor operating as a neuron. We focus on the simplest memristor neuron, where the spike time is defined as the time to trigger a memristor set event. The results can be extrapolated to other memristor neuron implementations as for example, the integer-and-fire memristor neuron [7]. On the one hand, if noise reduces the time required for a set event (spike), the system exhibits increased excitability, termed potentiation

regime. On the other hand, when noise prolongs set event times, the system experiences decreased excitability, known as depression regime. Considering the memristor in HRS, the memristor spike time is defined in more detail as the cumulative time needed to produce a set event when a staired constant voltage is applied (Fig. 4a). The staired voltage started at -1.2 V adding -100 mV every 1.5 seconds; the sweep is stopped once the set event occurs (i.e., when the current abruptly increases and reaches 50 μ A). To ensure the memristor was at the HRS, the reset process was induced with voltage ramps as those described in section III. The staired constant voltage is applied to accelerate the set transition and to ensure that the device switches to the LRS in an acceptable time window. The voltage increase is slower than when a voltage ramp (as those in section III) is applied, so that, as observed in other works [16], for this new biasing, the beneficial role of noise is observed for different noise σ . This procedure (reset with a voltage ramp and set with a staired constant voltage) was repeated 100 times (i.e., cycles) with different σ_{noise} values in the same device.

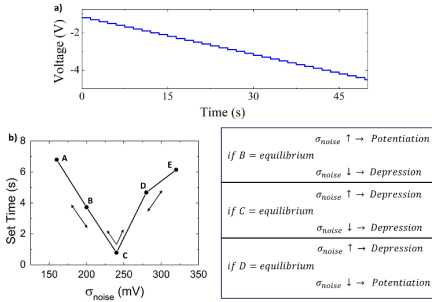


Fig. 4. a) Time evolution of the staired constant voltage. b) Stochastic resonance curve in the set event time against the noise σ . Schematic of homeostatic regulation possibilities for different equilibrium situations.

In Fig. 4b, we observe a stochastic resonance curve depicting the evolution of mean set time versus σ_{noise} . Different points are highlighted. Assuming brain as a noisy system, B point can be interpreted as an equilibrium point. When σ_{noise} is increased, shorter set times are obtained leading to a potentiation regime, meanwhile a decrease in σ_{noise} results in a depression regime. The dynamics are reversed if D is interpreted as the equilibrium point. The impact of noise on the memristor spike time has been analyzed in detail for three different noise σ : 160 mV, 200 mV and 240 mV (points A, B, and C respectively in Fig. 4b). Fig. 5a shows the experimental memristor current as a function of time for $\sigma_{noise} = 160$ mV (red curves) and $\sigma_{noise} = 200$ mV (black curves). The abrupt increase in current means the occurrence of the memristor spike. A depression regime is observed, being the spike time increased by reducing σ_{noise} . Oppositely, Fig 5.b shows the memristor current as a function of time for the experiments with $\sigma_{noise} = 200$ mV (black curves) and with $\sigma_{noise} = 240$ mV (blue curves). Now, a potentiation regime emerges, demonstrating reduced spike time with increased noise σ . Thus, modifying the σ_{noise} , memristor spike times are modulated,

thereby regulating the neuron speed [7] to maintain homeostasis.

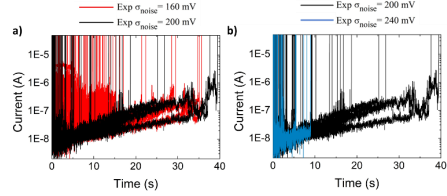


Fig. 5. a) Experimental current versus time evolution during a staired constant voltage for $\sigma_{noise} = 160$ mV (black curves) and $\sigma_{noise} = 200$ mV (red curves). b) for $\sigma_{noise} = 200$ mV (black curves) and $\sigma_{noise} = 240$ mV (blue curves).

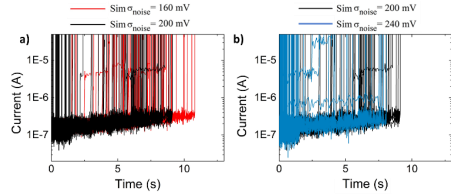


Fig. 6. a) Simulated current versus time evolution during a staired constant voltage for $\sigma_{noise} = 160$ mV (black curves) and $\sigma_{noise} = 200$ mV (red curves). b) for $\sigma_{noise} = 200$ mV (black curves) and $\sigma_{noise} = 240$ mV (blue curves).

The previous experimental results were compared with LTspice simulations carried out with the DMM memristor model. The DMM relies on two key equations, one governing the current-voltage characteristic and the other dictating the memristor memory state. A comprehensive description of this model and its practical implementation can be found in [17, 18]. Cycle-to-cycle variability was included in the model parameters related to the HRS current and set voltage, following the method presented in [20]. Calibration of the model parameters was performed by reproducing the experimental median I-V behavior using standard voltage sweeps. After calibration, the same input signal was reproduced including Gaussian noise in the applied signal. LTSPICE simulated results in Fig. 6 are qualitatively the same as the experimental results of Fig. 5 when, also observing the spike time modulation in both depression (Figs. 5a and 6a) and potentiation (Figs. 5b and 6b) regimes. This result demonstrates the suitability of the DMM for simulating the noise impact on the spike time.

V. CONCLUSION

This work presents a first experimental demonstration of noise-induced modulation of the spike time in memristor-based SNNs. Stochastic resonance has been observed in both memristor set and reset voltages and their respective standard deviations. Noise inclusion can modulate the memristor spike times, thereby facilitating both potentiation and depression of neural activity, crucial for maintaining system homeostasis. Experimental results have been correctly reproduced in LTspice using the DMM. The results highlight the pivotal role of noise in SNNs, thereby paving the way for further research of next-generation computing systems.

REFERENCES

- [1] Z. Shao, R. Zhao, S. Yuan, M. Ding, Y. Wang, "Tracing the evolution of AI in the past decade and forecasting the emerging trends", *Expert Systems With Applications*, Vol. 209, 118221, 2022, doi: 10.1016/j.eswa.2022.118221.
- [2] D. V. Christensen et al. "2022 roadmap on neuromorphic computing and engineering", *Neuromorphic Computing and Engineering*, Vol. 2, 022501, 2022, doi: 10.48550/arXiv.2105.05956.
- [3] G.W. Burr et al., "Neuromorphic computing using non-volatile memory", *Advances in Physics: X*, Vol.2 (1), pp. 89-124, 2017, doi: 10.1080/23746149.2016.1259585.
- [4] L. Wang et al., "Long-Term Homeostatic Properties Complementary to Hebbian Rules in CuPc-Based Multifunctional Memristor", *Scientific Reports*, Vol. 6, 35273, 2016, doi: 10.1038/srep35273.
- [5] G. Yang, D. Yu, S. Jia, X. Cui and Y. Wang, "A Homeostasis based Enhanced Training Method in Spiking Neural Networks for Pattern Recognition," *2021 China Semiconductor Technology International Conference (CSTIC)*, pp. 1-3, 2021, doi: 10.1109/CSTIC52283.2021.9461556.
- [6] N. J. Berman, L. Maler, "Interaction of GABAB-mediated inhibition with voltage-gated currents of pyramidal cells: computational mechanism of a sensory searchlight", *J Neurophysiol.*, Vol.80 (6), pp. 3197-3213, 1998, doi: 10.1152/jn.1998.80.6.3197.
- [7] Y. Wang, X. Xu, E. Wang, X. Zhang, Z. Wu, R. Gu, Q. Li, Q. Liu, "A Configurable Artificial Neuron Based on a Threshold-Tunable TiN/NbO₂/Pt Memristor", *IEEE Electron Device Letters*, Vol. 43 (4), pp. 631-634, 2022, doi: 10.1109/LED.2022.3150034.
- [8] X. Shi, Z. Zeng, L. Yang and Y. Huang, "Memristor-Based Circuit Design for Neuron with Homeostatic Plasticity", *IEEE Transactions on Emerging Topics in Computational Intelligence*, Vol. 2 (5), pp. 359-370, 2018, doi: 10.1109/TETCI.2018.2829914.
- [9] A. Grimaldi, V. Boutin, L. Perrinet, S. -H. Ieng and R. Benosman, "A homeostatic gain control mechanism to improve event-driven object recognition", *2021 International Conference on Content-Based Multimedia Indexing (CBMI)*, Lille, France, pp. 1-6, 2021, doi: 10.1109/CBMI50038.2021.9461901.
- [10] L.U. Perrinet, "Role of homeostasis in learning sparse representations", *Neural Computation*, Vol. 22 (7), pp. 1812-36, 2010, doi: 10.48550/arXiv.0706.3177
- [11] J. Sun, J. Han, Y. Wang, "Memristor-Based Neural Network Circuit of Memory with Emotional Homeostasis", *IEEE Transactions on Nanotechnology*, Vol. 21, pp. 204-212, 2022, doi: 10.1109/tnano.2022.3153518.
- [12] D. Querlioz, O. Bichler, P. Dollfus and C. Gamrat, "Immunity to Device Variations in a Spiking Neural Network with Memristive Nanodevices", *IEEE Transactions on Nanotechnology*, Vol. 12 (3), pp. 288-295, 2013, doi: 10.1109/TNANO.2013.2250995.
- [13] D. Querlioz, O. Bichler and C. Gamrat, "Simulation of a memristor-based spiking neural network immune to device variations", *2011 International Joint Conference on Neural Networks*, pp. 1775-1781, 2011, doi: 10.1109/IJCNN.2011.6033439.
- [14] J. Náprstek, C. Fischer, 'Stochastic Resonance and Related Topics', Resonance. InTech, Nov. 29, 2017, doi: 10.5772/intechopen.70178.
- [15] R. Rodriguez, J. Martin-Martinez, A. Rubio, E. Salvador, V. Ntinis, G. Ch. Sirakoulis, A. Crespo-Yepes, E. Miranda, M. Nafria, "Beneficial Role of Noise in Hf-based Memristors", *2022 IEEE International Symposium on Circuits and Systems (ISCAS)*, pp. 975-979, 2022, doi: 10.1109/ISCAS48785.2022.9937850.
- [16] E. Salvador *et al.*, "Stochastic resonance effect in binary STDP performed by RRAM devices", *2022 IEEE 22nd International Conference on Nanotechnology (NANO)*, 2022, doi: 10.1109/NANO54668.2022.9928738.
- [17] E. Miranda and J. Sune, "Memristive State Equation for Bipolar Resistive Switching Devices Based on a Dynamic Balance Model and its Equivalent Circuit Representation", *IEEE Trans. Nanotechnol.*, vol. 19, pp. 837-840, 2020, doi: 10.1109/TNANO.2020.3039391.
- [18] F. Aguirre, J. Suñé, E. Miranda, "SPICE Implementation of the Dynamic Memdiode Model for Bipolar Resistive Switching Devices", *Micromachines*, Vol. 13, 330, 2022, doi: 10.3390/mi13020330.
- [19] M. Saludes, M.B. Gonzalez, F. Campabadal, J. Suñé, E. Miranda, "SPICE model for complementary resistive switching devices based on anti-serially connected quasi-static memdiodes", *Solid State Electronics*, Vol. 194, 108312, 2022, doi: 10.1016/j.sse.2022.108312.
- [20] E. Salvador, M.B. Gonzalez, F. Campabadal, J. Martin-Martinez, R. Rodriguez, E. Miranda, "Assessment of the variability of the I-V characteristic of HfO₂-based resistive switching devices and its simulation using the quasi-static memdiode model", *Solid State Electronics*, Vol. 206, 108667, 2023, doi: 10.1016/j.sse.2023.108667.
- [21] M. Maestro-Izquierdo, M. B. Gonzalez, F. Jimenez-Molinos, E. Moreno, J. B. Roldan, F. Campabadal, "Unipolar resistive switching behavior in Al₂O₃/HfO₂ multilayer dielectric stacks: fabrication, characterization and simulation", *Nanotechnology*, Vol. 31, 135202, 2020, doi: 10.1088/1361-6528/ab5f9a.

Article TED24

Stochastic Resonance in HfO₂-Based Memristors: Impact of External Noise on the Binary STDP Protocol

E. Salvador, R. Rodriguez, E. Miranda,
J. Martin-Martinez, A. Rubio, A. Crespo-Yepes, V. Ntinis,
G. Ch. Sirakoulis, M. Nafria.

Stochastic Resonance in HfO_2 -Based Memristors: Impact of External Noise on the Binary STDP Protocol

E. Salvador¹, R. Rodríguez¹, E. Miranda¹, J. Martín-Martínez¹, A. Rubio², V. Ntinaz², G. Ch. Sirakoulis³, A. Crespo-Yepes¹, M. Nafria¹

Abstract— This paper deals with the stochastic resonance (SR) phenomenon experimentally observed in HfO_2 -based memristors. The SR impact on the binary spike time dependent plasticity (STDP) protocol at device level was investigated. We demonstrate that the two extreme conductance states of the device that represent the synaptic weights in neuromorphic systems can be better distinguished with the incorporation of Gaussian noise to the bias signal. This technique allows setting the memristor conductance which is directly related to the overlap between the pre- and post-synaptic pulses. The study is reproduced in the LTspice simulator using the dynamic memdiode model for memristors.

Index Terms—Memristor, RRAM, Stochastic resonance, STDP

I. INTRODUCTION

THE scientific community and microelectronics industry are highly interested in novel and emerging technologies for RAM memory devices [1-2]. In this regard, memristors have exceptional properties, including low power consumption and high integration capacity among others. Memristor's conductance can be changed when exposed to a suitable biasing scheme. When bias disappears, memristor's conductance is maintained in a non-volatile fashion. This makes the memristor a very promising device to be used in a huge range of applications, such as data storage, unconventional computing methods, Artificial Neural Networks (ANN), and cryptography [3-6]. Memristors present nonlinear current-voltage characteristics and nonlinear dynamical behavior enabling the utilization of properties linked with nonlinear systems. Despite noise in electronics is considered as a major drawback and commonly needs to be eliminated, in nonlinear systems it can play a favorable role,

such as enhancing the device performance or, in the particular case of memristors, modifying the switching phenomenon. This phenomenon is often referred to as stochastic resonance (SR) and it has been observed in several research fields including biology, physics, and engineering [7-10]. A detailed description of the well-known SR phenomenon is reported in [11]. SR occurs in nonlinear devices whose characteristic curves present thresholds, like occurs in memristors. From the literature, some works have considered noise as a beneficial element in these devices. For instance, in [12] the impact of additive noise in memristors was investigated using a physical model of a memory resistor. A different SR modeling for manganite-based memristors is presented in [13], which reports good concurrence between theory and measurements. An experimental investigation was conducted in [14], where memristors were exposed to sinusoidal signals with added noise to examine SR. In [15], a study of the effect of the SR in the resistance ratio of HfO_2 -based memristors is discussed. In [16], a noisy signal was applied to zirconium and tantalum pentoxide-based memristors. The analysis from both experimental and theoretical viewpoints and the constructive role of noise in these samples is reported. In addition, SR in 2D materials based memristors is analyzed in [17].

The use of memristor-based artificial neural networks (ANNs) has gained increasing importance in the recent years due to their potential to implement efficient and low-power computing architectures [18]. In neuromorphic systems, the aim consists in reproducing brain performance. In this sense, spike-timing-dependent plasticity (STDP), which is a learning approach inspired in biology, it is widely accepted in the scientific community as a way to describe the brain synapse when implemented with RRAM devices [19]. The STDP process updates the synaptic weight and direction as a function of the time difference or delay between the pre- and post-synaptic spikes [20,21]. In the specific case of the memristor based binary STDP, the resistive switching process is essential for the achievement of the two different states: ON and OFF, which correspond to the memristor low resistance (LRS) and high resistance (HRS) states respectively [22, 23] (Fig. 1).

Even though artificial neural networks are assumed to work with no noise or spike jitter, neurobiological systems are known to operate in noisy environments. Thus, noise can tune the activation threshold of neurons, enhancing the response of nonlinear circuits. In [24], Anderson reported that noise produced in the visual cortex facilitates the perception of the

This research was funded by the Spanish MCIN/AEI/10.13039/501100011033 and Project PID2019-103869RB and PID2022-136949OB-C22 funded by MCIN/AEI/10.13039/501100011033/FEDER, UE. The authors acknowledge the Instituto de Microelectrónica de Barcelona (IMB-CNM, CSIC) for sample fabrication. E.S. acknowledges the 'Departament de Recerca i Universitats de la Generalitat de Catalunya' for the 2020 FISDU 00261 scholarship.

¹Electronic Engineering Department, Universitat Autònoma de Barcelona, 08193 Bellaterra, Spain

²Electronic Engineering Department, Universitat Politècnica de Catalunya, 08034, Barcelona, Spain

³Dept. of Electrical & Computer Engineering, Democritus University of Thrace, 67100, Ximimeria, Xanthi, Greece

email: emili.salvador@uab.cat

optical signal. In [25], an increase of neuron sensitivity efficiency is reported, ascribing it to the SR effect.

The aim of this work is to experimentally study in detail the role of noise in the binary STDP implemented with HfO_2 -based memristors, considering the set, reset and complete set-reset processes, extending our preliminary work in [26] where only the set process was addressed. In this case, an improvement of the STDP protocol was observed when noise is added under different circumstances considering noise in both memristive state transitions separately and jointly. Moreover, after this analysis, we show that the study of the constructive role of noise in the binary STDP can be reproduced using the LTspice simulator with the help of the dynamic memdiode model (DMM) [27, 28]. The external signals with noise were applied to the device and the simulation results compared with the experimental data.

II. NOISE-INDUCED BINARY STDP

This section focuses on the SR effect on memristor-based binary STDP learning rule implementation. The devices used in our study are Metal-Insulator-Metal (MIM) structures consisting of $\text{TiN-Ti-HfO}_2\text{-W}$ layers, as shown in Fig. 1.a. These devices were fabricated on silicon. The HfO_2 layer was deposited via atomic layer deposition (ALD). A 50 nm-W layer acts as bottom electrode and a 200 nm-TiN layer over a 20 nm-Ti layer acting as oxygen-gettering material (top electrode). The Al layer at the wafer bottom performs as the bottom contact of the memristors in the wafer. The used devices are square cells with an active area of $5 \times 5 \mu\text{m}^2$. For more information regarding the fabrication process visit [29]. The Semiconductor Parameter Analyzer (SPA) Agilent 4156C was utilized to carry out measurements. The experiments were programmed and launched in MATLAB. Figure 1.b represents the typical I-V characteristics after the electroforming event (using a 1 mA current limitation) for the memristors analyzed in this section [30]. Now, the voltage sweeps were from 0 V to 0.7 V, from 0.7 V to -1.3 V and from -1.3 V to 0 V. The current was also read simultaneously to the voltage application. During measurements, current limitation was fixed to 25 mA to avoid any eventual irreversible breakdown of the dielectric film.

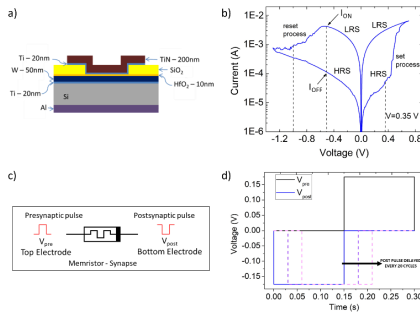


Fig. 1. a) Device structure, b) example of a current-voltage characteristic of the memristors studied in this work. c) Memristor schematics presenting the applied pulses (pre- and post-synaptic) at the top and bottom electrodes respectively. d) Initial situation of the

applied pre- and post-synaptic pulses (no overlap) is represented with continuous lines. Different situations with delay of the post-synaptic pulse are presented in dash lines.

In the analysis of the external noise impact on binary STDP, when no noise is applied, the memristor state is ensured not to change. However, the application of noise allows the memristor to switch, activating the set and/or reset processes.

We study binary STDP via the SR phenomenon following three different approaches: A) activating the set process, B) activating the reset process and C) activating both set and reset processes simultaneously.

To provoke binary STDP, the memristors were subjected to set and reset pulses to reach ON and OFF states respectively. Firstly, all the set and reset pulses are formed from a pre-synaptic pulse (V_{pre}) applied to the top electrode of the device and a post-synaptic pulse (V_{post}) applied to the bottom electrode. The resultant voltage drop at the memristor reads: $V_{tot} = V_{pre} - V_{post}$ as illustrated in Fig 1.c. The width of the pre- and post-synaptic pulses was always 150 ms. Also, we consider two different types of set and reset pulses: fixed and variable. The fixed ones consist in a constant pulse with voltage amplitude high enough to ensure the memristor state transition. The more complicated variable pulses follow an adaptive pulse-width scheme that is detailed in the following subsections. Depending on each investigated case, the set and reset pulses can be fixed or variable, and with or without noise addition. After completing every transition pulse (set or reset), the memristor conductance state was determined by means of a read voltage pulse, V_{read} , of 150 ms duration applied to the top electrode of the device and grounding the bottom one. In our case $V_{read} = -0.5 \text{ V}$ to ensure a clear separation between HRS and LRS. The complete sequence of applied signals will be presented in the corresponding subsection.

A fresh device was used for each experiment (one for measuring without noise and one for the noisy measurement). The added noise, for all the different considered test conditions, was Gaussian ($\sigma_{noise} = 150 \text{ mV}$), which was found to be the suitable value for the SR observation in these samples, after analyzing different values. The resistance ratio is calculated as follows: $R_{ratio} = \left(\frac{R_{reset}}{R_{set}} \right) = \left(\frac{V_{read}/I_{reset}}{V_{read}/I_{set}} \right) = \left(\frac{I_{set}}{I_{reset}} \right)$, where I_{set} and I_{reset} consist in the registered currents during the read pulse after the set and reset pulses, respectively. The following subsections summarize the information about the complete applied signal and the results corresponding to the three different tests.

A. Set Process Activation

In this first approach, the focus is to improve the binary STDP with the addition of Gaussian noise to the pulse that provokes the set transition. We ensure that the memristor remains in the HRS state by selecting appropriate amplitudes for the pre- and post-synaptic pulses without external noise. For this reason, we selected a set voltage, $V_{tot} = V_{set}$, slightly below the voltage required to activate the set transition. This ensures that once noise is added, there is a probability of overcoming the set threshold voltage. In this study, we set the maximum voltage to $V_{set} = V_{tot} = 0.35 \text{ V}$.

To induce a change from LRS to HRS, we generate a reset pulse by applying -0.5 V at the top electrode and 0.5 V at the

bottom electrode. Thus, the reset pulse consists of $V_{reset} = V_{tot} = -1$ V during 150 ms.

However, generating the set pulse, V_{set} , is more challenging because the post-synaptic pulse must allow for adaptive time-shifting to generate different overlap situations between the pre- and the post-synaptic pulses. This overlap induces the maximum value of V_{set} to have different values. In Fig. 1.d the initial situation of the pre- and post-synaptic pulses is illustrated. Notice that there is no delay between pulses. The dash lines in the figure represent the successive delays of the post-synaptic pulse.

For a better understanding, we describe the details of a variable set pulse generation. The duration of the set pulse at maximum voltage (0.35 V) starts at 0 ms, goes up to 150 ms and drops back to 0 ms following 15 ms steps. Figure 2 illustrates three cases for a variable set process: in a) the pre- and post-synaptic pulses are not overlapped that produces a 300 ms pulse of $V_{set} = V_{tot} = 0.175$ V; in b), a partial overlap situation that generates a 3-level voltage pulse. In this situation, the maximum $V_{set} = V_{tot} = 0.35$ V was during approx. 60 ms; in c), a complete pulses overlap, where $V_{set} = V_{tot} = 0.35$ V pulse that lasts 150 ms [26].

In Fig 3.a, the complete measurement sequence for this first approach is reported. In every post-synaptic pulse delay (Δt), the sequence is cycled 20 times to allow for statistical analysis. At the beginning of the measurement sequence, the pre- and post-synaptic pulses do not overlap, and the 20 cycles are performed. The post-synaptic pulse is then delayed 15 ms, and again the 20 cycles are executed. This process is repeated for each shift. $\Delta t = n * 15$ ms where n starts at 0 and grows until 21. Focusing again on Fig. 2: a) presents the initial situation where $n=0$. As Δt increases, the overlap grows until a maximum situation in c) for $n=11$. After the maximum overlap situation, n keeps growing until there is no overlap again, for $n=21$.

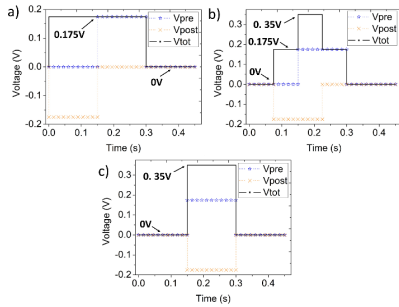


Fig. 2. Total set voltage, V_{set} , (black line) and pre- and post-synaptic pulses (blue and orange lines) for three different overlap cases: a) no overlap, b) intermediate, and c) complete.

The currents for the 20 cycles after each set and reset processes in all the previously mentioned iterations is illustrated in Figures 3.b and 3.c against Δt for experiments without considering noise and including it respectively. Orange symbols represent the read currents after a set transition and the

blue ones after a reset transition. In addition, in the figures, the mean value of the read current is shown with a solid line of the same color of the respective symbols. The comparison of both figures reveals that noise addition is crucial in identifying resistive states. Without noise, there is no state separation (see Fig. 3.b). However, with noise addition, both ON and OFF states are clearly distinguished because the set transition is enhanced. This state separation is proportional to the overlap between pre- and post-synaptic pulses. It is important to highlight that the maximum overlap situation is shown at $\Delta t=150$ ms. Figure 3.d displays the mean resistance ratio as a function of Δt for the measurements without (in blue) and with noise (in orange). The dash grey line in Fig. 3.d represents the overlap as a function of Δt , which supports the analysis reported in Figs. 3.b and 3.c. about the proportionality between pre- and post-synaptic pulses overlap and the R_{ratio} . In conclusion, the addition of noise to the set transition improves the R_{ratio} .

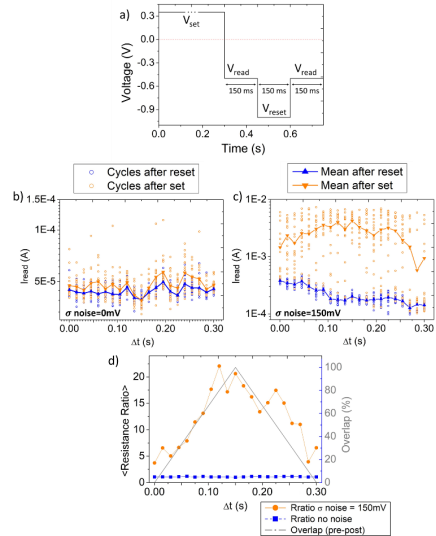


Fig. 3. Set process activated via noise addition. a) Complete applied signal for this study during one cycle. The maximum value timespan of V_{set} pulse varies every 20 cycles. The current during the 20 cycles for each Δt and mean current evaluated after a set transition, in orange, and after a reset in blue is presented in b) for the measurements without noise and in c) including noise ($\sigma = 150$ mV). In d) the mean value of R_{ratio} against Δt is presented. For the measurements without including noise, in blue, and with noise, in orange.

B. Reset Process Activation

This subsection presents the opposite situation to the previous approach. Set pulses are fixed while reset pulses are variable. Now, it is the reset process the one intended to be activated via noise addition. Hence, the applied voltages have the opposite sign with respect to case A. The set pulses maximum voltage is fixed to a voltage high enough to ensure

the transition to the LRS. Now, the pre- and post-synaptic pulses consist in 0.3 V and -0.3 V pulses respectively, resulting in a 150 ms pulse of $V_{set} = V_{tot} = 0.6\text{ V}$, which is the same in all cycles and iterations. However, the complexity appears now in the reset voltage, but the methodology used for its generation is the same as that considered in the previous subsection resulting, in this case, in a negative voltage pulse with a maximum value $V_{reset} = V_{tot} = -0.55\text{ V}$. This value is below the voltage required to activate the reset process. The noise intensity is the same than in the previous subsection ($\sigma_{noise} = 150\text{ mV}$). Here, the delay is in the post-synaptic pulse for the reset process, generating a different overlap condition every 20 identical cycles. In this section, the noise is applied during the reset process.

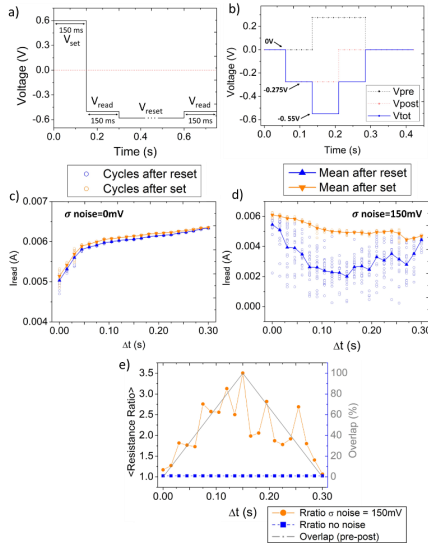


Fig. 4. Reset process activated via noise addition. a) Complete applied signal for this study during one cycle. b) medium overlap situation between the pre- and post-synaptic pulses to build the variable reset pulse. The maximum value timespan of V_{set} pulse varies every 20 cycles. The current during the 20 cycles for each Δt and mean current evaluated after a reset transition, in orange, and after a reset in blue is presented in c) for the measurements without noise and in d) including noise ($\sigma = 150\text{ mV}$). In e) the mean value of R_{ratio} against Δt is presented. For the measurements without including noise, in blue, and with noise, in orange.

As reported in the previous subsection, Fig. 4.a shows one cycle of the applied signal for this reset process activation, where the set process is a fixed pulse and the reset pulse is variable, changing every 20 cycles, as mentioned above. Figure 4.b illustrates an example of a medium overlap situation between the pre- and post-synaptic pulses to form the reset pulses in this subsection and highlights the resulting voltage values. Figures 4.c and 4.d show the currents measured after every transition and cycle as a function of Δt for the

experiments without and with noise, respectively. Again, the noise allows the device to switch, but in this case from LRS to HRS with a switching probability proportional to the overlap. This trend is confirmed by the results shown in Fig. 4.e, where the R_{ratio} of the two different situations (with and without noise inclusion) is shown as a function of the post-synaptic pulse delay. The figure includes the dash gray line showing the overlap evolution as a function of the delay as well. Once it is demonstrated that both set and reset processes can be activated separately with the addition of noise, the key part of this work is to combine both activations simultaneously. This study is presented in the following subsection.

C. Complete Switching Activation

In this subsection, the combination of the two previous studies is presented. This is the most realistic situation where a system is always driven by a noisy signal. Hence, both set and reset processes will be under noise influence. The applied voltages are $V_{set} = V_{tot} = 0.38\text{ V}$ and $V_{reset} = V_{tot} = -0.58\text{ V}$. Both values are not sufficient to activate the switching. The same noise ($\sigma_{noise} = 150\text{ mV}$) was applied. The slight set and reset voltage values differences with respect to the previous sections are a consequence of the inherent device-to-device (D2D) variability. These particular values were selected so as to achieve an initial condition as similar as possible for all the experiments. From the results in several devices (~ 25), we identified the optimal voltage ranges to be: V_{set} from 0.35 V to 0.4 V and V_{reset} from -0.55 V to 0.6 V . In the same line as in the previous subsections, Fig. 5 summarizes the experimental study carried out. Figure 5.a illustrates the applied voltage signal where both set and reset pulses timing is variable. A key point for the set and reset pulses timing in this subsection is that the evolution of the pre- and post-synaptic pulses duration is synchronized. This means that the timespan of the maximum value in both set and reset pulses is the same (i.e., the same overlap), for all the cycles. Figures 5.b and 5.c present the measured current after every set and reset transition against Δt for the experiments without noise and including it, respectively. The added noise enables both transitions simultaneously. In this subsection, the overlap between pre- and post-synaptic pulses evolves equally in both set and reset transitions.

It is worth mentioning that there are differences in the resistance ratio values obtained with the three approaches (see Figs 3.d, 4.e and 5.d) described above. In the first approach, where the set process is activated by noise, the maximum resistance ratio value is approximately equal to 20. In the second approach, where the reset process is activated, the maximum value is around 3.5, and in the third approach, with both transitions activated, the maximum value is 9. The resistance ratio differences observed in the three subsections can be ascribed to the widely known intrinsic memristor variability, the selection of noise sigma, and the voltage values for the constant pulses for reset and set transitions in subsections A and B respectively. The predominant factor is the different abruptness of the set and reset processes in the used memristors. Regarding the last issue, in the I - V curve shown in Fig. 1.b, the set process is notably more abrupt than the reset process, which is gradual. Hence, the noise activation of the set (section A) allows a high resistance ratio after a complete reset

process. However, for subsection B, the resistance ratio values are lower because of the progressiveness of the reset process, therefore noise does not allow a large resistance state change during this process.

In this section, a comprehensive investigation into the SR effect within neuromorphic systems utilizing memristors was presented. The study highlighted the positive impact of noise on the binary STDP protocol. Through the strategic introduction of noise in either the set pulse, reset pulse, or both simultaneously, we demonstrated the switching activation. The experiments detailed in this study were replicated using other devices from the same wafer to verify consistency and reproducibility of results.

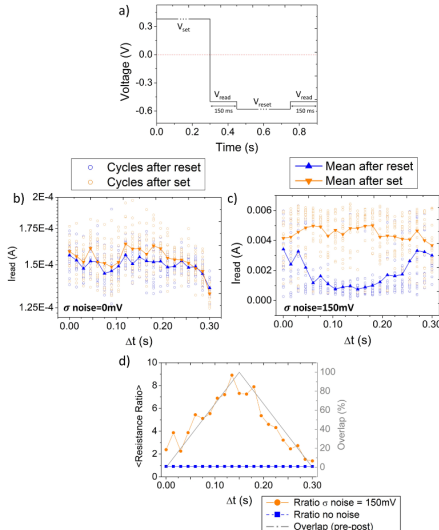


Fig. 5. Set and reset processes activated via noise. a) Presents the complete applied signal during one cycle. The duration of the maximum values of V_{set} and V_{reset} is the same. The current during the 20 cycles for each Δt and mean current evaluated after a set transition, in orange, and after a reset in blue is presented in b) for the measurements without noise and in c) including noise ($\sigma = 150\text{mV}$). In d) the mean value of R_{ratio} against Δt is presented. For the measurements without including noise, in blue, and with noise, in orange.

III. SIMULATING STDP ACTIVATION VIA SR

As part of this study, we report in what follows simulation results using the LTspice simulator. The goal is to reproduce the same input signal used for the third and more complex approach presented and to analyze the response of the memristor provided by the considered model. For the simulations we have used the dynamic memdiode model (DMM) [27, 28] for RRAM devices, which has demonstrated high versatility for a wide variety of input signals [31, 32]. In this work, the model will be tested with complex and noisy signals. The DMM is implemented in LTspice, and it basically

consists in two main equations, one for the current-voltage characteristic and another for the memristor memory state. Detailed information about the model and applications can be found in [27, 28].

Before the simulations, setting the model parameters is a necessary step. The procedure consisted in selecting the model parameters that reproduce the behavior of the devices used in this work, which are obtained by fitting the experimental data to the model equations. The result of this fitting process is shown in Fig 6.a, where the I - V curves corresponding to 10 experimental cycles (in grey) are compared to a simulated curve (in red). In addition, Fig 6.b presents the schematics of the LTspice circuit used for the simulations containing 4 voltage sources: the pre- and post-synaptic pulses (V_{pre} and V_{post}), and the noise sources for the set and reset processes (SetVn and ResetVn, respectively).

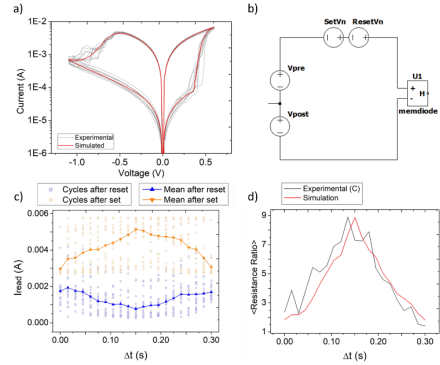


Fig. 6. a) Comparison of the experimental (grey) and fitted (red) I - V characteristic. b) LTspice circuit schematics used to simulate STDP activation via SR. c) Simulated current during the 20 cycles for each Δt and mean current evaluated after a set transition, in orange, and after a reset transition in blue including noise obtained using the LTspice simulator and the DMM model. d) Experimental (grey) and simulated (red) resistance ratio against Δt showing a good agreement between both curves.

The complex signals were generated in LTspice using the Piecewise linear (PWL) function, where time and voltage can be programmed point by point, while the white gaussian noise signal is added externally. Once the pulsed signals are generated, the noise is included in the transitions, the simulations run, and the results externally compiled and analyzed in MATLAB. The results reported in Fig. 6.c (symbols) show the reading current after every set (in orange) and reset (in blue) transitions versus the Δt for a simulation including noise. The continuous line corresponds to the mean value of the LTspice simulation. The HRS and LRS reading current values and dependence on the post-synaptic pulse delay obtained through simulation show that the model is able to reproduce the experimental behavior. Figure 6.d compares the experimental and simulated resistance ratio against Δt . The simulations demonstrate the binary STDP protocol can be activated through external noise addition in LTspice, showing a good agreement between experimental and simulated results.

IV. CONCLUSION

In this work, the beneficial effect of the addition of an external noise source to the base signal in the performance of HfO_2 based memristors was experimentally demonstrated. We reported a complete experimental study of the SR in STDP protocol implemented with memristors, showing the beneficial role of additive noise on the binary STDP protocol. Our study analyzes the SR phenomenon in a scenario where the memristor's HRS and LRS was not distinguishable. Nevertheless, we have demonstrated that by including noise to the set pulse, reset pulse or both pulses simultaneously, the resistive switching was activated. The slight impact of the D2D variability forces to define a narrow range of input signals for the set and reset transitions activation. The results unveiled the impact of noise was different for the set and reset transitions, being more evident for the set transition. This effect was attributed to memristor variability, noise sigma, selected set and reset voltages values and to the abruptness of the set event comparing with the more gradual reset event. We assessed the positive impact of noise by examining the relationship between the resistance ratio and the duration of the highest value of the noise-triggered transition pulse. Our findings showed that as the duration of the maximum noise-activated transitions (set, reset, or both) increases, the resistance ratio also increases. The case where both (set and reset) transitions were noise-activated was simulated using the DMM in LTspice. The obtained results well reproduce the experimental observations. The presented results are promising and offer a potential avenue for further exploration of the stochastic resonance phenomenon in more complex neuromorphic systems. This includes using multiple memristors for experimental analysis and simulation of artificial neural networks.

REFERENCES

- [1] I. H. Im, S. J. Kim, H. W. Jang, "Memristive Devices for New Computing Paradigms", *Advanced Intelligent Systems*, 2(11), 2000105, 2020.
- [2] T. Gong et al., "First Demonstration of a Design Methodology for Highly Reliable Operation at High Temperature on 128kb 1T1C FeRAM Chip", *2023 IEEE Symposium on VLSI Technology and Circuits (VLSI Technology and Circuits)*, 2023.
- [3] S.H. Lee, X. Zhu, W. D. Lu, "Nanoscale resistive switching devices for memory and computing applications", *Nano Research*, 13, pp. 1228–1243, 2020.
- [4] D. Ielmini, S. H. P. Wong, "In-memory computing with resistive switching devices", *Nature Electronics*, 1, pp. 333–343, 2018.
- [5] G. Pedretti, V. Milo, S. Ambrogio, R. Carboni, S. Bianchi, A. Calderoni, N. Ramaswamy, A. S. Spinelli, D. Ielmini, "Stochastic learning in neuromorphic hardware via spike timing dependent plasticity with RRAM synapses", *IEEE Journal on Emerging and Selected Topics in Circuits and Systems*, 8, pp. 77–85, 2018.
- [6] D. Li, M. Hu, Y. N. Li, H. Jiang, N. Ge, E. Montgomery, J. M. Zhang, W. H. Song, N. Dávila, C. E. Graves, et al., "Analogue signal and image processing with large memristor crossbars", *Nature Electronics*, 7, pp. 52–59, 2018.
- [7] R. Benzi, A. Sutera and A. Vulpiani, "The mechanism of stochastic resonance", *Journal of Physics A: Mathematical and General*, vol. 14(11), L453, 1981.
- [8] K. Wiesenfeld, F. Moss, "Stochastic resonance and the benefits of noise: from ice ages to crayfish and SQUIDs", *Nature*, 373, pp.33–36, 1995.
- [9] G.P. Harmer, B. R. Davis, D. Abbot, "A review of stochastic resonance: circuits and measurement", *IEEE Transactions on Instrumentation and Measurements*, 31(2), pp. 299–309, 2002.
- [10] S. Kasai, "Stochastic resonance and related phenomena in nonlinear electron nanodevices", *IEEE International Nanoelectronics Conference (INEC)*, 2014.
- [11] J. Náprstek and C. Fischer, "Stochastic Resonance and Related Topics", Resonance. InTech, Nov. 29, 2017.
- [12] A. Scotland, M. Di Ventra, "Stochastic memory: Memory enhancement due to noise", *Physical Review E*, 85, 011116, 2012.
- [13] G. A. Patterson, P. I. Fierens, D. F. Grosz, "On the beneficial role of noise in resistive switching", *Appl. Phys. Lett.*, 103, 074102, 2013.
- [14] V. Ntinas, A. Rubio, G. Ch. Sirakoulis, R. Rodriguez, M. Nafria, "Experimental Investigation of Memristance Enhancement", *IEEE/ACM International Symposium on Nanoscale Architectures (NANOARCH)*, 2019.
- [15] R. Rodriguez, J. Martin-Martinez, E. Salvador, A. Crespo-Yepes, E. Miranda, M. Nafria, A. Rubio, V. Ntinas, G. Ch. Sirakoulis "Beneficial Role of Noise in Hf-based Memristors," *2022 IEEE International Symposium on Circuits and Systems (ISCAS)*, pp. 975-979, 2022.
- [16] A. N. Mikhaylov et al., "Stochastic resonance in a metal-oxide memristive device", *Chaos, Solitons & Fractals*, 144, 110723, 2021.
- [17] J. B. Roldán, A. Cantudo, J. J. Torres et al. "Stochastic resonance in 2D materials based memristors", *npj 2D Materials and Applications*, 8, 7, 2024.
- [18] I. Boybat, M. Le Gallo, S. R. Nandakumar, T. Moraitis, T. Parnell, T. Tuma, B. Rajendran, Y. Leblebici, A. Sebastian, E. Eleftheriou, "Neuromorphic computing with multi-memristive synapses", *Nature Communications*, 9, 2514, 2018.
- [19] C. Zamarreño, L. A. Camuñas, Jose A. Perez, T. Masquelier, T. Serrano and B. Linares, "On spike-timing-dependent-plasticity, memristive devices, and building a self-learning visual cortex", *Frontiers in Neuroscience*, 5, 26, 2011.
- [20] C. de Benito, M. M. Al Chawa, M. Roca, R. Picos, S. G. Stravindes, "Self-learning perceptron using a digital memristor emulator", *2019 8th International Conference on Modern Circuits and Systems Technologies (MOCAST)*, 2019.
- [21] S. Vidya, Mohammed Riyaz Ahmed, "Advent of memristor based synapses on neuromorphic engineering", *2017 International conference on Microelectronic Devices, Circuits and Systems (ICMDCS)*, 2017.
- [22] C. Mohan, L. A. Camuñas-Mesa, J. M. de la Rosa, T. Serrano-Gotarredona, B. Linares-Barranco, "Implementation of Binary Stochastic STDP Learning Using Chalcogenide-Based Memristive Devices", *2021 IEEE International Symposium on Circuits and Systems (ISCAS)*, 2021.
- [23] Z. Zhou, C. Liu, W. Shen, Z. Dong, Z. Chen, P. Huang, L. Liu, X. Liu, J. Kang, "The Characteristics of Binary Spike-TimeDependent Plasticity in HfO_2 -Based RRAM and Applications for Pattern Recognition", *Nanoscale Research Letters*, 12, pp. 1–5, 2017.
- [24] J.S. Anderson, I. Lampl, D. C. Gillespie, D. Ferster, "The contribution of noise to contrast invariance of orientation tuning in cat visual cortex", *Science*, 290 (5498): 1968–1972, 2000.
- [25] A. Longtin, "Autonomous stochastic resonance in bursting neurons", *Phys. Rev. E*, 55 (1), pp. 868–876, 1997.
- [26] E. Salvador, R. Rodriguez, J. Martin-Martinez, A. Rubio, V. Ntinas, G. Ch. Sirakoulis, A. Crespo-Yepes, E. Miranda, M. Nafria, "Stochastic resonance effect in binary STDP performed by RRAM devices", *2022 IEEE 22nd International Conference on Nanotechnology (IEEE NANO)*, pp. 449-452, 2022.
- [27] E. Miranda and J. Sune, "Memristive State Equation for Bipolar Resistive Switching Devices Based on a Dynamic Balance Model and its Equivalent Circuit Representation", *IEEE Trans. Nanotechnol.*, 19, pp. 837–840, 2020.
- [28] F. Aguirre, J. Suñé, E. Miranda, "SPICE Implementation of the Dynamic Memdiode Model for Bipolar Resistive Switching Devices", *Micromachines*, 13, 330, 2022.
- [29] S. Poblador, M. Gonzalez, and F. Campabadal, "Investigation of the multilevel capability of TiN–Ti– HfO_2 –W resistive switching devices by sweep and pulse programming", *Microelectronic Engineering*, 187, pp. 148–153, 2018.
- [30] A. Marchewka, R. Waser, S. Menzel, "Physical modeling of the electroforming process in resistive-switching devices", *IEEE International Conference on Simulation of Semiconductor Processes and Devices (SISPAD)*, 2017.
- [31] E. Salvador, M.B. Gonzalez, F. Campabadal, J. Martin-Martinez, R. Rodriguez, E. Miranda, "SPICE modeling of cycle-to-cycle variability in RRAM devices", *Solid State Electronics*, 185, 108040, 2021.
- [32] M. Saludes, M.B. Gonzalez, F. Campabadal, J. Suñé, E. Miranda, "SPICE model for complementary resistive switching devices based on anti-serially connected quasi-static memdiodes", *Solid State Electronics*, 194, 108312, 2022.

Article TNANO24

Modeling and Simulation of Correlated Cycle-to-Cycle Variability in the Current-Voltage Hysteresis Loops of RRAM

E. Salvador, M.B. Gonzalez, F. Campabadal, J. Martin-Martinez, R. Rodriguez, E. Miranda

Modeling and Simulation of Correlated Cycle-to-Cycle Variability in the Current-Voltage Hysteresis Loops of RRAM Devices

E. Salvador, M.B. Gonzalez, F. Campabadal, R. Rodriguez, and E. Miranda, *Senior Member, IEEE*

Abstract—Resistive RAMs or memristors are nowadays considered serious candidates for the implementation of energy efficient and scalable neuromorphic computing systems. However, a major drawback of this technology is the instability of the device current-voltage (I - V) characteristic as is clearly revealed by the so-called cycle-to-cycle (C2C) variability. This lack of complete reproducibility is a consequence of the spontaneous or induced morphological changes of the filamentary conducting structure occurring at atomic level. Variability is an essential issue any compact model for the conduction characteristics of RRAM devices should be able to cope with to be considered realistic. In this work, a thorough investigation of the C2C variability in the I - V loops of HfO_2 -based memristive structures was carried out with the aim of incorporating this information into the equations of the Dynamic Memdiode Model. From the compact modeling viewpoint, C2C correlation effects are achieved using model parameters expressed as mean-reverting stochastic processes driven by Wiener noise (Ornstein-Uhlenbeck process). The direct and indirect links between the random behavior of the model parameters and the observable magnitudes (high and low resistance states, set and reset voltages, etc.) are discussed. The agreement between simulation and experimental results is statistically assessed using the Wasserstein's distance metric.

Index Terms—RRAM, memristor, variability, SPICE.

I. INTRODUCTION

Resistive Random Access Memories (RRAMs), also known as memristors, are electroformed two-terminal devices capable of modifying their resistance state in a non-volatile fashion in response to the application of an external stimulus (voltage, current, light, etc.) [1-2]. These devices are nowadays seriously considered for a number of applications in the areas of information storage, neuromorphic computing, logic circuits, cryptography, etc. Among their properties we can mention low power consumption, high scalability, velocity, endurance, retention, and what is remarkably important, CMOS compatibility [3-8]. RRAMs rely on the Resistive Switching (RS) phenomenon, which arises from the alternate formation and destruction of a conductive filament (CF) embedded in the dielectric layer of a metal-insulator-metal structure (MIM). The devices investigated in this work exhibit the so-called bipolar-type behavior in which opposite electric fields need to be applied to switch the device on and off alternately. These two extreme conduction states are often referred to as the low (LRS) and high (HRS) resistance states of the device, respectively. In memristive devices, the origin of the switching mechanism can be related to the movement of metal ions or oxygen vacancies

within the dielectric film. However, one of the major drawbacks for the massive application of these devices is their intrinsic instability. The current variability is largely related to morphologic changes in the CF occurring at atomic scale and can occur spontaneously or be induced [9-10]. An important aspect for the development of this technology, as well as for any other, is compact modeling. Having an accurate and robust model for the conduction characteristic of the device certainly helps in the understanding, design, and expansion of a new technology. Since variability is unavoidable in current RRAM devices, any compact model intended to reproduce their output characteristics should consider to a lesser or greater degree this phenomenology. However, this is not straightforward since variability is not only related to the particularities of the device under test but also to the kind of stimulus to which the device is subjected during its lifetime. As this is in principle unpredictable without further specification, one possibility is to adopt a broad-range application model capable of being adapted to specific circumstances. A number of works dealing with the compact modeling of C2C variability in RRAMs can be found in the literature [11-17]. A comprehensive review including the most recent advances in the variability assessment in RRAM modeling is presented in [11]. In [12], a variability study considering correlation of the HRS and LRS currents for the initial cycles using an analytical model is reported. In [13], an approach for emulating variability effects in a SPICE memristor model is discussed. In [14], a Monte-Carlo approach to reproduce C2C variability during the set and reset processes is described. In [15], an algorithm for the inclusion of variability in the Stanford-PKU model is presented and in [16], the connection between the temperature and filament shape with variability is analyzed. A time series analysis for the evolution of particular observables in RRAMs can also be found in [17]. None of these works considers C2C correlation effects in the most important observables associated with experimental I - V curves.

In this work, we report a method for including correlated C2C variability in the Dynamic Memdiode Model (DMM) [18-19] through the use of pseudo-Ornstein-Uhlenbeck (p -OU) processes. The proposed methodology basically consists in introducing correlation and noise in some key model parameters of the DMM. In a previous work [20], we added variability to the DMM parameters, but no correlation effects were considered. The objective of this work is to show how this new approach is able to generate I - V curves with a degree of dispersion and correlation comparable to what is experimentally observed in HfO_2 -based RRAMs. The agreement between simulations and experiments is statistically assessed using the Wasserstein's distance (WD) [21]. This

paper is organized as follows: Section 2 describes the devices investigated in this work, mainly their structure and fabrication process. In Section 3, the proposed approach to include variability in the compact model is discussed. Section 4 focuses on practical issues about the model implementation. Section 5 reports the results of this work including a comparison of different figures of merit for the simulated and experimental curves. Finally, Section 6 presents the conclusions of this work. Details of the proposed approach can be found in the Supplementary Material (SM) file.

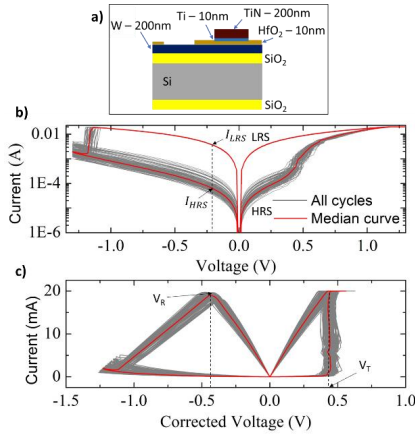


Fig. 1: a) Cross section of the investigated devices. b) All cycles and median I - V characteristics for the RRAM devices in logarithmic current axis. c) The same I - V curves using the snapback voltage correction ($V_{sb}=V-R \cdot I$). V_T is the transition voltage and V_R the reset voltage.

II. EXPERIMENTAL DEVICES AND METHODOLOGY

This Section describes the devices under test and the measurements carried out. The cross section of the investigated structures (TiN-Ti-HfO₂-W) is shown in Figure 1a. The 10 nm-thick HfO₂ layer was grown using the atomic layer deposition (ALD) technique at 225 °C. The active area of the device is 5x5 μm^2 . The precursors used for the deposition were TDMAH and H₂O. N₂ was used both as carrier and purge gases. The bottom electrode is a 200 nm-thick Ti layer, while the top electrode consists of a 200 nm-thick TiN layer deposited on a 10 nm-thick Ti layer, which acts as the oxygen scavenging material. I - V measurements were performed using the Semiconductor Parameter Analyzer (SPA) Agilent 4156C. Fresh devices were subjected to a 1 mA current-limited forming process, which in our devices occurs at voltages close to 3.5 V (not shown here). During cycling, the applied voltage was swept from 0 V to 1.3 V, from 1.3 V to -1.3 V, and finally from -1.3 V to 0 V (100 cycles). Current limitation was included during the set process (20 mA) to avoid an irreversible breakdown of the device. The reset process takes place with no kind of limitation. Further details about the electrical characterization can be found in [22]. In our devices, the HRS \leftrightarrow LRS transitions are related to

the formation and destruction of a vacancy-formed filamentary structure spanning the oxide layer [23]. Figure 1b shows 100 I - V cycles for an electroformed memristor. Cycled curves are shown in grey while the median curve is in red. For the analysis, HRS and LRS currents were also evaluated at $V = -0.2$ V. Figure 1c shows the resulting I - V curves after the snapback (SB) correction to the applied voltage $V_{sb} = V - R \cdot I$, where R is any internal/external series resistance. This SB correction allows us to extract the transition voltage which is related to the abrupt current increase at the transition voltage V_T . As can be seen in Fig. 1c, using an appropriate R value results in $V_T = -V_R$. More information about the effect of the series resistance and its extraction methods are reported in [24,25]. The current increase after SB is often ascribed to the accumulation of ions or defects in the CF or to its lateral expansion [10]. V_T represents the minimum voltage required for moving the ions or vacancies.

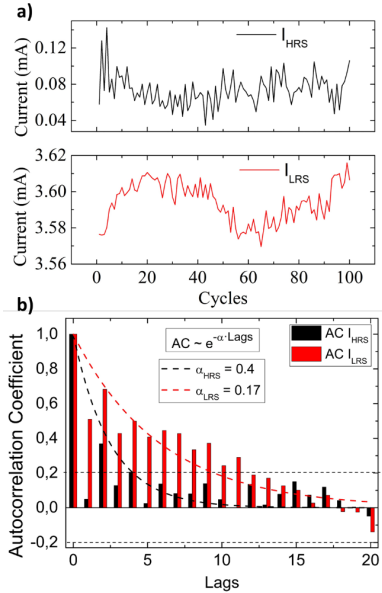


Fig. 2: a) HRS and LRS current values measured at -0.2V for all the cycles available. b) AC plots for HRS (in black) and LRS (in red) currents the dash lines are the theoretical exponential decay for AC in an OU process ($AC \sim e^{-\alpha \cdot \text{Lags}}$).

Figure 2a presents the HRS and LRS current evolution measured at -0.2 V for all the cycles reported in Figs. 1b and 1c. Notice that both the LRS and HRS currents exhibit correlated fluctuations, which are clearly detected in the autocorrelation (AC) plots of Fig. 2b. The AC of an OU process follows the exponential relationship $AC \sim e^{-\alpha \cdot \text{Lags}}$, where α is a constant. We found $\alpha_{HRS} = 0.4$ and $\alpha_{LRS} = 0.17$. Figure 2b graphically summarizes the strength of the relationship between the current and past observations, in our case, the current and past cycles. As it will be shown next, we propose to model these

correlated fluctuations using as a first approximation p -OU processes in the definition of the DMM parameters. Specific long-term trends in the lower and upper limits of the device resistance window caused by aging effects must be considered separately and can be later added to the C2C fluctuations if this is the case.

III. IMPLEMENTATION OF THE ORNSTEIN-UHLENBECK PROCESS IN LTSPICE

In this Section, the fundamentals of the OU process and its generation method in the framework of a circuit simulator like LTspice [26] are discussed. It is worth mentioning that the experimental curves were first explored with the aim of extracting statistical information about the measured observables (high and low resistance states, set and reset voltages) [20]. Then, the corresponding parametric distributions were used in the definition of the model parameters values. The best distributions for the different experimental observables were obtained using the *fidustrplus* package for the R language [27] and incorporated into the LTspice model script. In a second phase, an iterative process was carried out with the aim of obtaining the optimum combination of model parameter values. The mathematical steps towards this final goal are described next.

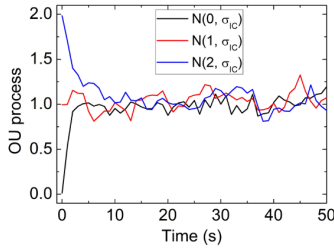


Fig. 3: Simulated OU processes, the considered parameters are $\mu = 1, \sigma = 0.1, \theta = 0.5$. The initial conditions are normal distributions centered at: 0 (black), 1 (red) and 2 (blue).

A. The Ornstein-Uhlenbeck process

Variability is introduced in the simulated curves through the use of OU processes [28]. OU is a widely known stochastic process that comprises a deterministic term for the evolution of the variable of interest plus a noise term which drives the system out of equilibrium. OU processes have a plethora of applications in physics, mathematics, biology, etc. and are the only stationary Gauss-Markov processes. Because of that, OU plays a central role in the theory of stochastic processes. Since the simulated variable drifts towards its mean value, the OU process is also called mean-reverting. The general expression for the OU process is given by the Itô-type stochastic differential equation (SDE):

$$dx_t = \theta(\mu - x_t)dt + \sigma dW_t \quad (1)$$

where x_t is the value of the variable at time t , μ its central location, θ the reversion coefficient, dt the time step, σ the volatility coefficient (noise amplitude) and W_t the Wiener

process (white noise). The discretized version of (1) is expressed as [28,29]:

$$X_{n+1} = X_n + \theta(\mu - X_n)\Delta t + \sigma\Delta W_n \quad (2)$$

where ΔW_n are independent identically-distributed Wiener increments, or in other words, a normal distribution with zero mean and Δt variance. Hence, $\Delta W_n \sim N(0, \Delta t) = \sqrt{\Delta t} \cdot N(0, 1)$. Accordingly, in practice, (2) reads:

$$X_{n+1} = X_n + \theta(\mu - X_n)\Delta t + \sigma\sqrt{\Delta t} \cdot N(0, 1) \quad (3)$$

Figure 3 presents three OU processes generated using (3). As shown in the figure, by selecting an appropriate initial condition (IC), the transient effect can be eliminated if required. In order to achieve this condition, the initial value is assumed to follow a normal distribution $N(\mu, \sigma_{IC})$ centered at the mean value of the OU signal and with standard deviation $\sigma_{IC} = \frac{\sigma^2}{2\theta}$. The implementation of (3) requires the use of a Gaussian number generator, a topic discussed in the SM file. The control of the initial condition is also advantageous in cases where the DMM parameters need to account for initial transient effects.

B. Simulation and characterization of the p -OU process

Since this work mainly concerns with the inclusion of variability in LTspice simulations for the conduction characteristics of RRAM devices, the proposed approach imperatively requires the use of a random number generator (RNG). In order to generate an OU process, a white Gaussian RNG must be implemented. A thorough examination of the tools provided by LTspice and the construction of an ad-hoc Gaussian RNG are reported in the SM file. The Box-Müller algorithm [30] was used for this task and the generator is referred to as Monte Carlo Gaussian (MCG). The Lilliefors test was considered for evaluating its statistical properties [31]. In what follows, we focus on the simulation and characterization of the complete stochastic process. The LTspice tool for generating a controlled recursive process as required by (3) is the *delay* function. Recall that otherwise the simulation timestep is always under the control of the simulation engine. The *delay* function considers two parameters: the variable of interest and in our case the time between two consecutive cycles (Δt or *del* in the model script). This Δt considered for simulations needs to be compatible with the experimental data. Simulations using (3) were first performed in LTspice. For a double check, the generated results were statistically compared with MATLAB simulations obtained under identical conditions. Since the timestep is not under the user's control in LTspice but only the maximum timestep, the simulated signal can contain unexpected points. The appearance of these unexpected points is the reason for calling the generated process a *pseudo*-OU (p -OU) process. Thus, in order to compare with the signal generated in MATLAB, the unwanted datapoints from the LTspice dataset must be removed (via software) taking into account Δt . The results obtained this way can then be analyzed in R. Figure 4a illustrates the comparison between the p -OU LTspice signal (pink) and the OU MATLAB signal (green). The same input parameters (θ, μ, σ, z) were used in both calculations. Similar distributions are observed. More in detail, Fig. 4b compares the associated probability densities.

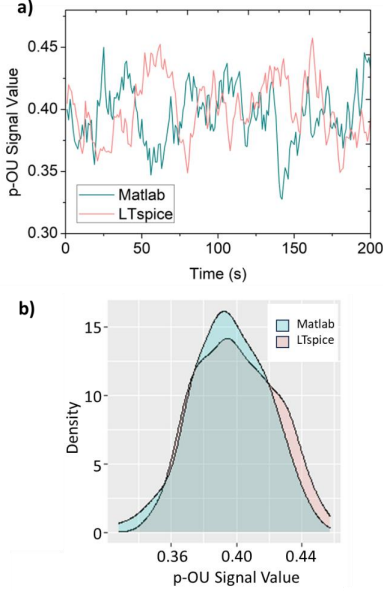


Fig. 4: p-OU signal comparison in LTspice (pink) and Matlab (green). a) Time evolution of the simulated signals. b) Density plots. The conditions for the obtention of both p-OU signals are: $\mu = 0.4$, $\sigma = 0.013$, $\theta = 0.15$, $z = 1$.

IV. SIMULATIONS USING THE DYNAMIC MEMDIODE MODEL

This Section focuses on the inclusion of correlated C2C variability in the DMM. The DMM describes the conduction characteristics of RS devices under the application of arbitrary input signals. The origin of the switching behavior is related to the creation and destruction of the CF that spans across the dielectric layer. This in turn is linked to the metal ions or oxygen vacancies displacement depending on the device type (CBRAM or OxRAM). In bipolar devices, the transition between HRS and LRS (CF generation) and viceversa (CF rupture) takes place at opposite voltages [32-33]. This is the case we are going to analyze next. The DMM reproduces the I-V characteristic of a bipolar-type memristive devices using two coupled equations. The first equation (4) deals with the electron transport while the second equation (5) relates to the internal state of the device. According to the DMM, the I - V characteristic reads:

$$I(V) = I_0(\lambda) \sinh\{\alpha(\lambda)[V - (R_c(\lambda) + R_l)I]\} \quad (4)$$

where V is the applied voltage, I_0 the current amplitude factor, R_c a variable series resistance, and α a fitting parameter. λ runs between 0 and 1 and it is called the memory state of the device. Its purpose is to control the transitions HRS \leftrightarrow LRS. R_l is a fixed resistance related to the snapback voltage correction discussed in Section II [34]. Notice that (4) includes three different parameters with λ -dependence. For simplicity, these parameters are assumed to change linearly and in the same way from a

minimum (*off*) to a maximum (*on*) value as a function of λ . For instance, $I_0(\lambda) = I_{off} + (I_{on} - I_{off}) \cdot \lambda$, where I_{off} and I_{on} represent the minimum (HRS) and maximum (LRS) current values, respectively. According to (4), in HRS, the current depends exponentially on V , while in LRS, the current depends linearly on V because of the potential drop across the series resistances R_l and R_c . λ is described by a balance-type voltage-driven differential equation [18]:

$$\frac{d\lambda}{dt} = \frac{1 - \lambda}{\tau_S(\lambda, V_{sb})} - \frac{\lambda}{\tau_R(\lambda, V_{sb})} \quad (5)$$

where $\tau_{S,R}$, called TS and TR , respectively in the model script (details in the SM file), are the characteristic times for the set and reset transitions. These characteristic times are expressed as:

$$\tau_S(V) = \exp[-\eta_S(V_{sb} - V_{S,T})] \quad (6)$$

$$\tau_R(V) = \exp[\eta_R \lambda^\gamma (V_{sb} - V_R)] \quad (7)$$

where $\eta_{S,R}$, also called η_{TS} and η_{TR} respectively in the model script, are the transition rates. $V_{S,R}$ are the set and reset switching voltages, respectively. The snapback current (isb in the model script) acts as a threshold current for the snapback effect. The snapforward parameter $\gamma \geq 0$ (called *gam* in the model script) controls the reset transition rate. Further details about the DMM can be found in [18,19]. In addition, more references to the snapback and snapforward effects in the I-V characteristic can be found in [19]. The model script, the schematics used in the LTspice simulator, and a short explanation about the inclusion of variability in the model parameters specifying each variable parameter type (p-OU or probability distribution) are reported in the SM file. It is worth mentioning that simulations were performed using the same timing and voltage conditions as those used for the measurements. The adjustment of the model parameters takes into account the shape of the I - V curves, their statistical distribution and the autocorrelation. In order to find the best set of parameters, the simulated and experimental curves were subjected to an iterative process in which the global deviation is calculated. The median of the experimental curves is considered as the initial guess for this process. For the sake of simplicity, and to avoid over-randomness, only 4 parameters, one for each key region of the hysteretic loop, were selected to be described as p-OU processes: I_{off} , I_{on} , V_T and V_R . The remaining parameters are constant or follow a specific probability distribution. The simulated results, including variability, are compared with the measurements cycle after cycle until a final target is reached. Further details are discussed in the next Section.

V. COMPARING EXPERIMENTAL AND SIMULATED CURVES

In this Section, the comparison between the simulated and experimental I - V curves is discussed. Figure 5 shows typical results obtained with the DMM. As it can be seen, the main features of the curves are correctly addressed. Fitting the LRS current is by no means straightforward since the corresponding observable is the result of the combination of several model parameters associated with HRS (I_{off} , R_{off} , a_{off}). In turn, the model parameters associated with the LRS current

(I_{on} , R_{on} , a_{on}) directly impact on the voltage location and variability of the reset transition. This is referred to as variability propagation. The complete simulation requires the strict control of some model parameters like I_{off} for example in order not to crash the simulator by an improper combination of model parameters.

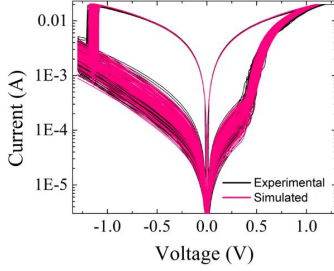


Fig. 5: Simulated and experimental I-V curves in pink and black respectively in logarithmic axis for the current. The simulated curves were obtained by using the model script and schematics presented in the Supplementary Material.

More in detail, Fig. 6 presents the evolution of the Wasserstein distance for the four selected observables: I_{HRS} (in black), I_{LRS} (in red), V_T (in green) and V_R (in violet) for different stages of the optimization process. Here, we use the WD as a measure of the difference between the simulated and experimental distributions [21]. For the y axis, WD is normalized by the mean value of the experimental observable. This allows plotting the four different observables in the same scale. It is clearly seen that as the optimization process proceeds, WD decreases, which indicates more accurate results in a statistical sense. The optimization process ends when WD reaches a predefined threshold value. If a given change in the model parameters leads to an increase of WD, this change is rejected. For the sake of clarity, Fig. 6 also includes the set of experimental and simulated I-V curves for three different stages of the optimization process: initial (S1), intermediate (S5) and final (S11) situations. The reduction of WD coincides with the improvement of the fitting results.

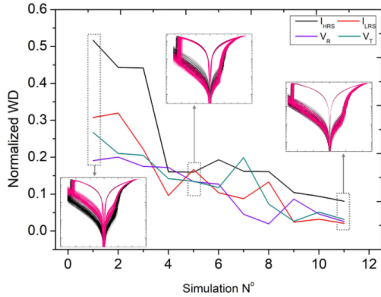


Fig. 6: Wasserstein distance for the four selected observables in chronologically ordered simulations. For illustrative purposes, the simulated curves are included for initial (S1), intermediate (S5), and final (S11) chronological situations.

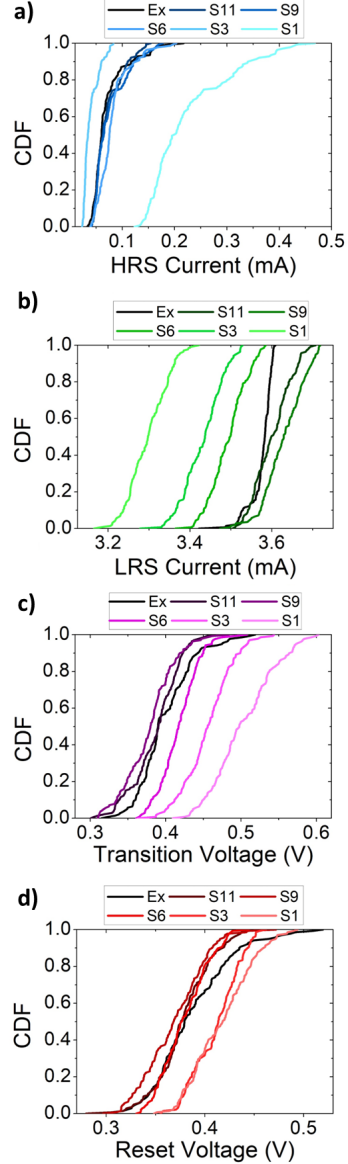


Fig. 7: Evolution of the CDF plot. In black, the experimental and in a darkness-fade, from initial (lighter) to late (dark) simulations. a) for HRS current, b) for LRS current, c) for the transition voltage and d) for the reset voltage.

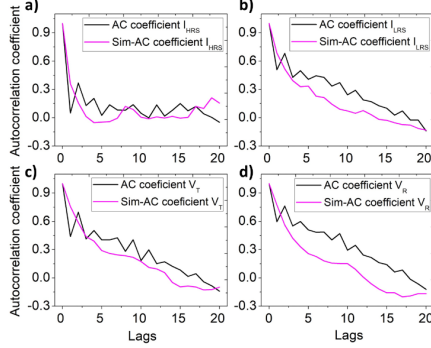


Fig. 8: Comparison of the autocorrelation coefficients as a function of the lag (cycle number) for the four selected parameters corresponding to the simulated (pink) and experimental (black) curves. a) for HRS current, b) for LRS current, c) for the transition voltage and d) for the reset voltage.

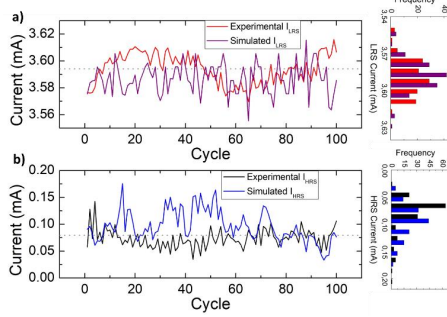


Fig. 9: Comparing the time evolution and histograms of the a) LRS and b) HRS currents in experimental and simulated curves. In dashed lines the experimental mean values are highlighted.

Notice that the selected observables are strategically chosen so as to summarize the information about the complete loop: I_{HRS} for the HRS curve, transition voltage V_T for the SET transition, I_{LRS} for the LRS curve, and V_R for the reset transition. Other selection is also possible. Figure 7 shows the cumulative distribution functions for the four selected observables, in black for measurements and in a darkness-fade for simulations (initial-bright, late-dark). Again, in agreement with the above discussed process, the darker curves are closer to the black ones as the optimization proceeds. Figure 8 shows the AC plots for the selected observables (experimental in black and simulated in pink) as a function of the measurement cycle for: a) I_{HRS} , b) I_{LRS} , c) V_T and d) V_R . Finally, Fig. 9 presents the C2C evolution of the HRS and LRS currents for the experimental (Fig. 9a) and simulated (Fig. 9b) curves. Both HRS and LRS currents were evaluated at $V = -0.2$ V. The dashed lines represent the experimental mean value. This visual representation summarizes the temporal evolution of the two alternate states enriching the preceding statistical analysis. This last exercise illustrates the capability of the proposed approach to reproduce

the two extreme conduction states, an essential feature for memristor-based digital applications. Of course, as mentioned several times along this work, an appropriate calibration process for each specific test considered is always necessary.

VI. CONCLUSION

In this work, a compact approach for SPICE simulations based on a modified version of the Dynamic Memdiode Model (DMM) able to account for correlated cycle-to-cycle variability in RRAM devices was presented. In order to generate such correlation effects, Ornstein-Uhlenbeck processes were assumed for the DMM parameters. A comprehensive study on the random number generation in LTspice was also carried out. It was shown that care should be exercised when invoking the internal functions of the simulator. The reported SPICE model includes the capability of simulating correlation effects in all the regions of the current-voltage characteristics of RRAM devices, a clear innovation with respect to the available approaches found in the literature. The ability of the model to reproduce the C2C experimental results was evaluated using the Wasserstein distance for the evolution of four strategically selected observables corresponding to the positive and negative quadrants of the I - V curves. The analysis was accompanied by a thorough assessment of the evolution of the autocorrelation and cumulative distribution plots for the observables.

ACKNOWLEDGMENT

This work was supported in part by Spanish MCIN/AEI /10.13039/501100011033/FEDER under projects PID2019-103869RB-C32, PID2022-139586NB-C41 and PID2022-139586NB-C42. The authors thank CSIC funding through project 20225AT012. E.S. acknowledges the Departament de Recerca i Universitats de la Generalitat de Catalunya for the 2020FISDU00261 scholarship. M.B.G. acknowledges the Ramón y Cajal grant No. RYC2020-030150-I.

REFERENCES

- [1] I. H. Im, S. J. Kim, H. W. Jang, "Memristive Devices for New Computing Paradigms", *Advanced Intelligent Systems*, vol. 2, no. 11, 2000105, 2020.
- [2] S. Yu and P. Y. Chen, "Emerging Memory Technologies: Recent Trends and Prospects", *IEEE Solid State Circuits Magazine*, vol. 8, no. 2, pp. 43-56, 2016.
- [3] S.H. Lee, X. Zhu, W. D. Lu, "Nanoscale resistive switching devices for memory and computing applications", *Nano Research*, 13, pp. 1228-1243, 2020.
- [4] D. Ielmini, S. H. P. Wong, "In-memory computing with resistive switching devices", *Nature Electronics*, vol. 1, pp. 333-343, 2018.
- [5] G. Pedretti, V. Milo, S. Ambrogio, R. Carboni, S. Bianchi, A. Calderoni, N. Ramaswamy, A. S. Spinelli, D. Ielmini, "Stochastic learning in neuromorphic hardware via spike timing dependent plasticity with RRAM synapses", *IEEE Journal on Emerging and Selected Topics in Circuits and Systems*, vol. 8, pp. 77-85, 2018.
- [6] D. Li, M. Hu, Y. N. Li, H. Jiang, N. Ge, E. Montgomery, J. M. Zhang, W. H. Song, N. Dávila, C. E. Graves, et al. "Analogue signal and image processing with large memristor crossbars", *Nature Electronics*, vol. 7, pp. 52-59, 2018.
- [7] H. Aziza, J. Postel-Pellerin, H. Bazzi, P. Canet, M. Moreau, V. Della Marca, A. Harb, "True Random Number Generator Integration in a Resistive RAM Memory Array Using Input Current Limitation", *IEEE Transactions on Nanotechnology*, vol. 19, pp. 214-222, 2020.
- [8] S. H. Jo, T. Chang, I. Ebong, B. B. Bhadviya, P. Mazumder, and W. Lu, "Nanoscale memristor device as synapse in neuromorphic systems", *Nano Letters*, vol. 10, no. 4, pp. 1293-1301, 2010.

- [9] A. Chen and M. R. Lin, "Variability of resistive switching memories and its impact on crossbar array performance", *IEEE IRPS*, pp. 843-846, 2011.
- [10] V. Karpov, D. Niraula, I. Karpov, "Thermodynamic analysis of conductive filaments", *Appl. Phys. Lett.*, vol. 109, pp. 1-5, 2016.
- [11] J. B. Roldán et al., "Variability in resistive memories", *Advanced Intelligent Systems*, vol. 5, 2200338, 2023.
- [12] G. Piccolboni et al., "Investigation of Cycle-to-Cycle Variability in HfO₂-Based OxRAM", *IEEE Electron Device Lett.*, vol. 37, pp. 721-723, 2016.
- [13] F. García-Redondo, M. López-Vallejo, C. L. Barrio, "Advanced integration of variability and degradation in RRAM SPICE compact models," *2017 14th International Conference on Synthesis, Modeling, Analysis and Simulation Methods and Applications to Circuit Design (SMACD)*, pp. 1-4, 2017.
- [14] H. Li et al., "Variation-aware, reliability-emphasized design and optimization of RRAM using spice model", *2015 Design, Automation Test in Europe Conf. Exhibition*, pp. 1425-1430, 2015.
- [15] J. Reuben, M. Biglari, D. Fey, "Incorporating Variability of Resistive RAM in Circuit Simulations Using the Stanford-PKU Model", *IEEE Transactions on Nanotechnology*, vol. 19, pp. 508-518, 2020.
- [16] G. González-Cordero et al., "A new compact model for bipolar RRAMs based on truncated-cone conductive filaments-a Verilog-A approach", *2016 Semicond. Sci. Technol.*, vol. 31, 115013, 2016.
- [17] F.J. Alonso, D. Maldonado, A. M. Aguilera, and J. B. Roldán, "Memristor variability and stochastic physical properties modeling from a multivariate time series approach", *Chaos, Solitons and Fractals*, vol. 143, 110461, 2021.
- [18] E. Miranda and J. Sune, "Memristive State Equation for Bipolar Resistive Switching Devices Based on a Dynamic Balance Model and its Equivalent Circuit Representation", *IEEE Trans. Nanotechnol.*, vol. 19, pp. 837-840, 2020.
- [19] F. Aguirre, J. Suñé, E. Miranda, "SPICE Implementation of the Dynamic Memdiode Model for Bipolar Resistive Switching Devices", *Micromachines*, vol. 13, 330, 2022.
- [20] E. Salvador, M.B. Gonzalez, F. Campabadal, J. Martín-Martínez, R. Rodríguez, E. Miranda, "Assessment of the variability of the I-V characteristic of HfO₂-based resistive switching devices and its simulation using the quasi-static memdiode model", *Solid State Electronics*, vol. 206, 108667, 2023.
- [21] C. Villani, "Optimal transport", *Grundlehren der Mathematischen Wissenschaften [Fundamental Principles of Mathematical Sciences]*, vol. 338, 2009.
- [22] S. Poblador, M. Gonzalez, and F. Campabadal, "Investigation of the multilevel capability of TiN-Ti-HfO₂-W resistive switching devices by sweep and pulse programming", *Microelectronic Engineering*, vol. 187, pp. 148-153, 2018.
- [23] A. Marchewka, R. Waser, S. Menzel, "Physical modeling of the electroforming process in resistive-switching devices", *IEEE International Conference on Simulation of Semiconductor Processes and Devices (SISPAD)*, 2017.
- [24] D. Maldonado, F. Aguirre, G. González-Cordero, A. M. Roldán, M. B. González, F. Jiménez-Molinos, F. Campabadal, E. Miranda, J. B. Roldán, "Experimental study of the series resistance effect and its impact on the compact modeling of the conduction characteristics of HfO₂-based resistive switching memories", *J. Appl. Phys.*, vol. 130, no. 5, 054503, 2021.
- [25] D. Maldonado, F. Jiménez-Molinos, J. B. Roldán, M. B. González and F. Campabadal, "An enhanced Verilog-A compact model for bipolar RRAMs including transient thermal effects and series resistance," *2022 37th Conference on Design of Circuits and Integrated Circuits (DCIS)*, Pamplona, Spain, 2022.
- [26] G. Brocard, "The LTspice XVII Simulator: Commands and Applications", Adolf Würth GmbH & Co. KG, 2021.
- [27] M. L. Delignette-Muller, C. Dutang, "fitdistrplus: An R package for fitting distributions", *J. Stat. Softw.*, vol. 64, pp. 1-34, 2015.
- [28] C. Gardiner, "Handbook of Stochastic Methods", *Springer Series in Synergetics*, vol. 13, 2004.
- [29] G. E. Uhlenbeck, L. S. Ornstein, "On the theory of Brownian Motion". *Phys. Rev.*, vol. 36, no. 5, pp. 823-841, 1930.
- [30] J. E. Gentle, "Random Number Generation and Monte Carlo Methods", *Statistics and Computing*, 1998.
- [31] H. W. Lilliefors, "On the Kolmogorov-Smirnov Test for Normality with Mean and Variance Unknown", *Journal of the American Statistical Association*, vol. 62, no. 318, 1967.
- [32] Y. Dai, Y. Zhao, J. Wang, J. Xu and F. Yang, "First principle simulations on the effects of oxygen vacancy in HfO₂-based RRAM," *AIP Advances*, vol. 5, 017133, 2015.
- [33] J. Blasco, N. Ghenzi, J. Suñé, P. Levy, and E. Miranda, "Equivalent circuit modeling of the bistable conduction characteristics in electroformed thin dielectric films," *Microelectron. Reliab.*, vol. 55, no. 1, pp. 1-14, 2015.
- [34] D.J. Wouters, S. Menzel, J.A.J. Rupp, T. Hennen, R. Waser, "On the universality of the I-V switching characteristics in non-volatile and volatile resistive switching oxides", *Faraday Discuss.*, vol. 213, pp. 183-196, 2019.

TNANO24-SM Supplementary Material

Modeling and Simulation of Correlated Cycle- to-Cycle Variability in the Current-Voltage Hysteresis Loops of RRAM

E. Salvador, M.B. Gonzalez, F. Campabadal, J. Martin-
Martinez, R. Rodriguez, E. Miranda

Supplementary material

A – Model script, schematics and guidelines

Subcircuit definition

```
.subckt memdiode + - H
.params
+ H0=0 RPP=1E10 vs=2; initial condition, parallel resistance, set voltage
+ etar=40 del=1 fps=1; reset transition rate, time between cycles, RNG rate
+ gam=0.1; snapforward factor, isb=1/gam=0 no snapback/snapforward
+ th1=0.15 mu1=ln(1.28E-4) s1=0.19 ic1=mu1+gauss((s1**2)/(2*th1)) n1=1; Ioff, HRS current
+ th2=0.45 mu2=20.3E-3 s2=0.7e-3 ic2=mu2+gauss((s2**2)/(2*th2)) n2=2; Ion, LRS current
+ mu3=6e-5 s3=0.2E-5 n3=3; Isb, snapback current
+ th4=0.25 mu4=-0.51 s4=0.009 ic4=mu4+gauss((s4**2)/(2*th4)) n4=4; Vr, reset voltage
+ mu5=27 s5=0.2 n5=5; ri, fix series resistance
+ th6=0.25 mu6=ln(0.415) s6=0.0415 ic6=mu6+gauss((s6**2)/(2*th6)) n6=6; Vt, transition voltage
+ mu7=3.0 s7=0.16 n7=7 mu8=1.9 s8=0.01 n8=8; aoff/aon
+ mu9=20 s9=1.8 n9=9 mu10=5 s10=0 n10=10; roff/ron, variable series resistance
+ mu11=34 s11=3 n11=11; etas, set transition rate
*Memory Equation
BI 0 H I=if(V(+,-)>=0,(1-V(H))/TS(V(C,-)), -V(H)/TR(V(C,-))) ; current generator for the memory state
CH H 0 1 ic={H0} ; initial state
*I-V
RI + C R=V(P05) ; fixed series resistance, ri
RS C B R=K(V(P10),V(P09)) ; variable series resistance
BF B - I=K(V(P02),exp(V(P01)))**sinh(K(V(P08),V(P07)))*V(B,-) ; current generator for electron current
RB + - {RPP} ; parallel resistance
*Parameters and variability using pOU process
BP01 0 P01 I=-th1*(delay(V(P01),del)-mu1)+delay(V(P01),del)+sqrt(del)*MCG(0,s1,fps,n1) IC=ic1 Rpar=1; Ioff
BP02 0 P02 I=-th2*(delay(V(P02),del)-mu2)+delay(V(P02),del)+sqrt(del)*MCG(0,s2,fps,n2) IC=ic2 Rpar=1; Ion
BP03 0 P03 I=mu3+MCG(0,s3,fps,n3) Rpar=1; Isb
BP04 0 P04 I=-th4*(delay(V(P04),del)-mu4)+delay(V(P04),del)+sqrt(del)*MCG(0,s4,fps,n4) IC=ic4 Rpar=1; Vr
BP05 0 P05 I=mu5+MCG(0,s5,fps,n5) Rpar=1; ri
BP06 0 P06 I=-th6*(delay(V(P06),del)-mu6)+delay(V(P06),del)+sqrt(del)*MCG(0,s6,fps,n6) IC=ic6 Rpar=1; Vt
BP07 0 P07 I=mu7+MCG(0,s7,fps,n7) Rpar=1; aoff
BP08 0 P08 I=mu8+MCG(0,s8,fps,n8) Rpar=1; aon
BP09 0 P09 I=mu9+MCG(0,s9,fps,n9) Rpar=1; roff
BP010 0 P10 I=mu10+MCG(0,s10,fps,n10) Rpar=1; ron
BP011 0 P11 I=mu11+MCG(0,s11,fps,n11) Rpar=1; etas
*Auxiliary functions
.func K(on,off)=off+(on-off)*limit(0,1,V(H)) ; distribution function
.func TS(x)=exp(-V(P11))*(x-VSB(I(BF)))) ; characteristic set time
.func TR(x)=exp(etar*ISF(V(H))*(x-V(P04))) ; characteristic reset time
.func VSB(x)=if(x>V(P03),exp(V(P06)),vs) ; snapback voltage
.func ISF(x)=if(x==0,1,pow(limit(0,1,x),gam)) ; snapbforward effect
.func MCG(x,y,z,n)=x+(y)*sqrt(-2*ln(rand((1E3*n)+time*z)))*cos(2*pi*rand((1E3*n)+time*z+1E5)) ; Gaussian generator
.ends
```

TABLE A Model script. LTspice DMM script including the parameters (fix, probability distributed, and p-OU type), the model equations and auxiliary functions for simplicity.

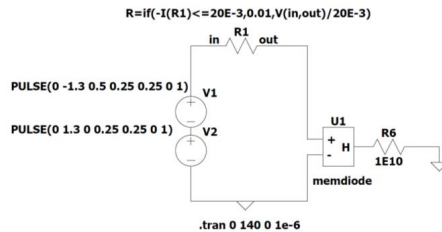


Figure A: LTspice schematics used to perform the simulations. Combining V1 and V2, the bipolar voltage sweep signal is achieved (from 0 to 1.3 V, to -1.3 V and back to 0). Other signals can be applied if required. R1 is used for setting the current compliance at 20 mA. By combining the model script and schematics, the simulated I-V curves shown in Fig. 5 in the manuscript were obtained.

Explanation for the model script

The model script is described in Section A of this Appendix. In Table A, + and – are the conventional device terminals, while H is the output terminal for the memory state (not used here). The first section defines the model parameters. *del* specifies the timing of the autoregressive part of the function and corresponds to the period of the measurement cycle. *fps* (fluctuations per second) is the sampling rate for the random part of the function. *H0* is the initial memory state and V_t the transition voltage. *RPP* is a parallel resistance required by the output current generator. The complete circuit is illustrated in Figure A shows the details of the model parameter distributions. The following lines define the parameters used to account for the variability: 4 *p*-OU processes were considered here. Notice that there are 4 building parameters per line: *thX*, *muX*, *sX* and *nX*, where *X* is the line number and each value represents a different model parameter. *thX* is the cycle-to-cycle reversion coefficient, *muX* is the mean value of the parameter, *sX* is the standard deviation of the noise term, and *nX* is a factor for differentiating the noise amplitude for each parameter. Next, the *p*-OU generators are defined, again one line for each model parameter (specified at the end of the line after a semicolon).

$$I = -th1 * (delay(V(P01), del) - mu1) + delay(V(P01), del) + sqrt(del) * MCG(0, s1, fps, n1) IC = ic1 Rpar = 1 \quad (1)$$

(1) is an example of a *p*-OU process defined in the model script. The corresponding parameter is generated using a current source in parallel to a resistance of value unity ($Rpar = 1$). However, it is worth pointing out that for some specific parameters (for example I_{off}), the best probability distribution is lognormal, not normal as expected from an expression like (1). In such cases, a simple transformation of the *p*-OU signal is performed when calling the parameter in the corresponding model equation. In other words, if the natural logarithm of a variable is normally distributed, the variable itself is lognormally distributed. Hence, by computing the exponential of the *p*-OU signal presented in (1), we achieve a lognormally distributed *p*-OU signal. The *p*-OU processes include three terms: the reversion factor, the value of the variable corresponding to the previous cycle, and the random term generated by the MCG RNG (defined in Supplementary Material, Section B). In addition, in the script line of each *p*-OU process, a proper initial condition (*IC*) is included. This helps to eliminate the transient effect as explained in subsection III.A of the manuscript. Alternatively, (2) describes a direct approach (PD) for generating a random parameter value with a given distribution (no correlation effect is assumed in this case).

$$I = mu3 + MCG(0, s3, fps, n3) Rpar = 1 \quad (2)$$

Table B summarizes for each model parameter the variability type (PD or *p*-OU) considered, the associated probability distribution, and the reason behind the underlying assumption. *Extracted* means the distribution is selected via *fitdistrplus* (R package) and *support* means the parameter is set as variable for accuracy issues. For the sake of simplicity, and to avoid over-randomness, only 4 parameters, one for each key region of the hysteretic loop, were selected to be described as *p*-OU processes: I_{off} , I_{on} , V_T and V_R . The rest are considered PD-type.

| Parameter | Type | Distribution | Origin |
|------------------------|------|--------------|-----------|
| I_{on} | p-OU | Normal | Extracted |
| I_{off} | p-OU | Lognormal | Extracted |
| I_{sb} | PD | Normal | Extracted |
| V_T | p-OU | Lognormal | Extracted |
| V_R | p-OU | Normal | Extracted |
| a_{on}, a_{off} | PD | Normal | Support |
| R_{on}, R_{off}, R_i | PD | Normal | Support |
| $etas$ | PD | Normal | Support |

Table B: Summary of the model variable parameters. Information about the variability type (p-OU or PD), the used distribution, and the origin of this distribution, either extracted from the experimental, or just for support or reproduction issues.

B – Random number generation (RNG) in LTspice

In order to generate an OU process, a white Gaussian RNG must be implemented. To this aim, LTspice offers different base functions: *white*, *rand*, *random* and *gauss*. From this list, the *gauss* function can be straightforwardly disregarded because it only operates when used in the model parameters definition, *i.e.*, before the simulation starts and remains fixed ever since. It is indeed useful when independent cycles are generated as in [1]. Although the three remaining candidate functions are supposed to generate a uniform distribution of numbers in the range $[0,1]$, they have subtle differences: *random* is a smoothed version of *rand*, and *white* is a bit smoother than *random*. *white* is not just an offset version of *random*. More in detail, Fig. B illustrates the generation of random numbers using the functions: a) *rand*, b) *random*, and c) *white*. The histograms are the result of $4 \cdot 10^5$ generated data points. As can be seen, the best candidate function is *rand* since the other two distributions are far from being uniform.

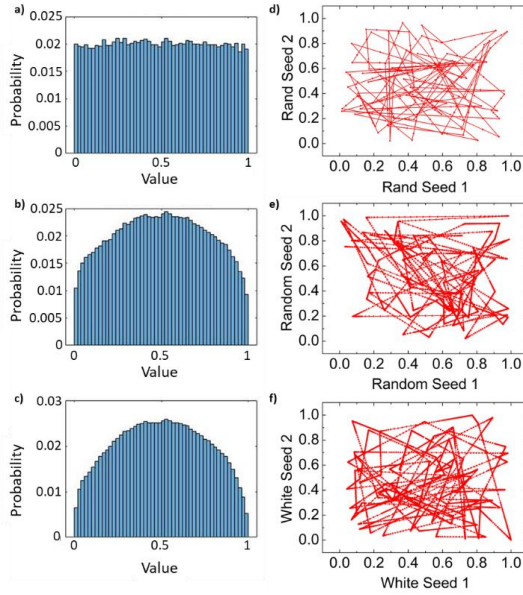


Figure B: Histograms for the signals obtained with the different LTspice functions: a) for *rand*, b) for *random* and c) for *white*. Correlation plots for two signals obtained with the same LTspice function but different seed: d) for *rand*, e) for *random* and f) for *white*.

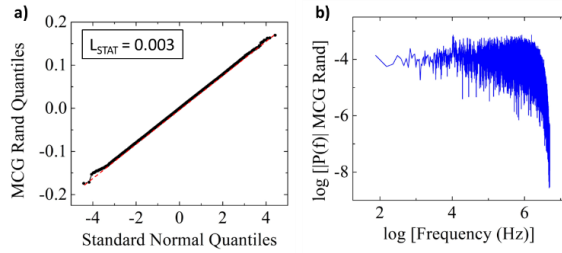


Figure C: a) Q-Q plot for normality test and b) FFT spectrum in logscale, for the signal generated with the Box-Müller algorithm using the *rand* function from LTspice with a 10^7 sampling rate.

Next, in order to generate normally distributed random numbers, we consider the Box-Müller (BM) algorithm

[2]. The method requires two independent uniformly distributed random variables (U_1 and U_2) as the inputs. The output is a normally distributed random variable (Z_0) with average 0 and variance 1. The BM algorithm is expressed as:

$$Z_0 = \sqrt{-2 \cdot \ln(U_1)} \cdot \cos(2\pi \cdot U_2) \quad (3)$$

In order to confirm the independence of the two inputs, Fig. B also presents the correlation plots for two different signals generated with the same LTspice function: d) for *rand*, e) for *random*, and f) for *white*. The figures show that the correlation coefficients (CC) are very low in all the cases. These results were obtained by ensuring a high enough offset between the seeds of the two inputs. The correlation, and therefore the dependence between these two generated random variables is strongly affected by this offset: the lower the offset, the higher their interdependence. Importantly, the correlation plots in Fig. B highlight the simulator limitation concerning RNGs. Since the internal computation timestep is not under the control of the user, a uniform time grid cannot be straightforwardly generated. In this connection, the correlation plots shown in Fig. B are expected to exhibit a 2D randomly distributed set of points, however, intermediate points always appear in between the extremes of each segment. This undesirable effect is more pronounced in the cases of the *random* and *white* functions.

In the DMM script (see Supplementary Material - Section A), the BM algorithm is implemented using (4) with some additional specific features. The function is called Monte Carlo Gaussian (MCG) and it is expressed as:

$$MCG(x, y, z, n) = x + y \cdot \text{sqrt}(-2 \cdot \ln(\text{rand}(\text{time} \cdot z + \kappa \cdot n))) \cdot \cos(2 \cdot \pi \cdot \text{rand}(\text{time} \cdot z + \kappa \cdot n + \Delta)) \quad (4)$$

In (4), x and y represent the mean value of the variable of interest (μ) and its standard deviation (σ), respectively. z refers to the sampling rate of the noise generator and n is an integer number in the range $[1, d]$ that forces a different seed for each model parameter (d parameters) considered for variability. More in detail, in (4), three different bolded terms appear: *time* · z , $\kappa \cdot n$ and Δ as arguments of the *rand* functions. *time* · z corresponds to the generation of z random numbers per unit of time. Both the sampling rate z of the MCG generator and the parameter Δ must be chosen accordingly. Δ ensures a different seed for both multiplicative terms considered in BM. In general, this number needs to be large (10^5 in the simulations shown in this work). Finally, $\kappa \cdot n$ specifies the seed for each model parameter (10^3 in our simulations). The obtained results are reported in Fig. C. Figure Ca shows the quantile-quantile (Q-Q) plot and Fig. Cb the Fast Fourier Transform (FFT) of the generated data with the MCG function at a sampling rate of 10^7 . These results are assessed using the Lilliefors test [3], which is a specialized variant of the Kolmogorov-Smirnoff statistical test for normality. As can be seen in Fig. Cb, the signal spectrum remains almost flat until the frequency reaches the chosen sampling rate. Despite of the simulator limitation, *i.e.*, the generation of undesired intermediate points, the analysis carried out reveals that the dataset generated by the *rand*-based MCG generator approximately follows the requirements of an OU process. However, this must be imperatively assessed for each specific situation.

Another practical issue that requires attention is the timestep effect in the LTspice simulated signals in connection with the sampling rate (z) in the RNG. It was found that the use of a very short maximum timestep (Max_{ts}) is crucial for obtaining changes in the signal at the expected time values. Figure D illustrates this point by comparing identical processes using $z = 10^4$ with two different Max_{ts} values: 10^{-3} and 10^{-6} , in pink and green, respectively. For the sake of clarity, the green signal includes a 0.4 offset in the y-axis. The main differences between both signals occur at the points where the RNG value is expected to change. For a low Max_{ts} (pink signal) the transitions show glitches. The problem is solved by using a shorter Max_{ts} as in the case of the green signal. As a rule of thumb, $z \cdot Max_{ts} < 10^{-2}$ should be used in LTspice.

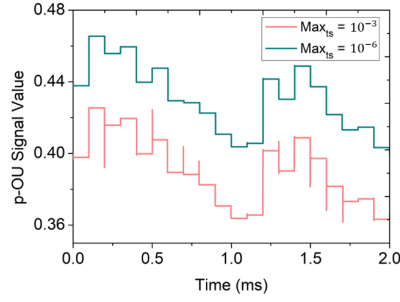


Figure D: p-OU signal value of the same signal with a $z = 1E4$ in two different simulation Max_{10} values: 10^{-3} in pink and 10^{-6} in green. The conditions for the obtention of both p-OU signals are $\mu = 0.4$, $\sigma = 0.013$, $\theta = 0.15$, $z = 1E4$.

REFERENCES

- [1] E. Salvador, M.B. Gonzalez, F. Campabadal, J. Martin-Martinez, R. Rodriguez, E. Miranda, "Assessment of the variability of the I-V characteristic of HfO₂-based resistive switching devices and its simulation using the quasi-static memdiode model", *Solid State Electronics*, vol. 206, 108667, 2023.
- [2] J. E. Gentle, "Random Number Generation and Monte Carlo Methods", *Statistics and Computing*, 1998.
- [3] H. W. Lilliefors, "On the Kolmogorov-Smirnov Test for Normality with Mean and Variance Unknown", *Journal of the American Statistical Association*, vol. 62, no. 318, 1967.

Conference MIEL21

One-way Sensitivity Analysis of the Quasi-static Memdiode Model for RRAM Devices

E. Salvador, M. B. Gonzalez, F. Campabadal, J. Martín-Martínez, R. Rodríguez and E. Miranda

One-way Sensitivity Analysis of the Quasi-static Memdiode Model for RRAM Devices

E. Salvador, M.B. Gonzalez, F. Campabadal, J. Martín-Martínez,
R. Rodríguez, E. Miranda

Abstract - In this work, we assess the impact that changes in the parameters of the quasi-static memdiode model (QMM) for RRAM devices will have on the simulated conduction characteristics. Sensitivity analysis is recognized as the most important technique for identifying which parameters are key drivers of the model's results. The model's reference parameters are extracted first from a typical (median) experimental I-V curve of an electroformed HfO₂-based metal-insulator-metal (MIM) structure. Then one parameter is changed at a time (so-called univariate or one-way analysis) in the LTSpice script and the variation of some selected observables recorded. Special attention is paid to the voltage span-induced sensitivity effect.

I. INTRODUCTION

Memristors or resistive RAMs (RRAMs) are two terminal devices with a non-volatile switching resistance property. The devices can switch from a high-resistance state (HRS) to a low-resistance state (LRS) in a process called the set event. The opposite process (transition from LRS to HRS) is called the reset event [1]. This kind of devices are currently considered as good candidates for a plethora of applications including memory arrays, neuromorphic computing, logic gates, cryptography, etc. [2-3]. For this reason, the development of appropriate compact simulation tools is urgently needed. As there is still no definite model for these devices and the number of approaches relentlessly grow year after year, the different proposals must be thoroughly evaluated before considering them reliable. In this work, we have focused the attention on a particular feature of the quasi-static memdiode model (QMM). This is also valid for any other model. This feature is the sensitivity of the model, that is, how uncertainty in the simulation output can be apportioned to different sources of uncertainty in the model input [4]. In our case, we must consider as inputs not only the model parameters but also the applied voltage span. This is a relevant issue because of

the hysteretic nature of the memristor conduction curve: the current that flows through the device depends on the applied voltage as well as on its previous history. This work is also motivated by the need to ensure consistency with a previous work concerning cycle-to-cycle (C2C) variability in RRAM devices simulation [5]. In [5], a method for including uncorrelated C2C variability by extracting some parameter distributions from the experimental data and their incorporation into the QMM's parameters for Monte Carlo simulations was proposed. The obtained results showed that simulations can reasonably reproduce the main features exhibited by the experimental curves. In this work, a one-way sensitivity analysis, which consists in the change of one parameter at a time and the evaluation of its impact on the model output, is carried out [6]. The method was applied to the QMM for four significant observables related to the I-V characteristic. They are: *i*) the high (I_{HRS}) and *ii*) low (I_{LRS}) resistance state currents extracted at $V=0.3V$, *iii*) the set voltage (V_S) corresponding to the current jump in the positive bias region, and *iv*) the reset voltage (V_R) corresponding to the maximum current reached at negative bias. These four observables, the two extreme conducting states and the set and reset transitions, are selected so as to cover the different regions of a typical RRAM I-V curve.

II. THE QUASI-STATIC MEMDIODE MODEL

As mentioned in the Introduction, the one-way sensitivity analysis was applied to the QMM model [7]. This model describes the conduction characteristics of bipolar resistive switching devices. The switching is originated by the formation of a conducting filament (CF) inside the dielectric caused by the application of an external field. This filament is related to the accumulation of metal ions or oxygen vacancies (depending on the device type). The CF can be ruptured by the application of a field with the opposite sign.

The QMM comprises two equations, one for the electron transport, consisting in a double-diode circuit with series resistance (1), and a second equation for the internal memory state of the device based on the logistic hysteron (2). According to this model, the I-V characteristic of a RRAM device reads:

$$I(V) = I_0(\lambda) \sinh\{\alpha(\lambda)[V - (R_S(\lambda) + R_I)I]\} \quad (1)$$

E. Salvador¹, M.B. Gonzalez², F. Campabadal², J. Martín-Martínez¹, R. Rodríguez¹, E. Miranda¹

¹Dept. d'Enginyeria Electrònica, Universitat Autònoma de Barcelona, 08193 Cerdanyola del Valles, Spain.

²Institut de Microelectrònica de Barcelona, IMB-CNM, CSIC, 08193 Cerdanyola del Valles, Spain

E-mail address of corresponding author:

emili.salvador@uab.cat

where $I_0(\lambda) = I_{min} + (I_{max} - I_{min})\lambda$ is the diode current amplitude, R_s and R_t series resistances, α a fitting parameter and I_{min} and I_{max} , minimum and maximum current amplitude values, respectively. Both R_s and α can change in a similar fashion. From (1), as I_0 increases the I - V curve modifies its dependence from an exponential function to a linear one. This is a consequence of the series resistance effect. The memory state λ , which is a control parameter that runs from 0 (HRS) to 1 (LRS), is related to the voltage across the filament's constriction $V_C = V - R_t I$ through the recursive operator:

$$\lambda(V_C) = \min\{\Gamma^-(V_C), \max[\lambda(\bar{V}_C), \Gamma^+(V_C)]\} \quad (2)$$

where $\lambda(\bar{V}_C)$ is the memory value a timestep before and Γ^+ and Γ^- are the so-called ridge functions. These functions are expressed as:

$$\Gamma^\pm(V_C) = \frac{1}{1 + \exp[-\eta^\pm \cdot (V_C - V^\pm)]} \quad (3)$$

which represent the sequential creation (+) and dissolution (-) of the conductive filament. η^\pm are the set (+) and reset (-) transition rates and V^\pm are the threshold voltages for set (+) and reset (-). The model uses other parameters for the fine-tuning of the simulated curves (see the script in Table 1) and it is implemented in LTSpice using an equivalent circuit with behavioral current sources. **H** is the output node corresponding to the memory state. The model includes the snapback (*isb*) and snapforward (*gam*) effects.

subckt memdiode + - H

.params

```
+ H0=8E-3 ri=190 vt=0.45 isb=43E-6
+ etas=200 vs=2 etar=10 vr=-0.63 CH0=1E-3
+ imax=4.8E-3 amax=2 rsmx=15 gam=0.12
+ imin=1E-5 amin=2 rsmn=15 RPP=1E10
```

*Memory equation

```
BH 0 H I=min(R(V(C,-)),max(S(V(C,-)),V(H))) Rpar=1
CH H 0 {CH0} ic={H0}
```

*I-V

```
RE + C {ri}
RS C B R=RS(V(H))
BD B - I=I0(V(H))*sinh(A(V(H))*V(B,-))
RB + - {RPP}
```

*Auxiliary functions

```
.func IO(x)=imin+(imax-imin)*x
.func A(x)=amin+(amax-amin)*x
.func RS(x)=rsmn+(rsmx-rsmn)*x
.func S(x)=1/(1+exp(-etas*(x- if(I(BD)>isb,vt,vs))))
.func R(x)=1/(1+exp(-etar*pow(V(H),gam)*(x-vr)))
```

.ends

Table 1 : LTSpice QMM script. The listed parameters are set to fit the median curve of the experimental data. Model parameters are not directly linked to the corresponding observable.

III. EXPERIMENTAL RESULTS AND ANALYSIS

The devices investigated in this work are HfO₂-based MIM structures with oxide thickness of 10nm and area of 5x5μm². The electrodes are Ti and W. The device structure can be seen in Fig. 1.a. Further details about the devices, fabrication, and measurements can be found in [8]. The model parameters are chosen so as to reproduce the median curve of the experimental data obtained from 450 consecutive voltage sweeping cycles. Fig. 1.b shows the comparison between the simulated curve and the median curve obtained from the experimental data. The four observables that will be analyzed are indicated in the figure. Notice that the current magnitude in HRS and LRS is independent of the bias sign. The complete set of measurements is presented in Fig. 1.c in log-lin scale.

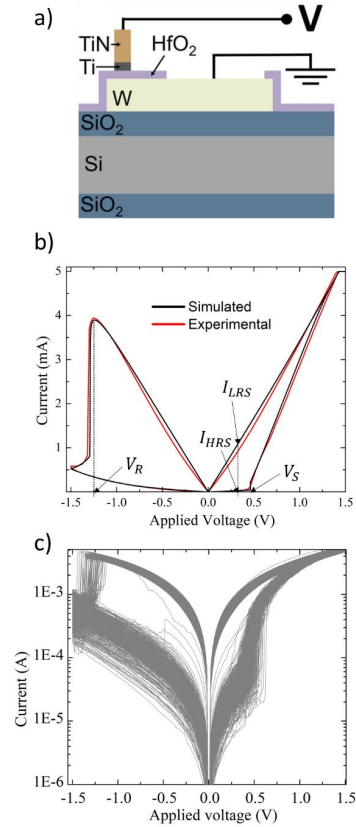


Figure 1: a) Device structure, b) simulation results compared to the experimental median I - V curve extracted from c) experimental 450 voltage sweeps with current in logscale.

The one-way analysis was carried out considering a bias voltage high enough to achieve the full set and reset states. Hence, Fig. 2 illustrates the effect of the maximum applied voltage (V_{app}) on the simulations. The figure also indicates the trends for the four different observables as the applied voltage is increased. Notice that for a maximum applied voltage of 1.5V (red curve), the simulation does not achieve a full reset state so this voltage affects the sensitivity studies performed on the rest of observables. This is an important point to consider.

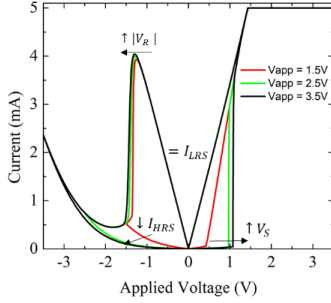


Figure 2: Simulated I - V curves for different applied voltages. The change in the observables is indicated.

In what follows, we will only consider only full set and reset states. This can be achieved with a maximum applied voltage of $\pm 2.5V$ (see Fig. 2). The parameters were swept one at a time (50 steps each) in a reasonable range and the obtained I - V curves analyzed. Fig. 3 shows the relative variation of the observables as a function of the relative variation of selected model parameters: a) η_r (reset transition rate), b) α (I - V slope parameter), c) I_{max} , and d) I_{min} (maximum and minimum currents). Table 2 summarizes the magnitude and trend associated with the variation of the four observables in terms of all the modified model parameters (a change of $\pm 30\%$ from its reference value was considered for the analysis). The reference parameters are those obtained from the fitting of the median curve (see Fig. 1.b).

Notice that there are colors and signs in Table 2. Red means almost no dependence between the observable and the model parameter; orange indicates that for a 10% model parameter variation, less than 10% variation is detected in the observable. Finally, green corresponds to a variation larger than 10%. (+) or (-) indicate direct or inverse dependence, respectively. Reading the first column of Table 2, we can see the impact of all the inputs over the observable I_{HRS} , it has a strong and positive dependence on α , I_{min} and γ . It also exhibits strong and inverse dependence on V_{app} and η_r . Weak and positive effect

from V_r and I_{max} and scarcely affected by R_i , η_{as} , R_s and I_{sb} .

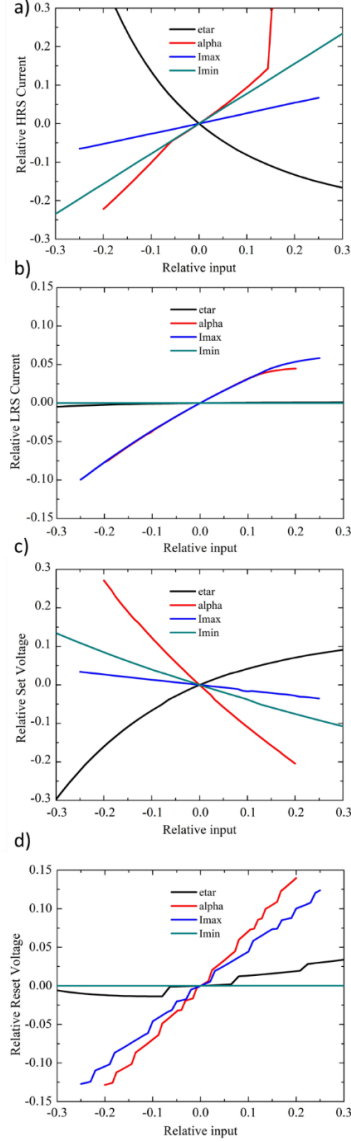


Figure 3: One-way sensitivity plots for the relative change of the observables a) I_{HRS} , b) I_{LRS} , c) V_S and d) V_R against the relative change of the model parameters: ϵ_{tar} , α , I_{max} and I_{min} .

Notice that this kind of analysis is a necessary step for the incorporation of C2C variability in the model script. Modelers can test a wide range of scenarios and need to know how this variability in the model inputs can modify their simulations.

| | I_{HRS} | I_{LRS} | V_S | V_R |
|------------------|-----------|-----------|-------|-------|
| Vapp | - | - | + | 0 |
| Ri | 0 | - | 0 | + |
| ϵ_{tar} | 0 | 0 | 0 | 0 |
| ϵ_{tar} | - | 0 | + | + |
| α | + | + | - | + |
| V_r | + | 0 | - | + |
| R_s | 0 | - | 0 | - |
| I_{sb} | 0 | 0 | + | 0 |
| I_{max} | + | + | - | + |
| I_{min} | + | 0 | - | 0 |
| gam | + | 0 | - | 0 |

Table 2: Intensity and sign (direct or opposite) of four observables against all the analyzed parameters. + and - signs for direct and inverse dependence, respectively. Green: >10%, orange: <10% and red 0%.

IV. CONCLUSION

A one-way sensitivity analysis was performed on the quasi-static memdiode model. The impact that variations in the model inputs will have in the model outputs was investigated. The work was motivated by the need to extend the analysis carried out in a previous work [5] where a first attempt to include C2C variability in RRAM simulations, particularly in the QMM for LTSpice, was reported. Here, the role played by the different model parameters was assessed. The results were graphically represented in a table summarizing the intensity and relation between the model inputs and outputs (direct or inverse).

ACKNOWLEDGEMENT

This work was supported by the Spanish Ministry of Science, Innovation and Universities through projects TEC2017-84321-C4-1-R, TEC2017-84321-C4-4-R, and PID2019-103869RB/AEI/10.13039/501100011033.

REFERENCES

[1] S. Yu and P. Y. Chen, "Emerging Memory Technologies: Recent Trends and Prospects," *IEEE Solid-State Circuits Mag.*, vol. 8, no. 2, pp. 43–56,

[2] J. S. Lee, S. Lee and T. W. Noh, "Resistive switching phenomena: A review of statistical physics approaches", *Applied Physics Reviews*, vol. 2, 031303, 2015.

[3] S. H. Jo, T. Chang, I. Ebong, B. B. Bhadviya, P. Mazumder, and W. Lu, "Nanoscale memristor device as synapse in neuromorphic systems", *Nano Lett.*, vol. 10, no. 4, pp. 1297–1301, 2010

[4] A. Saltelli, S. Tarantola, F. Campolongo, and M. Ratto, "Sensitivity analysis in practice: a guide to assessing scientific models", *John Wiley & Sons, Ltd*, 2004.

[5] E. Salvador, M. B. Gonzalez, F. Campabadal, J. Martin-Martinez, R. Rodriguez, and E. Miranda, "SPICE modeling of cycle-to-cycle variability in RRAM devices", *Solid State Electronics*, vol. 185, 108040, 2021.

[6] A. Saltelli et al., "Global Sensitivity Analysis. The Primer", *John Wiley & Sons, Ltd*, 2008.

[7] E. Miranda, I. S. Member, J. Suñé, and I. Fellow, "Fundamentals and SPICE Implementation of the Dynamic Memdiode Model for Bipolar Resistive Switching Devices", *IEEE TNano.*, vol. 14, pp. 787-789, 2020.

[8] S. Poblador, M. B. Gonzalez, and F. Campabadal, "Investigation of the multilevel capability of TiN/Ti/HfO2/W resistive switching devices by sweep and pulse programming", *Microelectron. Eng.*, vol. 187–188, pp. 148–153, 2018

Review Section AIS23

Variability in Resistive Memories

J. B. Roldán, E. Miranda, D. Maldonado, A. N. Mikhaylov,
N. V. Agudov, A. A. Dubkov, M. N. Koryazhkina, M. B.
González, M. A. Villena, S. Poblador, M. Saludes-Tapia, R.
Picos, F. Jiménez-Molinos, S. G. Stavrinides, **E. Salvador**, F.
J. Alonso, F. Campabadal, B. Spagnolo, M. Lanza, and L. O.
Chua

Variability in resistive memories

J.B. Roldán, E. Miranda, D. Maldonado, A.N. Mikhaylov, N.V. Agudov, A.A. Dubkov, M. N. Koryazhkina, M.B. González, M.A. Villena, S. Poblador, M. Saludes-Tapia, R. Picos, F. Jiménez-Molinos, S. G. Stavrinides, **E. Salvador**, F.J. Alonso, F. Campabadal, B. Spagnolo, M. Lanza, L.O. Chua

***This document is only a section of the above presented review paper.**

5.2.- Application of the Dynamic Memdiode Model for C2C variability

As highlighted in the introduction and previous sections, variability in resistive memories in general and in bipolar-type filamentary RS devices in particular are hot research topics. Variability was shown to be the result of morphological changes in the CF at the atomic scale [Yu2016, Lee2015]. Since this kind of variability is inherent to RRAMs operation, any compact model intended to reproduce as realistically as possible their behavior in the circuit simulation landscape must contemplate this phenomenon. In particular, this section focuses on the inclusion of non-correlated C2C variability in the Dynamic Memdiode Model (DMM) for RRAM devices [Miranda2020, Aguirre2022]. The DMM describes the conduction characteristics of RS devices under the application of arbitrary input signals. The origin of the switching behavior is related to the creation and destruction of the CF that spans across the dielectric layer. This in turn is linked to the metal ions or oxygen vacancies displacement depending on the device type (CBRAM or OxRAM). In bipolar devices, the transition between HRS and LRS (CF formation) and vice versa (CF rupture) takes place at opposite voltages [Dai2015, Blasco2015]. This is the case we are going to analyze next.

The DMM reproduces the hysteretic behavior of the memristive device by means of two nonlinear coupled equations: one for the electron transport (Equation 5.2.1) and one for the memory state (Equation 5.2.2). According to the DMM, the I - V characteristic reads (see expression (3.2.5)):

$$I(V) = I_0(\lambda) \sinh\{\alpha(\lambda)[V - (R_c(\lambda) + R_i)I]\} \quad (5.2.1)$$

where V is the applied voltage, I_0 is the current amplitude factor, R_c is a variable series resistance, and α is a variable model parameter. R_i refers to a fixed resistance related to the snapback voltage correction ($V_{sb} = V - R_i \cdot I$) [Wouters2019]. The R_i value corresponds to a vertical current increase at the transition voltage V_T . Notice that Equation 5.2.1 includes three different parameters with λ -dependence. For simplicity, these parameters are assumed to change linearly and in the same way from a minimum (off) to a maximum (on) value as a function of λ . For example, $I_0(\lambda) = I_{off} + (I_{on} - I_{off}) \cdot \lambda$, where I_{off} and I_{on} represent the minimum (HRS) and maximum (LRS) current amplitude values, respectively. λ runs from 0 to 1 and is called the memory state of the device (a state variable in the general memristor model). Its purpose is to control the transitions $HRS \leftrightarrow LRS$. According to Equation 5.2.1, HRS depends exponentially on V , while LRS depends linearly on V (because of the potential drop across the series resistances R_i and R_c). λ is described by a balance-type voltage-driven differential equation [Miranda2020]:

$$\frac{d\lambda}{dt} = \frac{1-\lambda}{\tau_S(\lambda, V_{sb})} - \frac{\lambda}{\tau_R(\lambda, V_{sb})} \quad (5.2.2)$$

where $\tau_{S,R}$ [s], called TS and TR respectively in the model script in Table 5.2.1, are the characteristic times for the set and reset transitions. They are expressed as:

$$\tau_S(V) = \exp[-\eta_S(V_{sb} - V_{S,T})] \quad (5.2.3)$$

$$\tau_R(V) = \exp[\eta_R \lambda^\gamma (V_{sb} - V_R)] \quad (5.2.4)$$

where $\eta_{S,R}$ [V^{-1}], also called $etas$ and $etar$ respectively in the model script shown in Table 5.2.1, are the transition rates; $V_{S,R}$ [V] are the set and reset switching voltages, respectively. The snapback current (isb in the model script) acts as a threshold current for the snapback effect and the snapforward parameter $\gamma \geq 0$ (called gam in the model script) controls the reset transition rate. $H0$ is the initial memory state. RPP in Table 5.2.1 is a parallel resistance required by the output current generator. Further details about the Dynamic Memdiode Model can be found in [Miranda2020, Aguirre2022].

The model script is presented in Table 5.2.1. The script contains the model parameters as well as the transport and memory equations. + and - are the conventional device terminals, while H is the output terminal for the memory state (not used in this work). For illustrative purposes, Figure 5.2.1 shows a simulated curve with the DMM for a sinusoidal applied signal with amplitude 1.5 V and frequency 1 Hz. While Figure 5.2.1a shows the I - V characteristic in logarithmic scale, Figure 5.2.1b shows the same I - V curve (in black) in linear axis and the resulting curve after the snapback correction (in red). Notice the vertical current increase in the red curve occurring at V_T .

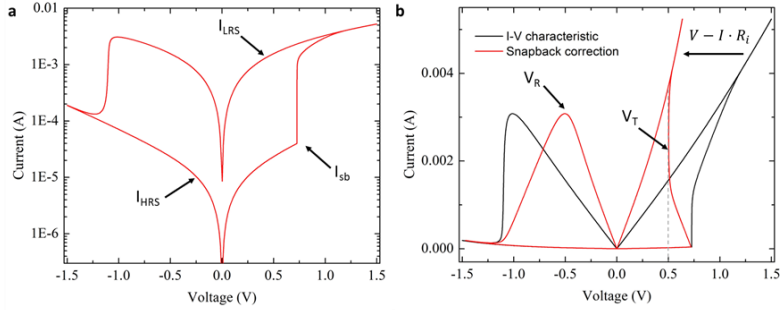


Figure 5.2.1. Simulated I - V curve obtained with the script and parameter configuration in Table 5.2.1, without including variability. **a** in logscale and **b** in linear scale (black) presenting the snapback correction (red).

```
.subckt memdiode + - H
.params
+ H0=0 ri=150 RPP=1E10 vs=2.0 vt=0.45 gam=0.2; if gam=0 no SF
+ etas=40 etar=20 aoff=2 roff=10 aon=2 ron=10
+ vr=vr0+gauss(sigvr) vr0=-0.4 sigvr=0.02
+ isb=isb0+gauss(sigisb) isb0=40E-6 sigisb=5E-6; if isb=1 no SB
+ ion=ion0*exp(gauss(sigion)) ion0=3E-3 sigion=0.1
+ ioff=ioff0*exp(gauss(sigioff)) ioff0=20E-6 sigioff=0.25
```

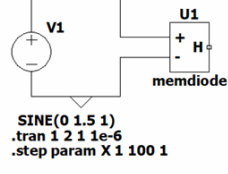
| | |
|--|--|
| <pre> *Memory Equation BI 0 H I=if(V(+,-)>=0,(1-V(H))/TS(V(C,-)), -V(H)/TR(V(C,-))) CH H 0 1 ic={H0} *I-V RI + C {ri} RS C B R=K(ron,roff) BF B - I=K(ion,ioff)*sinh(K(aon,aoff)*V(B,-)) Rpar={RPP} *Auxiliary functions .func K(on,off)=off+(on-off)*limit(0,1,V(H)) .func TS(x)=exp(-etas*(x-if(I(BF)>isb,vt,vs))) .func TR(x)=exp(etar*pow(V(H),gam)*(x-vr)) .ends </pre> |  |
|--|--|

Table 5.2.1 – LTSpice DMM script including the transport and memory equations. Variability is included in several key parameters. The Gaussian function is added in red for normal distributions and in blue for lognormal distributions. The LTSpice schematic is included for simulating 100 cycles under the voltage and timing considerations.

Before introducing variability in the script, it is essential to understand the model behavior and the role each parameter plays within it. In [Salvador2021b], a one-way sensitivity analysis was performed in a simpler version of the memdiode model. In the referred paper, the impact of the model parameters in the simulated I - V characteristics was evaluated for four observables (HRS and LRS current magnitudes, SET and RESET voltage transitions) and the results reported in a summary table. Similarly, in this subsection, the effect of considering variability in the key model parameters is studied one at a time using the σ (*sig*) values incorporated into the model script. The inclusion of C2C variability in the DMM is performed by adding a Gaussian random number generator to the model parameters (*gauss* function in LTSpice). This function returns a zero centered normal distribution function with a standard deviation σ . This is indicated in Table 5.2.1: red for a normal distribution and blue for a lognormal distribution. This selection is consistent with the experimental study carried out in [Salvador2021b]. Figure 5.2.2 shows the results obtained from this analysis varying a) *ioff*, b) *ion*, c) *isb*, and d) *vr* one at a time. The reported results correspond to 100 cycles.

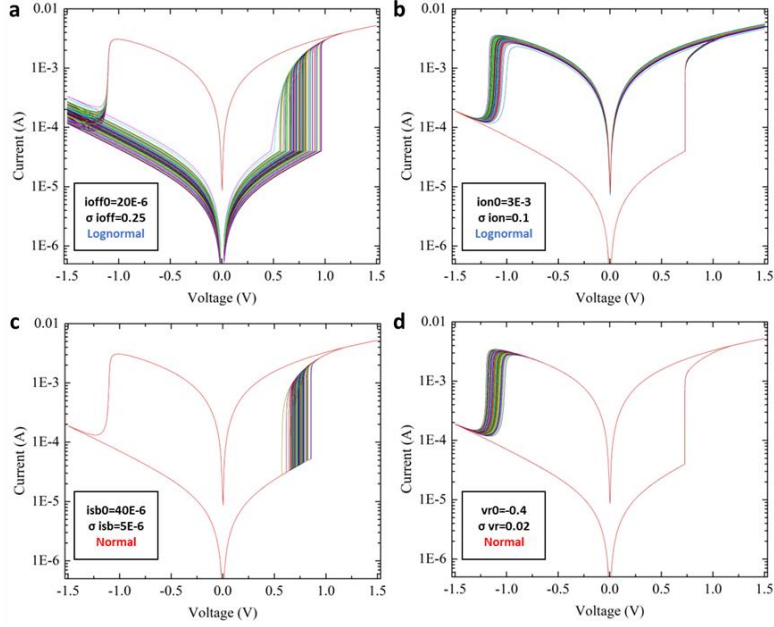


Figure 5.2.2. Impact in the I-V characteristics of including variability in model parameters one at a time: **a** *ioff*, **b** *ion*, **c** *isb*, and **d** *vr*.

Notice that *isb* and *vr* changes only affect the transition regions as expected. Nevertheless, *ioff* not only impacts the HRS current but also the set transition. Similarly, *ion* not only impacts the LRS current but also the reset transition. As it can be seen in Figure 5.2.1 as well as in our previous study [Salvador2021b], a single random parameter can impact more than one region of the simulated curves. This is a consequence of the hysteresis effect and is referred to as variability propagation in the simulation process. The results reported in Fig. 5.2.3 indicate that an excess of model parameters with variability (concurrent variability) can introduce over-randomness in the simulated curves which in the context of circuit simulation can be hard to keep under control. This is further discussed next.

Once the impact of including variability in a single model parameter at a time has been analyzed, the second step consists in investigating how a combination of random model parameters affects the DMM output results. Here, for the sake of simplicity, variability was included in some of the key model parameters without considering cross-correlation effects among them. In [Salvador2021b], the main features of C2C variability in a HfO₂-based RRAM device were reproduced using an iterative approach for the selection of the model parameters but the process was applied to a simpler version of the memdiode model. Notice that by including variability in 4 parameters (*ioff*, *ion*, *isb* and *vr*) simulations exhibiting C2C variability in all the curve regions can be achieved. As illustrated in the inset of Table 5.2.1, the procedure consists in generating a 100-cycle set of 1 second simulations, each one obtained after the application of the same input signal (sinusoidal voltage with frequency 1 Hz and amplitude 1.5 V). Importantly, each loop in the simulation is

computed independently from the others ruling out correlated C2C. The results are obtained using the model script and the parameter values reported in Table 5.2.1. Figure 5.2.3 shows the simulated I-V curves, a) in logscale and b) in linear scale. The magnitude of the fluctuations can be changed using the σ value associated with each model parameter. Variability in the rest of parameters: r_i , $etas$, $etar$, etc. is also possible but caution should be exercised since this can introduce over-randomness as discussed above.

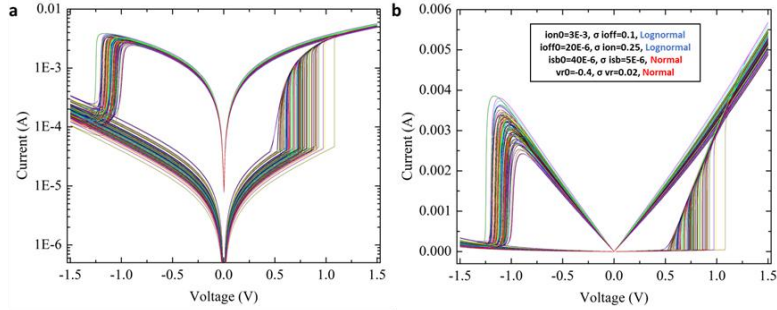


Figure 5.2.3. I-V curves from 100 cycles simulations including variability in the 4 specified parameters as presented in Table 5.2.1. **a** in logscale and **b** in linear scale.

After presenting the model response to concurrent variability, additional concerns about the variability propagation problem can arise. For instance, variability propagation can introduce an unexpected behavior in the HRS current: since for the example discussed here simulations start in the first quadrant and finish in the third quadrant, the initial and final spread of the resulting I-V curves (HRS) can be different if the experiment is not properly designed. However, this is a possible outcome that can occur under specific experimental circumstances. First, we have to take into account the impact of the applied voltage span, i.e., if this span is not large enough to produce a complete set or reset of the device, then variability in the simulated HRS curves will be different for positive and negative voltages. This aspect of the problem was studied in [Salvador2021b] and it was referred to as voltage-induced variability.

Second, the simulation cycle number can also have influence on the symmetry of the I-V loop if cycles are not independent. A difference between the first and the subsequent cycles can be interpreted as a propagation variability issue. In this case, the first HRS cycle is strongly connected with the initial memory state parameter H_0 which is sometimes unknown or simply put to zero. However, in the second cycle, if the cycles are not independent, the initial HRS current value is forced by the magnitude of the previous reset event. In Figure 5.2.4, a density plot comparing the initial and final HRS current values (extracted at ± 0.2 V, respectively) are compared for the first and second cycles and the maximum applied voltage: a) 1st cycle and $V_{max}=0.9$ V, b) 1st cycle and $V_{max}=1.5$ V, c) 2nd cycle and $V_{max}=0.9$ V, and d) 2nd cycle and $V_{max}=1.5$ V. Figures 5.2.4b and 5.2.4d show that the initial and final HRS current distributions coincide because the voltage span is high enough to induce the complete reset of the device.

However, Figs. 5.2.4a and 5.2.4c show a different behavior. In a), the densities are shifted, meaning that the initial and final HRS currents do not match as

experimentally expected. This difference is voltage-induced since 0.9 V is not high enough for the device to reach the full reset condition and therefore the final HRS current is ruled by this incomplete reset process. c) corresponds to the second cycle but since the initial HRS current is ultimately determined by the previous incomplete reset process, both the initial and final HRS current distributions (measured at opposite voltages) match. If the reset process is not complete, the I-V loop stabilizes only after one or more cycles.

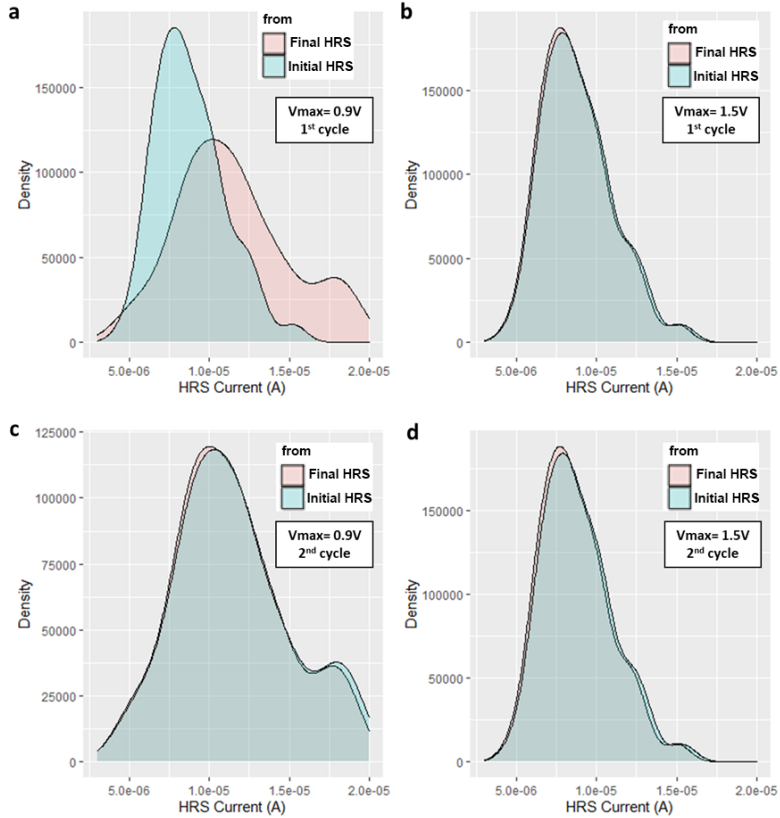


Figure 5.2.4. Comparison between the initial and final HRS current densities for different voltage and cycle situations: **a** 1st cycle and $V_{max}=0.9$ V, **b** 1st cycle and $V_{max}=1.5$ V, **c** 2nd cycle and $V_{max}=0.9$ V and **d** 2nd cycle and $V_{max}=1.5$ V.

In summary, this subsection reported a simple approach for including uncorrelated C2C variability in the DMM for RRAM devices. The model is able to generate random I-V curves with the desired variability. A more realistic scheme not only should include self-correlation effects in the model parameters but also cross-correlation effects. This imperatively requires a detailed time series analysis such as that reported in [Roldan2019]. In addition, the effects of variability propagation and the role played by the voltage sweep span were also discussed.

Conference ISCAS22

Beneficial Role of Noise in Hf-based Memristors

R. Rodriguez, J. Martin-Martinez, E. Salvador,
A. Crespo-Yepes, E. Miranda, M. Nafria, A. Rubio, V.
Ntinis, G. Ch. Sirakoulis

Beneficial Role of Noise in Hf-based Memristors

Rosana Rodriguez, Javier Martin-Martinez, Emili Salvador, Albert Crespo-Yepes, Enrique Miranda, Montserrat Nafria
Electronic Engineering Dept., REDEC Group
Universitat Autònoma de Barcelona (UAB)
Bellaterra, Barcelona, Spain
rosana.rodriguez@uab.es

Antonio Rubio, Vasileios Ntinis
Electronic Engineering Department
Universitat Politècnica de Catalunya (UPC)
Barcelona, Spain
antonio.rubio@upc.edu
vasileios.ntinis@upc.edu

Georgios Ch. Sirakoulis
Dept. of Electrical & Computer Engineering
Democritus University of Thrace (DUTH)
Xanthi, Greece
gsirak@ee.duth.gr

Abstract— The beneficial role of noise in the performance of Hf-based memristors has been experimentally studied. The addition of an external gaussian noise to the bias circuitry positively impacts the memristors characteristics by increasing the OFF/ON resistances ratio. The known stochastic resonance effect has been observed, when changing the standard deviation of the noise. The influence of the additive noise on the memristor current-voltage characteristic and on the set and reset related parameters are also presented.

Keywords— Stochastic resonance, memristors, RRAM devices, resistive switching

I. INTRODUCTION

Emerging devices as memristors are nowadays of great interest in the scientific community due to their properties, as low power consumption and large integration density [1]. The reversible change in memristor conductivity when subjected to a proper biasing opens the possibility of their use in a wide range of applications, such as non-volatile memory, alternative computing architectures, neuromorphic systems, security schemes, etc [2-6]. Memristors show a non-linear current-voltage characteristic, so the properties associated to nonlinear systems can be explored in these devices. In this sense, although noise in electronics should usually be avoided, in non-linear systems it can have a beneficial role, improving the performance of devices. This phenomenon is known as Stochastic Resonance (SR) and it is present in nature in several fields as biology, engineering, etc [7-10]. SR takes place in non-linear devices with thresholds in their characteristic curves, as it is the case of memristors.

Several previous works have analyzed the constructive role of noise in memristors. [11] analyzes theoretically the beneficial role of an additive noise in memristors through a memristor model. An alternative SR model in memristors can be found in [12], with a good agreement with experimental measurements in manganite samples. In [13] SR is experimentally studied in memristors subjected to sinusoidal signals with noise added. The SR was also shown to reduce the Bit Error Rate (BER) in Resistive Random Access Memory (RRAM) devices [14]. In [15], the addition of noise in metal-oxide memristors fabricated with zirconium dioxide and tantalum pentoxide is analyzed both experimentally and theoretically, observing the constructive role of noise in these samples.

In this work, we demonstrate experimentally the beneficial role of noise in CMOS compatible hafnium oxide-based memristors. Differently to other works where the noise signal is needed to observe the regular memristor hysteretic current-voltage characteristic (I-V, Figure 1), in this work we start

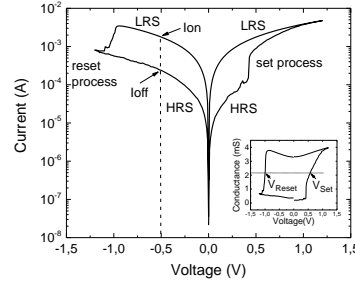


Figure1: Typical current-voltage characteristic of the memristors used in this work. Inset: The set/reset voltages were defined as the positive (V_{set}) /negative (V_{reset}) voltages for which the mean value between the maximum and minimum conductance values in the I-V curve characteristic were measured. Set and reset currents correspond to the currents associated to V_{set} and V_{reset} respectively.

from samples where the initial I-V curves (without noise) show a clear differentiation between the memristor low resistance state (LRS, ON state) and the high resistance state (HRS, OFF state), and study the impact of a noise added to the bias of the device on these I-V characteristic curves. In this case, noise is not used to initiate/achieve memristor state's switching, but to further improve/widen the existing resistance window. Statistical characterizations of the resistance ratio between the ON and OFF states (R_{OFF}/R_{ON}) and of the currents and voltages in the set and reset processes in the presence of noise are analyzed.

II. SAMPLES AND MEASUREMENT PROCEDURE

The tested samples consist in TiN-Ti-HfO₂-W Metal-Insulator-Metal (MIM) structures. A cross-sectional view is shown in Figure 2. The devices were fabricated on Si wafers with a thermally grown 200nm-thick SiO₂ layer. The 10nm-thick HfO₂ layer was deposited by atomic layer deposition (ALD) at 225°C using TDMAH and H₂O as precursors, and N₂ as carrier and purge gas. The bottom electrode consists of a 200nm-W layer and the top electrode of a 200nm-TiN on top of a 10nm-Ti layer acting as oxygen getter material. The resulting device structures are square cells with an area of 5x5μm². Further details of their fabrication process can be found in [16].

The measurements were performed using a Semiconductor Parameter Analyzer (SPA) Agilent 4156C. The equipment was controlled via GPIB bus, and the measurements programmed with Matlab software. Firstly, fresh (i.e. as-grown) memristors were subjected to a 1mA

current-limited forming process that takes place at voltages $\cong 4V$. After forming, the memristor I-V characteristics (Figure 1) were registered during 200 consecutive cycles. To measure the I-V curves, the samples were subjected successively to voltage ramps, sweeping the voltage from 0V to 1.2V, from 1.2V to -1.2V and from -1.2V to 0V and the current was registered during the application of voltage.

The memristors used in this work present a bipolar behavior. The set process (the change from HRS to LRS) is produced for positive voltages and the reset process (the change from LRS to HRS) takes place at negative voltages (Figure 1). The variation in the memristor conductivity is related to the formation/destruction of a conductive filament through the dielectric where oxygen-related species are responsible of this conductive variation [17].

Registration of each I-V curve takes several seconds, so that each voltage ramp can be considered as a series of DC measurements with increasing voltage. To analyze the noise impact, Gaussian noise, whose standard deviation (σ) ranged between 50 mV and 150 mV, was added to the ramp voltage by smart instrument control. Noise was generated by the SPA, programmed with a Matlab script to add point to point to the voltage ramp bias a gaussian signal of a determinate sigma. Fresh devices were used to analyze each noise condition. Noise impact on the difference between ON and OFF memristor resistance ratio (R_{OFF}/R_{ON}), I-V curves, set and reset voltages and currents (V_{reset} and I_{reset}) were studied.

Memristors were also subjected to pulsed voltages of 50 Hz and 1KHz frequency using the Keithley 4200A-SCS. For these measurements, Gaussian noise was added to the system by hardware, using the Keysight 81150A pulse function arbitrary noise generator.

III. RESULTS

A. Impact of noise on memristor R_{OFF}/R_{ON} resistance ratio

From the values of currents at a voltage of -0.5V in the I-V memristor characteristics (I_{OFF} and I_{ON} in Figure1) the resistance ratio R_{OFF}/R_{ON} was directly obtained through Ohm's law. The reading voltage of -0.5V was chosen because the probability to change the memristor state at this voltage

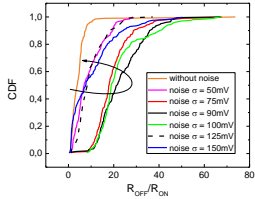


Figure 3: CDFs of the memristor R_{OFF}/R_{ON} ratio for different noise σ . The curves are ordered following the stochastic resonance behavior. Noise σ of 90 mV offers best R_{OFF}/R_{ON} ratio.

value is very low. R_{OFF}/R_{ON} was evaluated from the I-V's measured with and without additive noise. Figure 3 shows the cumulative distribution functions (CDFs) of the R_{OFF}/R_{ON} ratio measured for the 200 cycles at each noise condition. Note that the smallest R_{OFF}/R_{ON} ratio is measured when noise is not added and that the presence of noise always leads to larger values of this parameter. However, the improvement depends on the value of σ . Initially, as σ increases, the CDF curves are shifted to the right (i.e. to larger R_{OFF}/R_{ON} values), with a maximum shift for the case of $\sigma = 90$ mV. But, for larger noise σ values, the CDFs curves shift towards smaller values of R_{OFF}/R_{ON} . This result suggests that the phenomenon of the stochastic resonance is observed in memristors in the presence of noise. Figure 4 shows the mean value of the R_{OFF}/R_{ON} ratio as a function of the noise standard deviation. Each point in this graph is the mean value of the ratios measured in the 200 cycles applied for each noise condition. Clearly, an increment of the R_{OFF}/R_{ON} ratio is observed when noise is added, and the maximum improvement is observed for noise σ around 90 mV. The addition of noise has a clear beneficial role, and the typical stochastic resonance curve with a peak for intermediate noise levels is observed.

To further analyze the impact of noise in the memristor I-V characteristic, Figure 5 shows the memristor I-V curves without adding noise (left) and with a noise of 90 mV σ summed to the bias (right). Differences in the currents and voltages associated to set and reset processes are also observed in the presence of noise. These differences are analyzed in more detail in the next section. From the 200 cycles, cycles 12, 91 and 193 were selected as examples of initial, intermediate, and final cycles. The memristor I-V characteristic is clearly more open when noise is added, leading to the larger R_{OFF}/R_{ON} resistance ratios. In both cases, as the number of cycles increases, the difference between ON and OFF state currents decreases, and the hysteretic behavior of the I-V curves tends to decrease. This is a general trend for all the noise σ studied and can be attributed to a memristor degradation as the number of I-V cycles increases, that

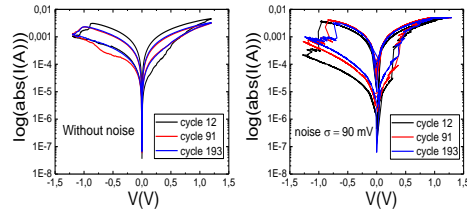


Figure 5: Memristor current-voltage characteristics at cycles 12, 91 and 193 without (left) and with 90 mV noise σ .

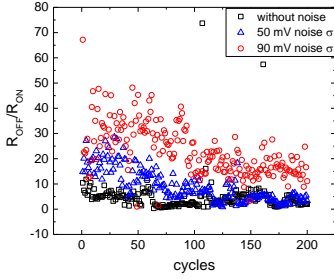


Figure 6: Memristor R_{OFF}/R_{ON} ratio as a function of the number of cycles for the without noise case and for additive noise σ s of 50 mV and 90 mV.

provokes a decrease of the memristor resistance ratio. As an example, Figure 6 shows the evolution of the R_{OFF}/R_{ON} ratio along the 200 I-V cycles, for the w.o.-noise case and when a noise of 50 mV or 90 mV σ is added. A clear difference in the evolution of the R_{OFF}/R_{ON} ratio with cycling is observed, depending on the presence or absence of noise. Again, a notable increment of the ratio for $\sigma=90$ mV is observed in the first cycles. However, as the number of cycles increases, the R_{OFF}/R_{ON} ratio tends to decrease, for the three cases represented, which is related to the reduction of the difference between the ON and OFF state currents observed in Figure 5, attributed to the memristor degradation.

The previous results have been obtained through the application of slow ramp voltages that can be considered a sequence of increasing voltage DC measurements. R_{OFF}/R_{ON} ratio was also investigated when memristors were subjected to bipolar pulsed voltages (with top and bottom voltages of 1.1V to -1.1V respectively) with frequencies of 50 Hz and 1KHz. For each frequency and noise σ , 200 pulse periods were applied. Memristor I-V curves are obtained from the rise and fall edges of the pulsed signal, and the R_{OFF}/R_{ON} ratio was calculated from the I_{ON} and I_{OFF} currents at -0.5V as in the DC case. Figure 7 shows the mean value of the R_{OFF}/R_{ON} and the standard deviation for each frequency/noise condition. As frequency increases, both the resistance ratio mean value $\langle R_{OFF}/R_{ON} \rangle$ and its standard deviation decrease, as expected [18]. A dependence of the R_{OFF}/R_{ON} ratio on the noise standard deviation is also observed, with larger R_{OFF}/R_{ON}

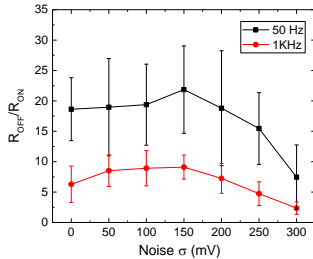


Figure 7: R_{OFF}/R_{ON} resistance ratio for memristors subjected to pulsed measurements. Error bars indicate the standard deviation.

values for noise σ ranged between 50 and 200 mV. However, the impact of noise in these pulsed conditions is lower than for the DC case.

B. Impact of noise on memristor set and reset parameters

The effect of noise on the voltages and currents associated to the set and reset processes (V_{set} , V_{reset} and I_{set} , I_{reset}) was also analyzed for the DC case.

Figures 8 and 9 show the V_{set} and V_{reset} voltages and their standard deviations, respectively, as a function of the noise σ . The results suggest that the addition of noise tends to decrease V_{set} . In the case of V_{reset} , the influence of noise is not so clear. Although, in general, larger values of V_{reset} (in absolute values) are measured in the presence of noise, for $\sigma=90$ mV, a change of tendency to lower reset values is observed. The effect of noise in the V_{reset} and V_{set} dispersion is more noticeable (Figure 9). For the noise σ where SR is more clearly observed (from 75mV to 100 mV), a lower dispersion of the V_{set} and V_{reset} values is obtained. Similar trends have been observed for the I_{set} and I_{reset} currents (Figure 10). For the noise cases where the SR is more visible, I_{set} and I_{reset} currents tend to increase (in absolute value), leading to a major difference between LRS and HRS conduction levels, that is, the R_{OFF}/R_{ON} ratio. Again, the impact of noise is more appreciable in the I_{set} and I_{reset} standard deviations, with lower current dispersions for noise σ between 75 mV and 100 mV (Figure 11).

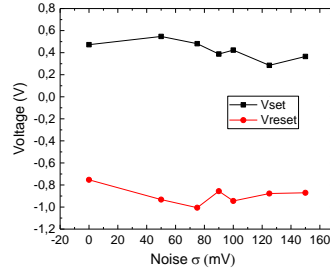


Figure 8: Mean values of V_{set} and V_{reset} as a function of noise σ .

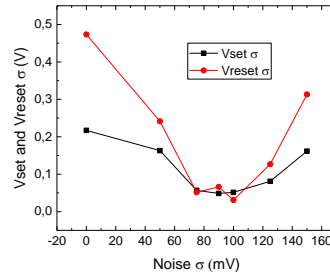


Figure 9: V_{set} and V_{reset} standard deviations as a function of noise σ .

IV. CONCLUSIONS

The potential beneficial role of external noise has been demonstrated in HF-based memristors. The addition to the bias of gaussian noise of a determined standard deviation increases the resistance difference between the memristor LRS and HRS by opening the resistance window between ON and OFF states. The typical stochastic resonance curve has been observed with a peak at a certain optimum noise level: the OFF/ON resistance ratio is the lowest for the case without noise, and in the presence of noise, it increases until the optimum noise standard deviation and decreases again for larger noise amplitudes. Clear differences in the memristor

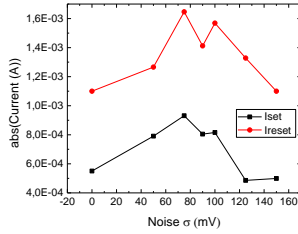


Figure 10: Mean values of Iset and Ireset currents as a function of noise σ

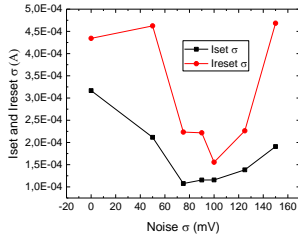


Figure 11: Iset and Ireset standard deviations as a function of noise σ .

current-voltage characteristics have been observed when noise is added, affecting the hysteretic memristor behavior. The impact of noise on the set and reset voltages and currents has also been studied, observing that the addition of the external noise provokes a lower dispersion of set and reset voltages and currents. Though more investigation about the constructive role of noise on memristors should be performed, this work paves the way for a promising scenario where characteristics and reliability of memristive circuits can be enhanced, taking advantage of the SR phenomenon.

ACKNOWLEDGMENT

This work was supported by project PID2019-103869RB / AEI / 10.13039/501100011033 and TEC2017-90969-EXP.

REFERENCES

- [1] I.H. Im, S.J. Kim, H.W. Jang, "Memristive Devices for New Computing Paradigms". Advanced Intelligent Systems, 2000105, 2020.
- [2] S.H. Lee, X. Zhu, W. D. Lu, "Nanoscale resistive switching devices for memory and computing applications", *Nano Research*, vol. 13, pp. 1228–1243, 2020.
- [3] D. Ielmini, S. H. P. Wong, "In-memory computing with resistive switching devices", *Nature Electronics*, vol. 1, pp. 333–343, 2018.
- [4] Giacomo Pedretti, Valerio Milo, Stefano Ambrogio, Roberto Carboni, Stefano Bianchi, Alessandro Calderoni, Nirmal Ramaswamy, Alessandro S. Spinelli, Daniele Ielmini, "Stochastic learning in neuromorphic hardware via spike timing dependent plasticity with RRAM synapses", *IEEE Journal on Emerging and Selected Topics in Circuits and Systems*, vol. 8, pp.77–85, 2018.
- [5] C. Li, M. Hu, Y. N. Li, H. Jiang, N. Ge, E. Montgomery, J. M. Zhang, W.H. Song, N. Dávila, C. E. Graves, et al. "Analogue signal and image processing with large memristor crossbars". *Nature Electronics*, vol. 7, pp. 52–59, 2018.
- [6] H. Aziza, J. Postel-Pellerin, H. Bazzi, P. Canet, M. Moreau, V. Della Marca, A. Harb, "True Random Number Generator Integration in a Resistive RAM Memory Array Using Input Current Limitation", *IEEE Transactions on Nanotechnology*, vol 19, pp. 214–222, 2020.
- [7] R. Benzi, A. Sutera and A. Vulpiani, "The mechanism of stochastic resonance", *Journal of Physics A: Mathematical and General*, vol. 14, (11), 1981.
- [8] Kurt Wiesenfeld, Frank Moss, "Stochastic resonance and the benefits of noise: from ice ages to crayfish and SQUIDS", *Nature*, vol. 373, pp.33–36, 1995.
- [9] G.P. Harmer, B. R Davis, D. Abbot, "A review of stochastic resonance: circuits and measurement", *IEEE Transactions on Instrumentation and Measurements*, vol. 31(2), pp299–309, 2002.
- [10] Seiya Kasai, "Stochastic resonance and related phenomena in nonlinear electron nanodevices", *IEEE International Nanoelectronics Conference (INEC)*, 2014.
- [11] A. Scotland, M. Di Ventura, "Stochastic memory: Memory enancement due to noise", *Physical Review E*, vol 85, 011116, 2012.
- [12] G. A. Patterson, P. I. Fierens, D. F. Grosz, "On the beneficial role of noise in resistive switching", *Appl. Phys. Lett.*, vol.103, 074102, 2013.
- [13] V. Ntinis, A. Rubio, G. Ch. Sirakoulis, R. Rodriguez, M. Nafria, "Experimental Investigation of Memristance Enhancement", *IEEE/ACM International Symposium on Nanoscale Architectures (NANOARCH)*, 2019.
- [14] V. Ntinis, A. Rubio, G. Ch. Sirakoulis, E. Salvador, M. Pedro, A. Crespo-Yepes, J. Martin-Martinez, R. Rodriguez, M. Nafria, "Power-Efficient Noise-Induced Reduction of ReRAM Cell's Temporal Variability Effects", *IEEE Transactions on Circuits and Systems II: Express Briefs*, vol. 68(4), 2021.
- [15] A.N. Mikhaylov, D.V. Guseinov, A.I. Belov, D.S. Korolev, V.A. Shishmakova, M.N. Koryazhkina, D.O. Filatov, O.N. Gorshkov, D. Maldonado, F.J. Alonso, J.B. Roldan, A.V. Krichigin, N. V. Agudov, A.A. Dubkov, A. Carollo, B. Spagnolo, "Stochastic resonance in a metal-oxide memristive device", *Chaos, Solitons & Fractals*, vol. 144, 110723, 2021.
- [16] S. Poblador, M. Gonzalez, and F. Campabadal, "Investigation of the multilevel capability of TiN–Ti–HfO₂–W resistive switching devices by sweep and pulse programming", *Microelectronic Engineering*, vol. 187, pp. 148–153, 2018.
- [17] A. Marchewka, R. Waser, S. Menzel, "Physical modeling of the electroforming process in resistive-switching devices", *IEEE International Conference on Simulation of Semiconductor Processes and Devices (SISPAD)*, 2017.
- [18] Mesbah Uddin, Md. Badruddoja Majumder, Garrett S. Rose, "Robustness analysis of a memristive crossbar PUF against modeling attacks", *IEEE Transactions on Nanotechnology*, vol.16, pp. 396 – 405, 2017.

Publications by the Author

Journal Publications

- J1:** E. Salvador, M.B. Gonzalez, F. Campabadal, J. Martin-Martinez, R. Rodriguez, E. Miranda, ‘SPICE modeling of cycle-to-cycle variability in RRAM devices’, *Solid-State Electronics*, vol. 185, 108040, 2021.
- J2:** E. Salvador, M.B. Gonzalez, F. Campabadal, J. Martin-Martinez, R. Rodriguez, E. Miranda, ‘Assessment of the variability of the I-V characteristic of HfO₂-based resistive switching devices and its simulation using the quasi-static memdiode model’, *Solid State Electronics*, vol. 206, 108667, 2023.
- J3:** E. Salvador, R. Rodriguez, E. Miranda, ‘SPICE simulation of the time-dependent clustering model for dielectric breakdown’, *Solid-State Electronics*, vol. 215, 108895, 2024.
- J4:** E. Salvador, R. Rodriguez, E. Miranda, ‘A Simple, Robust, and Versatile MATLAB Formulation of the Dynamic Memdiode Model for Bipolar-Type Resistive Random Access Memory Devices’, *Journal Low Power Electronics and Applications*, vol. 14, no. 2, p. 30, 2024.
- J5:** E. Salvador, R. Rodriguez, E. Miranda, J. Martin-Martinez, A. Rubio, A. Crespo-Yepes, V. Ntinis, G. Ch. Sirakoulis, M. Nafria, ‘Noise-

induced homeostasis in memristor-based neuromorphic systems’, *IEEE Electron Device Letters*, vol. 45, no. 8, pp. 1524-1527, 2024.

- J6:** E. Salvador, R. Rodriguez, E. Miranda, J. Martin-Martinez, A. Rubio, A. Crespo-Yepes, V. Ntinis, G. Ch. Sirakoulis, M. Nafria, ‘Stochastic Resonance in HfO₂-Based Memristors: Impact of External Noise on the Binary STDP Protocol’, *IEEE Transactions on Electron Devices*, vol. 71, no. 9, pp. 5761-5766, 2024.
- J7:** E. Salvador, M.B. Gonzalez, F. Campabadal, J. Martin-Martinez, R. Rodriguez, E. Miranda, ‘Modeling and Simulation of Correlated Cycle-to-Cycle Variability in the Current-Voltage Hysteresis Loops of RRAM Devices’, *IEEE Transactions on Nanotechnology*, vol. 23, pp. 758-764, 2024.

Conference Contributions

- C1:** E. Salvador, M.B. Gonzalez, F. Campabadal, J. Martin-Martinez, R. Rodriguez, E. Miranda, " In-depth Analysis of the Statistical Distribution of RRAM Electrical Parameters Intended for Compact Modeling," *13th Spanish Conference on Electron Devices (CDE)*, Sevilla 3-5 Feb, 2021.
- C2:** E. Salvador, M.B. Gonzalez, F. Campabadal, J. Martin-Martinez, R. Rodriguez, E. Miranda, "SPICE modeling of cycle-to-cycle variability in RRAM devices," *22nd conference on insulating films on semiconductors (INFOS)*, Rende, Italy, 28 June-2 July 2021.
- C3:** E. Salvador, M. B. Gonzalez, F. Campabadal, J. Martín-Martínez, R. Rodríguez and E. Miranda, ‘One-way Sensitivity Analysis of the Quasi-static Memdiode Model for RRAM Devices’, *2021 IEEE 32nd International Conference on Microelectronics (MIEL)*, Niš, Serbia, 12-14 September, 2021.
- C4:** R. Rodriguez, J. Martin-Martinez, E. Salvador, A. Crespo-Yepes, E. Miranda, M. Nafria, A. Rubio, V. Ntinis, G. Ch. Sirakoulis, ‘Beneficial Role of Noise in Hf-based Memristors’, *2022 IEEE International*

Symposium on Circuits and Systems (ISCAS), Austin, TX, USA, 27 May-1 June, 2022.

- C5: E. Salvador, R. Rodriguez, E. Miranda, J. Martin-Martinez, A. Rubio, A. Crespo-Yepes, V. Ntinis, G. Ch. Sirakoulis, M. Nafria, "Stochastic resonance effect in binary STDP performed by RRAM devices," in *22nd IEEE International Conference on Nanotechnology*, Mallorca, Spain, 4-8 July, 2022-
- C6: E. Salvador, R. Rodriguez, E. Miranda, J. Martin-Martinez, A. Rubio, A. Crespo-Yepes, V. Ntinis, G. Ch. Sirakoulis, M. Nafria, "Microstrip Lines Loaded with Metamaterial-Inspired Resonators for Microwave Sensors/Comparators with Optimized Sensitivity," *37th Conference on Design of Circuits and Integrated Systems (DCIS)*, Pamplona, Spain, 6-8 November, 2022.
- C7: E. Salvador, R. Rodriguez, E. Miranda, J. Martin-Martinez, A. Rubio, A. Crespo-Yepes, V. Ntinis, G. Ch. Sirakoulis, M. Nafria, "Effect of Stochastic Resonance on Memristor-Based Binary Neuromorphic STDP Protocol" in *14th Spanish Conference on Electron Devices (CDE)*, Valencia, 6-8 June, 2021.
- C8: E. Salvador, R. Rodriguez, E. Miranda, "SPICE Simulation of the Time-Dependent Clustering Model for Dielectric Breakdown," in *23rd Conference on Insulating Films on Semiconductors (INFOS)*, Pizzo, Italy, 27-30 June, 2023

Workshop Contributions

- W1: E. Salvador, R. Rodriguez, E. Miranda, J. Martin-Martinez, A. Rubio, A. Crespo-Yepes, V. Ntinis, G. Ch. Sirakoulis, M. Nafria, "Stochastic resonance to produce homeostasis in memristor-based neuromorphic systems," in *1st Workshop on Memristors*, Barcelona, Spain, 1st of July, 2024.

